The University Of Sheffield.

CFD modelling of pulverised coal and biomass combustion

PhD Thesis

Katarzyna Sabina Stęchły

A thesis submitted in fulfilment of the requirements

for the degree of Doctor of Philosophy

The University of Sheffield

Department of Mechanical Engineering

Energy Engineering Group, Energy 2050

July 2019

The candidate confirms that the work submitted is her own, except where work which has formed part of jointly authored publications has been included. The contribution of the candidate and the other authors to this work has been explicitly indicated below. The candidate confirms that appropriate credit has been given within the thesis where reference has been made to the work of others.

Acknowledgements

I am indebted to my supervisors, Prof. Mohamed Pourkashanian, Prof. Derek Ingham and Prof. Lin Ma for the opportunity of undertaking the PhD research. I would like to express my gratitude to Dr Alessandro Pranzitelli for the support and encouragement. I am also grateful for the help of Dr Janos Szuhanszki and Dr Alastair Clements during the period of my PhD. Lastly, but not the least, I would like to thank my family and friends who have stayed by my side through the good and the harder moments of my PhD journey.

Abstract

The energy sector faces a challenge of providing energy with limited carbon dioxide (CO_2) emissions due to its contribution to climate change. Currently the energy mix is dominated by fossil fuels and coal is the major contributor of CO_2 emissions. Since biomass is classified as a renewable source of energy, its combustion is considered to have a near–zero CO_2 emission, and thus it supports the climate change targets. Therefore, to reduce emissions from coal combustion, coal can be depleted by the usage of biomass by either co-firing or full conversion to biomass. Nevertheless, biomass combustion needs more investigations and development in order to increase its efficiency and to reduce the potential operational problems.

Computational fluid dynamics (CFD) assists with the predictions of the combustion process and therefore, gives an opportunity to develop and design the efficient biomass conversion and this enables the retrofitting of coal fired boilers to biomass fuel.

In this thesis pulverised coal and biomass combustion experiments on the 250 kW UKCCRC PACT Combustion Test Facility have been performed. The experimental data have been used for validation of the CFD model of coal combustion. Further, an extensive sensitivity study of the sub-models for coal combustion has been performed to provide an accurate and reliable CFD model. The validated CFD model has been employed to biomass combustion to investigate the limitation of the CFD predictions. It has been found that irregular shape and large size of the biomass particles causes major impact on the biomass combustion discrepancies in the CFD model. Thus, an in-house code has been developed and the effect of the implementation of irregular shape and large size biomass particles compared with experimental data presented improvement in the CFD predictions.

Contents

List of Figures

List of Tables

Nomenclature

Latin symbols

A	Arrhenius pre-exponential factor
A	mass fraction of ash
A	surface area
Al_2O_3	aluminium oxide
b_ϵ	emissivity gas temperature polynomial coefficient
Bi	Biot number
C_1	mass diffusion-limited rate constant
C_2	kinetics-limited rate pre-exponential factor
C_d	drag coefficient
C_p	specific heat
CaF_2	calcium fluoride
Cl	chlorine
CO_2	carbon dioxide
CO	carbon monoxide
C	carbon
CH_4	methane

$\bar{d}$ mean diameter

d diameter

D_0 diffusion rate coefficient

E Arrhenius activation energy

Fe_2O_3 ferric oxide

$\dot{g}$ gravity

g mass fraction

h heat transfer coefficient

H_r heat of reaction

H_2 hydrogen

H hydrogen

h enthalpy

H_2O water

I radiation intensity

k kinetic rate

k_i absorption coefficient

k kinetic energy

k thermal conductivity

K_2O potassium oxide

l length

L_c characteristic length

m mass

M	molecular mass
N_2	nitrogen
n_s	spread parameter
NO_2	nitrogen dioxide
NO_x	nitrogen oxides
NO	nitrogen oxide
N	nitrogen
n	refractive index
n	stoichiometric coefficient
O_2	oxygen
O	oxygen
p	pressure
$\dot{Q}_{cond}$	heat conduction
r	radius
$\mathcal{R}$	kinetic rate
$\mathbf{r}$	position vector
Re	Reynolds number
S_b	Burnout Stoichiometric Ratio
$\mathbf{s}$	direction vector
$\mathbf{s}'$	scattering direction vector,
SiO_2	silicon dioxide (silica)
SO_2	sulphur dioxide

SO_x sulphur oxides

S sulphur

s path length

θ_R radiation temperature

T temperature

V volume

vol volatile matter

W water/moisture

A ash

W moisture

X dimensionless distance

Y_d mass fraction of particles with a diameter greater than d

z mole fraction

Greek symbols

α_ϵ emissivity factor

ϵ turbulence dissipation rate

κ absorption coefficient

λ excess air ratio

Ω' solid angle

ϕ_s scattering phase function

ρ density

τ Fourier number

τ stress tensor

σ_s scattering coefficient

θ dimensionless temperature

Subscripts

0 initial

ac actual

ar as received

comb combustible

cyl cylinder

daf dry ash free

fg flue gas

∞ infinity

i initial

max maximum

min minimum

ox oxidant

oxi oxidizer

p particle

ref reference

sph sphere

st stoichiometric

vap vaporization

vol volatiles

w moisture

Abbreviations

AFT Adiabatic Flame Temperature

AF Air-Fuel ratio

APGTF Advanced Power Generation Technology Forum

AR Aspect Ratio

ASU Air Separation Unit

BECCS Bioenergy Carbon Capture and Storage

CAD Computer Aided Design

CCS Carbon Capture and Storage

CFD Computational Fluid Dynamics

CPD Chemical Percolation Devolatilization

CTF Combustion Test Facility

DNS Direct Numerical Simulations

DO Discrete Ordinates

DPM Discrete Phase Model

DTRM Discrete Transfer Radiation Model

EOR Enhanced Oil Recovery

FSCK Full Spectrum K-Distribution

FC Fixed Carbon

FG – DVC Functional-Group Depolymerization, Vaporization, Crosslinking

GCV Gross Calorific Value

GDP Gross Domestic Product

GHG GreenHouse Gas

HTVY High Temperature Volatile Yield

HHV High Heating Value

HMI Human-Machine Interface

IGCC Integrated Gasification Combined Cycle

IPCC Intergovernmental Panel on Climate Change

LCV Lower Calorific Value

LES Large Eddy Simulations

Mtoe Million Tonnes of Oil Equivalent

NAEI National Atmospheric Emission Inventory

sd Standard Deviation

SNCR Selective Non-Catalytic Reduction

PACT Pilot-scale Advanced Capture Technology

PF Pulverised Fuel

PM Particulate Matter

ppm Parts Per Million

RSM Reynolds Stress Model

RANS Reynolds Averaged Navier Stokes

RFG Recycled Flue Gas

RR Recycle Ratio

RTE Radiative Transfer Equation

SA/V Surface-Area-to-Volume Ratio

S2S Surface-to-Surface

SCADA System Control And Data Acquisition

SCR Selective Catalytic Reduction

SF Shape Factor

SIR Surface Incident Radiation

TGA Thermogravimetric Analyzer

UDF User Defined Function

UKCCSRC U.K. Carbon Capture & Storage Research Centre

UNFCCC United Nations Framework Convention on Climate Change

VM Volatile Matter

VOCs Volatile Organic Compounds

WSGG Weighted Sum of Gray Gas

Chapter 1

Introduction and motivation

This chapter provides an introduction to coal and biomass combustion for power generation. Firstly, general information on the current state of world energy demand is summarized in Section 1.1, followed by description of global carbon dioxide emissions in Section 1.2. In Section 1.3, the correlation between carbon dioxide emissions from coal combustion and global warming has been presented. Then, in Section 1.4, the near–zero carbon technologies are listed, focusing on coal and biomass combustion. A summary of carbon capture and storage technologies is described in Section 1.5. Next, the introduction to computational modelling techniques of combustion processes is given in Section 1.6, and this is followed by the aims and motivations of this thesis, which are summarized in Section 1.7. The research covered in this thesis is outlined in Section 1.8.

1.1 World energy demand

World energy consumption is constantly increasing and this growth is expected to continue [1–6]. Population and income are the key drivers behind the growing demand for energy [2, 4, 7].

The global economy is expanding at an average rate of 3.4% per year.

Also, the world's population has almost doubled in the past 40 years, from 4.1 billion in 1976 to 7.7 billion in 2018 [8] and it is projected to grow to more than 9 billion in 2040 [9]. As depicted in Figure 1.1, the world's population is projected to increase by an estimated 30% from 2010 to 2040 [10]. The largest contribution to demand growth, almost 30%, comes from India, whose share of global energy use is expected to rise to 11% by 2040 [9]. At the same time, the global GDP will rise by about 140% according to ExxonMobil projections [10]. As the technology develops and the world economy expands, more energy will be required to fuel the higher levels of activity and living standards [2,4,7]. However, the energy demand is projected to increase only by about 35% due to greater efficiency [10].

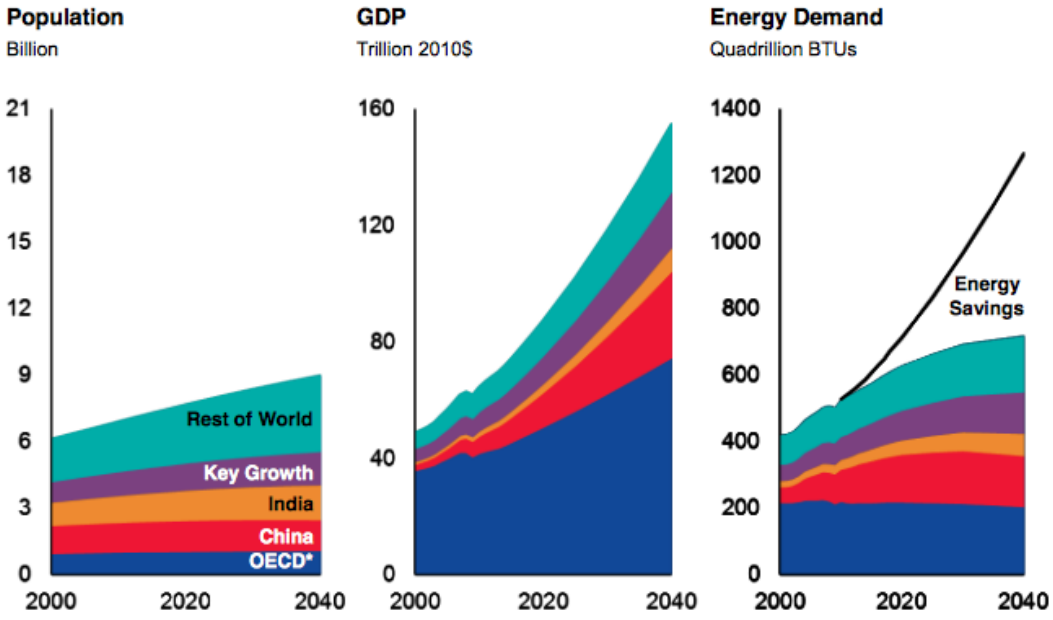

Figure 1.1: Predicted world population, global GDP and world energy demand between 2000 and 2040 [10].

World primary energy consumption grew by 2.9% in 2018, up from 2.2% in 2017 and the highest since 2010 and almost double the 10-year average, see Figure 1.2. The growth was below average in Asia Pacific, the

Middle East and South and Central America, but above average in other regions [5]. The total final world energy consumption has increased by over 15% in the past 10 years, from 11,705 million tonnes of oil equivalent (Mtoe) in 2008 to 13,865 Mtoe in 2018 [11]. Under current and planned policies, modelled in the New Policies Scenario, energy demand is set to grow by more than 25% by 2040, requiring more than $2 trillion a year of investment in new energy supply [12].

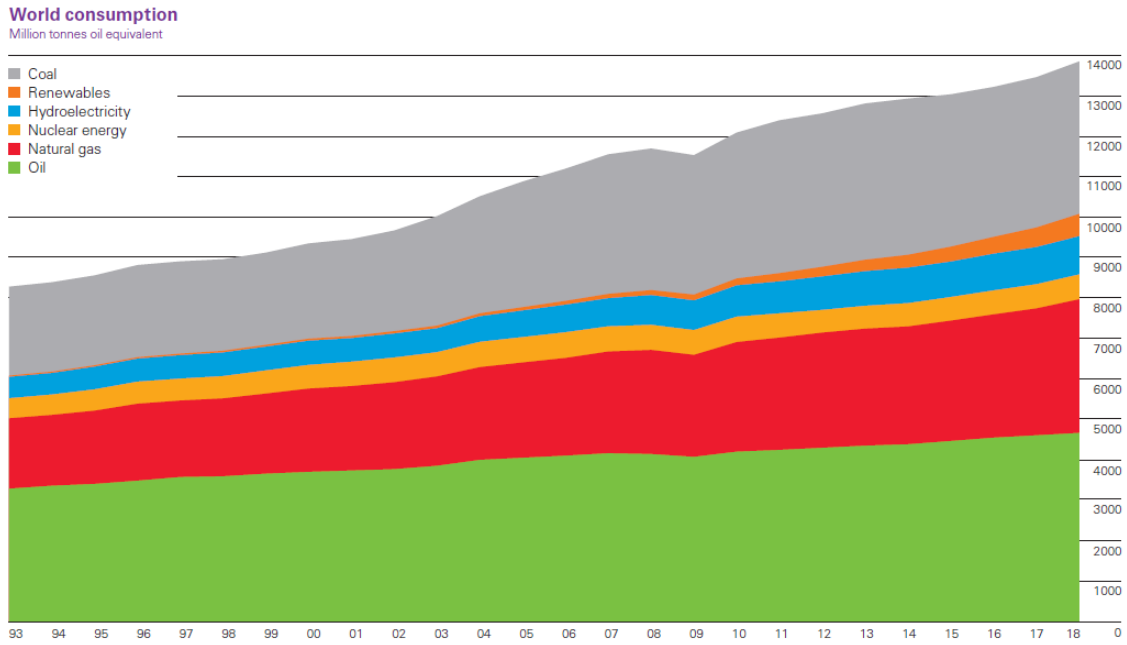

Figure 1.2: World primary energy consumption by fuel in Million tonnes oil equivalent between 1993-2018 [11].

Fossil fuels remain the dominant source of energy powering the global economy, providing about 60% of the growth in energy and accounting for almost 80% of the total energy supply in 2035 (down from 86% in 2014) [2, 13]. Even though renewable and nuclear energy sources are expected to grow faster than fossil fuels [13], the growth is not sufficient to keep pace with the strong gains in energy demand [11]. As presented in Figure 1.2, in 2018, oil remains the world's dominant fuel, making up just over a third of all the energy consumed. Coal's market share fell to

27%, the lowest level since 2003. Natural gas accounted for a record 24% of global primary energy consumption, while renewable power hit a new high of 4% [11] as can be observed in Figure 1.3.

Coal is the world's slowest-growing energy source, rising by only 0.6% per year through to 2040 [13]. However, in 2018 the coal consumption increased at its fastest rate since 2014 [11]. The vast majority of the coal consumption and production is concentrated in Asia. China alone currently accounts for almost half of the world's total coal consumption and production [13]. However, the slower growth of China's energy demand is related to the economy rebalance [2] and plans to implement policies to reduce carbon dioxide emissions mean that coal use in China will begin to decline [13]. Hence, the slow growing rate of coal throughout the projection period is influenced by the Chinese economy [2].

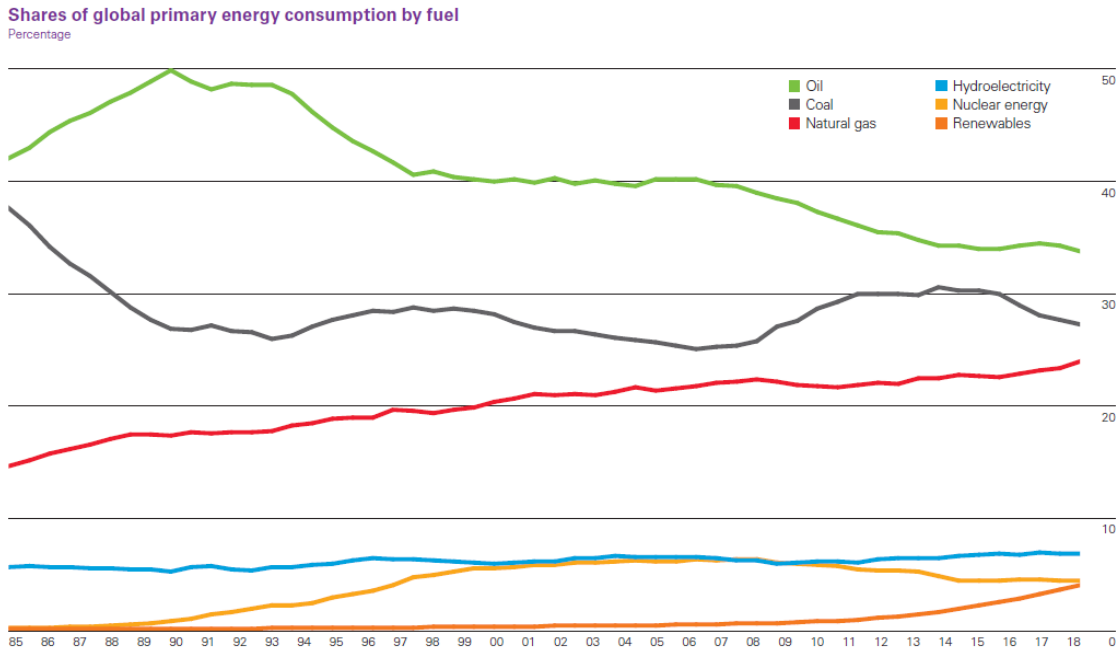

Figure 1.3: World primary energy consumption by fuel in % between 1985-2018 [11].

More than a half of the increase in global energy consumption is used for power generation. The share of energy used for power production will

continue to increase gradually from 42% in 2016 to 45% by 2035 [2]. Also, the fuel mix for power generation continues to shift, as depicted in Figure 1.4. The share of coal remains dominant, however it is predicted to decline from to about a third in 2035. In contrast, the share of non-fossil fuels will increase, reaching nearly 45% by 2035 [2].

In the long term, fossil fuel use must decline along with the declining reserves; however it is not projected to occur in the near future. In order to secure the increasing energy demand, more research and development in renewable sources of energy and efficiency of fossil fuel consumption is required.

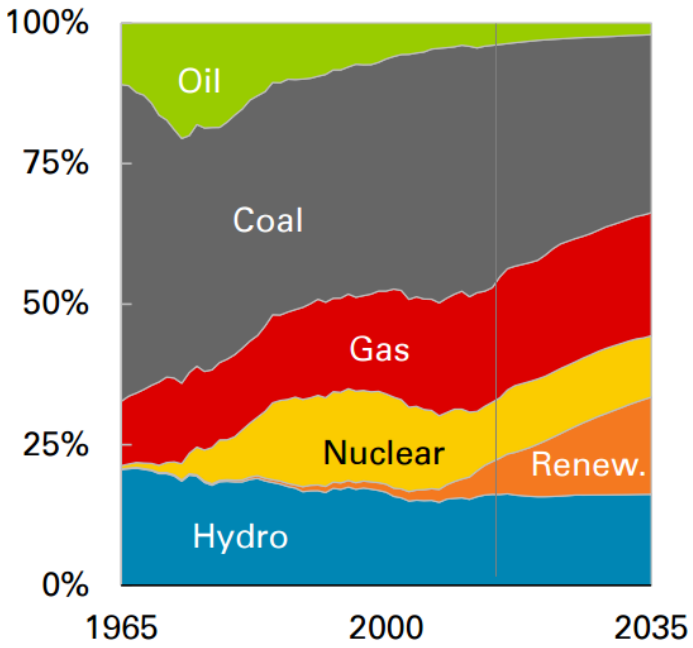

Figure 1.4: Primary inputs to power power generation by energy source in % between 1965-2035 [2].

1.2 CO_2 emissions

Worldwide increases in energy demand, coupled with a continued reliance on fossil fuel resources, have contributed to a significant increase

in the atmospheric levels of carbon dioxide (CO_2) [14]. In 2018, the CO_2 emissions grew by 1.7% to reach a historic high of 33.1 $GtCO_2$ (see Figure 1.6). It was the highest rate of growth since 2013, and 70% higher than the average increase since 2010. While emissions from all fossil fuels increased, the power sector accounted for nearly two-thirds of emissions growth. Coal use in power alone surpassed 10 $GtCO_2$, mostly in Asia. Moreover, the projection shows that the increments will continue with major contributions from liquid fuels and coal [7, 12, 13, 15, 16].

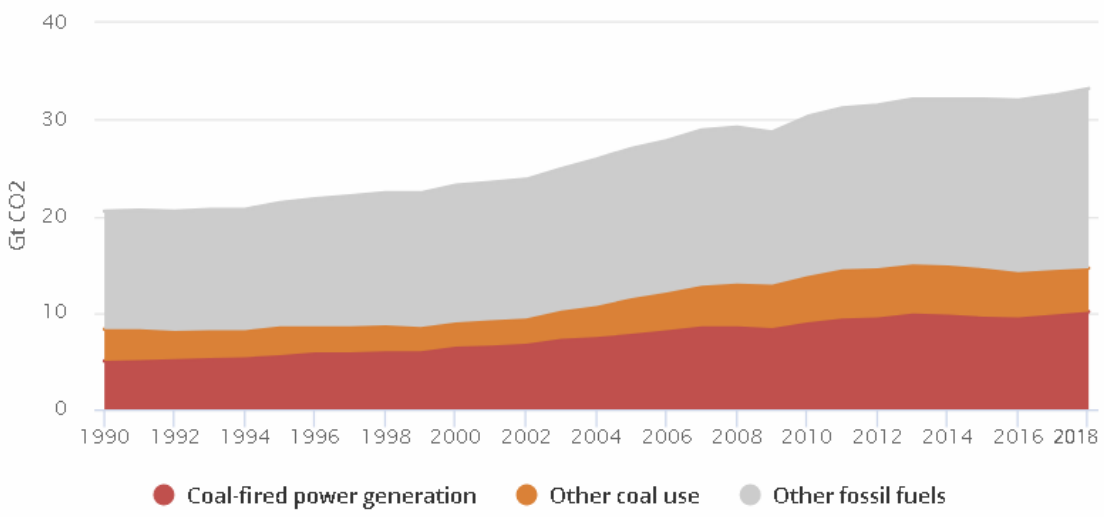

Figure 1.5: World energy-related CO_2 emissions by energy source between 1990 - 2018 in $GtCO_2$ [17].

In the Sustainable Development Scenario, low-carbon sources will double their share in the energy mix to 40% in 2040 and all avenues to improve the efficiency are being pursued with the coal demand going into an immediate decline and oil consumption will peak soon thereafter. The decarbonisation of power generation by 2040 relies on the electricity generation from renewables (over 60%), nuclear power (15%) as well as a contribution from carbon capture and storage (6%) - a technology that plays an equally significant role in cutting emissions from the fossil fuel

combustion [9].

1.3 Global warming and climate change

Greenhouse-gas emissions from the energy sector, especially fossil fuels, and a small fraction from cement production, represent approximately two-thirds of all greenhouse gas (GHG) emissions as seen in Figure 1.6. It is easily noticeable that CO_2 emissions from fossil fuel based power generation have risen over the past century. Atmospheric concentrations of CO_2 have now reached the 400 ppm level, which is considered to be its highest level in the last three million years [16], and this is approximately 40% higher than in the mid-1800s [7]. To reduce the CO_2 concentration in the atmosphere, we need to not only prevent further growth of the CO_2 emissions, but also decrease it significantly.

Carbon dioxide is not the only greenhouse gas of concern for global warming and climatic change. There are a range of greenhouse gases, which include methane, nitrous oxide, and a range of smaller concentration trace gases such as the so-called group of 'F-gases' [16]. It has been found that CO_2 and other GHG alter the Earth heat balance, and this is due to their radiation properties and acting as a one-way screen, thus causing the greenhouse effect [18]. Hence the rise in the accumulation of GHG in the atmosphere is believed to be a key driver of global warming and consequentially climate change [19].

As seen in Figures 1.6 and 1.7, a correlation between an increase in the average global temperature and the CO_2 concentration in the atmosphere has been observed [16, 18–20]. Both figures start at the time of the Industrial Revolution and since then the global average temperature has risen above the 1961-1990 baseline temperature. Also, it can be observed that that the average global temperature growth is correlated with the increased concentration of CO_2 in the atmosphere [16, 18–20].

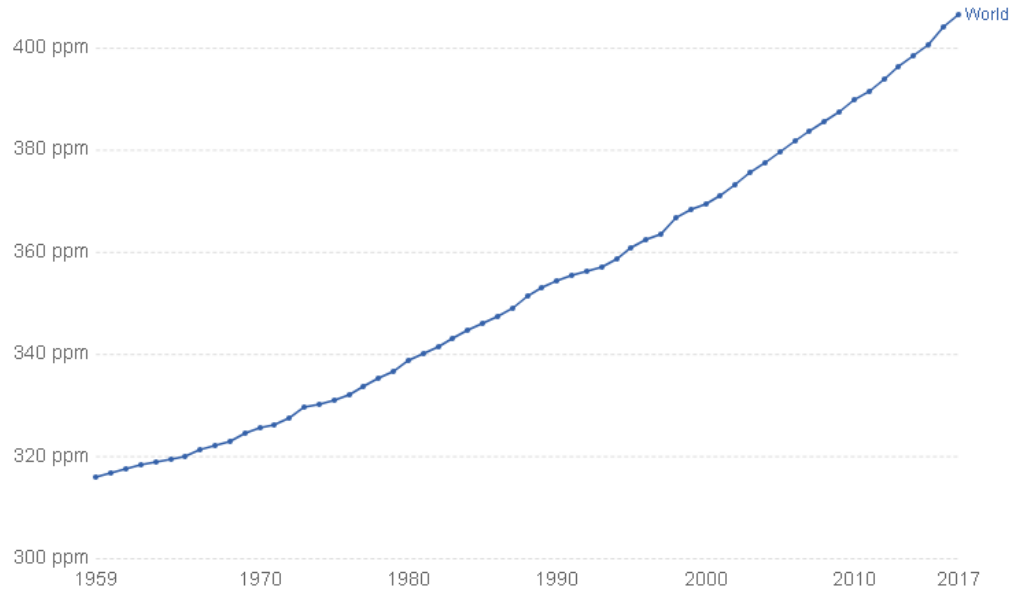

Figure 1.6: Global CO_2 emissions since 1850 [20].

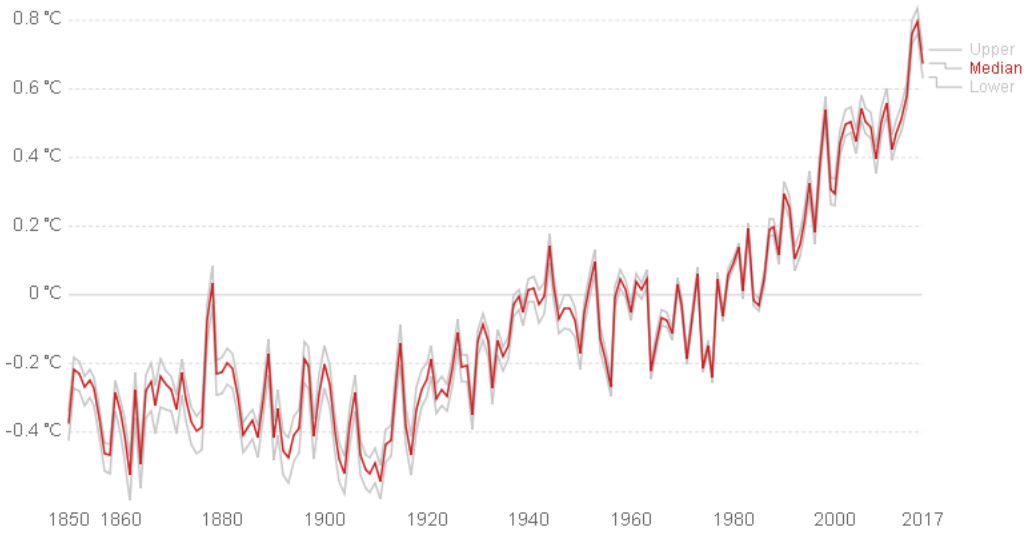

Figure 1.7: Global average temperature since 1850 [16].

Changes in climate related to the accumulation of GHG in the atmosphere have caused impacts on natural and human systems on all continents and across the oceans. Warming of the climate system is unequivocal, it has been observed that with the increment of the average global air temperatures, the sea ice, mountain snow and glaciers have dimin-

ished, and the global mean sea levels have risen and oceans have warmed and acidified [21, 22]. Effective action in the energy sector is, consequentially, essential to tackling the climate change problem [20].

Beginning in the early 2000s, concerns about the environmental consequences of GHG emissions heightened interest in the development of near-zero emission technologies and renewable energy sources [13]. The United Nations Framework Convention on Climate Change (UNFCCC) provides a structure for intergovernmental effort to stabilize GHG concentrations in the atmosphere at a level that would prevent dangerous anthropogenic interference with the climate system. The main target agreed by all the parties to the UNFCCC is to limit the upward trend in the average global temperature to be below 2°C above the preindustrial level [7].

1.4 Near-zero emission technologies

Given the potential danger of increasing CO_2 emissions in the atmosphere, and the associated global warming and climate change, some effort has been undertaken to reduce CO_2 emissions from electricity and heat generation – the main producers of the world CO_2 emissions [7]. The UK, in particular, has set the ambitious target of reducing its GHG by 80% by 2050 against a 1990 baseline [23–25].

There are several ways of cutting CO_2 emissions, e.g. the production of energy from renewable sources of energy or nuclear power plants.

Nuclear power has been the subject of continuous political debate. On the one hand, it is a low-GHG emitting technology, and hence could make a significant contribution towards reducing GHG emissions.
Moreover, the support for energy generated in nuclear power plants has grown [26]. On the other hand, other issues persist, namely public awareness and health, nuclear safety risk, fueling reservations or disposal of radioactive wastes [26].

Renewable sources of energy, such as wind, sun, wave/tides, geothermal have the potential for near zero CO_2 emission and are expected to be popular in the foreseeable future. However, currently they are not available in the quantities required to address the rising energy demand [27]. In addition, there is a need for improvement in energy storage capacity development and this is because of some of the renewable sources of energy, namely wind and solar, being intermittent [4, 19]. However, biomass is also considered as a renewable source of energy and has a potential for large scale heat and power production. This is described in more detail in Section 1.5.4.

Nevertheless, coal holds the main position in the global energy demand. This is because its resources exist in abundance in many developing countries [4] and due to its proven stability in supply and cost. Therefore the improvement of the coal-fired power generation is urgently required. Consequently, a target for the reduction of GHG emissions has driven the development of the coal-based near-zero emission technologies [7], and several possibilities can be perceived [27]:

- improving the efficiency of the coal-fired power plants,
- introduction of combined cycles,
- carbon capture and storage (CCS),
- co-firing coal with biomass or retrofitting to biomass combustion.

The incremental reduction of GHG can be achieved by a stepwise implementation of the efficiency improvement of the power plants, but it has limitations and cannot reduce CO_2 emissions sufficiently. To improve the efficiency of electricity production, there is a need to increase the temperature inside the combustion chamber to achieve steam which has a higher temperature and pressure, and hence more power is generated. However, the temperature increment is limited due to the material strength.

The technology that can make a significant reduction in the GHG emissions from the coal-based energy sector is Carbon Capture and Storage (CCS). This technology is designed to capture CO_2 emissions from industrial facilities before the CO_2 in the flue gas is emitted to the atmosphere. Therefore, the CO_2 produced at fossil-fuel fired power plants is collected, and then the captured CO_2 is transported through pipelines to convenient storage locations, where it is pumped into deep, secure underground rock formations, where the CO_2 is permanently stored without contact with the atmosphere.

The biomass co-firing with coal and retrofitting to biomass combustion is being considered as an important step in reducing environmental emissions. Co-firing biomass with coal and pure biomass combustion can significantly reduce the CO_2 emissions. Moreover, combining biomass combustion with CCS can have an effect in negative CO_2 emissions [28], which is explained in more detail in Section 1.5.5.

1.5 Carbon Capture and Storage

Carbon capture and storage (CCS) refers to a set of technologies that can greatly reduce CO_2 emissions from new and existing fossil fuel fired power plants, industrial processes, and other stationary sources of CO_2. An application of CCS technology to electricity generation can play an important role in achieving national and global GHG reduction goals. However, widespread cost-effective deployment of CCS will occur only if the technology is commercially available and a supportive national policy framework is in place [29].

The IPCC has declared that CO_2 produced during the combustion of fossil fuels process needs to be captured and geologically stored, because of its great potential for GHG emission reduction from coal-based energy production systems [21, 27, 30]. CCS allows for significant reductions in

CO_2 emissions from fossil-based systems. It can capture about 90% of the CO_2 from the burning of fossil fuels for power generation [14]. Thus, the CCS can reduce CO_2 emissions by over 10 $GtCO_2$ by 2050 [7] in order to meet the emissions reduction challenge. Therefore, it is a critical option in the portfolio of solutions available to combat climate change.

The International Energy Agency states that, as long as fossil fuels based industries and power plants play a dominant role in our economy and energy demand, CCS will remain a critical GHG reduction solution [7]. Additionally, without CCS, the overall costs to reduce emissions of CO_2 to 2005 levels by 2050 is predicted to increase by about 70% [7, 25].

The CCS chain comprises three main steps: CO_2 capture, transport and storage, see Figure 1.8. In power plants, CO_2 is a product of fossil fuel combustion and it is present in the exhaust gases. Separation of the CO_2 from the flue gases is called CO_2 capture. Captured gas with a high purity of CO_2 is separated by simple water condensation and downstream purification [31]. Separated CO_2 passes through a conditioning process to meet requirements before being transported [14, 31, 32]. CO_2 is then conveyed by a pipeline to suitable locations and stored for indefinite isolation from the atmosphere. This refers to the safe and secure storage of the carbon dioxide, for example in geological formations underground, or under the sea [14, 31–34].

1.5.1 CO_2 Capture

CCS is a broad term that encompasses a number of technologies. Capture of the CO_2 from the flue gases requires a modification of the traditional process. The approaches to separate the CO_2 are classified based on the method of modification of this process [7]. Capture technologies can be divided into three main categories [7, 27, 30, 32, 36–38] as outlined in Figure 1.9:

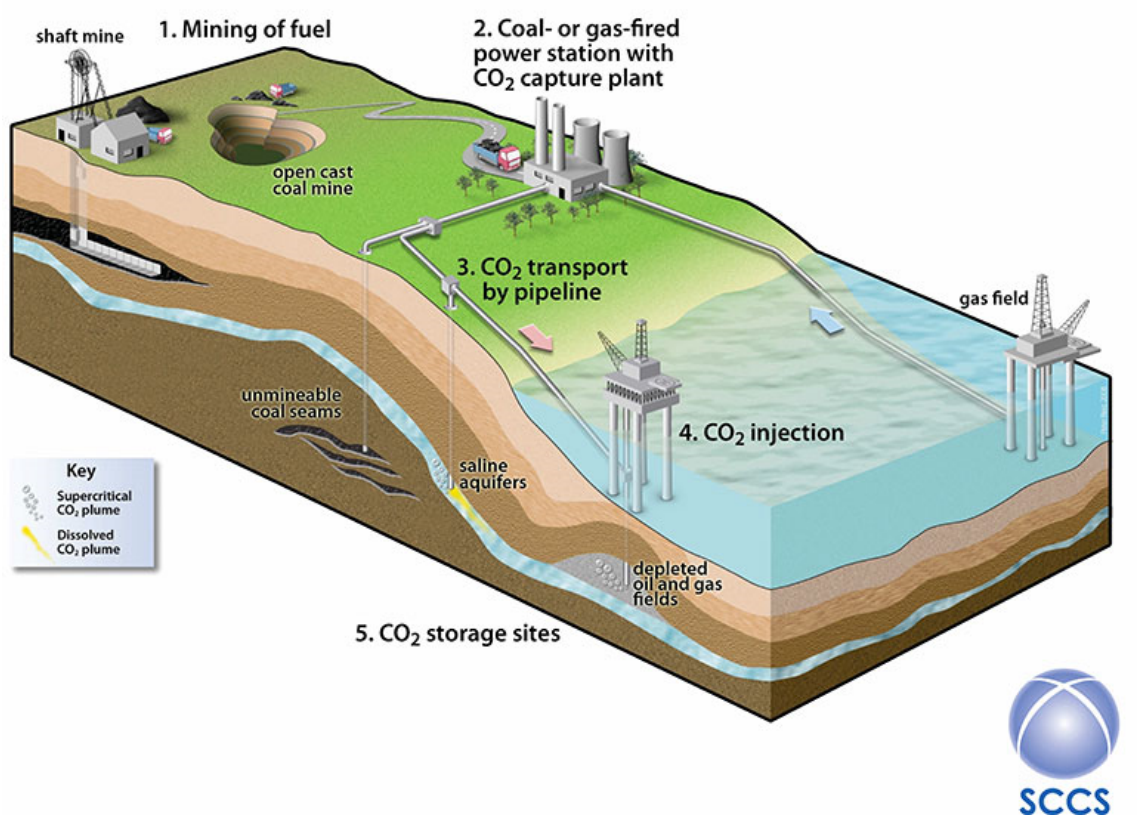

Figure 1.8: Schematic of the idea behind CCS [35].

- Post-combustion capture
- Pre-combustion capture
- Oxy-fuel combustion

1.5.1.1 Post-combustion

CO_2 in post-combustion processes is captured from the exhaust gases without any changes in the combustion process [7, 30, 39] as depicted in Figure 1.9. However, it requires an addition of a capture and compression system. Separation of CO_2 from the flue gas is performed by absorbing it in a suitable solvent. Once the CO_2 is absorbed, it is liberated from the solvent and then it is compressed for transportation and storage [14]. As the technology is commercially available, they can be retrofitted to existing power plants [30].

The post-combustion capture method is typically performed by the chemical absorption of CO_2 from the flue gas using an amine solvent e.g., monoethanolamine. Absorbed CO_2 is then released from the solvent-CO_2 mixture by heating to form a high purity CO_2 stream. Prior to the capture devices, the exhaust gases require cleaning from sulphur oxides and particulate matter [14]. Other methods for separating CO_2 from the flue gas include high pressure membrane filtration, adsorption/desorption processes and cryogenic separation [14].

The absorbing solvents lean the CO_2 in the flue gases in the scrubber, but its regeneration requires a large amount of energy in a stripper. The challenge is to reduce the energy requirements to avoid the energy penalty and associated costs for the capture unit [30, 34]. The United States National Energy Technology Laboratory estimated that CO_2 post-combustion capture would increase the cost of electricity production by 70% [34, 40]. A recent study reported that the cost of electricity would increase by 65% for post-combustion in coal-fired plants [34, 41].

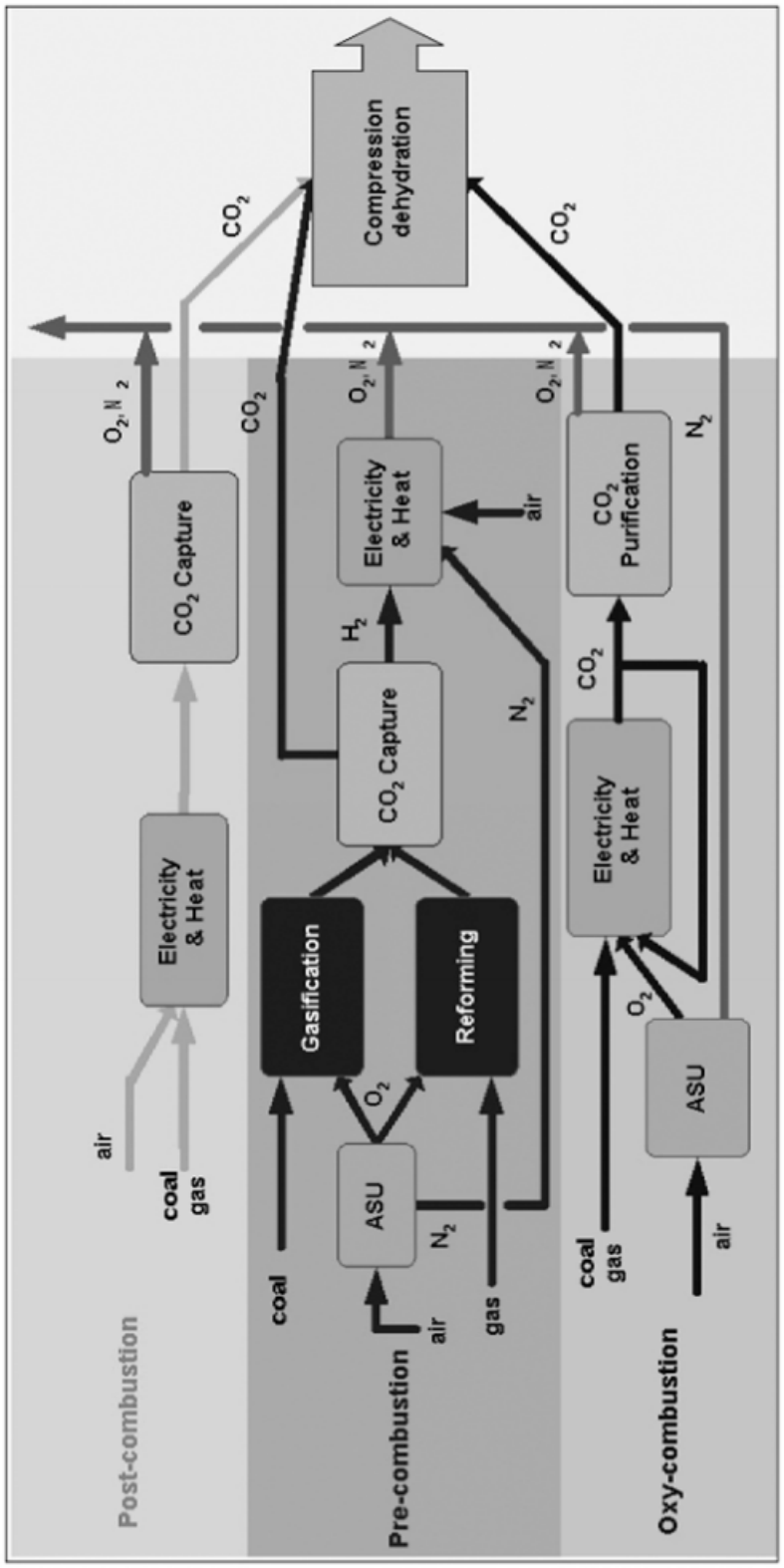

Figure 1.9: A schematic of the main CO_2 capture technologies [41].

1.5.1.2 Pre-combustion

Pre-combustion is a process when the capture of CO_2 is performed before combustion, as presented in Figure 1.9. The fuel is pretreated and converted into a mix of hydrogen (H_2) and CO_2. CO_2 is then separated from H_2, and the H_2 can be burned in a gas turbine, whereas CO_2 is compressed and transported to safe underground storage [7, 14, 30, 39].

Coal pretreatment involves a gasification process. Using a controlled amount of oxygen (O_2) from an air separation unit and water, the hydrocarbon fuel gasification is applied to produce a synthesis gas (syngas) containing carbon monoxide (CO), CO_2 and H_2. Then, a water-gas shift reactor is used to convert CO in the syngas and steam to CO_2 and H_2. This increases the concentration of CO_2, improves the CO_2 capture efficiency and increases the amount of carbon (in the form of CO_2) that can be removed using this process. CO_2 is then separated from the syngas and after conditioning it is transported to a storage site [7, 14, 30, 39]. The H_2 produced is then used as a zero-carbon fuel and can be combusted in a gas turbine to generate electricity and therefore can be applied to Integrated Gasification Combined Cycle (IGCC) with CCS [14, 39].

The hydrogen produced by these processes may be used, not only to fuel the electricity production, but also in the future to power cars and heat houses with near zero emissions [14].

The main disadvantage of this technology is the efficiency loss associated with the use of synthesis gas and the high capital and operating costs for current sorption systems [34].

1.5.1.3 Oxy-fuel combustion

Oxy-fuel combustion technology is possible by the substitution of air by almost pure O_2 and the recycled flue gas (RFG) to replace the nitrogen (N_2) [39]. As a consequence, the high CO_2 concentrated capture-ready gas stream is achieved, which increases the purification efficiency prior to

compression and transportation to underground storage [14]. This capture method is a mature technology being commercially deployed in industry [25, 27, 30, 34, 39].

Oxy-fuel combustion, the most promising technology for CCS, has been developed to achieve a capture-ready gas stream, which makes the sequestration process more efficient and economic. The conventional combustion process results in flue gas emissions, and the CO_2 is present in flue gases as a dilute gas. Whereas, the oxy-combustion results in a high concentration of CO_2 in the flue gas.

The oxy-fuel combustion is the technology which can be used for the retrofitting of existing power plants [36]. Conventional boilers use air as an oxidizer in the combustion process, and hence the main component in the flue gas is nitrogen (N_2), as its concentration in air is approximately 79% by volume. In the oxy-fuel combustion, air is replaced with oxygen and a RFG mixture as visible in Figure 1.9, which results in significant changes in the composition of the exhaust gas. This oxygen-rich, almost nitrogen-free atmosphere results in flue gases consisting mainly of CO_2 and H_2O. The flue gas produced in the oxy-fuel combustion process has a higher concentration of CO_2 and lower emissions of nitrogen oxides (NO_x) compared with the flue gas achieved in the air combustion. As a result, the flue gas produced in the oxy-fuel case is suitable and ready for more efficient sequestration processes. However, the compressed flue gas may have to be further cleaned of co-constituents to reach the transportation conditions [14].

Figure 1.10 presents a basic schematic of an oxy-fuel combustion system with RFG. Almost pure oxygen is supplied to the boiler (typically of greater than 95% purity [27, 39]). Pure O_2 is produced in a cryogenic air separation unit (ASU), which separates the O_2 and N_2 from the atmospheric air. The RFG in the oxy-fuel combustion process can be recycled in the form of a dry or wet mixture, depending on whether the flue gas

is dried and the water vapour is condensed out or not [39, 42]. The flue gas is recycled back to the combustion chamber to replace the N_2 in order to control the flame temperature [27, 36, 39] and make up the volume of the missing N_2 to ensure there is sufficient gas to carry the heat through the boiler [39]. The mass fraction of the flue gas recycled back to the combustion chamber to the total amount of the flue gas generated in the combustion process is called the recycle ratio (RR) [36, 42].

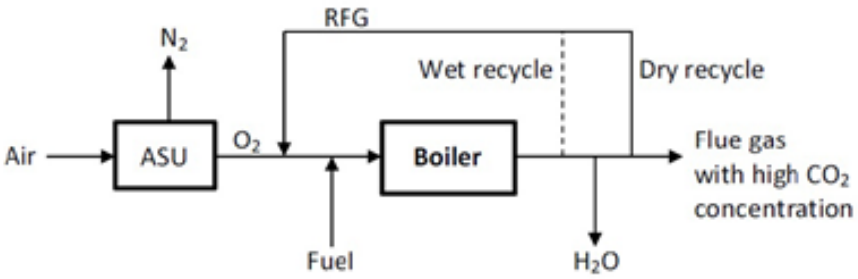

Figure 1.10: A schematic of a typical oxy-fuel system [43].

The difference between air and oxy-combustion has been observed due to the difference in the oxidizer composition and as a result the physical and chemical phenomena occurring in the combustion chamber. Some of these effects can be explained by the difference in density, heat capacity and radiative properties of N_2 and CO_2, the main diluting gases in air and oxy-fuel combustion, respectively [39, 44].

Nevertheless, it is possible to achieve similar temperatures during oxy-fuel combustion as in air-combustion by adjusting the recycle ratio of recycled flue gas and the oxygen fraction of the O_2/CO_2 mixture at the inlet to the boiler. Therefore, maintaining similar heat flux profiles in the furnace as in conventional air-firing allows the oxy-fuel technology to be applied to existing power plants.

Oxy-fuel combustion is seen as one of the major and the most competitive technology options for CO_2 capture for future clean coal technologies [39]. The main advantage is that oxy-fuel combustion is pos-

sible for retrofitting to existing power plants [25, 27, 30, 34, 39]. However, application of oxy-combustion results in an efficiency drop and energy penalty as the cryogenic CO_2 production in the air separation unit is costly [30, 34, 39].

1.5.2 Transportation

Transportation of CO_2 from point-of-capture to storage sites is an important linking step between capture and storage of CO_2 in the CCS project cycle. It is the most technically mature part among the other CCS steps [7, 14].

The CO_2 can be transported in a gas, liquid and solid state. Commercial-scale transport uses tanks, pipelines and ships for gaseous and liquid carbon dioxide. CO_2 transported at close to atmospheric pressure conditions occupies a large volume. The more compressed CO_2, the less volume it occupies. The volume can be further reduced by liquefaction or solidification [45].

Pipelines are the dominant mode of transporting compressed CO_2, as it is considered to be the most cost-effective and reliable method of transporting CO_2 for onshore CCS. Also it can deliver a constant and steady supply of CO_2 without the need for storage. However, ships and tanker trucks may also be utilised for this purpose [14].

The CO_2 transportation is a mature and proven technology. There is significant experience with CO_2 pipeline development and operation onshore and off-shore. There are already millions of kilometres of pipelines in the world that transport various gases, including CO_2. Just in the United States there is an estimated 6000 km of CO_2 pipelines which transport approximately 50 million tonnes per annum of CO_2, mainly for enhanced oil recovery operations [7, 14, 29]. There is also a good experience of using offshore pipelines in Norway [7].

1.5.3 Storage and utilization

The last element of CCS is the CO_2 storage, which involves injection of CO_2 approximately 1-3 km under the ground into the appropriate geological formation which may be onshore or offshore. The largest potential capacity for CCS is in saline formations, and it is this significant capacity that drives interest in CCS as a climate change solution [21]. However, there are other suitable locations, such as depleted oil or gas fields and potentially deep unmineable coal beds, basalts, or other formations [7, 14].

This technology is also known and has already considerable experience. The oil and gas industry has used CO_2 for enhanced oil recovery (EOR) for decades [7, 14]. Also CO_2 has been injected into carefully selected underground sites at a number of industrial-scale CCS projects. The evidence from monitoring confirms that the CO_2 has been completely and safely sealed in the geological formations [7, 14].

The challenge with geological storage is that no two sites are alike, even within the same geological formation. Hence, there is significant need for the flexibility, rather than standards and technical requirements for the siting, design, operation, and closure of storage projects [7, 14].

1.5.4 Biomass combustion

Biomass combustion has a potential of almost zero CO_2 emissions, provided that the biomass crops are based on the sustainable agricultural methods and harvested plants are replaced with another generation of biomass plantations consuming CO_2 from the atmosphere during its growth [46]. Hence, biomass combustion has a potential of producing nearly CO_2 emission free energy, which is important when considering the global warming and climate change. Energy production from the biomass increases the fuel diversity for power generation, and therefore the energy supplies security [47]. Moreover, it can replace the use and most of all it can decrease the dependency on the fossil fuels, such as coal, natural

gas, and oil [47]. Furthermore, biomass is becoming popular because it is seen to be the only sizeable renewable source of energy for large-scale power generation when it is needed and it can follow the increasing energy demand [46].

The biomass fuel for the large scale power generation rarely has been used, but retrofitting coal fired boilers to co-firing or pure biomass combustion and development of boilers designed to fire biomass fuel is already being employed. For example, on a domestic scale, in the UK between 2012 and 2015, Drax power station has proved the biomass combustion technology to be practical and commercially viable [48]. In 2016, Lynemouth coal-fired plant has been converted into a biomass-fueled power plant [49].

Biomass fuel combustion for large scale plant operation benefits in reduction the NO_x, SO_2, dust and CO_2 emissions, and thus it supports the climate change targets. Nevertheless biomass combustion needs more investigation and development to reduce the potential operational problems and increase efficiency of biomass combustion.

1.5.5 Biomass with CO_2 Capture and Storage

Bioenergy with CO_2 Capture and Storage (BECCS) is the combination of Carbon Capture and Storage with sustainable biomass conversion. Carbon Capture and Storage, as mentioned in Section 1.5, is an innovative technology that can reduce levels of CO_2 emitted to the atmosphere by fossil fuels. However, application of the biomass fuel combustion to the CCS technique can be a method of further reduction of the CO_2 concentration in the atmosphere. The BECCS is the only large-scale technology that can achieve net negative emissions of CO_2.

Since the biomass combustion is considered to be carbon and climate neutral, the biomass combustion with CCS technology may result in the negative CO_2 emissions, and potentially could have a beneficial effect on

the climate change. Yet BECCS is, to a large extent, an unexplored avenue of action, with a number of complex questions to be analysed and answered [50].

Recently, the Drax power station has become the world's first BECCS plant and therefore, the world's first negative emissions power station. The first CO_2 has been captured with employment of the C-Capture technology demonstration project enabling to capture one tonne of CO_2 a day [51].

Studies indicate a large global technical potential for BECCS: a removal of about 10 billion tonnes of CO_2 from the atmosphere every year by 2050 – equivalent to about a third of all current energy-related CO_2 emissions worldwide [50]. A potential of 800 Mt of negative emissions is highly significant for delivering an overall decarbonisation target of 80-95% by 2050 [50].

The oxy-combustion is a strong contender to be the preferred technology regarding CO_2 capture from biomass combustion. The oxy-combustion is relatively a new technology compared to air-combustion. Moreover, biomass combustion is not investigated as much as the coal-combustion. Hence, biomass combustion has to be investigated in detail in order to develop a reliable biomass combustion technology that is ready for firing in an oxygen regime for BECCS purposes.

1.6 Combustion CFD modelling

Computational Fluid Dynamics (CFD) is an engineering tool which can be used to model several processes involving fluid flow, heat transfer and associated phenomena, such as chemical reactions by means of computer based simulations [52]. Over the past few decades, the field of CFD has been developed due to the continuing increase in high performance computing and the improvements in the understanding of the physical and chemical phenomena underlying CFD theory [53].

Presently, CFD is becoming a critical part in the design process for a wide range of industrial and non-industrial topics of application. Some examples are as follows: power generation, aerospace, biomedical engineering, meteorology, environmental engineering and chemical engineering. CFD modelling allows the calculation of various scenarios without the need of constructing different models. Therefore, it increases the efficiency of the design process, reduces the cost and time, and moreover, it assists in the finding of the most efficient solution for optimised designs.

The CFD modelling is an essential tool of biomass combustion technology development and it has been well justified in [54]. Modelling of combustion improves the understanding of the fundamental processes involved in solid fuel combustion, as it can give an insight into the combustion process.

CFD was found to predict accurately the coal combustion performance. A CFD code has been validated for the coal combustion and employment of this technique, including additional extension, can be possible to predict biomass combustion [55]. Currently, the 100% biomass combustion for energy generation is not widely used and therefore little has been published. Therefore, further investigation into CFD modelling is needed to understand the process of biomass combustion and this will help to develop technology related to biomass combustion.

1.7 Aims and objectives

The current stage of knowledge underlying biomass combustion and the ability to predict real industrial processes need to be developed. Hence the studies in this thesis will assist in the understanding of several different phenomena behind the biomass combustion process and moreover, will assist in providing a numerical model that is applicable to industrial facilities in large scale power plants. Since it is important to provide a nu-

merical model that is validated with experiments to find the most efficient solution for application of biomass combustion for CCS technology, and therefore allow this technology to reach its full potential and to be used commercially.

The main objectives of the PhD are as follows:

- experimental investigation of the coal combustion in the 250 kW combustion test facility;
- validation of the CFD model for coal combustion with the experimental data;
- experimental investigation of the biomass combustion in the 250 kW combustion test facility;
- perform time-averaged RANS simulations in a combustion test facility (CTF) under air conditions for both coal and biomass and investigate the differences between the fuels in terms of species compositions, temperature profiles and heat flux distributions.
- application of a CFD model validated for coal combustion for biomass combustion numerical predictions and identification of the limitation of that model;
- develop a CFD model for biomass combustion with emphasis on development of the sub-models for biomass combustion incorporating the irregular shape and size of the biomass particles.

The main goal of this thesis is the CFD analysis of the detailed biomass combustion, and validation of the models against the experimental data. This will provide information about the limitations of the sub-models implemented in the commercial CFD code ANSYS Fluent for the biomass combustion simulations. Thus identifying the models and assumptions which need to be improved or updated when switching from coal to biomass combustion in numerical calculations.

Another objective of this thesis is to develop new computational sub-models for biomass combustion, focusing mainly on irregular wood particle shapes and sizes and devolatilization. The models are implemented in the form of user defined functions (UDFs), which can be implemented in ANSYS Fluent.

1.8 Scope of the PhD thesis

The thesis outline is as follows. The first chapter is an introduction on the energy demand, the carbon dioxide emissions and related global warming and climate change. Additionally, the importance of coal and biomass in the future energy demand and general information about low carbon technology – Carbon Capture and Storage are presented in this chapter.

In Chapter 2 the focus has been given to biomass in power industry. Furthermore, focus on biomass fuel combustion as one of the promising BECCS technologies is given. The biomass properties have been outlined and compared with coal fuel. Also, the challenges related to commercialisation of biomass in the large scale power industry has been summarised.

Chapter 3 comprises a description of the CFD approach used in the simulations of coal and biomass combustion, including the governing equations and sub-models used for solid fuel combustion.

In Chapter 4 experimental work on 250 kW PACT combustion test facility has been outlined, the measurements taken during the experimental programme have been summarized.

In Chapter 5 the experimental work form Chapter 4 has been used for validation of the CFD model for coal combustion. Numerical predictions and experiments have been compared with theoretical calculations of mass and energy balance. A sensitivity study on different sub-models used for coal combustion has been performed and summarized for use in

a further study.

Chapter 6 includes CFD modelling of coal and biomass combustion in a 15 kW jet flame. This work is aimed at obtaining a better understanding of the limitation of the sub-models used in commercial CFD codes for the predictions of biomass combustion.

Following the conclusion from Chapter 6, in Chapter 7 the investigation of the influence of the irregular particle shape and size on the prediction of biomass combustion has been presented. The user defined function, including the stages in the biomass fuel combustion has been employed for several non-spherical thermal thick particles and compared against the predictions for spherical particles. The developed code has been implemented in jet flame combustion and validated with experimental data.

The thesis is summarised in Chapter 8. The conclusions are presented and further research is proposed.

Chapter 2

Biomass in the power industry

In the previous chapter some general information on the world energy demand, awareness of global warming and climate change has been presented. The CCS has been outlined to be a promising technology for CO_2 emissions reduction. Moreover, combining CCS with biomass combustion has been identified to be beneficial because of the negative CO_2 emissions. However, there is a little research being done on biomass combustion and therefore, more investigation is needed before the biomass combustion can be applied to CCS. This chapter gives an overview of the biomass combustion process literature with a focus on biomass as a fuel source for large scale energy generation.

First of all, the biomass properties have been described and then the differences between coal and biomass have been compared. Further, the biomass technology has been presented along with common operational issues. Also, co-firing coal with biomass has been reviewed followed by the current state of art of the biomass combustion CFD modelling.

2.1 Introduction

Before the Industrial Revolution, when coal and other fossil fuels became dominant, biomass has been widely used for energy production.

Indeed biomass is one of humanity's earliest source of energy [28]. Historically, wood was the major fuel, and nowadays in many countries, in such as Africa or Asia, it is still the major source of energy. For example, in Nigeria about 78% of the total energy comes from biomass [3]. In 2013 biomass covered approximately 10% of the global energy supply [3]. Further, biomass is the most common form of renewable energy and it is a leader in global final renewable energy consumption [56, 57] contributing to over 90% of the world renewable energy production [28].

Bioenergy is the largest renewable energy source - 14% out of 18% renewables in the energy mix [56]. There are several processes of energy generation from biomass, such as pyrolysis, gasification, anaerobic digestion or alcohol production. However, the combustion of biomass is the most popular and is contributing to over 97% of the world's bioenergy production [58].

Even the biomass as a fuel is well-known and has been widely used in the past, there is still a considerable gap in the knowledge related to the science behind biomass combustion. This can be explained by the complexity of the combustion process of this type of fuel. Another reason for the lack of knowledge is that by the time when the engineers and scientists became adept at investigating the complexity of the solid fuel combustion phenomena, which is since the start of the Industrial Revolution, the major fuels of interest were fossil fuels (coal, gas, oil).

Nonetheless, the interest in the combustion of biomass has grown in the last decade since the emphasis on displacing the non-renewable energy coming from fossil fuels with renewable sources of energy, such as biomass.

At the moment, biomass supplies 57.7 EJ, which is 10% of global energy supply [56, 57]. Biomass is expected to make a significant contribution to the world energy production [3, 46, 47], as it provides a solution for energy security concerns and the limited availability of fossil fuels. Also, it

brings the opportunity to decrease the reliance on fossil fuels [47, 59] and it meets the worldwide concerns on global warming and climate change related to the CO_2 emissions. For example, the United States Energy Information Administration [13] forecasts increases in the share of biomass in US energy production from 8% in 2009 to 15% by 2035.

2.2 Biomass fuel - general information

Undoubtedly, biomass is abundant, widely available and a storable fuel [28]. The term biomass is given for any type of fuel which is composed of organic origins material that stems from plants, which has not yet undergone the process of metamorphosis that leads to peat and coal [47]. There are different origins of the biomass biological materials, it can come from grasses, straws, wood, crops residuals, paper, algae, sewage sludge, etc. [47]. Biomass is produced by green plants converting sunlight into plant material through photosynthesis and includes all land- and water-based vegetation, as well as all organic wastes [60]. The biomass resource can be considered as organic matter, in which the energy of sunlight is stored in chemical bonds. When the bonds between adjacent carbon, hydrogen and oxygen molecules are broken by digestion, combustion, or decomposition, these substances release their stored chemical energy [60].

Therefore, biomass is a renewable source of energy with a wide range of materials that can be treated as biomass. Reasoning in the tremendous diversity of biomass feedstock, the classification of the biomass fuels is required. Furthermore, the physical and chemical properties of biomass can not be specified by one parameter, and because of the diversity of the feedstock, they have a broad range of parameter values.

There are various classifications of biomass, for instance the UK Biomass Strategy classified the biomass resources as follows: conventional forestry, short rotation forestry, sawmill conversion products, agricultural

crops and residues, oil bearing plants, animal products, municipal solid waste and industrial waste [61]. Another categorization of biomass is given in [55], which classifies biomass into wastes (such as sewage sludge, refuse-derived fuel), herbaceous (such as grasses, stalks, and straws), aquatic (such as kelp), woody (hardwood and softwood) and derivatives (such as paper).

Categorization of the biomass fuel can be used as a mean of predicting the combustion behaviour of the biomass fuel type. The aim is to provide properties of biomass, such as devolatilization rates, volatile matter composition, high temperature volatile yields, composition and reactivity of char, etc. without time-consuming and expensive measurements, based on simple tests, for example on the biomass composition [55].

The most popular biomass fuel for power and heat generation is wood [58]. Overall, woody biomass provides about 90% of the primary energy annually sourced from all forms of biomass [56, 57]. Next to woody types of biomass, straw is considered to have a high potential as a feedstock. It is essentially a residue from the production of agricultural crops [46]. There are other agricultural waste products in industrial processes as depicted in Figure 2.1, namely rice husks, sunflower seed husks, peanut shells, leftovers in the olive oil production, corn stalks, etc. [46]. Most of them are pelletized to increase their energy density.

Although, agriculture is a large source of biomass, it is not popular for the large scale power production and this is because the agricultural materials tend to have high nitrogen and ash content in contrast to wood and woody materials [58]. The high ash, chloride and salts content of agricultural biomass are responsible mainly for the corrosion, slagging and fouling in the boilers, whereas the higher content of nitrogen may result in higher NO_x emissions [46]. An extended explanation of these issues is included in Section 2.5.

Figure 2.1: Schematic of the diversity of the agricultural biomass types [62].

2.3 Emissions from biomass combustion

Emissions are of primary concern for power generation by means of any fuel firing. The primary pollutants from biomass, particulary wood firing, are similar to other fossil fuels and comprise both gases and particles. These include particulate matter (PM) and gases such as products of incomplete combustion - carbon monoxide (CO) and a range of trace species, including polyaromatic hydrocarbons, carbon dioxide (CO_2), nitrogen oxides (NO_x) sulphur oxides (SO_x) and volatile organic compounds (VOCs) [46, 63]. A comprehensive review of combustion processes and the main formation routes for combustion products is given in [47].

The techniques for emission reduction are developed and ready to use. The amount of the pollutants from combustion can be reduced in a similar manner to coal combustion primarily by the design of the burner (combustion-control techniques) and by post-combustion technologies [64].

2.3.1 CO_2

Similar to coal combustion, biomass oxidation results in CO_2 emissions. However, biomass combustion is recognized as carbon neutral, which is associated with the so-called neutral CO_2 emissions [65].

It is thought that the CO_2 emitted into the atmosphere during the combustion of biomass fuels is part of a closed loop - the natural carbon cycle, as presented in Figure 2.2. Biomass during its growth absorbs CO_2 from the atmosphere, then during photosynthesis, the CO_2 is converted into organic carbon and it is stored in the plants. In consequence, this chemically-stored energy can be converted into power through combustion. When the biomass crops are harvested and then combusted, the carbon stored in the plant matter oxidises to CO_2 and is emitted back to the atmosphere, thus closing the carbon cycle. It is believed that biomass

consumes a similar amount of CO_2 from the atmosphere during growth as it releases during combustion [58, 66]. Therefore, biomass fuels are considered to be carbon neutral with respect to the CO_2 emissions [65].

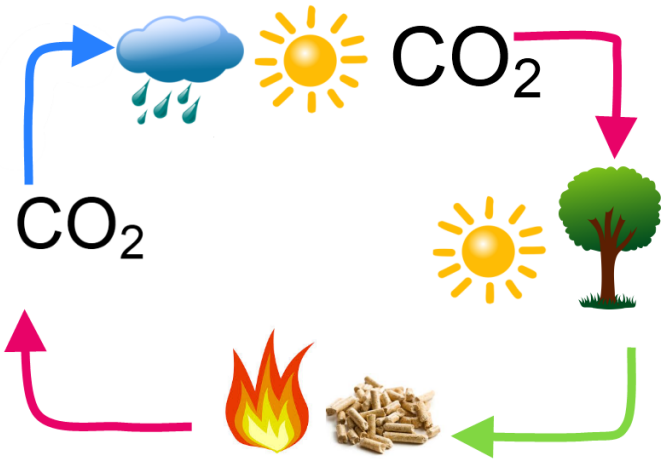

Figure 2.2: Schematic of biomass carbon neutrality [67].

2.3.2 SO_x

The sulphur content of wood is low and therefore SO_x is not likely to pose a particular problem from its combustion. However, in coal-fired power plants, wet and dry scrubbers are used to eliminate the SO_x from the flue gas. These methods can be used for biomass combustion, especially for the types of biomass with high sulphur content.

2.3.3 Particulate matter

Particulate matter emissions are perhaps of the greatest concern, particularly for domestic appliances. National energy statistics, as used within the National Atmospheric Emission Inventory (NAEI), show an increasing trend of particulate matter emissions in the combustion of wood [63]. However, in coal-fired power plants, electrostatic precipitators and

bag filters are used to reduce the number of fine particles in the flue gas to a minimum. These methods can be adapted in biomass combustion systems.

2.3.4 NO_x

Emissions of NO_x are one of the greatest concerns for the combustion of any fuel. The NO_x emissions from biomass strongly depend on the type of the biomass and its fuel-nitrogen content. Therefore, NO_x emission reduction techniques are playing a significant role for biomass combustion as well as for fossil fuels.

The NO_x formation is a complex process and the majority of NO_x is emitted in the form of NO with only small fraction of NO_2 [68]. During the combustion process there are three different mechanisms for the formation of NO_x, namely fuel-NO_x, thermal-NO_x and prompt-NO_x. Fuel-NO_x is formed as a result of fuel-bound nitrogen, thermal-NO_x originates from the high-temperature oxidation reaction of gaseous nitrogen and prompt-NO_x is formed due to the reaction of gaseous nitrogen in the presence of hydrocarbons.

The NO_x emissions reduction methods for biomass combustion are adapted from coal combustion process. Firstly, the optimum combustion conditions have to be provided with appropriate excess air and temperature. Further, a water or steam injection to the combustion chamber can reduce the combustion temperature and thus reduce thermal-NO_x formation. Other ways to control the NO_x emissions is fuel staging, flue gas recirculation or using the low-NO_x burners with air staging. All techniques mentioned above are ways of reducing the NO_x emissions by controlling the combustion process, see Figure 2.3 where the schematic of the NO_x control techniques have been depicted. In the low-NO_x burners the air supplied to the combustion chamber is divided into at least two parts. This enables a good mixing of the combustion air with the combustible

gases. Further, the primary air creates a fuel rich zone which reduces the combustion gases temperature which prevents the formation of thermal-NO_x. The air deficiency is made up by the secondary air in the second combustion zone, so that complete combustion can be carried out [69]. The combustion products can be cooled and recirculated into the combustion zone in the region of the fuel and primary air entry.

Control of NO_x emissions, originated in biomass combustion, is becoming a very significant technical challenge due to the imposition of increasingly strict emission limits [68]. As the NO_x emission is more strongly influenced by the nitrogen content of biomass fuels (especially of those with significant nitrogen content) rather than the operating conditions, the emphasis is placed on the post-combustion (flue gas treatment) measures and the most successful among them – selective catalytic reduction (SCR) and selective non-catalytic reduction (SNCR) [68].

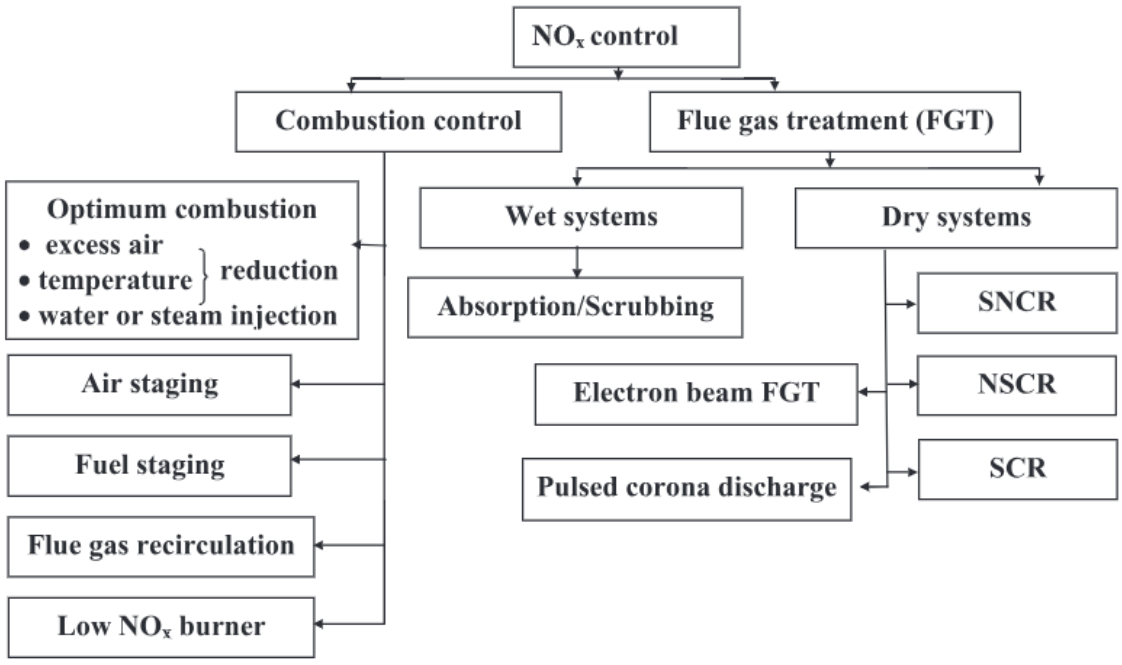

Figure 2.3: Overview of the NO_x emissions control techniques [68].

For biomass combustion, fuel-NO_x is the main source of the NO_x emissions. However, woody biomass fuel has usually less nitrogen content

than coal, therefore this reduces the fuel-NO_x emissions in comparison to coal combustion. Whereas thermal-NO_x and prompt-NO_x are formed in lower quantities than during coal combustion, as the temperature in biomass boilers is lower than in coal-fired boilers and this decreases thermal-NO_x formations.

2.3.5 CO

Carbon monoxide is mostly created due to incomplete combustion and consequently low excess air (deficiency of available oxygen for oxidation of fuel) or not sufficient residence time of the fuel particles. Recent experimental studies show that biomass requires better aeration in the combustion zone than coal [70]. This indicates that higher excess air is needed for complete combustion of biomass fuel. Among different biofuels being compared, the highest CO emissions have been observed for straw, whereas the lowest one for willow [70].

2.3.6 Organic compounds

The organic compounds present in biomass combustion vary depending on the combustion conditions and biomass characteristics, such as lignin or resin content. The organic compounds include a variety of aldehydes, phenols, alcohols, ketones, carboxylic acids, methane, ethane, ethanol, formaldehyde, acetaldehyde, acrolein, phenol, cresol, formic acid and acetic acid [63, 71].

The experimental measurements performed for coal and biomass combustion show that total organic compounds were higher for biomass fuels. The highest emissions of organic compounds have been identified for straw, the lowest for willow and bark [70].

2.3.7 Inorganic components

The combustion of biomass fuels for power generation results in the formation of major flue gas constituents and the partitioning of inorganic components, such as potassium, sodium, calcium, phosphorus, iron, sulphur, nitrogen and chlorine. These are present in raw biomass and can either be released into the vapour phase during combustion, or are retained in the solid phase as ash [72, 73].

A notable characteristic of solid biomass fuels as compared to coal is their significantly higher potassium content [74]. The softwood has been recognized as a high potassium release rate when compared to the other biomass, which shows that optimisation is necessary for each biomass [72].

Potassium is an essential nutrient for plant growth and is present in the biomass fuel. The presence of potassium during combustion has been recognized as causing ash deposition and corrosion mechanisms in furnaces, which can increase the operating cost of biomass combustion [72, 74]. During combustion, potassium is released over three stages in the combustion: volatile combustion, char combustion and 'ash cooking'. The relative importance of each of these stages depends on the biomass type and the other inorganics present in the fuel.

It has been found that for wheat straw, there is a rapid release of potassium while the particles heat up and burns, and then there is a slow release of potassium from the ash [72]. This has an important influence on the slagging in the boiler. The study described in [72] showed that an aluminosilicate additive is an effective way for mitigating the release of potassium throughout the different stages of combustion in the case of wheat straw.

2.4 Biomass fuel combustion properties

Biomass, as mentioned in Section 2.2, is treated as a renewable source of energy if it originates from well-sustained regions. The age of biofuels ranges from a few months to several years [46]. Biomass characteristics can vary among the feedstock and this can affect the combustion performance and plant operation.

Some of the main properties of biomass fuels are summarized in following sections.

2.4.1 Ultimate and proximate analysis

Proximate analysis provides information about the moisture, volatiles, char and ash content. The ultimate analysis tests give more comprehensive results that determine the content of the carbon, oxygen, hydrogen, nitrogen, sulphur and chlorine in the material. The composition of the fuel given by the proximate and ultimate analysis determines the combustion properties of biomass. For instance, a higher oxygen content reduces the heating value, whereas the higher carbon and hydrogen fraction contributes to the higher heating value. Nitrogen determines the fuel-NO_x emissions and similarly, sulphur is the source of the SO_x emissions [46].

2.4.2 Moisture

Raw biomass is characterised in the high moisture content, which decreases its heating value. To reduce the water content, energy for drying (evaporization of moisture) is needed and this is considered as an energy loss. In some cases, the amount of the moisture content in biofuels can the minimised at low cost by employing an air drying process [46].

2.4.3 Volatiles

The biomass fuel is usually characterised by the high content of volatiles, which makes it easy to ignite. The volatile matter is created due to the thermal degradation of the biomass material, and then can be divided into light volatiles and tars [46]. The amount of volatiles and tars produced depends on the pyrolysis conditions, such as temperature, heating rate as well as the the type of pyrolysed biomass [46].

2.4.4 Ash

Ash is a residue after the solid fuel combustion. The ash fraction in the biomass fuel is not significant compared to volatile matter, which dominates the biomass composition. The alkaline nature of the biomass ashes lowers its melting point, and as a consequence, this usually leads to fouling and slagging, which is the main operation problem during biomass combustion [46].

2.4.5 Heating value

Biomass fuels have lower heating value compared to other fossil fuels, such as coal, oil or gas. The lower heating value is mainly a consequence of low carbon content, high oxygen fraction in the biomass, as well as the high moisture fraction.

Biomass volatiles have lower heating value than solid residues after the devolatilization process, as the volatiles oxidise mainly to H_2O, CO_2. However, as most of the biomass composition are volatiles, the highest energy release from the biomass combustion is due to devolatilization rather than solid residual combustion [46].

2.4.6 Biomass composition – cellulose, hemicellulose, lignin

The main differences in the biomass fuel is caused by the variety in its structural composition [75]. All woody and herbaceous biomass is composed of three main components, namely cellulose, hemicellulose, such as xylan, and lignin [47, 55, 75], which physically and chemically influences the processes taking place during the combustion of biomass fuel. The composition of the dominant three biomass components varies for different types of biomass, part of the biomass plant and other factors related with crop treatments [47]. Also, there are several minor components of wood, such as lignans, volatile oils, tannins, resins, proteins, etc., which complete the organic fraction of the fuel.

Cellulose is a crystalline polymer of glucose and represents about 50 wt% of the biomass. Whereas hemicellulose contributes approximately 25 wt% of the biomass and is the most reactive component in biomass fuel, as it is a complex mixed polymer of 5 – and 6 – carbon sugars [76]. Much less reactive is lignin, which accounts for about 25 wt% of the biomass and is in general higher for woody biomass than herbaceous material [76]. Lignin is a random structure three–dimensional phenolic polymer of which there are three classes based on the different phenyl-propane monomeric units with increasing number of methoxy groups ($C_9H_{10}O_2$, $C_{10}H_{12}O_3$, $C_{11}H_{14}O_4$).

Table 2.1: Higher heating values and elemental anaysles of hemicellulose, cellulose and lignin [75].

Structural component	C, %	H, %	O, %	HHV, MJ/kg
Cellulose	44.4	6.2	49.4	17.6
Hemicellulose	45.5	6.1	48.4	17.9
Lignin	60.4	6.3	33.3	24.1

The exact quantities of cellulose, hemicellulose and lignin can be measured analytically, and usually they are in the range of 30 – 90 wt%, 20 – 40 wt%, 10– 25 wt%, respectively. In general, the composition of hardwood is typically 40 – 44 wt% cellulose, 18 – 25 wt% lignin and 10 – 35 wt% hemicellulose. Softwood has usually a similar fraction of cellulose, however the fraction of lignin is higher and is usually in the range 25 – 35 wt%, the hemicellulose fraction is lower and it is approximately 10 – 15 wt% on the dry basis.

The cellulose, hemicellulose and ligning has a major impact on the combustion performance. Generally, it is assumed that these species react independently, based on the chemical structure of each component [47].

The heating value depends on the elemental composition of the fuel. Since the three major components of biomass have a slightly different composition, the heating values vary between them. It was found that there are no direct relations between high heating value and cellulose and hemicellulose content, however the fraction of lignin appears to have a significant impact on the biomass calorific value [75]. Lignin has a higher heating value than cellulose and this is because of its lower degree of oxidation.

An example comparison of the ultimate analysis and higher heating value for cellulose, hemicellulose and lignin is presented in Table 2.1. Cellulose and hemicellulose have a similar and lower heating value of about 17.6 – 17.9 MJ/kg than lignin, which is in the range 23.3 – 26.6 MJ/kg [75]. Therefore, the structural composition of the biomass fuel has an impact on the heating values, with the higher lignin content increasing the overall biomass calorific value [75, 77, 78].

Also, studies using a Thermogravimetric Analyzer (TGA) concluded that there is a difference between the release of the cellulose, hemicellulose

and lignin from the biomass particles. Hemicellulose is the easiest to be degraded and its pyrolysis is focused at the lowest temperature, the cellulose release has a peak characteristic, however lignin pyrolysis has a constant release during the whole temperature range [78].

2.4.7 Biomass particle shape and size

Because of the fibrous nature of the biomass, this type of fuel does not mill easily and this results in poor grindability characteristics [47]. Thus the pulverised biomass particles commonly have irregular shapes and large sizes [79]. The size of a biomass particle covers a wide range, from 5 – 100 mm or even higher [55, 80].

The wide range of the biomass particle sizes and shapes plays a significant role in the performance of the biomass fuel combustion [47]. Larger particle sizes establish the potential for large internal temperature and composition gradients [79]. Furthermore, various particle shapes result in different particle exterior surface area-to-volume ratios, which are essential to the heat and mass transfer and further affect the devolatilization and surface burnout [79]. This aspect is described in more detail in Chapter 7.

2.4.8 Biomass vs. coal – comparison of fuel properties

As mentioned in Section 2.2, the biomass is a material which undergoes the process of metamorphosis to coal. Also, coal combustion is being retrofitted to biomass combustion. Hence, both types of fuels, having similar origins, tend to be compared.

Coal composition depends on the geographic origin and its rank. Regarding the composition of biomass, it depends on numerous factors, such as geographic location, time of harvest, fertilizer treatment, length of storage, etc. Therefore, in the case of biomass it is more difficult to establish a

representative biomass composition and properties. However, a comparison of the general properties for the coal and biomass for averaged and most common values are summarized in Table 2.2.

In general, biomass is almost three times less dense than coal and has lower friability, followed by the higher reactivity of the char in comparison to coal.

Regarding the ultimate analysis, biomass has more oxygen content and less carbon, which explains its lower heating value compared to coal. Biomass usually has less nitrogen and sulphur than coal. In the case of inorganic components – coal has more aluminium, iron, titanium than biomass. Relative to coal, biomass has more silica, potassium and calcium [58].

Comparing the proximate analysis of both fuels, biomass characterises with significantly higher volatile matter content than coal. The raw biomass has a much higher moisture content and has less fixed carbon than coal. Biomass in comparison to coal has less ash [58].

Comparing the pulverised solid fuels, the biomass particles have larger aspect ratio (AR) and larger size than pulverised coal [79]. Coal has a crystalline structure which makes it easy to grind into the fine powder. Whereas, the biomass fuel requires approximately five times more energy than coal to achieve particles ground to less than 1 mm in size due to its fibrous nature [47, 81]. Thus, in most cases, the biomass particles are larger in size when compared to coal, and this is because the process of milling of biomass particles to the particle size of coal is not feasible. The typical averaged size of the pulverised coal particle is approximately 65 µm. Whereas biomass has an average particle sizes about 200 – 300 µm. Pulverised biomass particles commonly have more irregular shapes and much larger sizes than pulverised coal [79]. Differences in the shape of the coal and biomass particles can be seen in Figure 2.4. Coal particles tend to be spherical in shape, whereas biomass usually

has an extended cylindrical shape. The aspect ratios of pulverised biomass particles are in the range of 2 to 15, whereas for coal the aspect ratio is that of a spherical particle and in this thesis is usually assumed to be 1 [79]. Further, unlike coal that softens and forms spherical particles during devolatilization and char combustion, the biomass particles tend to retain their initial form, that is irregular in shape, during all the combustion stages [82].

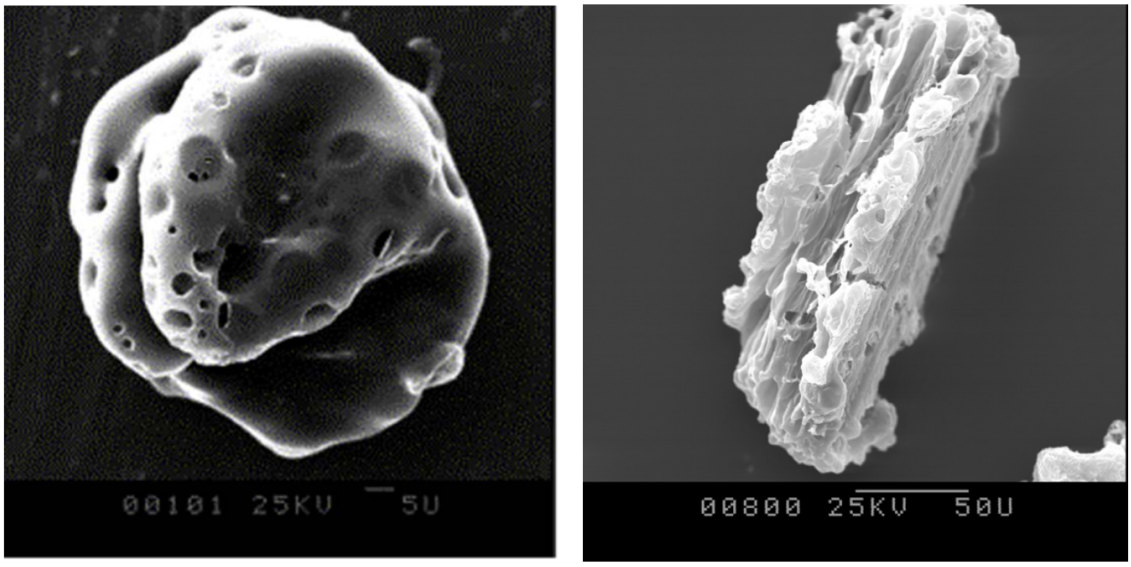

Figure 2.4: Comparison of coal and biomass particle shapes [83].

2.5 Biomass combustion technology

Most of the types of biomass in a raw state (when harvested) have a low energy density. Therefore, the biomass fuel before transportation has to be dried to reduce the moisture content and compacted to reduce its volume (pelletized). The drying of the biomass crops increases the energy density, hence it creates the high-density product, which saves the energy used for the transportation of the biomass fuel [46]. The process of drying

Table 2.2: Comparison of the physical and chemical fuel properties for coal and biomass fuels [58].

Property	Biomass	Coal
Density, kg/m^3	∼500	∼1300
Particle size, mm	∼3	∼0.1
Particle shape	irregular	spherical
C, wt%, dry	42 – 54	65 – 85
O, wt%, dry	35 – 45	2 – 15
S, wt%, dry	max 0.5	0.5 – 7.5
H/C, (molar)	∼1.5	∼0.8
O/C, (molar)	0.4 – 1.0	0.02 – 0.4
Volatiles, wt%, daf	80+	40+
SiO_2, wt%, dry ash	23 – 49	40 – 60
K_2O, wt%, dry ash	4 – 48	2 – 6
Al_2O_3, wt%, dry ash	2.4 – 9.5	15 – 25
Fe_2O_3, wt%, dry ash	1.5 – 8.5	8 – 18
Ignition temperature, K	418 – 426	490 – 595
Friability	low	high
Dry heating value, MJ/kg	14 – 21	23 – 28

the biomass fuel can appear in the combustion chamber, without any special preparation. However, the evaporation of the moisture consumes the energy of the biomass fuel and the high moisture content is difficult to maintain combustion [46].

The most popular type of pulverised biomass comes from natural forests, woodlands and forestry plantations. It is produced by the fine grinding process of the dried woodchips, as well as sawdust and other residues from forestry and wood processing activities [46,66]. Usually, the dried and ground form of wood is pressed into pellets, which consequently is denser in energy and is not easily degradable. These features make the pellet form of biomass preferred for the long-distance transportation and storage, because it reduces the transportation cost and storage space [46]. The process of pelletizing does not change the biomass fuel combustion properties. However, it prepares the feedstock for the further processing, mainly transportation and milling [46]. Wood pellets need energy for their production, but most of the required energy can be achieved from the bark of the tree which has to be removed anyway before pelletizing process [46].

2.5.1 Biomass combustion techniques

There are three techniques for the large–scale combustion technology for biomass fuels, namely vibrating or moving grate firing, fluidised bed and suspension firing of pulverised biomass [46,55,80]. The choice of the technology to be employed depends on the quality of the biomass feedstock which is intended to be burned [46].

Grate firing is limited by its capacity to approximately 50 MW_e and has lower efficiency compared to suspension firing. However, in this type of furnaces any type of biomass, regardless its condition, can be burned, so the biomass can be fired as received or with minimum preprocessing [46, 55,80].

The fluidized bed method is flexible regarding the fuel, produces less

thermal NO_x emissions and is efficient [46]. However, it has a complex setup with difficulties running on a part load and has high cost for air supply as well as wear and tear of the boiler surfaces due to bed attrition [46, 55, 80].

The suspension boiler requires high-quality, preprocessed, namely dried and milled fuel. The technique of pulverised biomass combustion is widespread and, as a result of the possibility of deployment of the biomass into existing coal-fired units, co-firing or using the well-known methods of pulverised coal combustion [46]. Therefore, if the high quality fuel is available, such as the wood pellets, or torrefied biomass, then the pulverised combustion is an option.

As the pulverised wood is the most popular biomass fuel combustion technology and the pulverised biomass combustion process is the most suitable technology for the large scale energy production from this type of biomass, the next chapter is focused on the pulverised combustion of woody biomass.

2.5.2 Operational issues with PF biomass combustion

In pulverised fuel (PF) boilers, the fuel is in the form of fine powder, that is achieved by grinding in mills. It is transported pneumatically and blown into the combustion chamber with the primary air supply, called carrier/conveying air.

The experimental and theoretical results indicate that there is a significant difference in the combustion behaviour of biomass and coal, and this is related to the influence of the fuel properties [84]. Therefore, to employ biomass combustion for the large-scale power generation, there may be problems related with differences in the comparison to coal such as larger biomass particle size and its irregular shape, lower heating value, biomass composition, and in consequence flame instability, slagging, fouling, corrosion, etc. during the combustion process [28]. Also, biomass fuels

are characterised with high volatile matter content and high reactivity of both the volatile matter and the char [58] which affects the combustion performance. Moreover, the temperature inside the boiler needs to be lower compared to the temperatures in conventional coal-fired furnaces due to the lower melting point of the biomass ash and this decreases the combustion efficiency [46].

A lower content of carbon, and more oxygen in the biomass, in comparison to coal, can cause problems with flame stability. The high moisture and ash content in some of the biomass fuels may be accompanied by ignition delay. Further, certain biomass fuels have high chlorine and alkali content, which are found to be responsible for corrosion [58]. Chlorine is a major factor in the ash formation, since it facilitates the mobility of many inorganic compounds. Hence, if the biomass contains chlorine then it is more likely that the ash particles depositioned on the heating surfaces of the boiler. Fouling and slagging can create resistance to the heat transfer and therefore diminish the heat transfer rates and this causes corrosion on the heating surfaces [46].

Wood and wood-derived fuels are reported not to cause serious fouling issues as opposed to the herbaceous fuels, which explains their widespread popularity. Wood and coal have low alkali index and low fractions of chlorine [46]. Therefore, in the case of wood combustion, the most challenging operational issue identified with pulverised wood combustion is the irregular shape and large size of particles.

2.5.3 Co–firing

Currently biomass combustion technology is based on coal combustion, which has been widely described in the literature [36, 43, 55, 81, 85–96]. Large scale power generation units were developed for the conventional fuels, namely coal or lignite, and then adapted for the usage of biomass. The first deployment of the biomass combustion in the large-scale

combustion systems was by co–firing in the coal-fired power stations [46]. It has undergone only minor adjustments and modifications to the equipment designed for the coal firing [28, 82, 83, 90, 97–104].

If the boiler is supplied with 100% biomass, the design of the burner needs to be modified to ensure the flame stabilization [47].

The co–firing creates less difficulties than pure biomass combustion, as long as the fraction of the biomass in the fuel mix is kept low. This is because of the chemical composition and properties of the coal that mitigate the problems related to pure biomass combustion [46]. It was observed that blending biomass with coal reduces the flame stability problems present during pure biomass combustion [58]. Further, the same mill and burner can be used for co–firing up to 10% biomass in a blend. In general, the pure biomass combustion is more expensive than co–firing and has relatively low efficiency. In comparison to co–fired power plants with an efficiency 33 – 38%, biomass power plants have an efficiency 12 – 25% [76]. If the boiler is supplied with 100% biomass, the design of the burner needs to be modified to ensure the flame stabilization [47]. Nonetheless, biomass offers some advantages related to the combustion performance, apart from emissions reduction, namely much higher volatile matter content and high reactivity of the fuel and char on the top of the CO_2 emission reductions [58].

2.6 CFD modelling of biomass combustion

The coal combustion has been widely investigated and a significant number of studies have been performed. The CFD codes are available to predict the performance of the coal-fired boilers with air- and oxy-combustion [36, 43, 55, 85–90].

CFD modelling techniques of biomass combustion are still in need of development. At the moment, there are only a few papers on pure bio-

mass modelling predictions for large scale combustion for power generation [105]. Most of the studies, if pulverised biomass is used as a fuel, have been on co-firing coal with biomass [82, 98–100], and these studies have illustrated that it is possible to predict the behaviour of biomass combustion in coal flames. However, the majority of the studies have employed models validated with coal combustion.

2.6.1 CFD simulations of co-firing coal with biomass

Co-firing of pulverised coal and biomass was investigateded by Backreedy et al. [82]. This work focused on the CFD simulations of co-firing coal with 10 wt% biomass in a 1 MW_{th} combustion test facility using ANSYS Fluent. The CFD model assumed similarity in the prediction of the combustion of coal and biomass. Similar sub-models were used to simulate biomass and coal, taking into account the different properties of these two fuels. Also, for the biomass, the assumption of interconnected devolatilization rates of cellulose, hemicellulose and lignin under high heating rates and the high temperatures were used. The biomass particles were assumed to be uniformly distributed spheres with the equivalent diameter size of 750 µm. The irregular biomass particle shape has been considered only in the drag coefficient calculations as a shape factor. The CFD simulations suggested the importance of the biomass particle shape and size.

Ma et al. [99] presented a CFD model of the biomass combustion in an existing 1 MW industrial pulverised coal boiler. The shape factor of the biomass particle has been introduced as a drag coefficient to take into account the effect on irregular particle aerodynamics. However, heat and mass transfer was simulated with the assumption of spherical particles. For the devolatilization of the biomass fuel a single rate model has been used with values calculated using the FG-BioMass [106] networking program, and the oxidation of the volatiles was simulated using the global one-step reaction mechanism. The biomass char has been found to be

influenced by the shape and size of the fuel particle as well as being more reactive than coal char, and this is because of the catalytic effect. The char combustion was modelled using the Smith intrinsic model [107] with an increased pre-exponential factor of 4.

Ma et al. [100] in the next paper investigated CFD modelling of co-firing coal and biomass blend in a 0.5 MW Didcot combustion test facility. Again, the shape factor was used only to account for the aerodynamic behaviour of the non-spherical particles in the drag coefficient calculations. A two-step reaction mechanism has been used for volatiles and char combustion, and the devolatilization and char combustion was set up as previously [99]. During this study it was found that the moisture content of the biomass affects the ignition time. In this model the biomass particles were also assumed to be spherical and thermally thin as in the previous paper [99]. The biomass devolatilization has been assigned to be the main contributor of the mass loss in the fuel particle, and the biomass particles were found to burn slowly or do not burn completely.

Recently Black et al. [98] studied co-firing in a 500 MW_e utility boiler located at the Didcot Power Station equipped with 48 Doosan Babcock Low-NO_x coal burners. The CFD predictions for coal-air combustion were validated with the experimental data. Also, the co-firing coal with biomass in air and under oxy-fuel conditions have been analysed. As a biomass fuel the pelletised wood has been used with assumed cylindrical particle shape with an aspect ratio of 10 for the drag coefficient [108], thus affecting the cylindrical particles trajectory as in previous publications [99, 100]. For the devolatilization of the biomass fuel, a single rate model has been used with the pre-exponential factor and activation energy based on [99, 106]. Oxidation of the volatile matter was simulated using the two-step global reaction mechanism. The char combustion for wood particles has been modelled using the intrinsic char combustion model proposed for coal by Smith [107].

The evaluation study showed that switching from coal to co-firing, and keeping the same thermal input, resulted in reduced heat transfer by approximately 15%, different temperature distributions and lower temperatures of the exit gas. This was explained by the large biomass particle size compared to the size of the coal particles.

Szuhanszki et al. [105] presented a study on the same facility introduced in [98] with the extinction to 100% pure biomass air and oxy-combustion. The models were set up in a similar way to [98]. The results showed that the temperature of the gas at the exit is lower and the total heat transfer is reduced. The author explained this difference as being sue to the large particle size and lower total surface area of the biomass particles compared to finely grounded coal fuel. The latter was suggested to be associated with the reduction of the particle radiation.

All of these papers underline the importance of the large particle size and irregular shapes of the biomass fuel particles. In all of these papers, the particles are modelled as thermally thin and the shape of the biomass particles is not included for the heat and mass transfer calculations. However, the mentioned papers state that it is possible to predict the co–firing of coal with biomass using models validated with coal combustion.

None of these papers have compared the experimental data with the modelling of co-firing and biomass combustion. It was mentioned that there is a possibility to predict co-firing coal with biomass using existing models validated for pure coal combustion. However, this can be explained by the low fraction of biomass in the blend and coal being the main fuel that controls the combustion process. Adding small amounts of biomass to a coal flame, the reaction environment in the furnace is determined by the combustion of the coal rather than by the biomass kinetics, which can explain good accuracy of CFD predictions. It should be noted that these models may be less reliable when the fraction of biomass in the blend increases, especially when pure biomass combustion is considered.

Therefore, more research is needed to develop models which specifically take into account the unique biomass properties, especially its size and irregular particle shapes, in order to predict not only pure biomass combustion, but also give reliable predictions of the co–firing of coal with any fraction of biomass in a blend.

2.7 Conclusions

In summary, the interest in biomass fuel is increasing because of the biomass carbon neutrality, and therefore almost zero CO_2 emissions from its combustion. The study of different biomass technologies shows that wood is the most popular type of biomass fuel. The comparison of coal and biomass properties highlighted the differences in the fuel properties and the impact on the combustion process.

Nevertheless, the pulverised wood combustion needs further investigations. There is a considerable gap in the knowledge regarding biomass combustion CFD modelling. Currently there are only few studies on pure pulverised biomass combustion for large scale power generation. The biomass, according to the literature, is modelled using models validated for coal combustion, which may not be reliable for pure biomass combustion. The literature suggests that the main difference between combustion of biomass and coal is the large and irregular shape of the biomass particles.

Chapter 3

CFD in coal and biomass combustion modelling

In this chapter the methodology of biomass combustion CFD modelling has been described. Firstly the governing equations have been summarized and presented, and this is followed by the turbulence and radiation models description. As the pulverised biomass combustion involves models of particles combustion, the stages have been outlined with the models used for the simulations. Then, the particle shape and size have been discussed in detail with a literature review on the current state of art of the numerical modelling of this phenomena.

3.1 Introduction

The advantage of the CFD modelling is that it is a relatively inexpensive tool that can be used for simulations of the combustion processes to perform a comprehensive investigation of the fluid flow, heat transfer, radiation distribution, temperature profiles and chemical reactions [36]. The use of CFD models to describe the combustion of coal and biomass has become an important part of the design process alongside analytical modelling and experimental diagnostics [109]. However, combustion is one of

the most difficult processes to simulate since it is a complex process which involves the three-dimensional two-phase fluid dynamics, turbulent mixing, fuel evaporation, radiative and convective heat transfer, and chemical kinetics [110]. Thus, numerical simulations require activation of multiple models of the physical and chemical phenomena.

For the purpose of numerical simulations of coal and biomass combustion, a complex commercially available CFD software – ANSYS Fluent was used in this thesis. For the CFD analysis of the solid fuel combustion, numerical calculations involve the employment of several models and sub-models to accurately describe the combustion processes. The following list shows the models that are required to simulate combustion of the pulverised solid fuel in commercial CFD software – ANSYS Fluent:

- energy transport
- radiation
- turbulence
- species transport — model of combustion of volatiles
- discrete phase model — model of transport, devolatilization and char combustion of coal particle

3.2 Governing equations

The analysis of the behaviour of the combustion process begins with the consideration of the fundamental laws of fluid mechanics and heat transfer as encapsulated in the laws of conservation mass, momentum, energy and chemical species [111]. The purpose of this section is to recall these governing equations.

To solve the flow physics within the specified domain, it needs to be divided into a finite number of control volumes. This subsequently results

in the generation of a mesh covering the whole physical domain. The essential fluid flows that are described in each of these control volumes are solved numerically through the fundamental equations governing the fluid dynamics. Discrete values of the flow properties, such as the velocity, pressure, temperature, etc. are determined at each control volume [111].

3.2.1 The momentum equation

The balances of mass, momentum and energy provide the framework for the development of the CFD-based mathematical models. Consider the Navier-Stokes equation which is the momentum conservation equation, and this is given as follows:

$$\frac{\partial(\rho \mathbf{w})}{\partial t} + \nabla(\rho \mathbf{w}\mathbf{w}) = \nabla\tau - \nabla\mathbf{p} + \rho\mathbf{g} \tag{3.1}$$

where:

ρ – fluid density,

w – velocity vector, which is a function of time and coordinates,

τ – stress tensor,

∇p – gradient of the static pressure,

g – gravitational acceleration vector.

3.2.2 The continuity equation

The Navier-Stokes equation is accompanied by the continuity (mass balance) equation:

$$\frac{\partial \rho}{\partial t} + \nabla(\rho \mathbf{w}) = 0 \tag{3.2}$$

The continuity equation is a mass balance stating that the overall mass of the system is conserved.

3.2.3 The energy equation

The conservation equation of energy can be written as follows:

$$\frac{\partial}{\partial t}(\rho h) + \nabla(\rho \mathbf{w} h) = \nabla\left[\frac{k}{c_p}\left(\sum_{k=1}^{N_s}\left(\frac{\rho D_k c_p}{k} - 1\right) h_k \nabla g_k + \nabla h\right)\right] \tag{3.3}$$

where:

h – specific enthalpy,

k – thermal conductivity,

c_p – specific heat at a constant pressure,

N_s – number of species,

D_k – diffusion coefficient,

g_k – mass fraction of a species k.

3.2.4 The species transport equation

The conservation equation of chemical species can be written as follows:

$$\frac{\partial}{\partial t}(\rho g_k) + \nabla(\rho \mathbf{w} g_k) = \nabla(\rho D_k \nabla g_k) + S_k \tag{3.4}$$

where:

S_k – source term of a species k.

3.2.5 The equation of state

The relationship between the pressure, temperature and fluid density is provided through the equation of state. The equation of state is given as follows:

$$\rho = \frac{p \cdot M}{R \cdot T} \tag{3.5}$$

where:

R – universal gas constant, R = 8.314 kJ/kmolK,

M – molar mass of a gas mixture,

T – temperature,

p – pressure.

The equation of state provides the necessary linkage between the energy conservation equation and the equation for the conservation of mass and momentum [111].

3.3 Turbulence

Most practical combustion devices create conditions that the oxidizer and fuel flow enter the combustion chamber as a turbulent flow [112]. Furthermore, the most important phenomena during the combustion process are dominated by turbulence [36].

The turbulent flow can be described as the motion of a fluid becoming intrinsically unstable and unsteady, so its behaviour is random and chaotic [111]. Nearly every boiler operates in this manner and this is because turbulence enhances the mixing, which affects the chemical reaction rates, hence the heat release, temperature profiles and particles residence time [112].

Thus, modelling of the turbulence plays a crucial role in the combustion process. However, the turbulence itself is probably the most complex phenomenon in fluid mechanics [113], therefore, some simplifications are introduced into the CFD modelling.

A description of the turbulent combustion process using CFD may be achieved using three levels of computations:

- Reynolds Averaged Navier Stokes (RANS)
- Large Eddy Simulations (LES)

- Direct Numerical Simulations (DNS)

Although DNS is the most accurate and can resolve the full instantaneous Navier-Stokes equations without any model for the turbulent motion, it is still limited to simple academic geometries and this is because of its computational complexity, time and cost. In most of the situations the DNS is not feasible, thus the turbulence models are used based on RANS or LES approximations [36].

The RANS-based methods time-average the governing equations and characterise the flow by the mean value and fluctuations.

The LES falls between DNS and RANS with accuracy of turbulence predictions. The turbulent large scale eddies are explicitly resolved in a time-dependent simulations [114] whereas the effects of a smaller scales are modelled using subgrid closure rules. LES requires more computational effort than the RANS approach, as a time-dependent simulations increase the computational time.

In practice, the turbulence model choice depends on the considered problem, the level of accuracy required, the available computational resources and time available for the calculations. In current engineering practice of coal and other solid fuel combustion the steady-state RANS-based modelling approach is extensively used, as it greatly reduces required computational cost comparing to the LES or DNS and it has acceptable accuracy of the numerical predictions. Therefore, in this thesis, turbulence modelling is based on steady-state RANS calculations.

In order to be able to compute turbulent flows using RANS-based models, it is necessary to include turbulence models to predict the Reynolds stress and the scalar transport terms as a closure model [114].

There are several closure models, however, the most popular in the simulations of coal combustion are the Standard k-ε, Realizable k-ε and Reynolds-Stress models. The major difference in those models is the computational time and cost [114].

3.3.1 Standard k-ε model

The standard k-ε model, proposed by [115], is the most well-known turbulence model and has several adaptation which are suitable for certain combusting flow simulations. It is an semi-empirical model based on model transport equations for the turbulence kinetic energy (k) and turbulence dissipation rate (ε) [115].

The model transport equation for k is derived from the exact equation, while the model transport equation for ε is obtained using physical reasoning.

The standard k-ε model employs the assumption of fully turbulent flow and negligible molecular viscosity effect. Therefore, it is valid only for fully turbulent flows [114, 115].

3.3.2 Realizable k-ε model

The realizable k-ε model [116] is a relatively new development of the standard k-ε model and differs in two ways. A new formulation for the turbulent viscosity is used in the realizable k-ε model and a new transport equation has been derived for the dissipation rate (ε) from an exact equation for the transport of the mean-square vorticity fluctuations [114, 116].

3.3.3 Reynold Stress model

The Reynold Stress model, proposed by Launder [117–119], closes the RANS equations by solving transport equations for the Reynolds stress, together with an equation for the dissipation rate. This means that seven additional transport equations are solved in the three - dimensional modelling [114].

The Reynold Stress accounts for the effect of swirl, rotation and rapid changes in strain rate in a more rigorous manner than the two-equation standard or realizable k-ε models. As a result, it has greater potential to

give more accurate complex flow predictions but with the cost of increased computational time [114, 117].

3.4 Radiation

The correct way of radiation modelling have a significant impact on the energy balance in the combustion chamber. This is because of the high temperature of the flame and hence, combustion gases within the furnace [111] and the fourth-order dependence of the temperature on the radiative heat flux. Therefore, radiation heat transfer dominates in the energy balance of the combustion chamber, and is the principal mode of heat transfer in most furnaces [39, 110]. Moreover, the accurate prediction of the temperature inside the combustion chamber based on the radiation plays a dominant role because of the coupling with other reactions occuring during the combustion process, namely, chemical phenomena, turbulence or pollutant formation [120].

The radiation heat transfer is resolved with the radiative transfer equation (RTE), which describes the energy transport along the direction of a pencil of rays within a certain elemental solid angle [110], namely

$$\frac{dI(\mathbf{r},\mathbf{s})}{ds} = -(\kappa+\sigma_s)I(\mathbf{r},\mathbf{s}) + \kappa n^2 \frac{\sigma T^4}{\pi} + \frac{\sigma_s}{4\pi}\int_0^{4\pi} I(\mathbf{r},\mathbf{s}\,')\phi_s(\mathbf{s},\mathbf{s}\,')d\Omega\,' \qquad (3.6)$$

where:

$\mathbf{r}$ – position vector,

$\mathbf{s}$ – direction vector,

$\mathbf{s}\,'$ – scattering direction vector,

s – path length,

κ – absorption coefficient,

σ_s – scattering coefficient,

I – radiation intensity,

n – refractive index,

T – local temperature,

σ – Stefan-Boltzmann constant,

Ω' – solid angle,

ϕ_s – scattering phase function.

The direct solution of the RTE in combustion flows, due to their integro-differential complexity, is not possible [110]. Therefore, to enable analysis of radiation in numerical simulations different solution methods were developed. ANSYS Fluent provides five radiation models [114], namely:

- Discrete Transfer Radiation Model (DTRM),
- P-1 Radiation Model,
- Rosseland Radiation Model,
- Surface-to-Surface (S2S) Radation Model,
- Discrete Ordinates (DO) Radiation Model.

Nevertheless, the most accurate models of radiation, such as Monte Carlo, Boundary Element Method [121], etc., are time-consuming, hence they are not implemented in ANSYS Fluent.

In the literature, several reviews of radiation model implementation for solving the RTE can be found, however the major solvers used for radiation involve the DO model [110, 122]. Hence, in this thesis, the DO model has been used to solve the radiative heat transfer equation.

3.4.1 Discrete Ordinates Model

The Discrete Ordinates radiation model solves the radiative heat transfer equation for the discretized entire solid angle into a finite number of discrete directions fixed in the global Cartesian system. The radiative intensity is assumed to be constant in each division of the solid angle. Hence

the RTE is solved for each specified angle, with corresponding weight factors associated with each discrete direction [110, 120, 123].

The number of discrete solid angles is controlled by the ANSYS Fluent user by specifying the angular discretization, called the Theta Division and Phi Division parameters [114]. These parameters define the number of control angles to discretize each octant of the angular space (1/8 of the full solid angle 4 π) [124]. Consequently, the accuracy of the solutions depends on the number of control angles, because the DO model solves for as many transport equations as the number of specified directions [123].

The calculation of the radiative energy transfer equation is time-consuming, and therefore, it is not considered in every step of the iteration of the fluid mechanics.

3.4.2 Radiative properties of gases

The combustion process results in the production of the combustion gases, such as CO_2, H_2O, CO, char, soot and fly ash particles [39, 110]. However, mainly the CO_2 and H_2O play active role in the radiative heat transfer due to their radiative properties. To predict the radiative heat transfer in the combustion chamber with a good accuracy, the radiative properties of the combustion products within the furnace has to be accurately defined.

The CO_2 and H_2O do not scatter radiation significantly [110], as they are tri-atomic gases and are strong selective absorbers and emitters of radiant energy [110]. Therefore, the properties such as the spectral absorption/emission characteristics of CO_2 and H_2O has to be taken into account in the radiation heat transfer analysis. Spectral calculations can be performed with different accuracy based on the division of the entire wavelength spectrum into several bands and assumptions of the absorption/emission characteristics.

Radiative property models can be divided into three categories: line-

by-line methods, band models and global methods [110, 122]. The most accurate calculations are the line-by-line methods — each discrete absorption-emission line is analysed. This method is not practical in common engineering calculations because of its computational cost and time [110]. In contrast, for the evaluations of radiation properties, the gray gas model is employed in CFD tools. Although it reduces computational cost, it assumes the combustion gases to be gray hence this model does not account for spectral dependence [120].

Currently used CFD tools — ANSYS Fluent, employs a Weighted Sum of Gray Gas (WSGG) model to calculate gas absorption and emissivity, and this is widely used in combustion numerical simulations.

3.4.2.1 Weighted Sum of Gray Gas (WSGG) model

The weighted sum of gray gas (WSGG) model is a reasonable compromise between the oversimplified gray gas model and a complete model which takes into account particular absorption bands [122, 125]. The total heat flux is a sum of the heat fluxes of the gray gases multiplied by certain weight factors [122, 125].

However, the WSGGM implemented in ANSYS Fluent does not solve the heat transfer rate for each gray gas. It computes the mean beam length emissivity based on the average dimension of the domain and from this value calculates the absorption coefficient of the gases [122, 125].

The WSGGM replaces the non-gray gas by the i^{th} number of gray gases. The total emissivity of the gas mixture is evaluated as a sum of the emissivity weighting factor for each grey gas, its temperature, absorption coefficient and partial pressure – path length product as follows [126]:

$$\epsilon = \sum_{i=0}^{I} \alpha_{\epsilon,i}(T) \left[1 - e^{-k_i ps}\right] \tag{3.7}$$

where:

$\alpha_{\epsilon,i}$ – the emissivity factor for the i^{th} grey gas based on the temperature T,

k_i – the absorption coefficient,

p – the sum of the partial pressures of all absorbing gases,

s – the path length.

The absorption coefficient for $i = 0$ is assigned a value of zero, which accounts for the windows in the spectrum between spectral regions of high absorption and the weighting factor is evaluated as follows [126]:

$$\alpha_{\epsilon,i} = 1 - \sum_{i=0}^{I} \alpha_{\epsilon,i} \tag{3.8}$$

The temperature dependence of $\alpha_{\epsilon,i}$ can be approximated by any function, but the most common approximation is as follows:

$$\alpha_{\epsilon,i} = \sum_{j=0}^{J} b_{\epsilon,i,j} T^{j-1} \tag{3.9}$$

where:

$b_{\epsilon,i,j}$ – the emissivity gas temperature polynomial coefficients.

The coefficients $b_{\epsilon,i,j}$ and κ_i are estimated by fitting the equation (3.7) to the table of total emissivities that is obtained experimentally [126].

The WSGGM is commonly used to predict the coal combustion. As the biomass combustion in air has similar combustion gases composition, the usage of this model for biomass is a reasonable choice. The CO_2 and H_2O ratio in the case of wood and coal is relatively similar, therefore the WSGG model is assumed to be a good approximation of the radiative properties inside the biomass-fired furnace.

3.5 Pulverised coal and biomass combustion

This section reviews the method of CFD modelling of coal and biomass combustion. The coal combustion has been widely investigated, CFD has been applied to predict coal combustion at small laboratory scales [127–129], pilot and demonstration scales [87, 130–140] and large industrial scales [98, 141, 142].

However, CFD modelling techniques of biomass combustion still are in need of development, as currently there is lack of a model which is validated with the biomass combustion experiments and the models validated for coal combustion have been employed for biomass combustion predictions.

3.6 Coal and biomass particle combustion modelling

The process of coal combustion can be divided in to several steps [143–146]: heating-up, devolatilization, volatile combustion and char burnout.

The general process of pulverised solid fuel particle combustion that takes place in the furnace is presented in Figure 3.1. Analogous to combustion of coal particles, particles of biomass are assumed to follow the same steps. When the particle enters the combustion chamber, it is heated-up by the convection and radiation of the surrounding gas and the walls of the combustion chamber. During this process, moisture evaporates from the particle (after reaching its boiling temperature). When the particle reaches the temperature of devolatilization typical for every fuel, the stage of heating-up is followed by the release of the volatile matter during the decomposition of the carbonaceous structure. Volatiles reaching the ignition temperature burn as a diffusion flame around the particle [28,47,55]. When the devolatilization process is completed, the ignition of char and its combustion begins and lasts until only ash remains in the coal particle. Then particles containing ash move further into the combustion chamber and are carried out with the flue gas as flyash or fall to the hopper as bottomash.

The pulverised solid fuel combustion is a multiphase flow and requires a special simulation model for the particles trajectory. The Discrete Phase

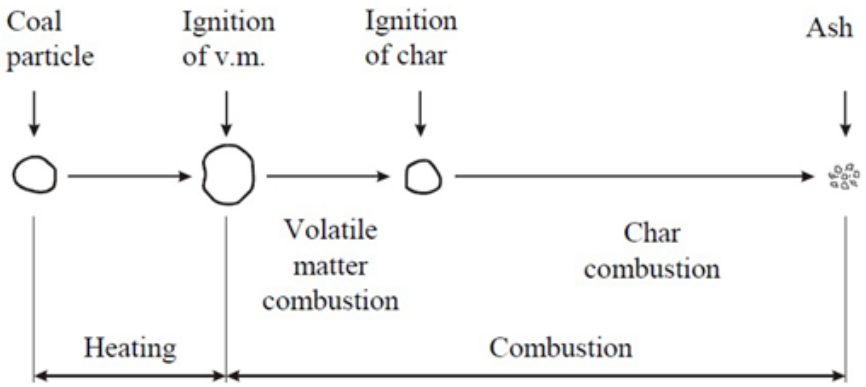

Figure 3.1: Stages of single coal particle combustion [143].

Model (DPM) implemented in ANSYS Fluent follows the Euler – Lagrange approach, which is based on the assumption that the fluid velocity field is determined, and the trajectory of the coal particles is predicted for this velocity field. The transport of the fluid phase is treated as a continuum and is solved using the Euler's method, whereas the transport of the dispersed solid particles is simulated using Lagrange's method. The dispersed phase can exchange momentum, heat, and mass with the fluid phase.

3.6.1 Heating-up process

The process of drying and heating-up of the particle is determined by the temperature of the surrounding gases and the particle size and shape. The convective and radiative heat transfer from the furnace walls and combustion gases dominates the particle heating-up process. The extent of the temperature uniformity is defined by the Biot number, which is a dimensionless quantity describing the ratio between the convection at the surface of the particle to the conduction within the fuel particle [147]. The Biot number is small for small particles, thus the uniform temperature of the particle can be assumed, because the conduction effect within the particle can be neglected.

In contrast to the small pulverised coal particles, pulverised biomass

particles have larger particle size and no longer can be treated as being thermally thin. The large particles and therefore larger Biot number, increases the importance of the temperature gradients of the fuel particle and thermal conductivity throughout the biomass fuel particle.

However, in contrast to the small pulverised coal particles, pulverised biomass particles have larger particle size and Biot number may change. This increases the importance of the temperature gradients of the fuel particle and thermal conductivity throughout the biomass fuel particle.

Most of the CFD codes for combustion of solid fuel particles are developed for the thermally thin fuel particles and assume uniform temperature gradient across the particle. However, to account for the large and thermal thick biomass fuel particles, which can be up to 20 – 200 times as large as average pulverised coal [47], then it can be necessary necessary to introduce a non-uniform thermal gradient. The noticeable internal thermal gradients of the biomass particle can create a further effect on the combustion performance and its efficiency.

Since the combustion starts when the volatiles released for the biomass particles reach the ignition temperature, this moment can be also delayed because of the delay of the heating-up and devolatilization caused by large particle size. Consequently, the problems with flame stability may occur [47]. Therefore, a model that considers the particle shape, size, thermo-physical properties of the biomass and the internal heat conduction within the biomass fuel particle is outlined for a further development.

3.6.1.1 Heating of the fuel particle

The coal particle is heated until its temperature reaches the defined vaporization temperature and the moisture fraction within the fuel particle is consumed, this may be written as follows [114]:

$$T_p < T_{vap} \tag{3.10}$$

where:

T_p – particle temperature,

T_{vap} – vaporization temperature.

$$m_p \leq (1 - g_{w,0}) m_{p,0} \tag{3.11}$$

where:

m_p – current particle mass,

$g_{w,0}$ – mass fraction of the moisture,

$m_{p,0}$ – initial mass of the particle.

3.6.2 Devolatilization

The devolatilization process starts when the fuel particle reaches a temperature that is sufficient for the chemical decomposition, and this temperature is characteristic for each fuel. Biomass fuels ignite at lower temperatures compared to coal.

During the devolatilization process, a large portion of the particles is converted from solid to gaseous form, which consists of inorganic species such as CO, CO_2, H_2O, CH_4 and a range of higher hydrocarbons [47]. The process finishes when all the volatile matter undergoes decomposition to gas and only char remains in the fuel particle. Typically the temperature at the beginning of the devolatilization process is within a range 433 – 523 K for biomass and at 623 K for a bituminous coal [47].

The studies on coal devolatilization show that the rate of the total yield of volatiles released during the devolatilization process depends on the temperature at which the process occurs [47]. The volatiles released determines how fast is the volatile matter mass transfer from the particle to the combustion gases, and therefore the combustible gases combustion.

The amount of the released volatiles from the fuel particles depends

on the initial composition of the fuel. However, it has been noticed that volatiles release in the high-heating rates is higher than that of the one measured in the proximate analysis [148, 149].

The biomass initially has over twice more volatiles than coal based on the proximate analysis, as presented in Table 2.2. Furthermore, it has been found that at high temperatures, the devolatilization of biomass is rapid, namely up to 95 wt% (daf) of the mass is released during that process [150]. Additionally, during devolatilization, the coal shows a significant swelling that is not seen in the biomass [151].

Generally, devolatilization of pulverised solid fuel is influenced by several chemical and thermo-physical properties of the fuel, for example its composition, inorganic content, density, thermal conductivity, heat capacity, particle size and shape [76]. Although drying and devolatilization are found to be primarily controlled by the heat transfer, the oxidation is dominated by the mass transfer [150].

The devolatilization process of a solid fuel particle is complex and has been implemented in several models in the ANSYS Fluent software.

3.6.2.1 Devolatilization model

The devolatilization process starts when the fuel particle reaches the specified vaporization temperature and the mass of the particle exceeds the mass of the nonvolatiles in the particle [114], which can be expressed as follows:

$$T_p \geq T_{vap} \tag{3.12}$$

$$m_p > (1 - g_{vol,0})(1 - g_{w,0})m_{p,0} \tag{3.13}$$

where:

$g_{vol,0}$ – mass volatile fraction.

The devolatilization process of a single coal particle is complex and the ANSYS Fluent software has been implemented in several models in the devolatilization process:

- The Constant Rate Devolatilization Model,
- The Single Kinetic Rate Model,
- The Two Competing Rates (Kobayashi) Model,
- The CPD Model.

In this thesis, two of the devolatilization process models provided by Fluent were used and compared, namely the Constant Rate Devolatilization Model and the Single Kinetic Rate Model, as these models are the most popular and widely used to predict the coal devlatilization.

3.6.2.1.1 The Constant Rate Devolatilization Model

The constant rate devolatilization model [152] assumes that the volatile matter is released from the coal particle at a constant rate, i.e.

$$-\frac{dm_p}{dt} = A_0[g_{vol,0}(1-g_{w,0})m_{p,0}] \tag{3.14}$$

where:
A_0 – rate constant, s^{-1}.

3.6.2.1.2 The Single Kinetic Rate Model

The Single Kinetic Rate Model, proposed by [153], assumes that the devolatilization rate depends on the temperature of the coal particle, i.e.

$$-\frac{dm_p}{dt} = k[m_p - m_{p,0}(1-g_{vol,0})(1-g_{w,0})] \tag{3.15}$$

where:
k – kinetic rate, s^{-1}.

The kinetic rate, is defined by the input of an Arrhenius type pre-exponential factor and an activation energy, namely

$$k = A_1 e^{-(\frac{E}{RT_p})} \tag{3.16}$$

where:

T_p – temperature of the coal particle, K.

3.6.3 Char combustion

The biomass char combustion mechanism is based on the model validated for coal char combustion [47]. Although, the biomass fuel particle has over four times less fixed carbon than volatiles, the char combustion is an important stage in the biomass combustion. It is partially responsible for the NO_x and CO emissions [47]. The formation of char and its shape influences its combustion process and pollutants formation. Some of the biomass char combustion can result in carbon-in-ash, in pulverised biomass fuel boilers and it can be up to 10 wt% of the ash. The unburned carbon-in-ash indicates incomplete combustion which reduces the combustion efficiency.

Numerical calculations can predict coal char combustion using different sub-models and these models were developed for the coal combustion. However, in comparison to coal, biomass for instance, has catalytic elements which strongly influence the reaction between carbon and O_2, CO_2 or H_2O which may influence the biomass char combustion process.

There have been studies regarding biomass char combustion rates. However, few studies has been performed at high temperatures. Wornat et al. [154], in his experiments on the reaction rates for two biomass chars, namely pine and switchgrass, noticed that biomass char rates are 2 – 4 times faster than the for coal chars.

The char structure and activation energy depends on the type of fuel,

the initial particle volatiles content, initial porosity, heating rate, composition of the combustion atmosphere during devolatilization, mineral matter content, etc. [47]. Since the biomass char has a more disordered carbon structure and higher oxygen content, it tends to be more reactive than coal char [47]. The coal particles during the combustion process becomes more spherical [151]. Biomass, in contrast to coal, tends to retain its irregular initial shape during devolatilization [47].

In pulverised fuel combustion, it is assumed that around the char particle is a gas film through which the oxygen has to diffuse to be able to react with the char surface. However the increased surface area of the biomass area might increase the diffusion rate of the oxidant to the biomass char surface [47].

The metal and inorganic elements may effect the char biomass combustion, however it is thought that in the high heating rates it does not affect the combustion performance.

3.6.3.1 Char combustion model

When the devolatilization process is completed and the volatiles are completely evolved, the surface combustion of the char, which remained in the coal particle, begins [114]:

$$m_p > (1 - g_{vol,0} - g_{comb})(1 - g_{w,0})m_{p,0} \tag{3.17}$$

where:

g_{comb} – combustible fraction.

ANSYS Fluent provides a choice of four surface reaction rate models for combusting particles:

- diffusion-limited rate model
- kinetics/diffusion-limited rate model

- intrinsic model
- multiple surface reactions model

In this thesis, the two most commonly used [43] surface reaction rate models for combusting particles are implemented in Fluent and compared, namely the kinetics/diffusion-limited rate model and the intrinsic model [114].

3.6.3.1.1 The Kinetics/Diffusion Limited Rate Model

The kinetics/diffusion-limited rate model assumes that the surface reaction rate is determined either by the kinetics or by a diffusion rate. The diffusion rate coefficient is given by [152]:

$$D_0 = C_1 \frac{((T_p + T_\infty)/2)^{0.75}}{d_p} \tag{3.18}$$

and the kinetic rate by,

$$\mathcal{R} = C_2 \cdot e^{-(E/RT_p)} \tag{3.19}$$

are weighted to yield a char combustion rate of

$$\frac{dm_p}{dt} = -A_p p_{ox} \frac{D_0 \mathcal{R}}{D_0 + \mathcal{R}} \tag{3.20}$$

where:

D_0 – the diffusion rate coefficient,

$\mathcal{R}$ – the kinetic rate,

A_p – surface area of the particle,

p_{ox} – partial pressure of oxidant species in the gas surrounding the combusting particle,

C_1 – the Mass Diffusion-Limited Rate Constant,

C_2 – the Kinetics-Limited Rate Pre-Exponential Factor.

3.6.3.1.2 The Intrinsic Model

The intrinsic model in Fluent is based on the Smith model [107] and it assumes that the order of the reaction is equal to unity. As in the kinetic/diffusion model, the intrinsic model assumes that the surface reaction rate includes the effects of both the bulk diffusion and the chemical reactions.

3.6.4 Species Transport

In the coal combustion, numerical calculations of the mixing and transport of chemical species is crucial. Therefore, in ANSYS Fluent these can be modelled by solving the conservation equations that describe the convection, diffusion, and reaction sources for each component species [114].

The simulation of the volatiles combustion involves the chemical reactions between the fuel and the oxidizer, its mixing and transport. The chemistry of the combustion is a complex phenomenon, hence for numerical simulations it has to be simplified. The species transport model is related to the volumetric reactions with specified stoichiometric coefficients.

The reaction rates that appear as source terms in the species transport equation (3.4) can be computed in Fluent using one of the following models:

- Laminar finite-rate model,
- Finite-Rate/Eddy-Dissipation model,
- Eddy-Dissipation model,
- Eddy-Dissipation concept.

Since the fuel combustion is a rapid process, the reaction rate can be assumed to be controlled fully by the turbulent mixing, thus the de-

tailed and computationally expensive Arrhenius chemical kinetic calculations and its turbulent fluctuations can be avoided [114]. A turbulence-chemistry interaction model, called the Eddy-Dissipation model, based on [155], was employed. For realistic results, the two-step reaction mechanism was employed. This model allows for the simulation of the volatiles combustion without the detailed knowledge of the combustion kinetics [155].

The Eddy-Dissipation model with a two-step reaction of the volatiles combustion, is used for the calculation of the species transport in this thesis, i.e.

$$volatiles + n_1 O_2 \rightarrow n_2 CO + n_3 H_2 O + n_4 N_2 \tag{3.21}$$

$$CO + 0.5 O_2 \rightarrow CO2 \tag{3.22}$$

where:

n_1, n_2, n_3, n_4 are the stoichiometric coefficients.

Calculations of the stoichiometric coefficients are presented in the next Chapter.

3.6.5 Challenges in the CFD modelling of biomass combustion

3.6.5.1 Biomass particle shape

CFD uses the assumption of spherical particle shape for simplicity. A sphere, among other shapes, has the lowest surface-area-to-volume ratio. However, the assumption of a spherical shape for the fuel particles is commonly used in coal combustion modelling but it may be inappropriate for biomass combustion modelling. Moreover, coal tends to maintain the spherical shape during the combustion process, therefore for coal combustion this assumption is very good. As mentioned in Sections 2.4.7 and

2.4.8, pulverised biomass has an irregular shape and a larger size than the coal particles.

To describe the irregular shape of the biomass then some parameters have to be introduced, such as the aspect ratio (AR) and shape factor (SF), and those are described in detail in Chapter 7.

3.6.5.2 Drag coefficient

The irregular shape of the biomass particle may influence the aerodynamics of the biomass particle flow inside the furnace. The transfer of momentum between the continuous gas phase and the solid particle is represented using the drag coefficient. To account for the non-spherical shape of biomass particles, the shape factor is implemented in the drag coefficient calculations by applying the method based on [108]. The drag coefficient (C_d) is calculated for non-spherical particles with a given SF is as follows:

$$C_d = (24/Re)\left(1 + b_1 \cdot Re^{b_2}\right) + \frac{b_3 \cdot Re}{b_4 + Re} \tag{3.23}$$

where:

$$b_1 = exp\left(2.3288 - 6.4581 \cdot SF + 2.4486 \cdot SF^2\right) \tag{3.24}$$

$$b_2 = exp\left(0.0964 + 0.5565 \cdot SF\right) \tag{3.25}$$

$$b_3 = exp\left(4.9050 - 13.8944 \cdot SF + 18.4222 \cdot SF^2 - 10.2599 \cdot SF^3\right) \tag{3.26}$$

$$b_4 = exp\left(1.4681 + 12.2584 \cdot SF - 20.7322 \cdot SF^2 + 15.8855 \cdot SF^3\right) \tag{3.27}$$

The Reynolds number Re, see equation (3.23), is computed using the diameter of the sphere having the same volume as the actual particle volume.

3.6.5.3 State-of-the-art of the CFD of pulverised biomass combustion

At present, biomass particle models that are used in CFD modelling generally assume that the particles are spherical and isothermal [91,156].

There are studies that introduce a simplified way of dealing with irregular biomass particle shapes. The extension of the outer surface area of the spherical particles is applied to take into account the effect of the availability of the larger external surface area of non-spherical biomass particles.

Spherical, cylindrical, and flat/flake wood particles with similar volumes (masses) but different shapes form the basis of the investigation by Lu [79]. Samples were classified into two groups: hardwood sawdust particles ($\sim$ 300 μm) and poplar dowel particles ($\sim$ 2 mm), based on the size range. Particle images are shown in Figure 3.2, and the three images are for hardwood sawdust particles which are flake-like, cylinder-like, and near-spherical shapes.

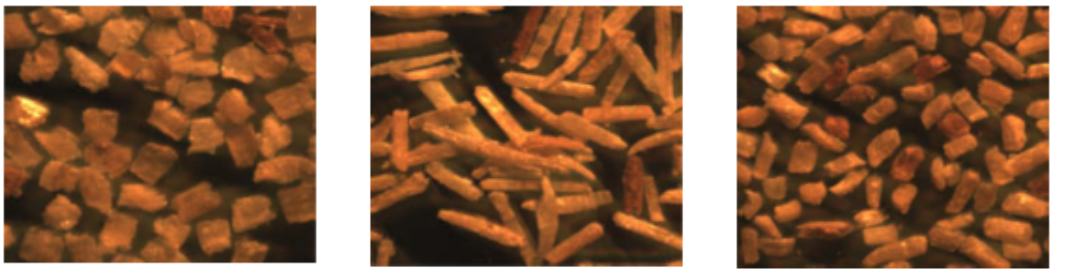

(a) flake-like particle (b) cylinder-like particle (c) near-spherical particle

Figure 3.2: Images of the hardwood sawdust particles with flake-like (a), cylinder-like (b), and near-spherical (c) shapes. [79].

The mathematical model for the mass loss of a single cylindrical particle of wood during the combustion process was proposed by Porteiro et al. [157]. The one-dimensional model that predicts biomass particle de-

gradation includes moisture evaporation at constant temperature. Also, the pyrolysis has been modelled with three parallel reactions for the transformation of wood into gas, tar and char. Char oxidation can be considered as being kinetically or diffusionally controlled, however, the predictions find that the char oxidation is mainly diffusion controlled at high temperatures. Furthermore, the particle shrinking during char combustion has been also implemented and this substantially reduces the time of pyrolysis.

This model has been validated with experimental data by Larfeldt et al. [158]. The experiments measured the internal temperature distribution and mass loss of a large cylindrical sample of wood with a radius 25 mm and length 300 mm during pyrolysis in an inert atmosphere at 973 K. The study indicates that the thermal diffusivity for dry wood is approximately 0.2 mm^2/s.

The model prediction showed that the time for completed burnout for a briquettes depends on the initial moisture content, size and density. Also, at the start of the pyrolysis and the end of the char combustion differs between the models and the measurements. This difference can be explained with the cooling effect of the evaporation water from the biomass particle, thus creating a layer enclosing the particle from the radiation coming from the walls. The experiments show the delay on the start of the pyrolysis and this may be related with the time needed for the outer layer of the particle to reach the temperature when pyrolysis starts.

The model describing the heating-up of the particle for pyrolysis and char combustion were derived using a single step first-order Arrhenius reaction, since the first stage devolatilization was found to be dominant in the high heating rates [159]. Further, the empirical relationship between the particle mass, moisture content and ignition delay, the volatile flame duration and char burn duration has been evaluated. The particle surface temperature predictions were validated with the measurement data

taken using an imaging technique. Moreover, the effect of the shape of the single particle on the volatile flame duration has been investigated. The measured differences were found to be only minor. It has been found that with increasing particle aspect ratio, the time of devolatilization decreases. The effect of the orientation of the particle has also been examined with marginal and not significant differences against other measurement data. This was confirmed by other modelling [160] and experimental [161, 162] studies.

Miller and Bellan [163] performed parametric studies of the reactor temperature, heating rate, porosity, initial particle size and initial temperature effects on the char yields and conversion time using a spherically symmetric particle pyrolysis model. The results show that the increment in the heating rate decreased the char yield and the conversion time time for cellulose and wood. Further, the char yield and the conversion times were found to be an increasing function of the initial particle size.

Di Blasi [164] performed theoretical and experimental investigations on the influence of the biomass particle size, reactor heating rates and final reactor temperature. This study presents results similar to those published by Bharadwaj et al. [165], with the large size of the particles increases the char yield. Further, higher heating rates result in higher volatile yield and a lower char yield.

Di Blasi [166] performed an investigation of the impact of the physical properties on biomass devolatilization. The energy and mass transfer model of the biomass particle predicted the influence of the density, thermal conductivity and specific heat capacity. The study conclusion was that the variation in the physical properties mainly affect the reactivities of the secondary reactions of the tar vapours and the conversion time for the conversion in a thermally thick regime. The biomass density and the thermal conductivity of the char are found to be the most sensitive parameters.

Gera et al. [145] investigated large aspect ratios of the biomass particles on carbon burnout and also the temperature distribution inside the non-spherical particles. The study shows that the isothermal assumption of the spherical particles significantly underpredicts the temperature of the particles, and as a consequence, the burnout. The results from the CFD calculations presented in this paper suggest that the cylindrical shape of the biomass particles with large aspect ratio may be beneficial when co-firing compared to the spherical particles. These results indicate the importance of the particle shape factor while specifying the criteria for biomass processing for co-firing applications. Further, the CFD results illustrate how important is the shape factor in predicting the particle trajectories, residence time, carbon burnout, heat and mass exchange.

Bharadwaj et al. [165] applied models of kinetics and heat mass transfer to predict the effect of particle size, shape, density, composition and internal thermal gradient. The drying and devolatilization stages of the combustion processes were found to be driven by heat-transfer, where oxidation was found to be mass-transfer controlled for most biomass type fuels. Also, they found that during devolatilization, most of the volatiles are released from the particle, thus removing most of the mass from the biomass particle. Therefore, under high-temperature pyrolysis conditions, up to 95 wt% (daf) of the mass is removed during devolatilization.

In Jalan and Srivastava [167], cylindrical shaped biomass particles of different sizes were investigated and its influence on the pyrolysis with various heating rates. Furthermore, in other models, namely the Horbaj [168] and Liliddahl [169] models, the particle geometric factor has been introduced to take into account the effect of biomass non-spherical particle shape. Those models can deal with different particle shapes, such as a sphere, cylinder, or slab.

In another research paper by Janse and Westerhou [170], this investigates the influence of the spherical, cylindrical and flat particle shapes

on the flash pyrolysis of a single wood particle. It has been found in this study that when considering the characteristic size of the particles as the minimum particle dimension, the spherical in shape particles, when compared to other shapes, react the quickest, as they have the highest area-to-volume ratio. The flat particle, in this case, reacts the slowest. This trend has been a reason of introduction of the characteristic dimension – spherical-equivalent diameter, which is the diameter of the spherical particle with the same volume as the non-spherical particle. The spherical particles, in this case, react the slowest among all the other shapes investigated. Further, it has been investigated that at small particle diameters (typically less than 200 µm), the rate of reaction becomes dominant and the different particle shapes have nearly the same conversion times [170].

Much interest has been given to the char reactivity and oxidation in the literature. Char derived from biomass is considered to be composed mainly form carbon [171]. Therefore, in the sense of the chemical structure, the biomass and coal char are similar. However, there are differences in the physical and thermal properties, namely density, thermal conductivity, porosity, surface area, shape and size. Moreover, the shirking mechanism of these two chars is different [47, 55, 82, 84, 100].

It was found that the combustion of particles of biomass below the size of 200 µm was rapid, but the rate for the larger particles was dependent on their composition, size and shape.

An experimental and mathematical study with a moving and suspended biomass particle has been performed by Yang et al. [172] and they found that the isothermal particle assumption is no longer valid for particles exceeding 150 – 200 µm in size.

Lu at al. [173] investigated the drying, devolatilization, char gasification and char oxidation behaviour of biomass particles in a single-particle reactor. The measurements include the mass loss, surface and centre

temperature of the particle of poplar dowel particles. Further, a one-dimensional mathematical model that describes the single-biomass combustion was proposed and the model predictions show reasonable agreement with the experimental data. It was founded that the isothermal assumption for non-spherical particles of biomass that exceeds a few hundred microns in size poorly represents the combustion process. In particular, the temperature rise is affected by the implementation of the thermal gradient in the fuel particles, large particles reacting slower than the one predicted neglecting thermal conduction.

An experimental and theoretical study of the effects of the particle shape and size on the devolatilization of biomass particle has been parformed by Lu et al. [79]. Further, the work introduced a particle shape reconstruction algorithm based on the particle volume and surface area. Also, the one-dimensional, time-dependent single particle pyrolysis model was developed, being that it is able to simulate particles with different shape and size. Experiments showed that the biomass particle shape and size have an influence on the overall particle reactivity and reaction rates. It was found from theoretical studies that the spherical mathematical assumption for the particles poorly represents the combustion behaviour when the particle exceeds 200 – 300 µm in size. Further, experiments and modelling predictions indicate that the pyrolysis process is driven mainly by heat transfer rather than kinetics since both shape and size influence the conversion time significantly, especially for large particles.

Gubba et al. [160] investigated the influence of the particle shape and thermal gradients of biomass particles on pulverised coal/biomass co-fired flames. In this paper, the introduction of the thermal conductivity in the commercial CFD software ANSYS Fluent has been proposed to include the thermal conduction in the large biomass particles. This model had been validated against experimental measurements by [173] and [145]. The developed code, on the top of the thermal gradient comprises of the

different shapes of biomass particles, namely sphere, cylinder, disc and slab. The predictions are stated to be in good agreement with the measurements. A significant influence of the thermal gradients on the CFD prediction has been observed. Therefore, the thermally thick particles cannot be neglected in the CFD modelling of co-firing and pure biomass combustion.

Weber et al. [174] lead the experimental studies on combustion of alternative fuels, including coal and different types of biomass in jet flame furnaces by investigating flame ignition, temperature levels, NOx emissions, burnout and fly ash slagging propensity. The in-flame temperature measurements for the coal flame were higher by 100 K compared to the biomass flames. Also, the ignition was faster for the coal fuel in the 1.2 excess air. The latter is related to the finer milling, and therefore smaller particles of the coal fuel. Burnout was observed to be above 94.2% for all fuels.

Recently, Mason [48] presented some single biomass combustion studies. These measurements were aimed at examining the duration of the different stages of single biomass particle combustion. The types of woody biomass were investigated, namely pine, eucalyptus and willow. Each particle has a cylindrical/cuboid shape with dimensions in the range of 0.5 mm to 4 mm. However, for the heat transfer calculations, the equivalent spherical particle size was used. In the experiments performed, the Meker type natural gas burner was used to produce a flat flame for temperatures about 1800 K and oxygen concentration of approximately 10.75%. The particles of the biomass were supported on a fine steel needle. A moveable coaxial water-cooled sleeve protected the fuel sample from the gas flame. The measurements were taken using a video camera, and when the sleeve was withdrawn, it exposed the biomass particles to the high temperature of the flame. However, this study has some limitations in terms of application to industrial combustion cases:

- The fuel particles are not moving, which is affecting the Reynolds number. Most of the particles in the combustion test facilities experience a particle Reynolds number less than 5 during the majority of their residence time.
- The particles in the experiment are heated-up from the flat flame only on one side.
- The temperature of the surroundings is about 300 K, and in the real furnaces the temperature reached approximately 800 K.
- The moisture content is higher than in the biomass used for industrial boilers.

Mehrabian et al. [175] proposed a CFD model for the thermal conversion of biomass particles for the biomass grate furnace and this model has been validated with experiments [173]. A one-dimensional model was developed for spherical and cylindrical shaped particles. The particle is considered in four layers, wet fuel, dry fuel, char and ash corresponding to the four main stages of biomass thermal conversion. The moisture evaporation was simulated at a constant temperature. The biomass pyrolysis is modelled with three competing decomposition reaction for three compositions of biomass, namely cellulose, hemicellulose and lignin. Char oxidation is kinetically and/or diffusionally controlled.

Porteiro et al. [157] presented a one-dimensional mathematical model of a single wood particle degradation under combustion conditions in a fixed bed combustion system. Vaporization of the moisture for the biomass particle occurs at a constant temperature, while the wood pyrolysis was assumed with three parallel reactions of wood into gas, tar and char. Char oxidation is kinetically and/or diffusionally controlled and shrinking of the fuel particle has been included in the model.

Yang et al. [172] published a study on a single biomass particle combustion. A two-dimensional mathematical model that predicts the beha-

viour of different sizes of a cylindrical particle of biomass surrounded by a passing gas stream was proposed as a way of modelling the combustion of pulverised biomass fuel.

3.7 Conclusions

CFD modelling of combustion systems has the advantage of allowing for the optimisation of the process with relatively low cost. Applied to the biomass combustion process, modelling techniques will serve to optimise the novel combustion environment so that it can become a competitive low-carbon technology. However, models that are specific for an coal-fired combustion need to be re-evaluated for their applicability to predicting biomass-fired systems, specifically models for particles heat exchange.

This chapter has reviewed a series of models to represent the solid fuel combustion. CFD is widely used for predicting the fluid flow within combustion systems, however the models that are widely used for particle heat exchange are often chosen for their computational efficiency rather than their physical accuracy. CFD models use the assumption of an isothermal spherical shape of solid fuel particles neglecting the irregular and large size of biomass fuel.

Chapter 4

Experimental study of the 250 kW PACT facility

In this chapter the techniques employed in the investigation of the air preheated and non preheated coal combustion experiments in the 250 kW furnace and retrofit to biomass fuel have been presented. The experimental programme has been conducted to collect the data useful for validation of the CFD models. The experimental facility used to obtain the data has been described followed by the measurement techniques that were utilised during the experimental programme. The chapter concludes with a summary of the results for the air-firing of coal using non-preheated and preheated air. The comparison of the cases is drawn against the in-furnace temperature measurements, radiative heat flux on the furnace walls and the flue gas emissions.

4.1 250 kW Combustion Test Facility

The experimental programme has been performed on a 250 kW Combustion Test Facility (CTF), which is one of the UK Carbon Capture & Storage Research Centre (UKCCSRC) Pilot-scale Advanced Capture Technology (PACT) Facilities — the national specialist research and development fa-

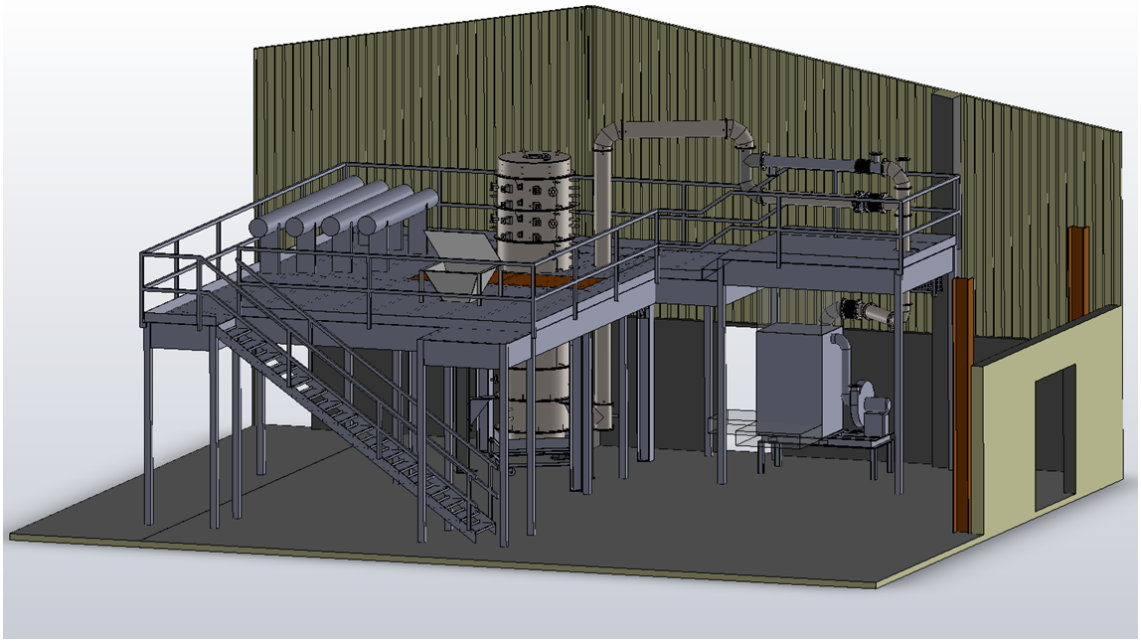

Figure 4.1: A schematic of the PACT Combustion experimental facility [140].

cilities for combustion and carbon capture technology. The PACT facility is located near Sheffield in South Yorkshire. The Combustion Test Facility (CTF), depicted in Figure 4.1, consists of a 250 kW down-fired cylindrical furnace, fired with pulverised solid fuel, namely coal and biomass, under both air and oxy-firing conditions. The plant is equipped with a fuel feeding system, separate for coal and for biomass, an interchangeable coal/biomass burners, a gas heaters for the purpose of preheating the oxidizer in the preheated cases, a dedicated air and O_2/CO_2 metering skids, a temperature and flow monitored cooling water system for the furnace, a flue gas heat exchanger, a high temperature candle filter for the purpose of reducing the fly ash present in the flue gas, an exhaust fan and a connection to the central flue gas duct to the stack. There is a possibility of connecting the remaining flue gas to the solvent-based carbon capture plant for the purpose of CO_2 sequestration and capture. The plant is operated and monitored using a local Human-Machine Interface (HMI), which is connected to an industry standard System Control And

Data Acquisition (SCADA) system located in the control room, hence all the measurements are controlled on-line [176]. A schematic diagram of the Air and Oxy-fuel PACT Combustion Plant is presented in Figures 4.2 and 4.3, respectively.

The Oxy-fuel Combustion Plant showed in Figure 4.3 has the same scheme as the Air Combustion Plant, however, it is supplied with a different oxidizer — a mixture of CO_2 and O_2 instead of conventional air. This prevents nitrogen in the air generating flue gases with around 95% CO_2 suitable (after processing) for geological storage or CO_2 utilisation applications. The UKCCSRC PACT facility is equipped with gas tanks with these gases. Furthermore, there is a possibility of exhaust gas recirculation and the O_2 make-up mixing, hence a dry and wet oxidizer mixture is possible to simulate oxy-combustion with dry and wet recycle of the flue gas.

In both cases, under air or oxy-fuel combustion, the PACT CTF is fired up with a natural gas pilot to preheat the combustion chamber and prepare conditions to assist the solid fuel ignition.

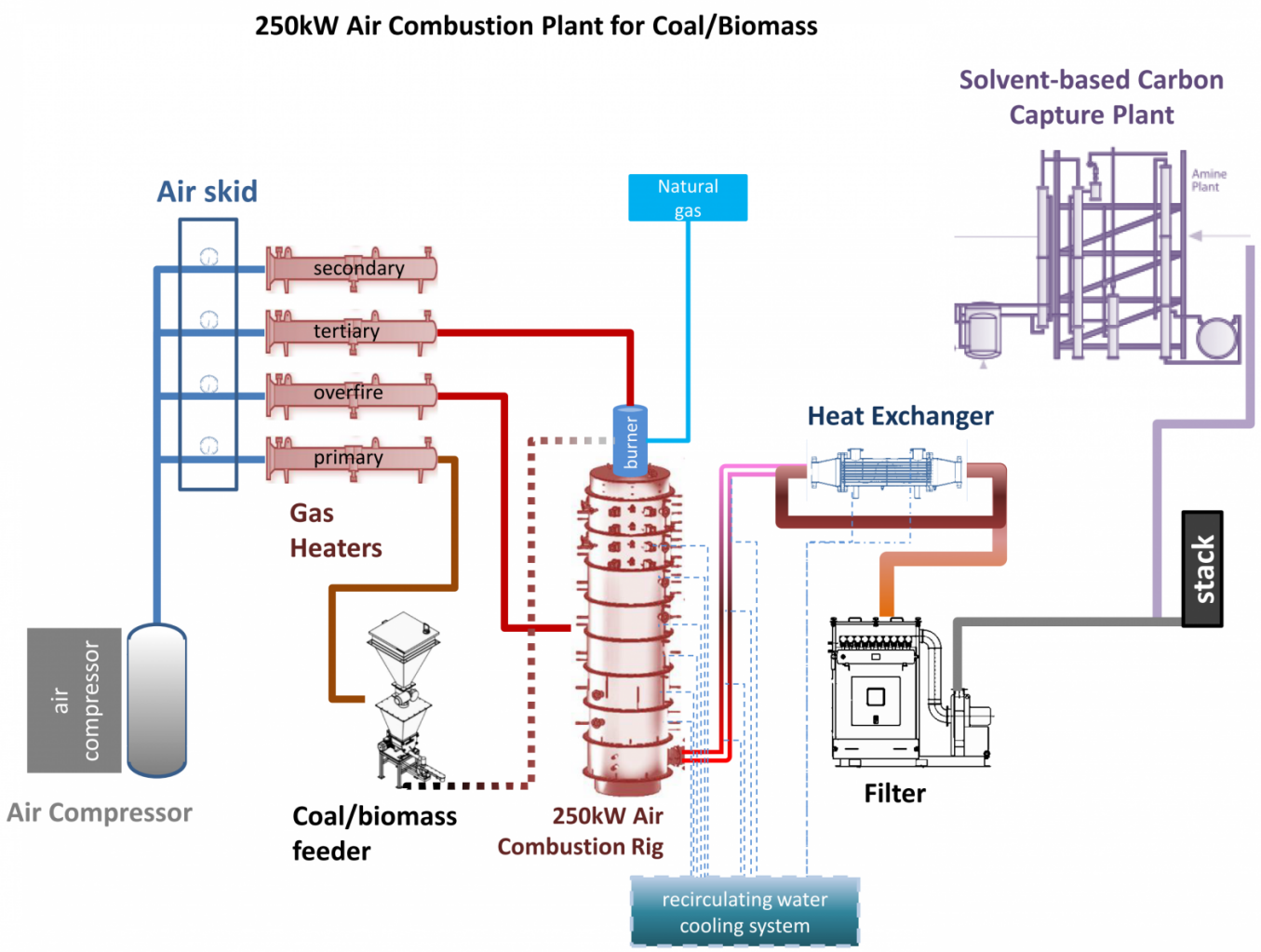

Figure 4.2: Schematic of the 250 kW Air PACT Combustion Plant [176].

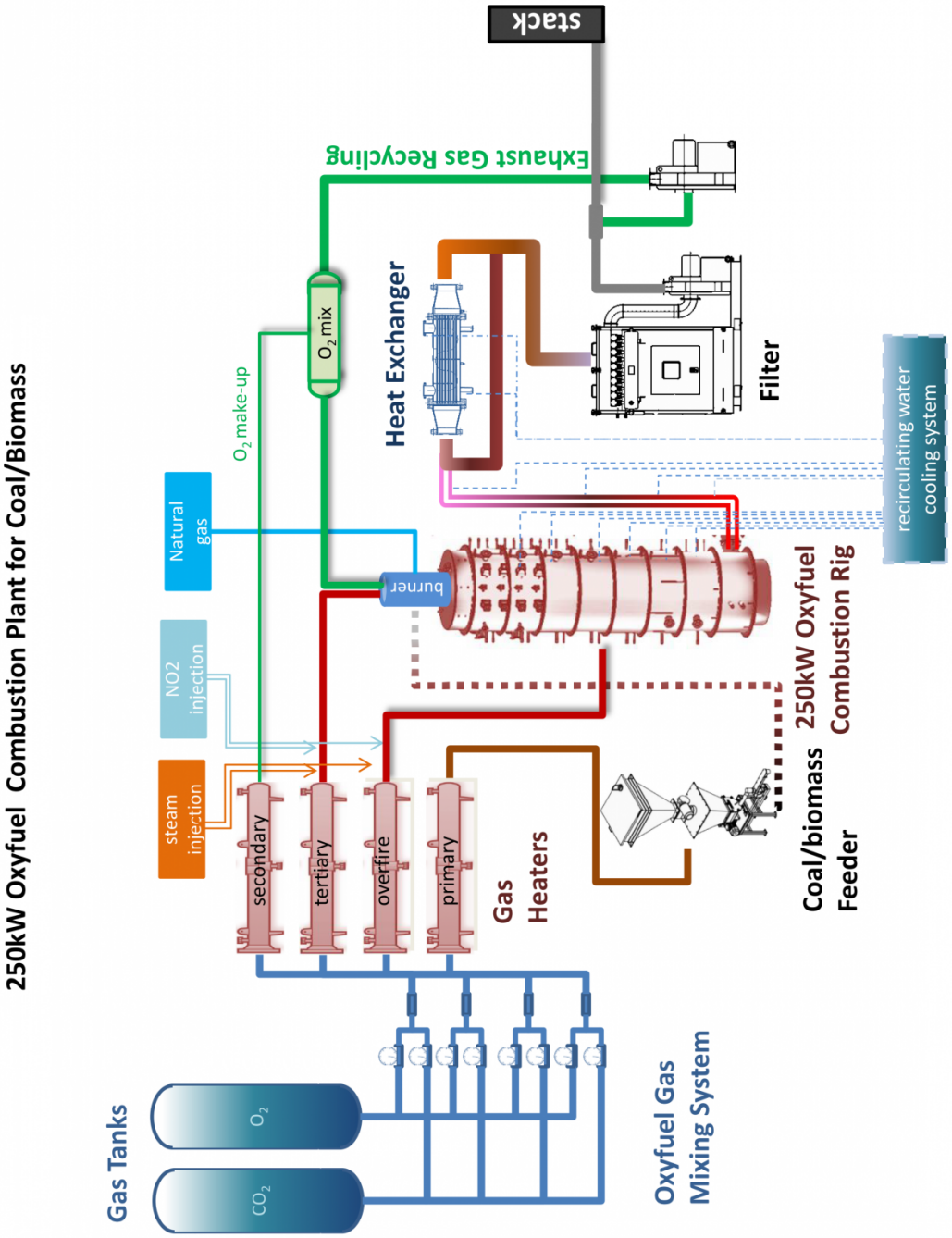

Figure 4.3: Schematic of the 250 kW Oxy-fuel PACT Combustion Plant [176].

4.2 Geometry of the PACT Combustion Rig

The combustion rig is cylindrical, down-fired, 4 m high and it is made up of eight 0.5 m long sections lined with 0.1 m thick, lightweight alumina silicate refractory. The inner and outer diameters of the furnace are 0.9 m and 1.1 m, respectively. Viewing ports are installed in the top three sections of the furnace to allow for visual inspection of the flame. Ports for in-furnace measurements are installed along the furnace. A general outline and a CAD drawing of the PACT combustion rig are presented in Figures 4.4 and 4.5, respectively. An outer view of the geometry of the 250 kW Combustion Rig with the burner and viewing ports for measurements are presented in Figures 4.6 and 4.7.

The top sections of the CTF are made from a high density concrete to enable the flame stability enhancement. The bottom of the rig is sealed with a water tray aimed at preventing the escape of the combustion gas from the facility. The flue gas escapes the furnace through the exhaust pipe located approximately 4 m away from the burner exit. The upper six sections of the furnace are cooled with the recirculating water for the purpose of taking out the thermal output from the combustion process. The furnace pressure is balanced by the exhaust fan, maintaining the furnace below atmospheric pressure at -1 mbar to ensure safe operation [176].

4.3 Measurements taken on the 250 kW Combustion Rig

The combustion rig is designed to operate at 250 kW maximum thermal input. For safety reasons, the maximum thermal input selected for these experiments is 200 kW. The furnace is preheated by natural gas using a premixed torch igniter. In each testing day, after reaching a steady tem-

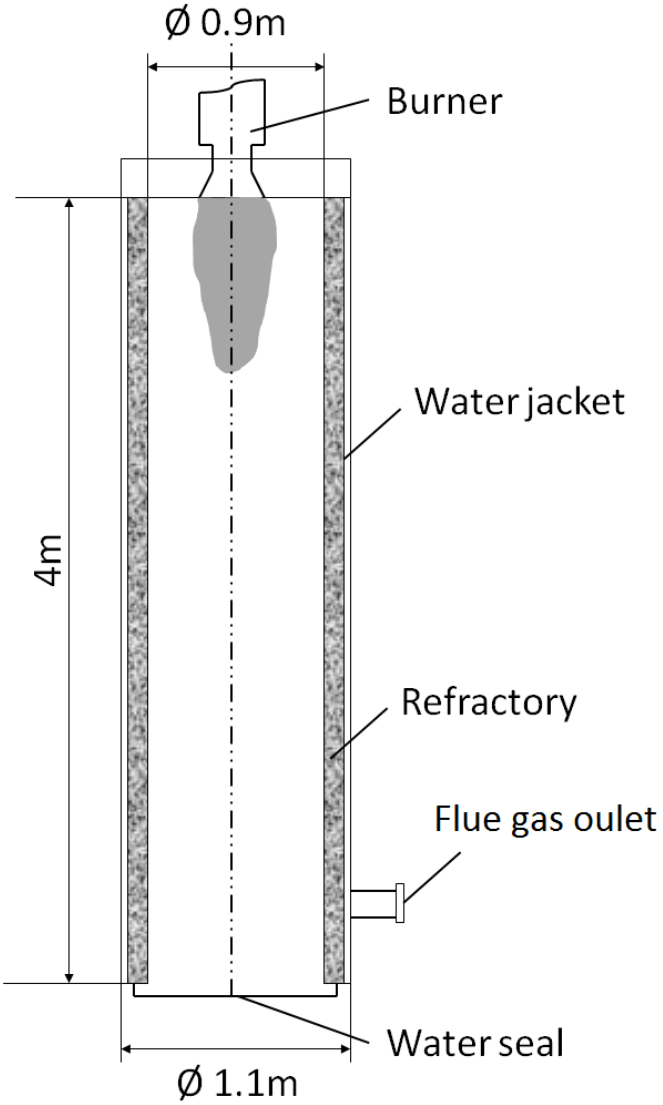

Figure 4.4: A schematic of the PACT Combustion Furnace [140].

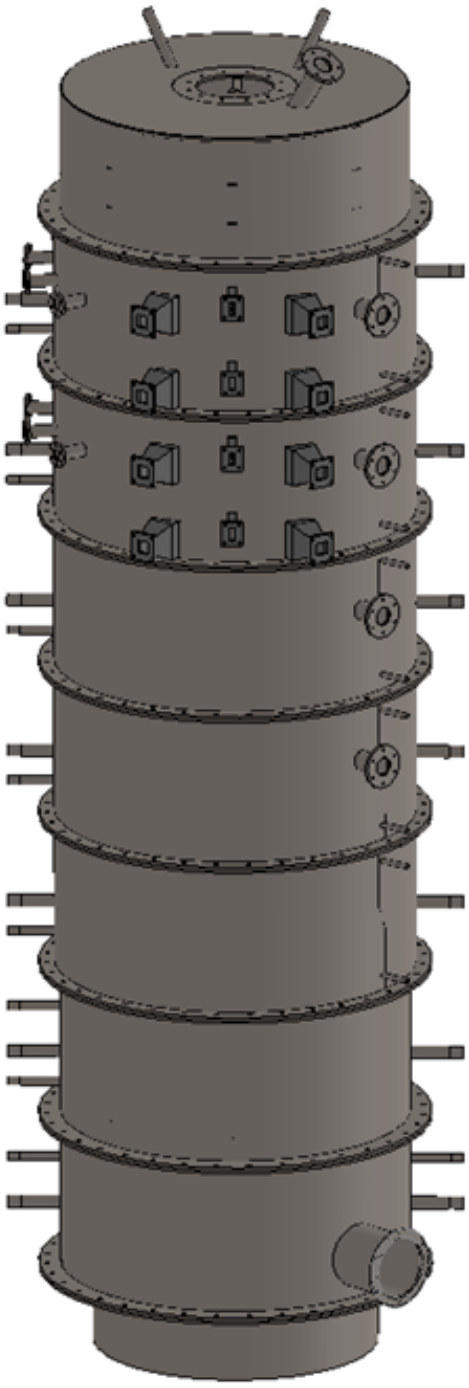

Figure 4.5: A CAD drawing of the geometry of the PACT Combustion Furnace [176].

Figure 4.6: Upper sections of the PACT Combustion Rig with viewing ports and burner on the top [176].

Figure 4.7: Photograph of the lower sections of the PACT Combustion Rig [176].

perature with firing natural gas for about 2 hours, switching to coal starts at about 160 kW thermal input then the coal feed rate is increased until the 200 kW is achieved.

The experiments are based on a constant thermal input, a target exit oxygen ratio and a target primary/total combustion air split. In this study, the selected baseline thermal input is 200 kW, the exit oxygen is 3.3-3.8% by volume, and the primary oxidant is 18-20% of the total combustion air.

Accordingly, the baseline case parameters such as the fuel flowrate, oxidant flowrates, tertiary oxidant temperature, air/fuel ratio, and primary/tertiary air split, were determined prior to the current study experiments based on the stoichiometric calculations for each case tested (air preheated and non-preheated cases). The optimisation process of the baseline cases are described in details in [176].

The furnace has a number of viewing ports along the furnace, thus allowing various measurements to be taken, namely heat flux and temperature profiles and flue gas composition (O_2, CO, CO_2, SO_2, NO_x). Additionally, the viewing ports in the top sections of the furnace are installed to allow for three-dimensional flame imaging to be undertaken.

4.3.1 Temperature measurements

Process temperature measurements were made using ceramic sheathed Type R thermocouples installed within the furnace and Type K thermocouples within the flue gas ducts and cooling water pipes. These measurements were available on-line during the operation to aid monitoring and the control of the combustion facility.

The in-flame temperatures were measured in each section of the combustion chamber at several depths inside the boiler for the purpose of the combustion gas temperature profiling inside the furnace. The in-furnace temperature measurements were taken using a suction pyrometer, see Figure 4.9 with a Type B thermocouple located at the tip of the probe,

within the inner alumina sheath protecting the thermocouple from deposits and chemical attack. This inner sheath is surrounded by an outer radiation shield, thus reducing the radiative heat exchange. While the measurements were taken the probe was cooled with the cooling water [176].

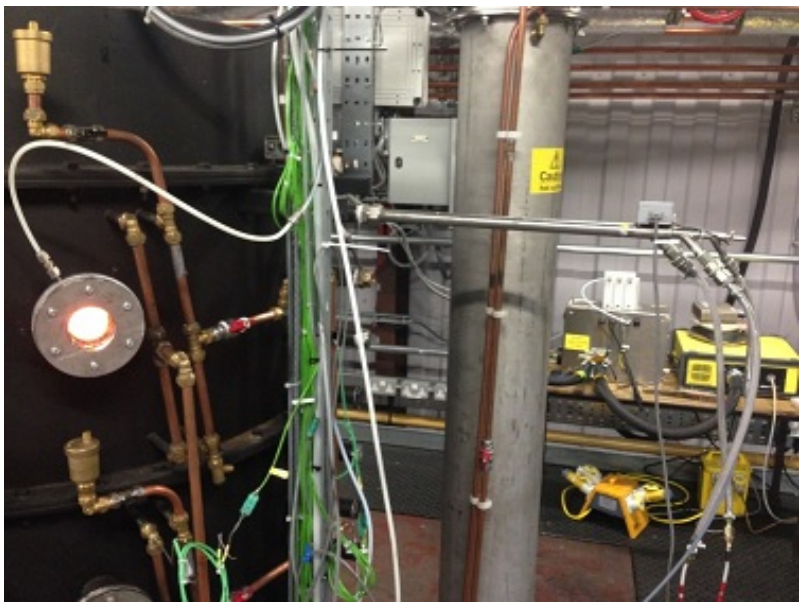

Figure 4.8: Photograph of the suction pyrometer during temperature measurements - Suction pyrometer positioned in the first 38.1 mm measurement port during an air-fired experiment [176].

The manufacturer's recommendations stated that the probe required 3 minutes for the thermocouple to reach steady state temperature when placed within the furnace, and a further 1 minute was needed for each 100 K temperature change. However in practice this time was observed to be less and the readings stabilised within 0.5-1 minute and the sample period was considered to commence. Sampling was performed for 3 minutes at each locations, except for the locations directly under the coal collectors which clogged up the probe within a couple of minutes. Sampling at these locations were conducted for just over a minute [176].

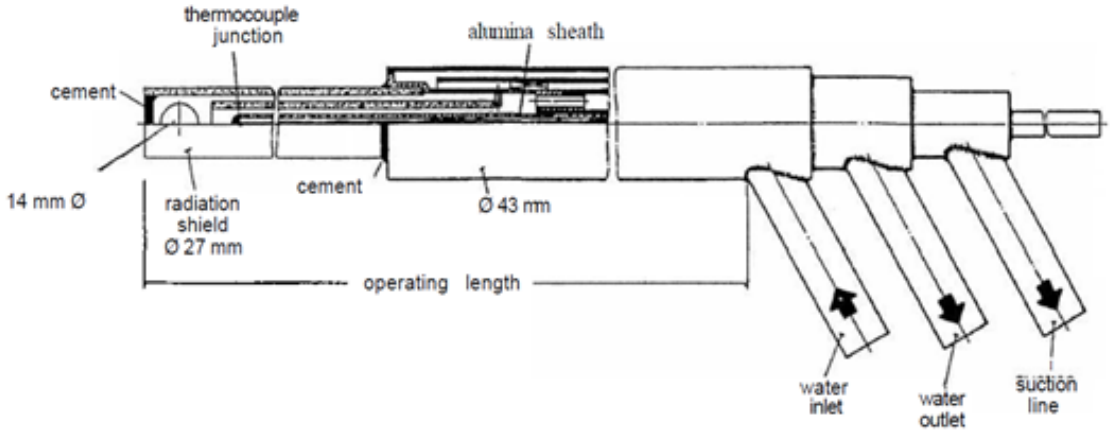

Figure 4.9: Schematic of a suction pyrometer [177].

4.3.2 SIR measurements

The measurements of the Surface Incident Radiation (SIR) were taken along the side wall of the combustion chamber along the burner centreline. The radiative heat transfer was measured using a MEDTHERM digital heat flux meter, which is convertible between total and radiative heat flux measurements. A MEDTHERM transducer is presented in Figures 4.10 and 4.11.

A MEDTHERM transducer is fitted with thermopiles at two points of the probe, namely 'hot' and 'cold'. The 'hot end' is located at the tip of the probe and the 'cold end' is placed inside the combustion chamber. The sensor is of the Schmidt-Bolter type, with a thermopile fitted at the probe tip. The heat flux is absorbed at the sensor surface and is transferred normal to that surface to the inner, cooled end of the sensor. A thermopile with junctions at both surfaces generates an emf signal corresponding to the temperature difference between the two surfaces. The sensor provides a linear output directly proportional to the heat transfer rate reaching the sensor tip [176].

The calibrations of the MEDTHERM digital heat flux meter were referenced to a blackbody. Further, the MEDTHERM transducer is convertible between total and radiative heat flux measurements. The radiative heat

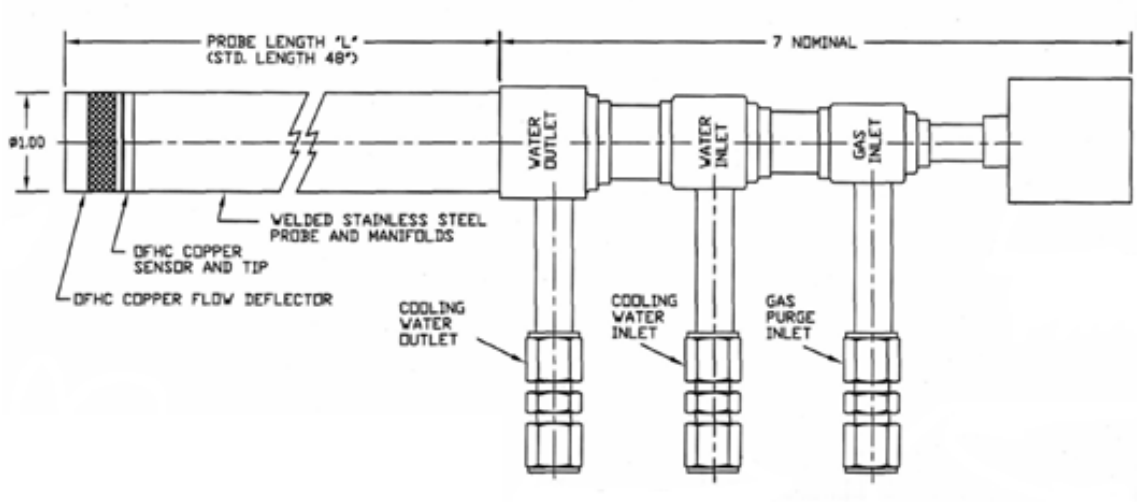

Figure 4.10: A schematic of the MEDTHERM heat flux probe [178].

flux measurements are taken using a gas purge to prevent the process of soot and ash building up on the surface of the probe and thus to reduce the convective heat transfer. O_2 free N_2 was chosen for this purpose, which is preferable to air or CO_2 - air would introduce O_2 at the probe tip, potentially altering the combustion environment close to the sensor, and CO_2 with its higher heat capacity would cool the surroundings of the probe and the flame more than N_2. An optional accessory for radiative measurements is a CaF_2 window attachment (Figure 4.11(b)). It shields the sensor from direct contact with the combustion gases, but it was prone to cracking, condensation and sooting even with the gas purge applied [176]. Therefore the radiative measurements were taken without the window attachment using the configuration shown in Figure 4.11(a).

Measurements of the total heat transfer flux was taken using the configuration shown in Figure 4.11(a), and the sensor tip was exposed to the combustion gases. The accuracy of the SIR measurements is $\pm$ 25 kW/m^2.

4.3.3 Gas sampling

Measurements of the flue gas composition were taken and the concentration of several species, namely O_2, CO_2, CO, NO_x and SO_2 were meas-

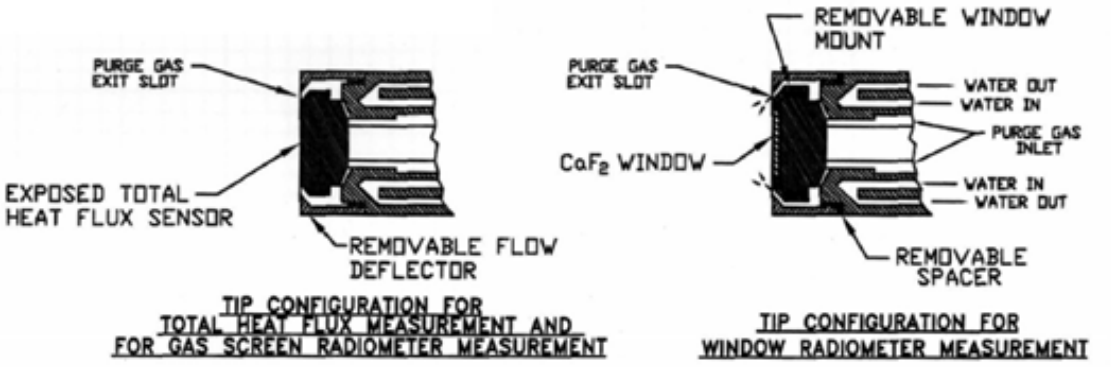

Figure 4.11: A schematics of different tip configurations a) and b) [178].

ured at the outlet of the UKCCSRC Combustion Rig. The custom made water cooled gas extraction probe was used for the gas sampling.

4.3.4 Experimental error estimation

Data were gathered from multiple sources at various time points during the experimental programme, leading to several sources of error. The main error sources identified in this study are discussed in this section.

The main equipment used for the measurements in the experimental work are: fuel feeder, thermocouples, air rotameters, gas analysers, MEDTHERM - heat flux meter, suction pyrometry. Most of the values are collected from the analysers and equipment manuals or calibration certificates [176].

The actual coal feed rate was fluctuating around the set point by less than 1% due to the vibration of the platform or due to the change in the ingress pressure. The temperature errors associated with the thermocouple measurements are determined by the manufacturer as $\pm$ 3%. Similarly, the air rotameters have a $\pm$ 2% error. The gas analyser accuracy and repeatability is $\pm$ 1% O_2, NO, CO_2, CO, and SO_2. The output is directly proportional to the absolute barometric pressure (measured at the exhaust port). However, due to the relatively constant pressure during the day, this effect is neglected. On the other hand, the ambient temperat-

ure influences the analyser unit readings. For the temperature range 278 – 313 K ± 0.03% is added to the zero and ± 0.1% to the span per K of highest range. The zero/span drift is less than 1% of the range in 1 hour at constant temperature and pressure [176].

The experimental error associated with the SIR measurements was determined by the manufacturer as ± 3%. An additional influence on the measurements was whether the probe was used with or without the window attachment. Due to the restricted view angle, 150°, associated with the window attachment, compared to the full hemispherical view angle of the probe with a bare tip. The measurements with the window attachment were also more susceptible to deposition on the probe tip, producing sharp dips in adjacent measurements. Although the probe was only pushed in up until the surface of the inner wall, the radiative heat flux measurements were still considered intrusive due to the use of the gas purge. Its effect was considered to be the strongest for the near flame measurements when the gas screen is directed at the flame, and this reduces in influence downstream of the flame [176].

The gaseous emissions are measured directly as volume fractions, either ppm or % of the flue gas, and therefore, the volumetric changes due to the pressure and temperature are avoided. Furthermore, the gas analyser calibration data of the zero and span conditions are used to correct the gaseous data for instrumental uncertainties. For the external temperature effect on the gas measurements, the actual data are normalised to the temperature of the coal baseline results [176].

4.4 Coal combustion

4.4.1 Coal burner

For the coal experimental tests, the facility has been equipped with a scaled-down version of a commercially available Doosan Babcock low-

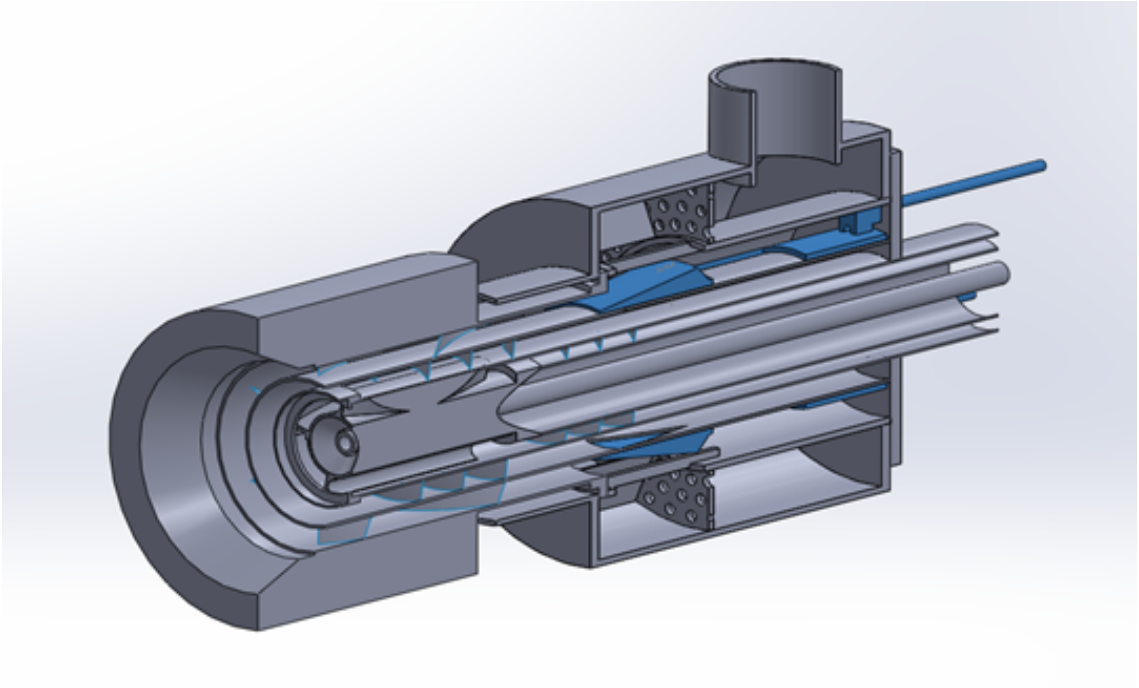

Figure 4.12: A CAD drawing of the burner and the secondary/tertiary split slide is highlighted [176].

NO_x burner. It is mounted at the top of the furnace in a down firing arrangement. The primary annulus is used for introducing the pulverised coal and carrier air, and the swirled secondary and tertiary annuli that delivers the rest of the oxidiser. The burner has an internal air splitting system that provides both secondary and tertiary air feeds from a single air supply. The exact amount of the individual flows of the secondary and tertiary oxidizer entering the furnace through the secondary and tertiary annuli is calculated with the use of a CFD analysis and the geometry of the burner with the known positioning for splitting [176], see Figure 4.12.

In Figure 4.13 an outer view of the burner is presented, and in Figure 4.14 the inner view of each inlet, with its blades and shape is visible.

As depicted in Figures 4.12, 4.14 and 4.15, the primary oxidizer and coal enters into an annulus with an inner and outer diameter 30.50 mm and 44.50 mm, respectively. The swirled secondary oxidizer enters through a surrounding annulus with inner and outer diameters 55.00 mm

Figure 4.13: Photograph of an outer view of the burner before being applied to the furnace [140, 176].

Figure 4.14: Photograph of the primary, secondary and tertiary inlets of the burner [140, 176].

Figure 4.15: A photograph of the front of the scale down version of the Doosan Babcock burner [140, 176].

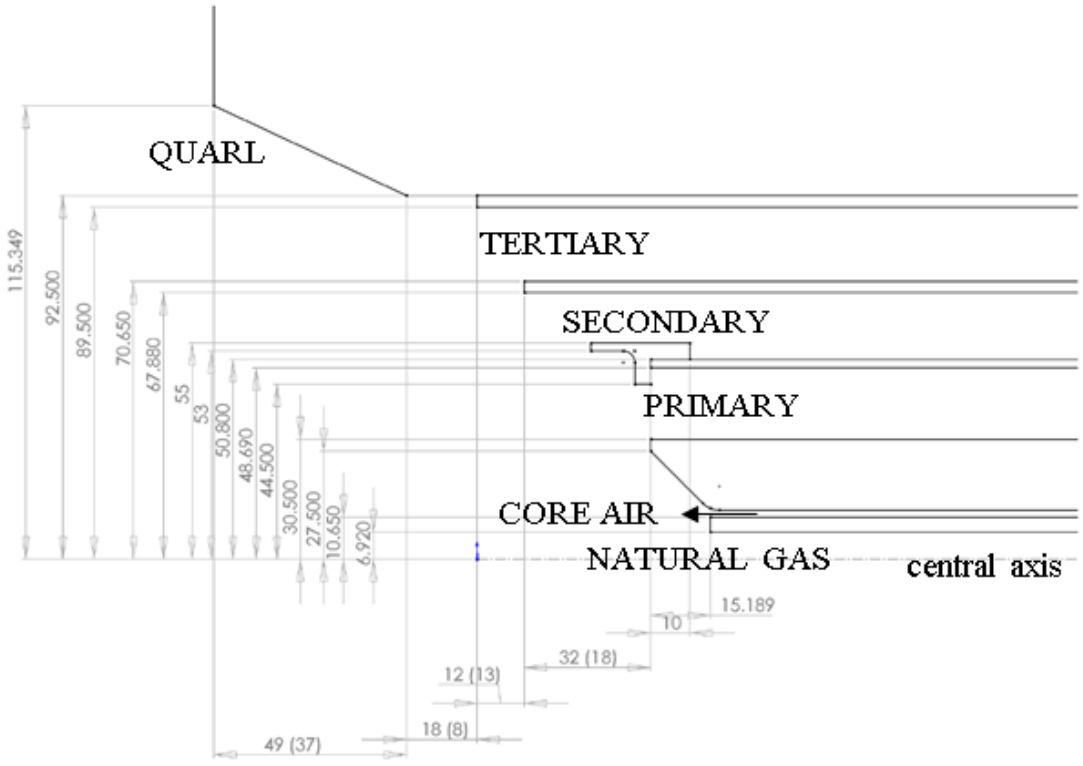

Figure 4.16: Burner annuli and quarl dimensions [140, 176].

and 67.88 mm, respectively. The swirled tertiary oxidizer enters the combustion chamber with an inner and outer diameters 70.65 mm and 89.5 mm [176], respectively.

4.4.2 Coal specification

A knowledge of accurate pulverised solid fuel properties is essential to the detailed modelling in combustion systems. The PACT facility is supplied with a Columbian pulverised coal, El-Cerrejon. The coal sample is characterised in two ways, namely by the ultimate and proximate analysis.

The ultimate analysis is the straightforward chemical analysis of the constituents of the coal, and the objective of the coal ultimate analysis is to determine the amount of chemical elements within the coal sample, such as: C, H, O, S, N. These data are measured in weight percent. The results of the ultimate analysis are expressed on as-received basis [179, 180].

The proximate analysis involves the determination of the amount of moisture, ash, volatile matter, and char within the coal sample using a thermogravimetric (TGA) analysis [179, 180]. In this thesis, the amount of all components of the proximate and ultimate analysis is given as a weight percent of the as-received coal. The ultimate and proximate analyses of the coal are given in Table 4.1.

The ultimate and proximate analysis and measurements of GCV has been performed externally and will not be described here as it is out of the scope of this thesis.

4.4.2.1 Calorific value

A term commonly used in conjunction with the combustion of fuels is the calorific value, which is defined as the amount of heat released by the completely burnt fuel. The calorific value is determined at constant

Table 4.1: Proximate and ultimate analyses of the El-Cerrejon coal.

Proximate Analysis, wt%		Ultimate Analysis, wt%	
W_{ar}	2.20	C_{ar}	70.30
A_{ar}	2.10	H_{ar}	5.30
vol_{daf}	42.50	N_{ar}	2.10
$char_{daf}$	53.20	O_{ar}	18.00
		S_{ar}	0.00

volume or pressure and with the assumption that the flue gas is cooled back to the initial temperature of the fuel and oxidizer [181].

Usually, two characteristic calorific values are used, namely lower calorific value (LCV) and gross calorific value (GCV). The difference between those values is the enthalpy of vaporization of the water vapour in the flue gas. The LCV does not contain the energy required to vaporize the water and the moisture in the flue gas is in the vapour form, whereas the GCV assumes that the water vapour condenses and the value of the GCV includes the enthalpy of vaporization of the water vapour and the moisture in the exhaust gas is in the liquid form [181]. The two calorific values are related by the equation:

$$GCV = LCV + m_{H_2O} \cdot h_{vap} \tag{4.1}$$

where:

GCV – gross calorific value, MJ/kg,

LCV – lower calorific value, MJ/kg,

m_{H_2O} – mass of moisture in the flue gas per unit mass of fuel, kg_{H_2O}/kg_{ar},

h_{vap} – enthalpy of vaporization, MJ/kg; h_{vap} (20°C) = 2.454 MJ/kg.

The mass of the water in the flue gas m_{H_2O} is calculated based on the ultimate analysis as follows:

$$
\begin{aligned}
m_{H_2O} &= \left(\frac{H_{ar}}{100 \cdot M_{H_2}} + \frac{W_{ar}}{100 \cdot M_{H_2O}}\right) \cdot M_{H_2O} = \\
&= \left(\frac{H_{ar}}{100 \cdot 2.016} + \frac{W_{ar}}{100 \cdot 18.015}\right) 18.015 = \\
&= 8.937 \cdot \frac{H_{ar}}{100} + \frac{W_{ar}}{100}
\end{aligned}
\tag{4.2}
$$

The El-Cerrejon coal has a gross calorific value (GCV) 30.79 MJ/kg, and therefore the LCV is 29.54 MJ/kg calculated based on Equations (4.1) and (4.2) as follows:

$$
\begin{aligned}
LCV &= GCV - 2.454(8.937 \cdot \frac{H_{ar}}{100} + \frac{W_{ar}}{100}) = \\
&= 30.79 - 2.454(8.937 \cdot \frac{5.04}{100} + \frac{5.81}{100}) = 29.54\ MJ/kg
\end{aligned}
\tag{4.3}
$$

4.4.2.2 Particle size distribution

Usually, for the power generation plants, the pulverised coal is milled to particle size below 500 µm. For a particle size distribution analysis a sieve shaker is utilized to sieve the coal sample. In this case, the sieve size fractions used were sequentially 53 µm, 150 µm, 212 µm, 335 µm and 600 µm.

A convenient representation of the particle size distribution is the exponential Rosin-Rammler expression. For simplicity, the pulverised coal particles are assumed to be spherical. A sieve analysis of the El-Cerrejon coal, which can be used to describe the size distribution of the pulverised coal, is presented in Table 4.2.

The Rosin-Rammler size distribution refers to the value of the mean diameter and spread parameter of the coal particles. To obtain these values, the measured size distribution of the Columbian coal presented in Table 4.2 has been fitted to the Rosin-Rammler equation:

$$
Y_d = e^{-(d/\bar{d})^{ns}} \tag{4.4}
$$

where:

d – particle diameter, m,

$\bar{d}$ – mean particle diameter, m,

Y_d – mass fraction of particles with a diameter greater than d,

n_s – spread parameter.

The size distribution of the coal particles is fitted to a Rosin-Rammler distribution ranging from 53 to 600 µm with mean diameter of 115 µm based on the experimental data. The exponential curve fit compared against the experimental data is illustrated in Figure 4.17 and the resulting parameters required to describe the size distribution are presented in Table 4.3.

Table 4.2: El-Cerrejon coal size distribustion measurements.

Sieve size, µm	Remainder on sieve, %
53	37.1
150	34.9
212	12.4
355	13.7
600	1.9

Table 4.3: Rosin-Rammler parameters used for the particle size distribution.

Parameter	Value
Mean Diameter, $\bar{d}$	115 µm
Spread Parameter, n_s	1.035
Minimum size of the coal particle diameter	1.0e-06 m
Maximum size of the coal particle diameter	5.9e-04 m

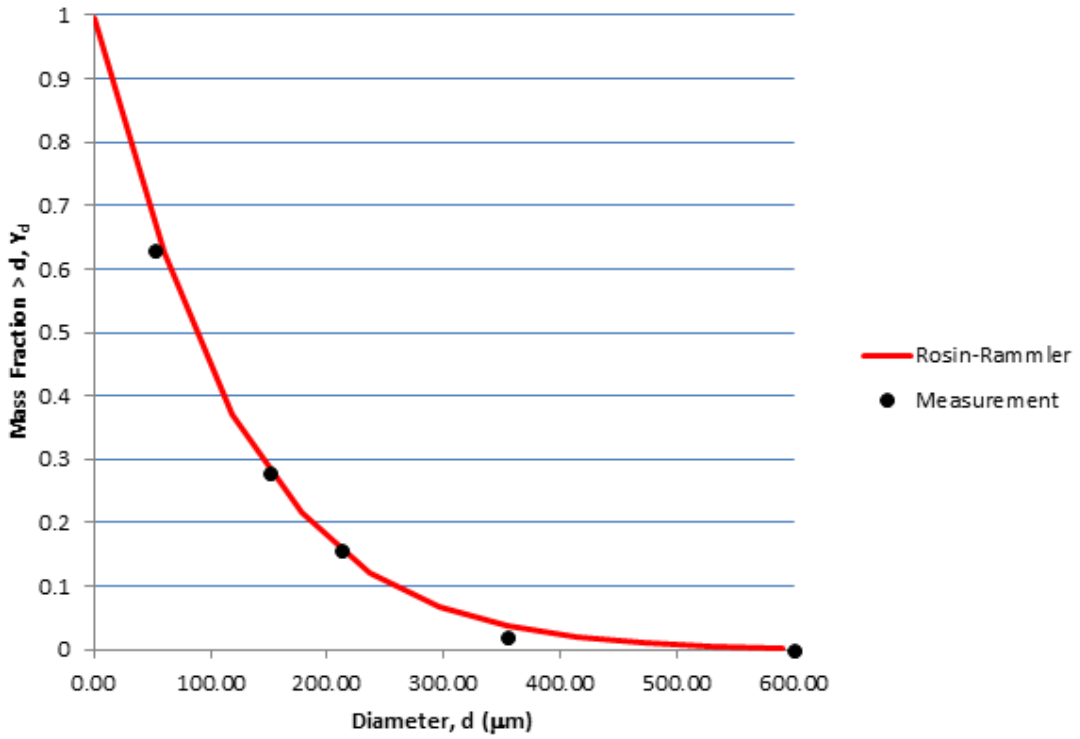

Figure 4.17: Particle size distribution of the El-Cerrejon coal — Rosin-Rammler curve.

4.4.3 Coal combustion experimental data

The measurements taken during the experimental programme include the surface incident radiation measurements on the walls of the combustion chamber, exit gas composition, in-furnace temperature along the central axis of the combustion test facility and along the flame for the flame profiling. An experimental programme includes air non-preheated and preheated cases. The coal feed rate was kept constant at the nominal value of 24.39 kg/h in each investigated case to keep the heat input at 200 kW. The inlet parameters for the air-fired preheated and non-preheated case are summarized in Table 4.4.

Table 4.4: Experimental inlet parameters for the non-preheated and preheated air-firing cases.

	Air non-preheat	Air preheat
Mass flow of coal, kg/s	0.00678	
Thermal output, kW	200	
	Primary oxidizer	
Mass flow, kg/s	0.01669	
Temperature, K	291.15	294.15
	Secondary + tertiary oxidizer	
Mass flow, kg/s	0.06786	
Temperature, K	293.15	531.15
	Purge (air)	
Mass flow, kg/s	0.00217	0.00086
Temperature, K	291.15	294.15

4.4.3.1 Air non-preheated case

Data from the experimental programme on the air non-preheated case are presented in Figures 4.18 - 4.20 and in Table 4.5. Figures 4.18 and 4.20 give the experimental measurements of the temperature of the combustion gases along the furnace axis and the surface incident radiation along the walls of the combustion chamber, respectively. Figure 4.19 shows the temperature on the flame profiling at the distance of z = 0.075 m from the burner end. In Table 4.5 the experimental measurements of the flue gas temperature and its composition are summarized.

The temperature readings of the sheathed Type R thermocouples presented in Figure 4.18 were taken at different axial position along the furnace. All of the measurements are at the same radial position, 200 mm from the inner wall of the furnace and 250 mm from the centre line. As it can be observed in Figure 4.18, firstly the combustion gases temperature

increases and then reaches the peak value at the third measurement port, then it decreases progressively when the flame length ends and the heat being extracted through the refractory sections. The highest temperature of the combustion gases was achieved at the distance of z = 0.8 m from the burner end.

The same technique was used for measurements of the temperature of the in-flame combustion gases. The readings of the temperature were taken at the same axial position, namely at the distance of z = 0.075 m from the burner end, while the changing the radial position of the probe. It can be noticed in Figure 4.19, the highest temperature of the flame is achieved at 0.85 m from the centre line, then the temperature of the combustion gases significantly decreases by approximately 500 K due to the impact of introduction of the non-preheated secondary and tertiary air to the combustion chamber.

Results of the radiative heat flux measurements using the MEDTHERM heat flux probe fitted with the CaF_2 window attachment are presented in Figure 4.20. Firstly the SIR on the combustion furnace walls increases and reaches the peak value at the third measurement port, then it decreases progressively which is due to the lower temperature of the combustion gases further away from the burner end. The highest heat flux was found to be, as expected, at the region of the combustion gases peak temperature, which is at the distance of of z = 0.8 m from the burner end.

The flue gas composition and temperature measurements with standard deviation values presented in Table 4.5 indicate that exit O_2, CO_2, CO, NO_x and SO_2 are 3.8%, 15.3%, 29 ppm, 291 ppm, 279 ppm on volume dry basis, respectively. The exit temperature is 959 K.

4.4.3.2 Air preheated case

In the air preheated case, the secondary and tertiary air has been preheated to the temperature of 531.15 K before entering the combustion

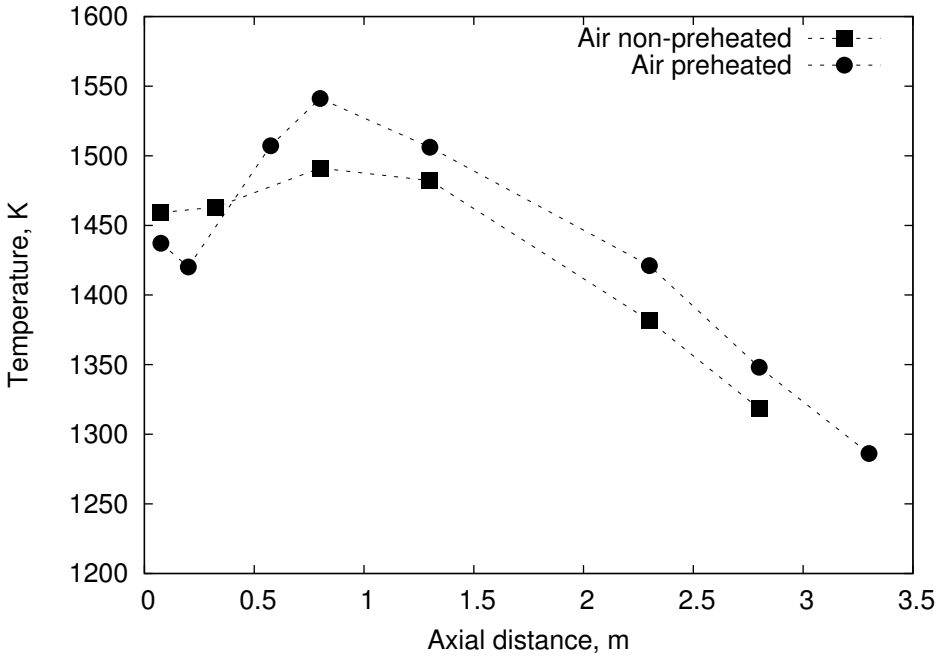

Figure 4.18: Experimental measurements of the temperature along the furnace axis — air non-preheated and preheated case.

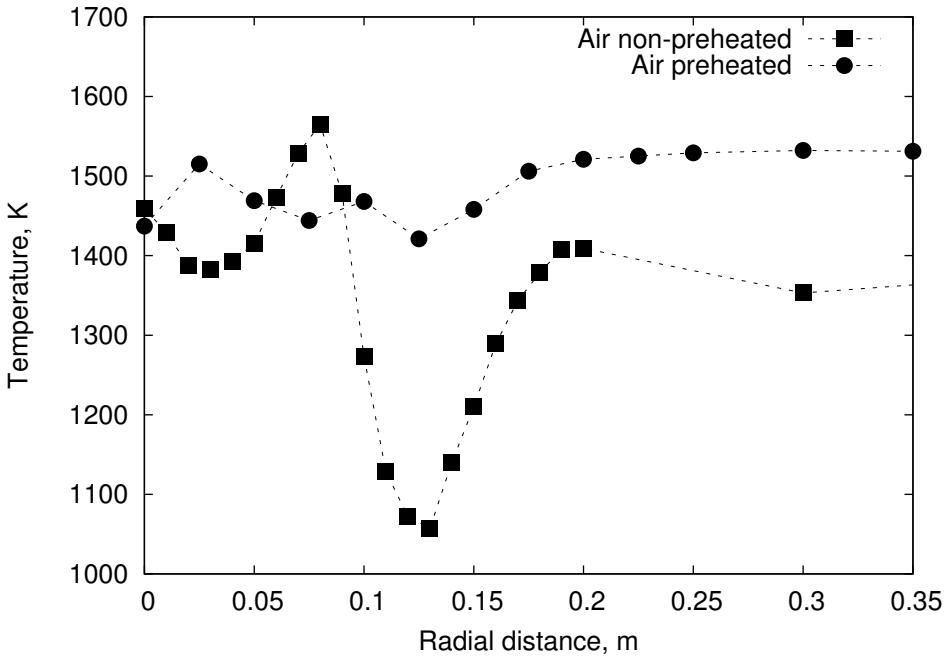

Figure 4.19: Experimental measurements of the temperature on the flame profiling at the distance of $z = 0.075$ m — air non-preheated and preheated case.

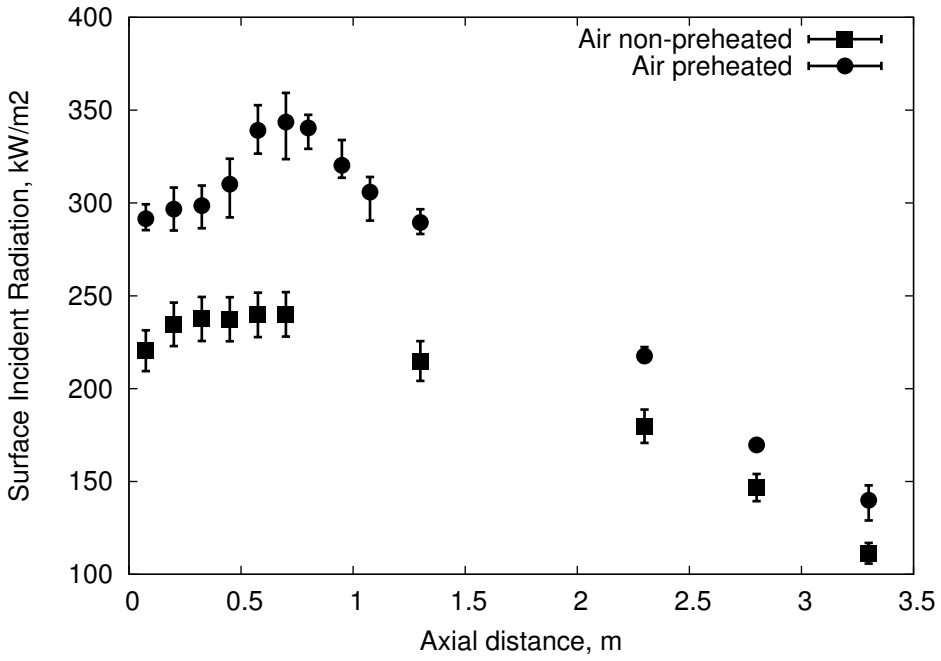

Figure 4.20: Experimental measurements of the SIR — air non-preheated and preheated case.

Table 4.5: Experimental measurements of the exit gas composition and flue gas temperature - 200 kW air non-preheated case.

	Unit	Value	sd
Exit temperature	K	959	± 42
Exit O_2, dry	%	3.8	± 0.2
Exit CO_2, dry	%	15.3	± 0.2
Exit CO, dry	ppm	29	± 5
Exit SO_2, dry	ppm	291	± 4
Exit NO, dry	ppm	276	± 8

chamber. The inlet conditions for the preheated air-fired case are given in Table 4.4.

Data from the experimental programme on the air preheated case are presented in Figures 4.18 - 4.20 and in Table 4.6, similarly to the non-preheated case.

The temperature measurements depicted in Figure 4.18 show a similar trend to air non-preheated case, namely firstly the combustion gases temperature increases and after reaching the highest value, it decreases further away from the burner end. The highest temperature of the combustion gases was found to be at the distance of z = 0.8 m from the burner end.

The readings of the temperature taken at the distance of z = 0.075 m from the burner end in Figure 4.19 show the peak temperature of the flame is achieved at 0.025 m from the furnace centre line, then the temperature of the combustion gases slightly decreases by approximately 100 K where the preheated secondary and tertiary air enters the combustion chamber.

Data from the measurements of the SIR presented in Figure 4.20 have similar trend to non-preheated case. The SIR profile on the combustion furnace walls increases reaching the highest value at the peak temperature region of approximately 350 kW/m^2 (at the distance of of z = 0.8 m from the burner end) and then it decreases linearly.

The exit gas temperature was measured to be 1012 K, while the flue gas composition of O_2, CO_2, CO, NO_x and SO_2 were measured to be 3.3%, 15.7%, 4 ppm, 284 ppm, 374 ppm on volume dry basis, respectively, as summarized in Table 4.6.

4.4.3.3 Comparison of the air non-preheated and preheated cases

The temperature readings of the air preheated case compared with non-preheated case show the effect of the air preheat on the combustion gases temperature along the furnace axis and the combustion gases temperature on the flame profiling at the distance of z = 0.075 m. The largest temperature difference between the air non-preheated and preheated case is in the near burner region as presented in Figure 4.18. The temperature profile along the axis has the peak temperature at the first measurement

Table 4.6: Experimental measurements of the exit gas composition and flue gas temperature - 200 kW air preheated case.

	Unit	Value	sd
Exit temperature	K	1012	± 49
Exit O_2, dry	%	3.3	± 0.2
Exit CO_2, dry	%	15.7	± 0.4
Exit CO, dry	ppm	4	± 8
Exit SO_2, dry	ppm	284	± 23
Exit NO, dry	ppm	374	± 17

port and then it decreases further down from the burner due to the heat being extracted through the refractory sections, as higher gas temperatures increase the heat transfer through the light density refractory wall. It can be noticed that axial temperature profile for the air non-preheated case is smoother than the profile for the preheated case. The peak temperature of the combustion gases for the preheated case is higher by approximately 70 K compared to non-preheated case, and by 50 K downstream of the furnace.

The measurements of combustion gases temperature at the distance of z = 0.075 m from the burner end in Figure 4.19 show the significant impact of the combustion air preheat on the flame profile. The flame profile for the air preheated case is much smoother than for the air non preheated case, where the introduction of the secondary and tertiary air is more pronounced.

The SIR measurements for the air non- preheated and preheated cases are presented in Figure 4.20. It can be noticed that the heat flux is higher in the preheated case by approximately 100 kW/m^2 at the distance of z = 0.8 m from the burner end, where the peak value is reached, when comparing with the reading for the non-preheated case. This is correlated with the higher temperatures of the combustion gases present during the

preheated case.

When comparing the flue gas emission of the non-preheated case (Table 4.5) and preheated case (Table 4.6), it can be observed that there is less O_2 in the air preheated case than in the non-preheated case. Also, the measurements show less CO and more CO_2 in the flue gas in the preheated case. Less CO indicates the effect of the improved burnout for the preheated case. The SO_2 emissions were not affected by the preheating. However, NO emissions were significantly increased, producing 36% higher emissions for the preheated case. This can be explained by the influence of the increased combustion air temperature which is affecting the shear combustion layer between the oxygen-lean primary and the staged-secondary streams, thus increasing the thermal NO_x formation.

4.5 Biomass combustion

The coal-fired power plant are retrofitting to biomass fuel, because of the high demand on CO_2 emission reduction, as outlined in Chapters 1 and 2. There is a need for investigation the influence of the retrofit coal to biomass on the combustion performance. Therefore, the retrofit of the coal to biomass combustion on the 250 kW PACT facility has been performed. As a biomass fuel for the experimental programme, the pulverised white wood has been used.

4.5.1 Biomass burner

For the test on the biomass combustion, a separate feeder for biomass has been installed and the coal burner has been replaced with the biomass burner design by Doosan Babcock. Figure 4.21 shows a photograph of the front of the biomass burner. The main difference between the coal and biomass burner is the dimension of the fuel inlet. As biomass is less dense than coal and has a lower calorific value, the amount of the biomass fuel

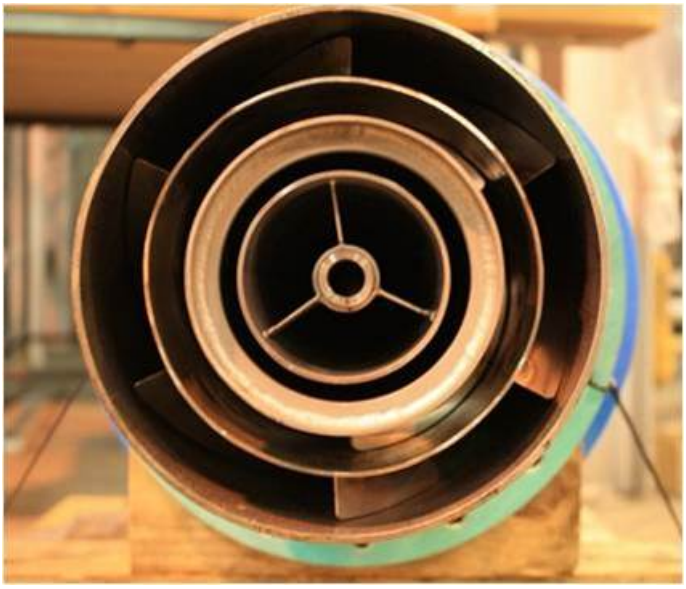

Figure 4.21: A photograph of the front of the Doosan Babcock biomass burner.

supplied to the combustion chamber to achieve a similar heat input to coal combustion, is higher. Therefore, the fuel inlet in the biomass burner has a larger cross sectional area of the annulus than that for the fuel inlet in the coal burner.

4.5.2 White wood specification

As a biomass fuel the Canadian white wood has been used. The proximate and ultimate analysis of the white wood has been summarized in Table 4.7. In comparison to coal, biomass has double content of the volatile matters, and half that of the char. Further, biomass has more than three times more oxygen and less carbon than coal. The lower fraction of carbon in the biomass composition, in consequence, gives a lower calorific value of the biomass fuel. The mixed wood GCV value is 14.8 MJ/kg and LCV 14.0 MJ/kg.

Table 4.7: Proximate and ultimate analyses of the white wood.

Proximate Analysis, %		Ultimate Analysis, %	
W_{ar}	8.28	C_{ar}	50.13
A_{ar}	0.74	H_{ar}	5.97
vol_{daf}	76.61	N_{ar}	1.45
$char_{daf}$	14.37	O_{ar}	42.45
		S_{ar}	0.00

4.5.2.1 Particle size distribution

For the representation of the particle size distribution the Rosin-Rammler equation has been used. A sieve analysis of the white wood describing the size distribution of the pulverised biomass, is presented in Table 4.9. The exponential curve fit compared against the experimental data is illustrated in Figure 4.22.

The mean diameter of the biomass particle is larger than the mean diameter of the coal particle by about seven times, namely biomass mean diameter is 718 μm, when coal mean diameter is 115 μm.

Table 4.8: Mixed wood particle size distribustion measurements.

Sieve size, μm	Remainder on sieve, %
250	21.24
500	22.47
1000	36.51
1400	12.83
2000	4.79

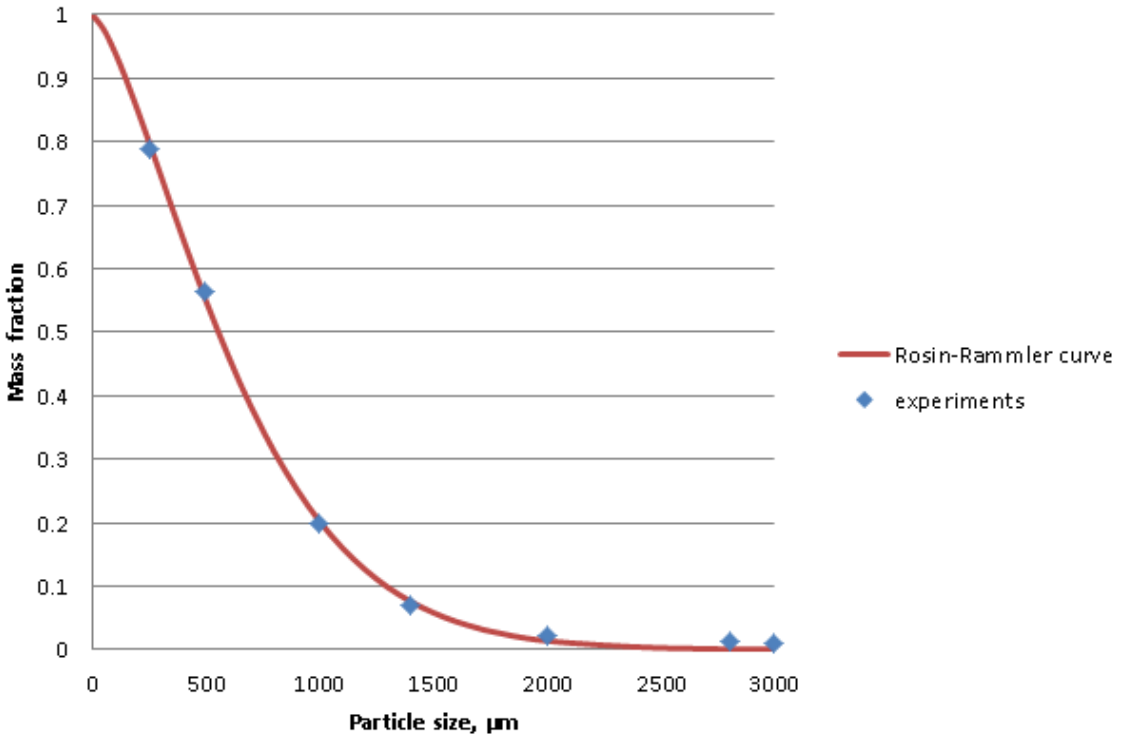

Figure 4.22: Particle size distribution — Rosin-Rammler curve for white wood.

Table 4.9: Rosin-Rammler parameters used for the particle size distribution of white wood.

Parameter	Value
Mean Diameter, $\bar{d}$	718 µm
Spread Parameter, n_s	1.419
Minimum size of the coal particle diameter	1.0e-05 m
Maximum size of the coal particle diameter	0.003 m

4.5.3 Biomass combustion experiments

During retrofit coal to biomass several problems have been encountered. Firstly, the biomass results in stuck of the screw feeder. This is because of the high moisture content in the biomass fuel as well as the large size of the particles of the pulverised biomass. Small particles of coal fuel are more feasible than large fibre-type biomass in order to maintain

a continuous flow. Secondly, it is very difficult to adjust a flame stability for the biomass fuel, even when the combustion chamber was preheated before the biomass fuel was introduced to the furnace. When there was a combustion, it was incomplete – the analysis of the ash showed that biomass particles did not participate in the combustion process. This can be explained by the large in size biomass particles having a too short residence time and there is not enough recirculation in the near burner region. Another observation is that the biomass particles, because of their size and shape, are not driven by the conveying air and are following a straight trajectory to the outlet.

The difficulties with biomass combustion, which was not taken into account for any of the measurements, as the steady state was not achieved, shows that biomass is a fuel which needs further investigation and prior to retrofitting coal to biomass in industrial applications it needs much more research.

4.6 Conclusions

The results obtained from the non-preheated and preheated coal combustion experiments on the 250 kW PACT facility have been performed and compared. It has been found that the combustion air preheat has significant advantages, namely it increases the efficiency of the fuel conversion process and increases the heat input to the furnace, thus facilitating ignition and improving the flame stability. Further, the heat flux on furnace walls also increases, which is significant in terms of the heat exchange, which is the main advantage for power generation, when the water is heated up in the large scale boilers to evaporate and change into steam to drive the steam turbine. However, the disadvantage of preheating combustion air is that it increases the thermal NO_x formation.

The experiments on the retrofit of coal to biomass has been investig-

ated. Biomass, because if its fibrous nature, has large in size particles. It also has lower calorific value and lower energy density in comparison to coal. Therefore switching fuel from coal to biomass can be difficult and problematic, as it was experienced during the experimental programme. However, these experiments highlighted the key problems which can be present during the retrofitting of the coal-fired boilers to biomass-fired boilers in industrial applications.

4.7 Summary

In this chapter the combustion test facility has been described and experimental techniques and measurements taken on this facility have been presented. Two coal combustion cases has been compared, namely the air non-preheated case and the air preheated case. The results provide an insight into the effect of the preheated combustion air on the combustion performance, the temperature profile along the furnace axis, the radiative heat flux and the flue gas emissions.

Flame temperatures were measured for the different axial positions of the furnace by suction pyrometry. The radiative heat flux was measured using the MEDTHERM digital flux meter. In general, the air non-preheated and preheated case have similar temperature profile along the furnace axis and SIR profile. The differences between the air non-preheated and the air preheated cases are in the higher temperature in the near burner region in the air preheated case, higher radiative heat flux in the case of the air preheated and more pronounced impact of the secondary and tertiary air on the flame profile. In general, the air preheated case has a better combustion performance (less CO in the flue gas). However, the increased temperatures within the flame region result in higher NO_x emissions in comparison to air non-preheated case.

The experimental programme on the biomass combustion highlighted

that biomass combustion needs further research. A further milling of the biomass fuel to achieve finer particles to maintain a continuous flow of the biomass fuel to the furnace and a new burner design in order to extend the residence time of the biomass particles and with more pronounced recirculation zones are proposed .

The results presented in this chapter assist in the CFD model validation presented in the next chapter.

Chapter 5

Combustion Modelling on a Coal Fired Test Furnace

5.1 Introduction

The main focus of this chapter is a validation study of the CFD model of the UKCCSRC PACT 250 kW Combustion Rig facility. The experimental data collected during the experimental campaign, presented in Chapter 4, are compared with the theoretical calculations of the mass and energy balances and numerical model. The extensive sensitivity study of the sub-models applied in the numerical calculations has been performed, including the two-step reaction mechanism, turbulence, devolatilization and char combustion. Theoretical calculations and numerical simulations are performed in order to develop a reliable CFD model that is able to reproduce the experimental measurements of the UKCCSRC 250 kW combustion rig and other coal-fired combustion chambers.

The study presented in this chapter is a part of collaborative work presented in [89]. The main objective of my contribution was the calculations of the mass and energy balances for the air-fired and oxy-fuel cases, and comparison of the theoretical calculations with experimental measurements and CFD results of the air non-preheated case. However, I was

fully involved in all other aspects of the work presented in this chapter.

5.2 Theoretical calculations

The theoretical calculations involve the mass and energy balances at the thermodynamic equilibrium, which is achieved if there is sufficient time for all the reactions to reach their equilibrium state [180]. When the residence time of the pulverised fuel particles is sufficient for the fuel to have burnt to completion and there is enough combustion air for oxidation of the fuel, it can be assumed that the thermal equilibrium is reached and combustion is completed [180]. For the steady state, at which there is equilibrium between the rate of heat generation and the rate of heat removal from it, the calculations of mass and energy balances have been performed.

5.2.1 Stoichiometry of combustion

The calculation of the stoichiometry of the combustion process differs depending on the type of fuel supplying the combustion chamber and the amount of the combustion air required for the complete combustion. In this chapter, the combustion of the pulverised El-Cerrejon coal is investigated and calculations for this fuel are presented, as this fuel has been supplying the UKCCRS Combustion Test Facility presented in Chapter 4. Further, the coal specification has been introduced in Chapter 4 and the proximate and ultimate analysis of the El-Cerrejon coal has been summarized in Table 4.1.

The stoichiometric calculations are performed with the complete combustion assumption. Hence, the minimum amount of the oxygen required for complete combustion of the coal unit depends on the composition of the fuel and is determined by [182]:

$$n_{o\,\min} = \frac{C_{ar}}{M_C} + \frac{1}{2} \cdot \frac{H_{ar}}{M_{H_2}} + \frac{S_{ar}}{M_S} - \frac{O_{ar}}{M_{O_2}} \tag{5.1}$$

where:

$n_{o\,\min}$ – minimum amount of oxygen required for complete combustion of as-received coal, $\mathrm{kmol_{O_2}/kg_{ar}}$,

C_{ar} – mass fraction of the carbon in as-received coal, $\mathrm{kg_C/kg_{ar}}$,

H_{ar} – mass fraction of the hydrogen in as-received coal, $\mathrm{kg_{H_2}/kg_{ar}}$,

S_{ar} – mass fraction of the sulphur in as-received coal, $\mathrm{kg_S/kg_{ar}}$,

O_{ar} – mass fraction of the oxygen in as-received coal, $\mathrm{kg_{O_2}/kg_{ar}}$,

M_C – molecular mass of the carbon, kg/kmol,

M_{O_2} – molecular mass of the oxygen, kg/kmol,

M_{H_2} – molecular mass of the hydrogen, kg/kmol,

M_S – molecular mass of the sulphur, kg/kmol.

Once the amount of oxygen required for complete combustion of a unit of as-received coal is known, it is possible to specify the amount of the oxidizer required for the complete combustion of a coal unit, called the stoichiometric amount of the oxidizer. The value of the stoichiometric amount of the oxidizer depends on the fraction of oxygen in the oxidizer as follows [182]:

$$n_{oxi\ st} = \frac{n_{o\,\min}}{z_{O_2}} \tag{5.2}$$

where:

$n_{oxi\ st}$ – stoichiometric amount of the oxidizer required for complete combustion of the coal unit, $\mathrm{kmol_{oxi}/kg_{ar}}$,

z_{O_2} – mole fraction of the oxygen in the oxidizer, $\mathrm{kmol_{O_2}/kmol_{oxi}}$.

When the air-fired cases are analysed, the mole fraction of oxygen in the oxidizer is equal to the mole fraction of oxygen in the air mixture, which is 20.9%.

The oxidizer mass flow rate is given as the input data, based on the operating experimental conditions (see Table 4.4), and as a result the mole flow rate of the actual oxidizer can be calculated using the following equation [182]:

$$n_{oxi\ ac} = m_{oxi} \cdot M_{oxi} \tag{5.3}$$

where:

$n_{oxi\ ac}$ – actual amount of the oxidizer, $kmol_{oxi}/s$,

m_{oxi} – mass flow rate of the oxidizer, kg_{oxi}/s,

M_{oxi} – molecular weight of the oxidizer, $kg_{oxi}/kmol$.

The molecular weight of oxidizer in equation (5.3) depends on the composition of the oxidizer and it is based on the molar fraction of each component and its molecular weight. Furthermore, the molecular weight differs in the case of the air and oxy-coal combustion. In this thesis it is assumed that in the air case the oxidizer (air) is composed of O_2 and N_2, whereas in the oxy-coal combustion the oxidizer is composed of O_2 and CO_2. For the analysed cases, the oxidizer molar mass can be written as follows [182–184]:

$$M_{oxi} = \sum_i z_i \cdot M_i \tag{5.4}$$

where:

z_i – mole fraction of the i component of the oxidizer, here: i = N_2, O_2 (air combustion) / CO_2, O_2 (oxy-coal combustion), $kmol_i/kmol_{oxi}$,

M_i – molecular mass of the i component of oxidizer, kg/kmol.

The value of the stoichiometric ratio is calculated using the excess air ratio and this may be expressed as follows [182, 183]:

$$\lambda = \frac{AF_{ac}}{AF_{st}} = \frac{(m_{oxi})_{ac}}{(m_{oxi})_{st}} = \frac{n_{oxi\ ac} \cdot M_{oxi}}{n_{oxi\ st} \cdot M_{oxi}} = \frac{n_{oxi\ ac}}{n_{oxi\ st}} \tag{5.5}$$

where:

AF_{ac} – actual air-fuel ratio,

AF_{st} – stoichiometric air-fuel ratio.

To determine the amount of the flue gas generated by the coal combustion process the following formula was used [182]:

$$n_{fg} = \frac{C_{ar}}{M_C} + \frac{S_{ar}}{M_S} + \frac{H_{ar}}{M_{H_2}} + \frac{W_{ar}}{M_{H_2O}} + \frac{N_{ar}}{M_{N_2}} + \\ + (\lambda - 1) \cdot z_{O_2} \cdot n_{oxi\ st} + (1 - z_{O_2}) \cdot \lambda \cdot n_{oxi\ st} \tag{5.6}$$

where:

n_{fg} – amount of the flue gas per as-received coal unit, $\mathrm{kmol_{fg}/kg_{ar}}$.

The molar composition of the wet flue gas depends on the composition of the coal and the oxidizer and the formulas differ for air and oxy-coal combustion [182], and are given by

$$(O_2) = \frac{(\lambda - 1) \cdot z_{O_2} \cdot n_{oxi\ st}}{n_{fg}} \tag{5.7}$$

$$(H_2O) = \frac{H_{ar}/M_{H_2} + W_{ar}/M_{H_2O}}{n_{fg}} \tag{5.8}$$

$$(SO_2) = \frac{S_{ar}/M_S}{n_{fg}} \tag{5.9}$$

For the air combustion case,

$$(CO_2) = \frac{C_{ar}/M_C}{n_{fg}} \tag{5.10}$$

$$(N_2) = \frac{N_{ar}/M_{N_2} + (1 - z_{O_2}) \cdot \lambda \cdot n_{oxi\ st}}{n_{fg}} \tag{5.11}$$

For the oxy-coal combustion cases,

$$(CO_2) = \frac{C_{ar}/M_C + (1 - z_{O_2}) \cdot \lambda \cdot n_{oxi\ st}}{n_{fg}} \tag{5.12}$$

$$(N_2) = \frac{N_{ar}/M_{N_2}}{n_{fg}} \tag{5.13}$$

where:

(O_2) – mole fraction of the oxygen in the flue gas, $\text{kmol}_{\text{O}_2}/\text{kmol}_{\text{fg}}$,

(H_2O) – mole fraction of the moisture in the flue gas, $\text{kmol}_{\text{H}_2\text{O}}/\text{kmol}_{\text{fg}}$,

(SO_2) – mole fraction of the sulphur dioxide in the flue gas, $\text{kmol}_{\text{SO}_2}/\text{kmol}_{\text{fg}}$,

(N_2) – mole fraction of the nitrogen in the flue gas, $\text{kmol}_{\text{N}_2}/\text{kmol}_{\text{fg}}$,

(CO_2) – mole fraction of the carbon dioxide in the flue gas, $\text{kmol}_{\text{CO}_2}/\text{kmol}_{\text{fg}}$.

The calculated values of the parameters introduced in this section, for the three analysed cases, are presented in Table 5.1. The composition of the flue gas (in round brackets) is given on a volume basis for the wet flue gas. The comparison of the theoretical calculations and experimental measurements for the air-non preheated case is presented in Table 5.2.

The same fuel has been used for the air non-preheated, air preheated and oxy-fuel cases, as summarized in Table 5.1. The coal feed rate has been kept constant, therefore the stoichiometric amount of oxygen is constant for all the three cases. In all three analysed cases, the stoichiometric ratio is greater than 1, which means that the amount of oxidizer is greater than its stoichiometric amount. However, the actual amount of the oxidizer has changed when switching from air-fired cases to oxy-combustion as the result of the different composition of the oxidizer in oxy-fuel case where N_2 is replaced with CO_2. Due to the oxidizer composition for the oxy-fuel case the composition of the flue gas has changed accordingly. The exit O_2 is kept at 5% as in the air-fired cases. However, the exit N_2 is reduced from 76% for air-fired cases to 1% in oxy-coal case , while the exit CO_2 increased from 13% for air-fired cases to 86% for oxy-combustion case when comparing with the air-fired cases.

For the oxy-fuel case, the objective is to achieve a high concentration

of CO_2 for the sequestration purposes, as the high concentration makes extraction of the CO_2 more efficient. The amount of the H_2O and SO_2 is the same in air-fired cases and oxy-fuel case, only the fraction of these components changed slightly, which is a consequence of the decrease in the volume of the flue gas in the oxy-combustion case and that is a result of the increased molecular weight of the oxidizer in the oxy-fuel case. Therefore, it can be observed from the theoretical calculations that keeping constant the fuel feed rate and exit O_2 for air-fired cases and oxy-fuel case, the change of the oxidizer composition has an impact on the flue gas volume and its composition.

Comparison of the theoretical results and experimental measurements indicate imbalance in the experiments. The theoretical mole fraction of the O_2 in the flue gas is 35% higher than the measured exit O_2. This indicates that there could be an in-leakage in the experimental facility, and therefore a higher exit O_2. It has to be taken into account that the bottom of the rig is open and the rig is sealed with a water tray. Further, the CO_2 is lower by 8%, which is a consequence of the in-leakage increasing the volume of the flue gas, and therefore decreasing the volume concentration of CO_2. The theoretical SO_2 is in line with the experimental data.

5.2.2 Energy balance

The process of combustion, either the air or oxy-fuel, can be described in the form of the energy balance, which shows how the energy from the fuel is transformed into the various energy flows and heat losses. The basic equation to be satisfied is that the enthalpy flux of the inflow to the combustion chamber (sum of the fuel and combustion air) must be equal to the enthalpy flux of the outflow from the chamber plus the heat flux to the walls of the chamber [180–182].

Table 5.1: Stoichiometry of the combustion of air preheated and non-preheated cases and oxy-fuel case – values of the governing quantities.

Parameter, unit	Air non-preheated	Air preheated	Oxy-27%
m_{coal}, kg/h	24.39		
LCV, kJ/kg	29,570		
$n_{o\ min}$, kmol/kg	0.0703	0.0703	0.0703
$n_{oxi\ min}$, kmol/kg	0.3365	0.3365	0.2607
z_{O_2}, kmol/kmol	0.209	0.209	0.270
m_{oxi}, kg/h	304.4	304.4	314.4
$m_{purge\ (air)}$, kg/h	7.8	3.1	3.1
M_{oxi}, kg/kmol	28.85	28.85	40.77
λ	1.3186	1.2987	1.2298
n_{fg}, kmol/kg	0.4639	0.4572	0.3410
(O_2), kmol/kmol	0.0483	0.0460	0.0473
(H_2O), kmol/kmol	0.0608	0.0617	0.0828
(N_2), kmol/kmol	0.7586	0.7581	0.0128
(SO_2), kmol/kmol	2.49e-06	2.52e-06	3.38e-06
(CO_2), kmol/kmol	0.1320	0.1340	0.8568

Table 5.2: Comparison of the theoretical calculations and experimental measurements of the exit gas composition and flue gas temperature for the air non-preheated case.

	Unit	Experiments	Mass balance
Temperature	K	959 ± 42	—
O_2, dry	%	3.8 ± 0.2	5.14
CO_2, dry	%	15.3 ± 0.2	14.06
CO, dry	ppm	29 ± 5	—
SO_2, dry	ppm	291 ± 4	300
NO, dry	ppm	276 ± 8	—

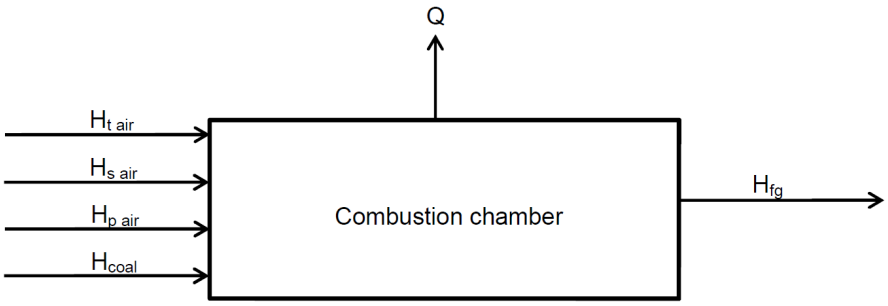

Figure 5.1: Schematic of the PACT combustion chamber energy balance.

Figure 5.1 presents a schematic of the energy balance of the UKCCSRC PACT Combustion Rig with the coal and primary, secondary and tertiary oxidizer at the inlet and the flue gas at the outlet and the heat losses through the walls of the combustion chamber.

The energy balance of the combustion chamber is based on the input data provided in Section 4.4.3 and this can be written as follows:

$$H_{coal} + H_{p\ oxi} + H_{s\ oxi} + H_{t\ oxi} = H_{fg} + Q \tag{5.14}$$

where:

H_{coal}– enthalpy of the coal, kW,

$H_{p\ oxi}$ – enthalpy of the primary oxidizer, kW,

$H_{s\ oxi}$ – enthalpy of the secondary oxidizer, kW,

$H_{t\ oxi}$ – enthalpy of the tertiary oxidizer, kW,

H_{fg} – enthalpy of the flue gas, kW,

Q – total heat transfer flux released from the walls, kW.

The enthalpy of the coal, primary, secondary and tertiary oxidizer and flue gas can be calculated from the following equations [182–184]:

$$H_{coal} = m_{coal}\left(LCV + h_c|_{T_{ref}}^{T_{p\ oxi}}\right) \tag{5.15}$$

$$H_{p\ oxi} = m_{p\ oxi} \cdot \sum_i \left(g_{p\ i} \cdot \Delta h_i|_{T_{ref}}^{T_{p\ oxi}}\right) \tag{5.16}$$

$$H_{s\ oxi} = m_{s\ oxi} \cdot \sum_j \left(g_{s\ j} \cdot \Delta h_j|_{T_{ref}}^{T_{s\ oxi}}\right) \tag{5.17}$$

$$H_{t\ oxi} = m_{t\ oxi} \cdot \sum_j \left(g_{t\ j} \cdot \Delta h_j|_{T_{ref}}^{T_{t\ oxi}}\right) \tag{5.18}$$

$$H_{fg} = m_{coal} \cdot \sum_k \left(g_k \cdot \Delta h_k|_{T_{ref}}^{T_{fg}}\right) \tag{5.19}$$

where:

m_{coal} – coal mass flow rate, kg/s,

LCV – low calorific value of coal, kJ/kg,

h_c – sensible enthalpy of coal, kJ/kg,

$T_{p\ oxi}$ – temperature of the primary oxidizer, K,

T_{ref} – reference temperature, K, here: T_{ref} = 298 K,

$T_{s\ oxi}$ – temperature of the secondary oxidizer, K,

$T_{t\ oxi}$ – temperature of the tertiary oxidizer, K,

T_{fg} – temperature of the flue gas, K,

$g_{p\ i}$ – mass fraction of the i component of the primary oxidizer, kg/kg, here: i = O_2, N_2/CO_2,

$g_{s\ j}$ – mass fraction of the j component of the secondary oxidizer, kg/kg,

here: $j = i$,

$g_{t\ j}$ – mass fraction of the j component of the tertiary oxidizer, kg/kg, here: $j = i$,

g_k – mass fraction of k component of the flue gas, kg/kg, here: k = O_2, CO_2, H_2O, N_2,

$\Delta h_{i,j,k}$ – specific enthalpy of the i, j, k components of the oxidizer or flue gas, kJ/kg.

To calculate the enthalpy of the components of the system, the specific enthalpy has to be defined. The specific enthalpy is the difference between the standard enthalpy of formation at the temperature of the component and the standard enthalpy of formation at the reference temperature, which is 298 K. The standard formation enthalpy values are calculated using the JANAF Thermochemical Table [185], as this method of evaluation of the enthalpy of formation is implemented in ANSYS Fluent. The enthalpy of coal is calculated on the specific heat basis.

The values of the enthalpy of the components of the combustion chamber for the three analysed cases are summarized in Table 5.3. The enthalpy of the secondary and tertiary oxidizer was calculated as the sum of the secondary and tertiary mass flows, which was possible due to the same oxidizer inlet conditions, namely the temperature, pressure and composition. In the primary inlet, the mass flow of the purge has been added.

The enthalpy of the secondary and tertiary oxidizer is higher for the preheated air-fired case and oxy-fuel case and that is a result of the preheat and therefore the higher temperature of the oxidizer than in the non-preheated case. Also, the enthalpy of the flue gas in the preheated air-fired case and oxy-fuel case is higher than in the non-preheated air-fired case, consequently to the higher exit temperature of the flue gas when compared to the non-preheated case. When comparing the total heat transfer rate,

which is the heat flux released from the walls of the combustion facility, similar values are achieved in all three cases. However, the enthalpy of the flue gas is 34%, 43% and 46% of the total input enthalpy for the non-preheated air-fired case, the preheated air-fired case and oxy-fuel case, respectively. Whereas, the heat loss through the walls is 66%, 57% and 54% of the total input enthalpy for non-preheated air-fired case, preheated air-fired case and oxy-fuel case, respectively.

The main objective of the boilers is to keep the flue gas enthalpy low and utilize the heat transfer of the combustion gases to heat up circulating medium. More heat available for heat exchange within the boiler increases the boiler efficiency. In the presented comparison, the highest efficiency is achieved in the non-preheated air-fired case, and the lowest efficiency is achieved in the oxy-fuel case.

Table 5.3: The values of the governing quantities in the energy balance.

	Air no-preheat	Air preheat	Oxy-27%
Enthalpy of coal (H_{coal}), kW	200.3		
Enthalpy of primary oxidizer (H_{poxi}), kW	-0.13	-0.0	-0.0778
Enthalpy of secondary and tertiary oxidizer (H_{s+toxi}), kW	-0.33	16.22	14.40
Enthalpy of flue gas (H_{fg}), kW	68.87	93.09	97.92
Total heat transfer rate (Q), kW	131.00	123.40	116.70

5.3 Numerical calculations

CFD modelling is a valuable tool providing insight into a particular problem, however it is prone to errors from the numerical schemes, mesh resolution, geometrical simplifications, boundary conditions and choices in the treatment of turbulence, heat transfer and combustion chemistry. To achieve confidence in the CFD predictions of coal combustion, sensitivity studies and comparisons with experimental data has been performed.

The CFD investigation of the UKCCSRC PACT Combustion Test Facility has been performed using the commercial CFD software ANSYS Fluent 14.5. For the purpose of the numerical analysis of the combustion process inside the combustion rig, the whole physical domain has been discretised and approximately one million cells have been created. The computational grid was generated in ANSYS ICEM CFD and then the mesh with the applied boundary conditions were solved numerically based on the fundamental governing equations of the fluid flow in ANSYS Fluent. Furthermore, the steady-state solution is analysed using the RANS approach.

5.3.1 Computational grid

Due to the complexity of the burner and the number of ports on the furnace of the 250 kW CTF, the burner and facility were simplified. Therefore, tetrahedral cells can be avoided and a hexahedral structured mesh can be obtained [140].

Taking advantage of the geometrical symmetry of the burner and the furnace, only one quarter of the CTF combustion chamber geometry was modelled and a periodic symmetry was assumed on the boundary. The analysis of one quarter of the geometry substantially reduces the computational time and cost [140]. The analysed one quarter of the mesh is presented in Figure 5.2.

The grid uses a structured hexahedral meshing scheme. The mesh

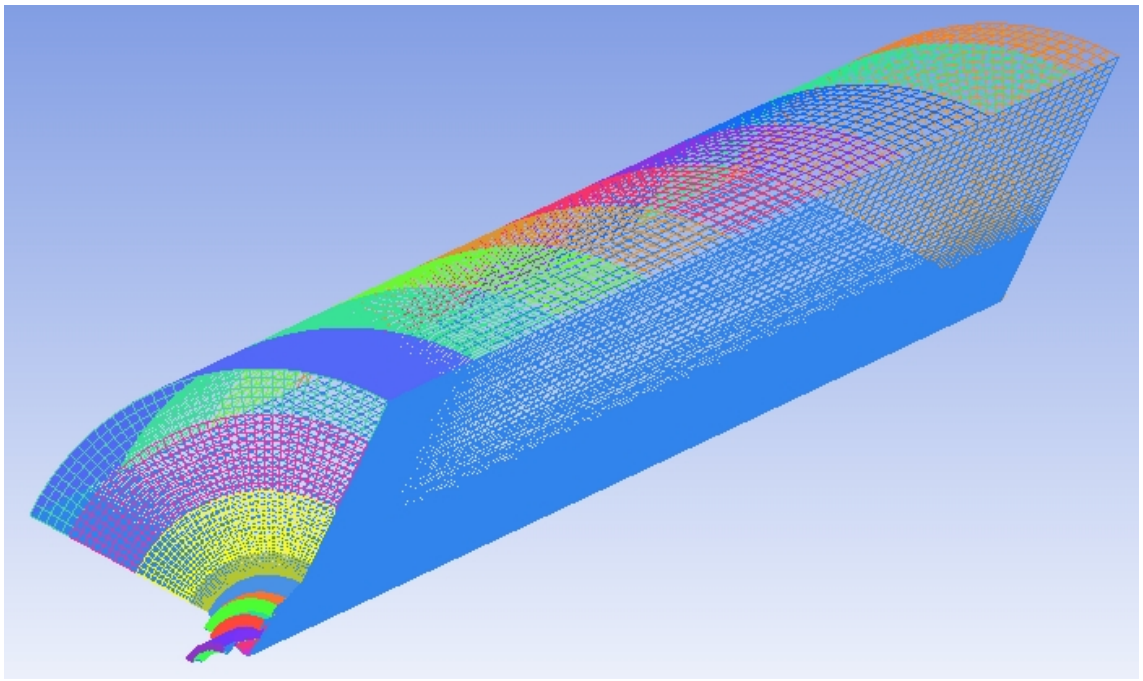

Figure 5.2: Computational mesh employed for the PACT Combustion Rig.

resolution is increased in the burner and the near-burner region, which is presented in Figure 5.3. In the near-burner region, when the oxidizer and the fuel enters the combustion chamber, and where the ignition and combustion process begins, the density of the computational cells have to be increased. The reason for this is the complexity of the occuring phenomena in the combustion, mixing and turbulence, which needs to be taken into account in the calculations. If the resolution in this region is low, the CFD analysis may not produce accurate results [140].

The mesh independence study has been conducted in [140], and applied in this work with some changes, including the refinement in the near burner region. As the mesh independent case has been justified in a previous study [140] and the reasoning in the objective of this study, the repeat of the grid independence study was not necessary.

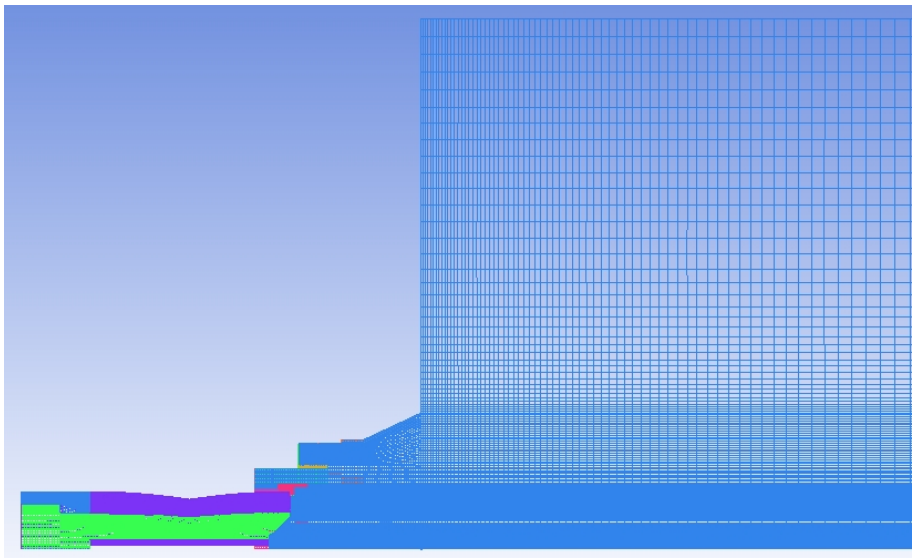

Figure 5.3: Mesh of the CTF in the near-burner region - view of the symmetry plane

5.3.2 Boundary Conditions

The boundary conditions are set as representative of the thermal resistances of the barrier between the hot furnace gases and the ambient temperature of the outer cooling water jacket (approximately 300 K). Further, the thermal conductivity of the combustion chamber walls was given by the manufacturer, whereas the temperature of the outer temperature was taken as an average of the experimental inlet and outlet temperature of the cooling water mass flow in each cooled section of the furnace [140].

The inlet conditions were set up according to the experimental settings presented in Table4.4 in Chapter 4. The primary, secondary, tertiary oxidizer and coal enter the combustion chamber as a swirled flow, as a consequence of the burner geometry and blades present on the primary, secondary and tertiary inlet pipes, as visible in Figure 4.14 in Chapter 4.

The burner geometry is not included in the computational domain in order to reduce the mesh size, improve mesh quality while using the hexahedral meshing scheme and therefore computational time [140]. Hence, the radial, axial and tangential components of the flow velocities are spe-

cified at the inlets. The assumption of the velocity components was found to predict the combustion performance in line with experimental data. However, for the future studies of the near burner region, the full geometry of the rig and burner is suggested to be used or a separate CFD simulation of the burner to predict the velocity profiles at the inlets and the mapping of them to the inlets of the simplified geometry of the combustion chamber without the burner. The components of the velocities of each inlet flow were calculated using the velocity triangle based on the cylindrical coordinate system knowing the angle of the burner blades [114, 140]. The values of the velocity components at the primary, secondary and tertiary inlets are summarized in Table 5.4.

Table 5.4: Velocity components of the primary, secondary and tertiary inlet mass flows.

Velocity Component	Inlets		
	Primary	Secondary	Tertiary
Radial, m/s	0	0	0
Axial, m/s	0.333	0.319	0.606
Tangential, m/s	-0.666	-0.680	-0.394
Swirl angle, °	64	65	33

5.3.2.1 Coal parameters employed in Fluent

For the numerical calculations in ANSYS Fluent several input parameters associated with coal combustion need to be provided. The coal proximate analysis is given as a mass fraction of each component on an as-received basis. The coal ultimate analysis is the mass fraction of atomic C, H, O, N and S in a dry ash-free (daf) coal. Hence the calculated daf composition of the El-Cerrejon coal and an as received proximate ana-

lysis values implemented in the ANSYS Fluent are as presented in Table 4.1.

5.3.2.2 Two-step reaction of the volatiles combustion

ANSYS Fluent gives a possibility to define the volatile matter as a mixture with given elemental composition. Thus the the volatiles chemical formula can be written as $C_nH_mO_kN_lS_o$. The combustion of the volatile matter is a complex and complicated process. To include the complexity of this process the two-step reaction of volatiles combustion is considered [155]. In the first step, the volatiles are oxidized to CO, H_2O, N_2, SO_2, whereas the second reaction involves the oxidation CO to CO_2. The two-step chemical reaction can be written as follows [182]:

$$\begin{gathered} VM + n_1 O_2 \rightarrow n_2 CO + n_3 H_2O + n_4 N_2 + n_5 SO_2 \\ CO + 0.5 \cdot O_2 \rightarrow CO_2 \end{gathered} \tag{5.20}$$

where: n_1,n_2, n_3, n_4, n_5 are the stoichiometric coefficients determined from the two-step chemical mechanism and are calculated from the ultimate and proximate analyses.

However, the enhanced devolatilization process causes the volatiles to exceed the values from the proximate analysis at higher temperatures. Hence, to include this phenomenon in the numerical calculations, the High Temperature Volatile Yield (HTVY) of 1.57 was used [148, 149]. Thus the actual volatiles are enhanced, and the fixed carbon is reduced to be as one minus the actual volatiles, moisture and ash fraction.

The stoichiometric coefficients in the two-step chemical mechanism of the volatiles oxidation, which are calculated based on the molar composition of the volatiles, are given as follows [182]:

$$n_1 = \frac{n_3}{2} + \frac{n_2}{2} + n_5 - \frac{O_{VM_{mol}}}{2} \tag{5.21}$$

$$n_2 = C_{VM_{mol}} \tag{5.22}$$

$$n_3 = \frac{H_{VM_{mol}}}{2} \tag{5.23}$$

$$n_4 = \frac{N_{VM_{mol}}}{2} \tag{5.24}$$

$$n_2 = S_{VM_{mol}} \tag{5.25}$$

The mole composition is determined as follows [182]:

$$C_{VM_{mol}} = \frac{C_{VM}}{M_C} \cdot M_{VM} \tag{5.26}$$

$$H_{VM_{mol}} = \frac{H_{VM}}{M_H} \cdot M_{VM} \tag{5.27}$$

$$O_{VM_{mol}} = \frac{O_{VM}}{M_O} \cdot M_{VM} \tag{5.28}$$

$$N_{VM_{mol}} = \frac{N_{VM}}{M_N} \cdot M_{VM} \tag{5.29}$$

$$S_{VM_{mol}} = \frac{S_{VM}}{M_S} \cdot M_{VM} \tag{5.30}$$

The components of the volatiles are determined as a fraction of the dry, ash-free component in the dry, ash-free volatiles [182]:

$$C_{VM} = \frac{C_{daf} - FC_{daf}}{VM_{daf}} \tag{5.31}$$

$$H_{VM} = \frac{H_{daf}}{VM_{daf}} \tag{5.32}$$

$$O_{VM} = \frac{O_{daf}}{VM_{daf}} \tag{5.33}$$

$$N_{VM} = \frac{N_{daf}}{VM_{daf}} \tag{5.34}$$

$$S_{VM} = \frac{S_{daf}}{VM_{daf}} \tag{5.35}$$

Taking into account the HTVY in the two-step reaction of the volatile matters, the chemical formula of the oxidation process is as follows [182]:

$$\begin{gathered} VM + 1.304 \cdot O_2 \rightarrow 1.691 \cdot CO + 1.263 \cdot H_2O + 0.045 \cdot N_2 + 0.006 \cdot SO_2 \\ CO + 0.5 \cdot O_2 \rightarrow CO_2 \end{gathered} \tag{5.36}$$

5.3.2.3 Burnout Stoichiometric Ratio

In the two-step combustion process, it is assumed that the fixed carbon (FC) oxidises first to the carbon monoxide as presented in equation (5.36). There is general agreement [128, 186–188] on CO as the product of coal devolatilisation in the Badzioch and Hawksley model [153]. Therefore, the Burnout Stoichiometric Ratio, Heat of Reaction for Burnout and Heat Fraction Absorbed by the Solid need to be specified for the CO. The Burnout Stoichiometric Ratio is the stoichiometric requirement (S_b) for the burnout reaction. Thus, it defines a mass of the oxidant per mass of char in terms of the stoichiometry in the coal particle surface burnout reaction [114, 182]:

$$FC + S_b \cdot O_2 \rightarrow products \tag{5.37}$$

In terms of the reaction:

$$FC + 0.5 \cdot O_2 \rightarrow CO \tag{5.38}$$

the S_b is the mass of the oxidant divided by the mass of the carbon.

5.3.2.4 Heat of reaction for burnout

The Heat of Reaction for Burnout is an input parameter that indicates the amount of heat released by the surface char combustion reaction, thus the heat release is given per unit mass of fixed carbon consumed in the surface reaction [114]. In the case of the reaction (5.38), the heat of reaction, also called the enthalpy of the reaction or the enthalpy of the combustion based on the calculation of the enthalpy of the formation reactants and the product, is expressed in this case as follows:

$$H_{reac} = H_{CO} - (H_C + H_{O_2}) \tag{5.39}$$

5.3.2.5 Heat Fraction Absorbed by the Solid

For the coal combustion, when the char burnout product is CO, the heat of reaction is entirely absorbed by the coal particle. Therefore, the

parameter called the Reaction Heat Fraction Absorbed by Solid f_h controls the distribution of the heat of reaction between the particle and the continuous phase and it is equal to 1 [114].

5.3.3 Air non-preheated case

The numerical calculations have been performed for the air non-preheated case. The sensitivity study of different sub-models has been discussed below. For each sensitivity analysis, the CFD predictions have been compared along the combustion rig centreline axis and traverses at the distances 0.075 m, 0.375 m, 0.575 m and 0.080 m away from the burner end. The location of the combustion facility axis and traverses is depicted in Figure 6.10.

5.3.3.1 Impact of the Eddy-Dissipation Mixing Rates

For the combustion modelling of pulverised coal, the transport equations are solved as a two-step reaction mechanism for each species. The reaction rates are fully controlled by the turbulent mixing and computed using the Eddy-Dissipation model, which is an adaption of the eddy breakup model proposed by Spalding [189], as discussed in Section 3.6.4. This model is commonly used in coal combustion simulations where the flow is fully turbulent [87, 98, 134, 140, 190].

For the two mixing rates, the empirical constants in the turbulent-chemistry interaction model have been compared. The one based on the work of Magnussen [155] (A = 4 B = 0.5), and Visser [131] (A = 0.5; B = 0.5 for the first step and A = 0.7; B = 0.5 for the second step of the reaction) is employed.

Implementation of different mixing rates and its influence on the numerical predictions is presented in Figures 5.5, 5.6 and 5.7. Figure 5.5 shows the comparison of Eddy-Dissipation mixing rates on the numerical predictions of the SIR and the experimental data. Further, Figures 5.6

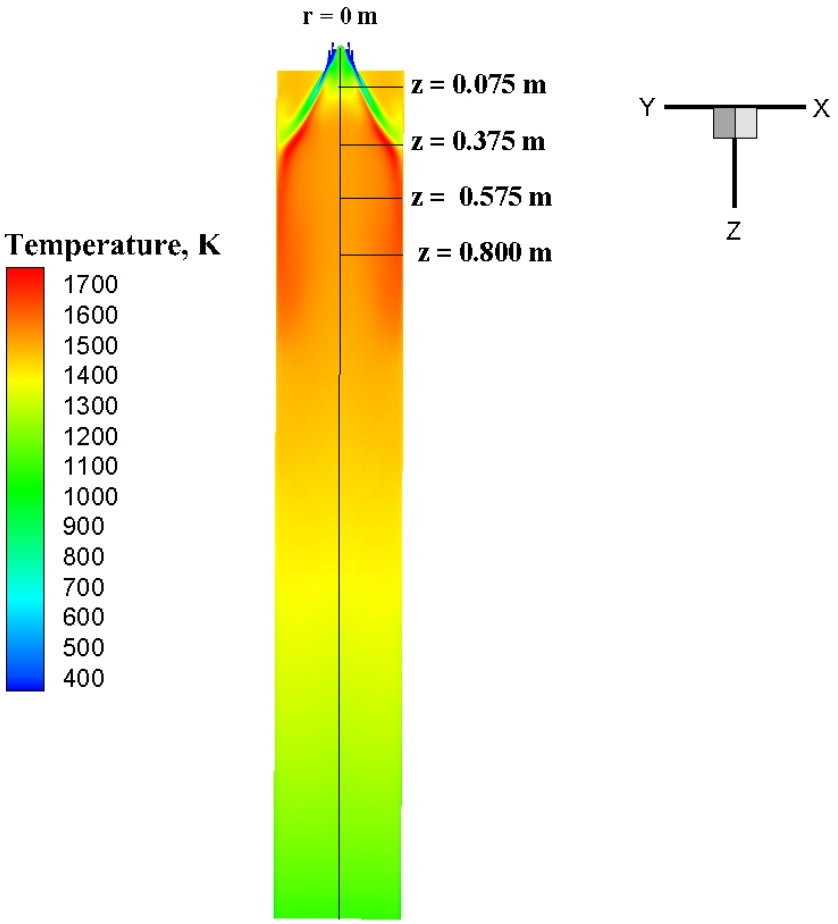

Figure 5.4: Contours of the computationally predicted temperature with specified locations of the traverses along the furnace (air non-preheated case).

and 5.7 shows the impact of Eddy-Dissipation mixing rates on the computational predictions of the axial temperature and the temperature profile at the distance of z = 0.075 m away from the burner end of the combustion gases within the combustion rig compared against the experimental data, respectively. It can be observed that the numerical predictions of the SIR for both approaches are similar in the region away from the burner. The mixing rates play significant role in the near burner region (as observed in Figures 5.5, 5.6 and 5.7) and the comparison of employment of the mixing rates based on [155] and [131] show the impact of the two mix-

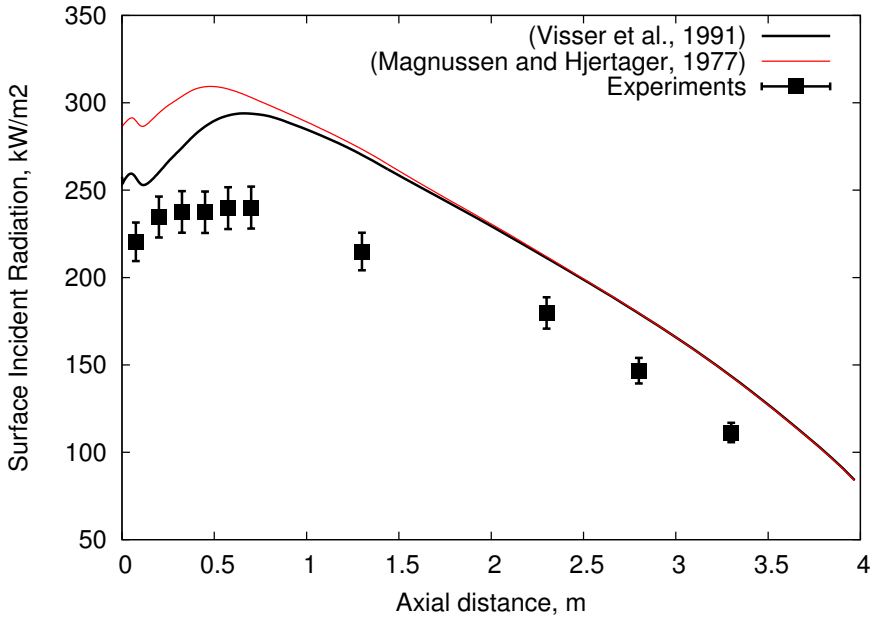

Figure 5.5: Comparison of the Eddy-Dissipation mixing rates on the SIR (air non-preheated case).

ing rates on the combustion performance in the near-burner region. In Figure 5.5, the numerical predictions of the SIR overpredict the experimental measurements for both approaches. However, the mixing rates proposed by Visser [131] applied in the numerical simulations gives results more in-line with the experimental data predictions of the SIR in the near-burner region. Moreover, the CFD predictions of the temperature profiles along the combustion facility axis and along the first viewing port at the distance of 0.075 m away from the burner end show that the mixing rates proposed by Magnussen [155] have higher temperatures than those measured during the experiments presented in Chapter 4 in the near-burner region. Whereas, the application of the mixing rates proposed by Visser [131] predict smoother temperature profiles, which are within the experimental data accuracy. In should be noted that the reaction rates are assumed to be controlled by the turbulence, so expensive Arrhenius chemical kinetic calculations can be avoided.

The exit temperature and flue gas composition values for the experi-

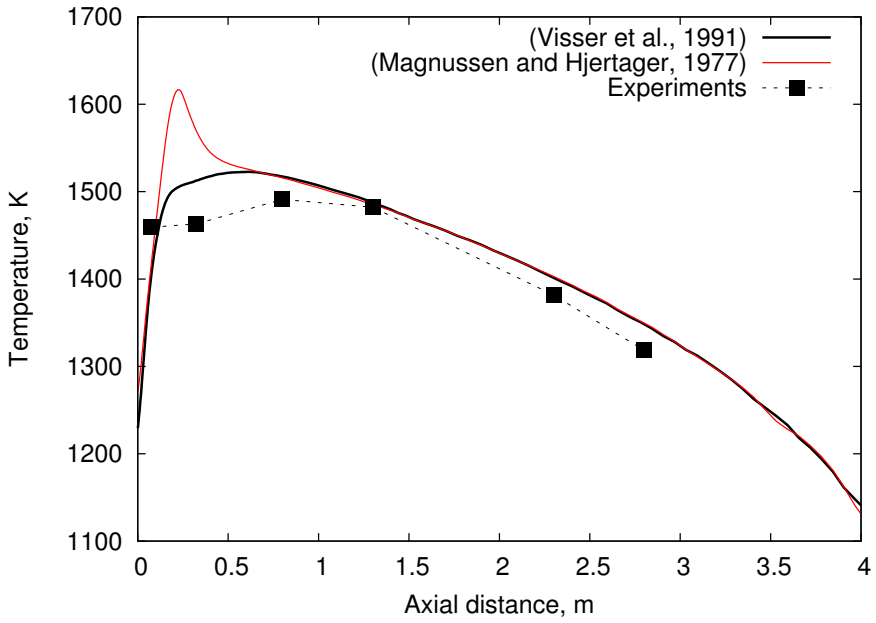

Figure 5.6: Comparison of the Eddy-Dissipation mixing rates on the axial temperature (air non-preheated case).

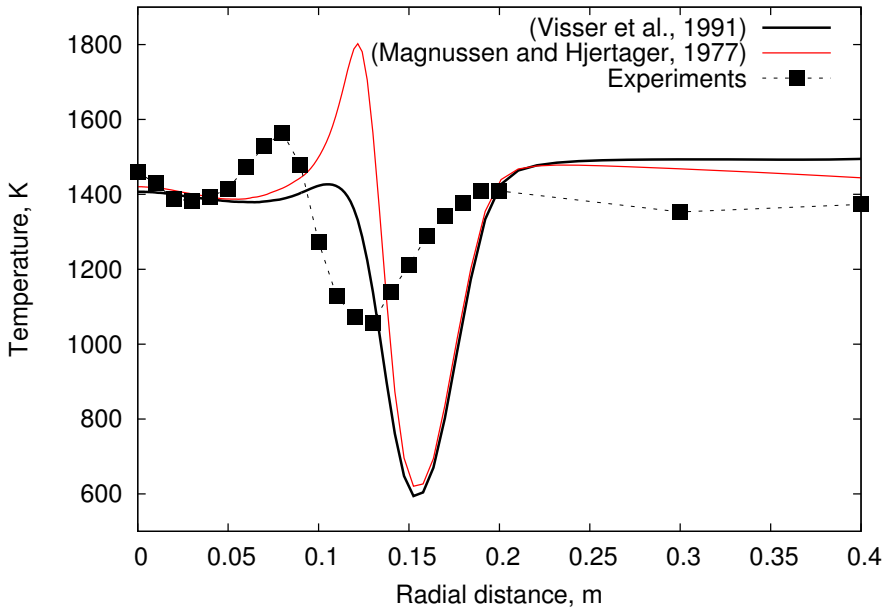

Figure 5.7: Comparison of the Eddy-Dissipation mixing rates on the flame profiling at the distance of z = 0.075 m (air non-preheated case).

Table 5.5: Comparison of the different two-step Eddy-Dissipation mixing rates and experimental measurements of the exit gas composition and flue gas temperature (air non-preheated case).

	Experiments	Mass Balance	CFD Mixing Rate	
			Visser [131]	Magnussen [155]
Temperature, K	959 ± 42	—	1076	1072
O_2, dry, %	3.8 ± 0.2	5.1	5.5	5.5
CO_2, dry, %	15.3 ± 0.2	14.1	13.7	13.7
SO_2, dry, ppm	291 ± 4	300	260	260

mental measurements, mass balance and CFD simulations are summarized in Table 5.5. It is observed that, in both cases, the exit temperature is overestimated by about 90 K, and there is almost no impact on the exit temperature when comparing these two approaches for Eddy-Dissipation mixing rates. Moreover, the mixing rates have negligible impact on the predictions of the O_2, CO_2 and SO_2 concentration in the flue gas and CFD results of CO_2 and SO_2 are in good agreement experimental measurements for both cases. The predictions of the O_2 overpredict the experimental measurements for the compared two approaches, and this has been explained when comparing the theoretical calculations of mass balance with the experimental data in Section 5.2.1. However, the CO_2 concentration in the flue gas is in agreement with the theoretical calculations of the stoichiometry (mass balance).

To conclude, the mixing rates strongly affect the near-burner region CFD predictions. Further, the empirical values based on Visser [131] are more in-line with the experimental data than the values based on work of Magnussen [155]. Therefore, in the further studies in this chapter, the values of A = 0.5; B = 0.5 for the first step and A = 0.7; B = 0.5 for the second step in the reaction mechanism have been chosen.

5.3.3.2 Impact of different turbulence models

The SIR is correlated with the temperature of the wall which is also affected by the temperature distribution in the furnace. Likewise, the temperature distribution within the combustion chamber is affected by many aspects in the combustion process, including the flame shape, turbulent flow, radiation heat transfer in the furnace, etc. The actual profile of the SIR appears to be much flatter than that predicted. This may be a result of the turbulence model employed, hence the impact of different turbulence models is investigated in this section.

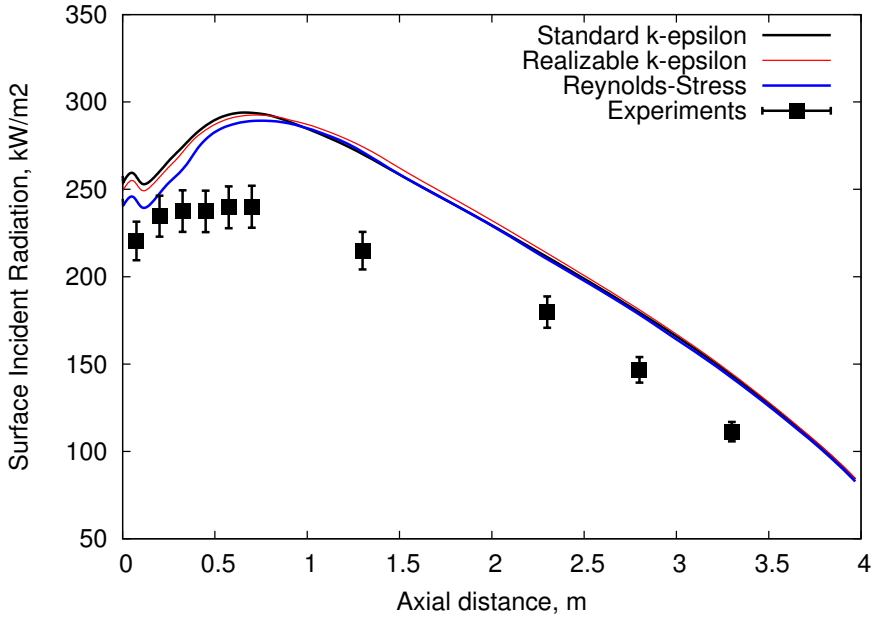

Figure 5.8: Comparison of the different turbulence models on the SIR (air non-preheated case).

Three turbulence models, namely, the Standard k-ε, the Realizable k-ε and the Reynolds Stress model, introduced in Chapter 3.3, have been compared. In Figure 5.8 we can see the comparison of the SIR numerical predictions for the three investigated turbulence models compared against the experimental data.

The prediction of the SIR differs in the near-burner region, and in all three investigated cases, the Standard k-ε, Realizable k-ε and the

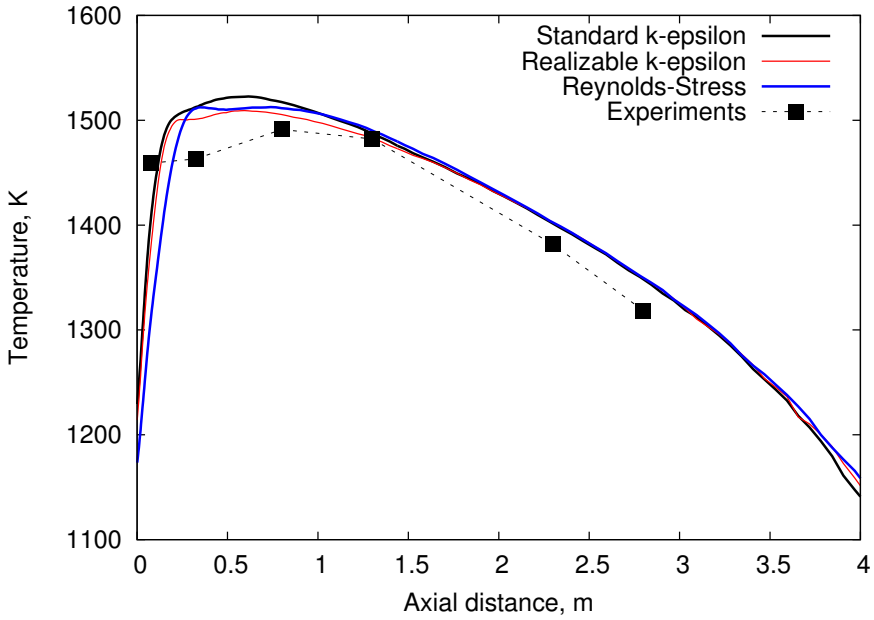

Figure 5.9: Comparison of the different turbulence models on the axial temperature (air non-preheated case).

Reynolds-Stress models overpredict the experimental data. It can be observed that the peak in the SIR plot (Figure 5.8) is moved downstream, compared to the measured SIR. In the near-burner region, the Reynolds-Stress model predicts slightly better the SIR than the other analysed turbulence models. The Reynolds-Stress model has better accuracy than the Standard k-ε, and the Realizable k-ε, and this is because the latter are the simplest models of turbulence. In contrast, the Reynolds-Stress model is the most elaborate turbulence model provided by ANSYS Fluent. Since the Reynolds Stress model accounts for the effects of streamline curvature, swirl, rotation, and rapid changes in strain rate in a more rigorous manner than two-equation models, it has greater potential to give accurate predictions for complex flows.

The axial temperature and flame profiling at the distance of z = 0.075 m away from the burner end, as obtained using the numerical predictions are compared with the experimental data in Figures 5.9 and 5.10, respectively. When comparing the CFD predictions of the axial temperature of the

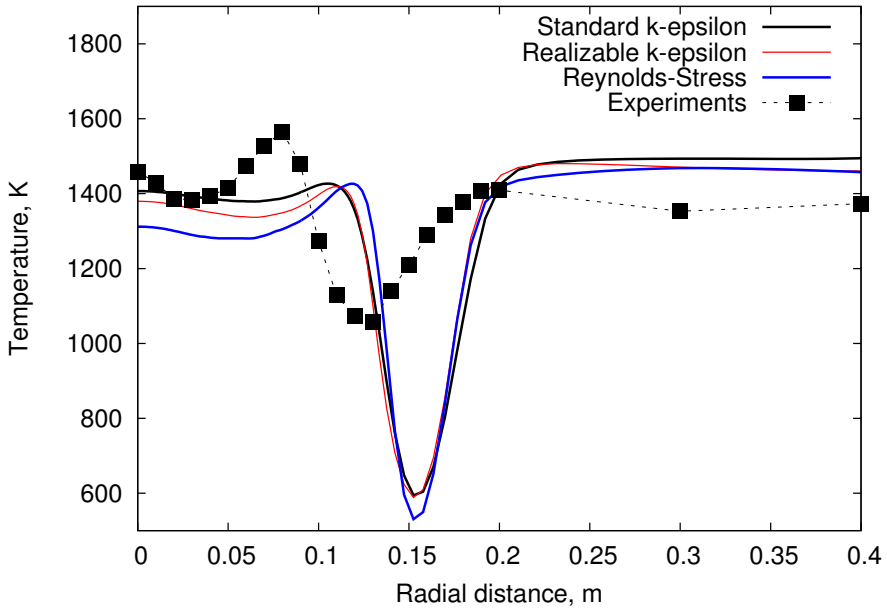

Figure 5.10: Comparison of the different turbulence models on the flame profiling at the distance of z = 0.075 m away from the burner end (air non-preheated case).

combustion gases for different turbulence models in Figure 5.9, it can be observed that the CFD predictions are similar for each turbulence model. The investigated models are overpredicting the temperature in the near-burner region. Further, the flame profiling at the distance of z = 0.075 m away from the burner end shows a better agreement when using the k-ε model. However, all the models used in this comparison have similar temperature profiles.

The exit temperature and the flue gas composition values for the experimental data and CFD simulations are summarized in Table 5.6. It is observed that the difference in the exit temperature and composition between the turbulence models is not significant. In each case, the exit temperature is overestimated, there is no impact on the exit temperature and on the predictions of the O_2, CO_2 and SO_2 concentrations in the flue gas and the CFD results for CO_2 and SO_2 are in good agreement with the experimental data for both cases. The O_2 predictions are higher than the

Table 5.6: Comparison of the results obtained using the different turbulence sub-models and the experimental data of the exit gas composition and the flue gas temperature (air non-preheated case).

	Experiments	Mass Balance	CFD turbulence model		
			Stand. k-ε	Real. k-ε	RSM
Temperature, K	959±42	—	1076	1076	1082
O_2, dry, %	3.8±0.2	5.1	5.5	5.5	5.5
CO_2, dry, %	15.3±0.2	14.1	13.7	13.7	13.7
SO_2, dry, ppm	291±4	300	260	260	293

experimental measurements. However, the O_2 concentration in the flue gas is in good agreement with mass balance.

For further studies, the Standard k-ε model was chosen due to its cheap computational cost and insignificant impact of the more advanced and more computationally expensive turbulence models.

5.3.3.3 Impact of the devolatilization models

The two devolatilization models, namely the Single Kinetic Rate and Constant Rate models, described in Section 3.6.2.1, were introduced into the CFD model. The simplest devolatilization model available in ANSYS Fluent - constant rate devolatilization model assumes that volatiles are released at a constant rate [152] with a value of 12 s^{-1} for coal and this is based on [191]. Whereas, in the Single Kinetic Rate devolatlization model, the rate of devolatilization is first-order dependent on the amount of volatiles remaining in the particle [153]. The influence of the different sub-models for the volatiles being released from the coal particles on the numerical solutions has been investigated and a comparison of the results obtained when using the two devolatilization models on the predictions of the SIR and temperature profiles on the furnace axis and at the distance

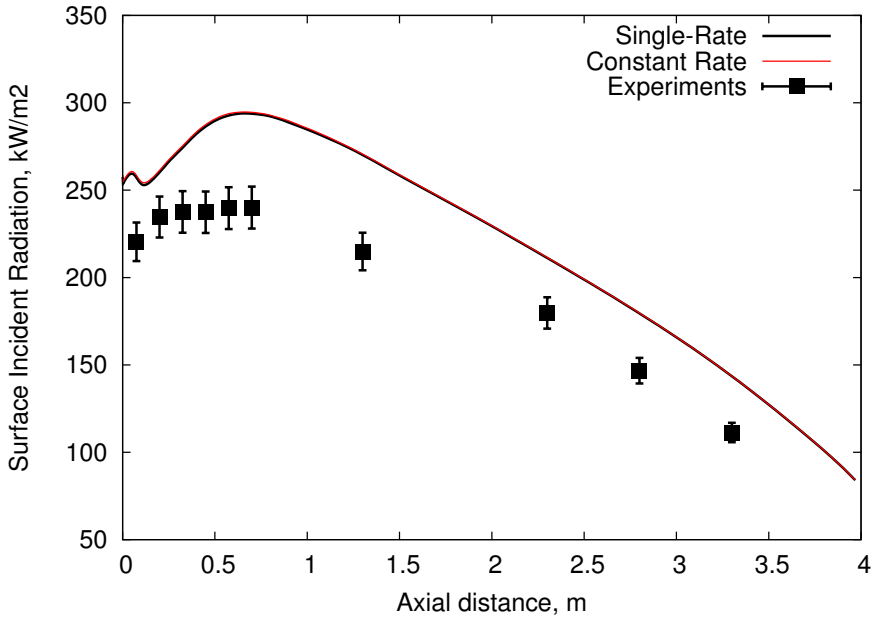

Figure 5.11: Comparison of the numerical pradictions when using the Single Kinetic Rate and Constant Rate devolatilization models with the experimental data - the SIR (air non-preheated case).

of z = 0.075 m away from the burner end are presented in Figures 5.11, 5.12 and 5.13, respectively. Further, it is found that the CFD predictions when using the Single Kinetic Rate and the Constant Rate models are overlapping and have no impact on the numerical results.

The exit temperature and flue gas composition values for the experimental data, theoretical calculations and CFD simulations are summarized in Table 5.7. It is observed that, similar to the SIR and the temperature predictions, the flue gas temperature and its composition are predicted to be almost exactly the same. The numerical predictions of the flue gas O_2, CO_2 and SO_2 concentrations are in good agreement with the mass balance calculations. However, the predicted O_2 concentration in the flue gas overpredicts the experimental measurements and mass balance. The higher O_2 concentration in the flue gas may suggest that some of the coal particles have not reached complete combustion, which is also indicated by the lower value in the CO_2 prediction when compared with

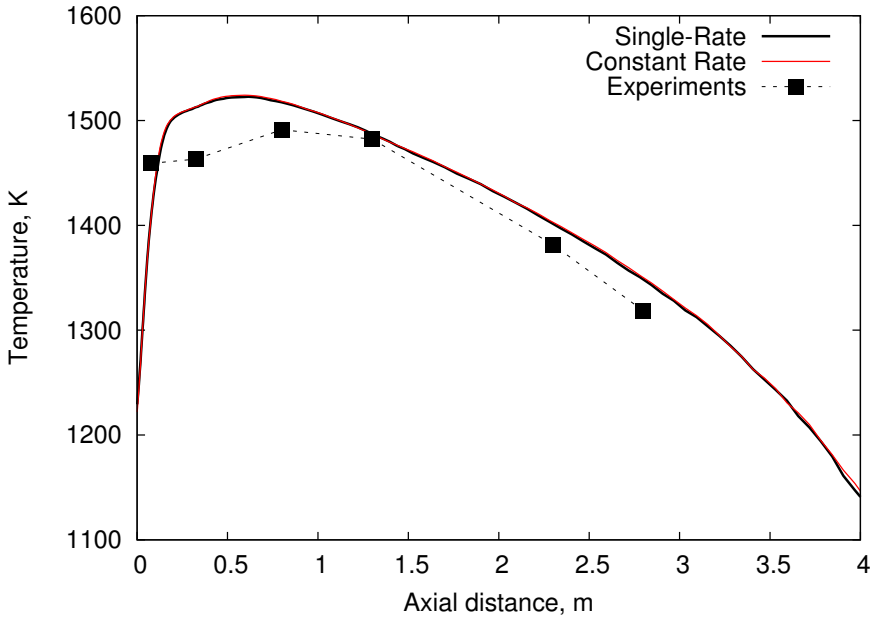

Figure 5.12: Comparison of the numerical predictions when using the Single Kinetic Rate and Constant Rate devolatilization models againt the epxerimental data on the axial temperature (air non-preheated case).

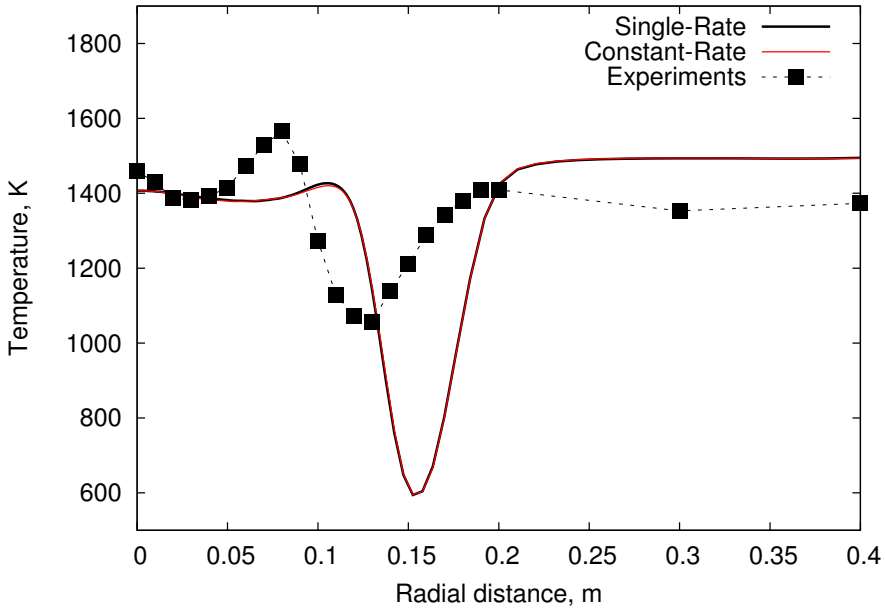

Figure 5.13: Comparison of the numerical predictions when using the Single Kinetic Rate and Constant Rate devolatilization models againt the epxerimental data on the flame profiling at the distance of z = 0.075 m away from the burner end (air non-preheated case).

Table 5.7: Comparison of the results obtained using the different devolatilization sub-models and the experimental data of the flue gas composition and the temperature at the furnace exit (air non-preheated case).

	Experiments	Mass Balance	CFD devolatilization model	
			Constant Rate	Single-Kinetic Rate
Temperature, K	959 ± 42	—	1076	1076
O_2, dry, %	3.8 ± 0.2	5.1	5.5	5.5
CO_2, dry, %	15.3 ± 0.2	14.1	13.7	13.7
SO_2, dry, ppm	291 ± 4	300	260	260

the mass balance calculations.

As it is seen in Figures 5.11, 5.12 and 5.13, the application of the Single Kinetic Rate and Constant Rate devolatilization models does not substantially affect the numerical predictions. For further numerical simulations then the Single Kinetic Rate devolatilization model has been chosen.

5.3.3.4 Impact of the char combustion models

For the estimation of the influence of the char combustion model on the numerical solution, the two models of char combustion were introduced, namely the Intrinsic Model and the Kinetics/Diffusion-Limited Rate Model. The char combustion models were described in detail in Section 3.6.3.

The numerical predictions with different char combustion models and their influence on SIR and temperature profiles are presented in Figures 5.14, 5.15 and 5.16, respectively. It can be observed that the numerical predictions of SIR presented in Figure 5.14 overestimates the experimental data. However, for both char combustion models, the predictions are overlapping and almost no influence of the implementation of the dif-

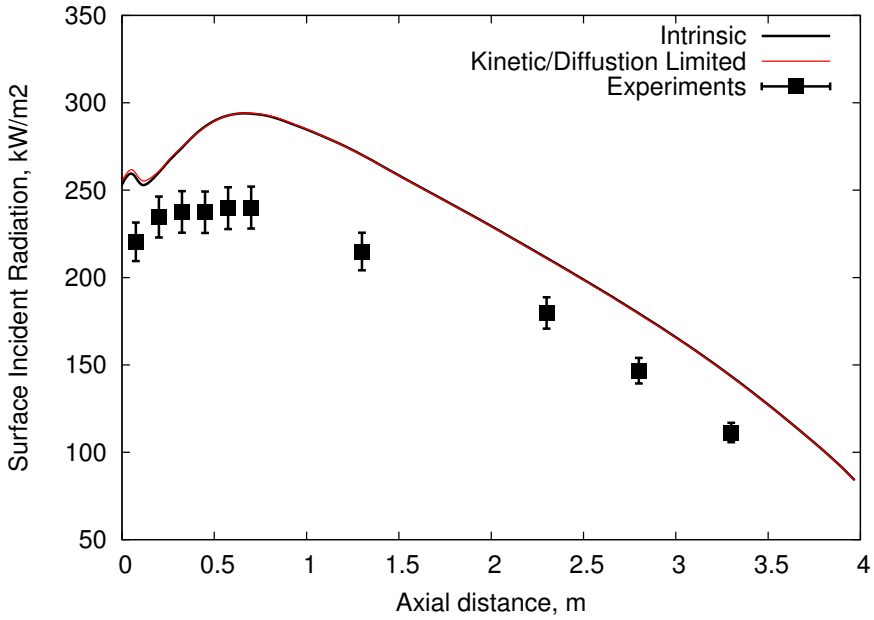

Figure 5.14: Comparison of the results obtained when employing the Intrinsic and the Kinetics/Diffusion-Limited Rate char combustion models with the experimantal data - the SIR (air non-preheated case).

ferent char combustion models has been noticed. The negligible impact when using the Intrinsic Model and the Kinetics/Diffusion-Limited Rate Model has been observed on the temperature profiles along the axis and on the flame profiling at the distance of z = 0.075 m away from the burner, as depicted in Figures 5.15 and 5.16, respectively.

The exit temperature and flue gas composition values for the experimental data, theoretical calculations and CFD simulations are summarized in Table 5.8. It has been observed that application of the Intrinsic and the Kinetics/Diffusion-Limited Rate char combustion models different devolatilization models do not have a substantial influence on the SIR and the temperature predictions and they also agree with the CFD results in a similar manner.

Similar to the SIR and the temperature predictions, the flue gas temperature and its composition predict similar values at the exit of the combustion facility. The numerical predictions of the flue gas O_2, CO_2 and

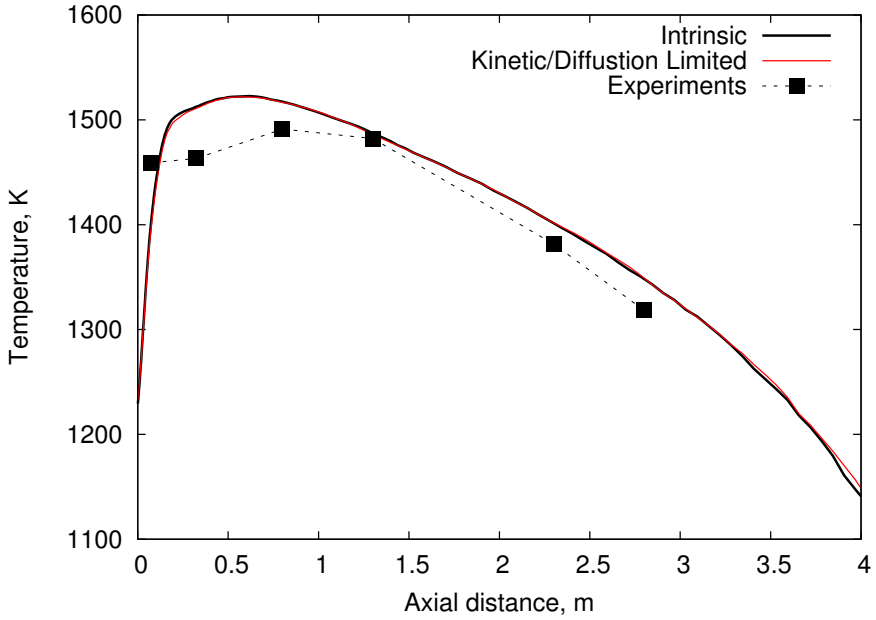

Figure 5.15: Comparison of the results obtained when employing the Intrinsic and the Kinetics/Diffusion-Limited Rate char combustion models with the experimantal data - the axial temperature (air non-preheated case).

Table 5.8: Comparison of the results obtained using the different char sub-models and the experimental data of the exit gas composition and flue gas temperature (air non-preheated case).

	Experiments	Mass Balance	CFD char sub-model	
			Intrinsic	Kinetic/Diffusion - Limited Rate
Temperature, K	959 ± 42	—	1076	1075
O_2, dry, %	3.8 ± 0.2	5.1	5.5	5.6
CO_2, dry, %	15.3 ± 0.2	14.1	13.7	13.7
SO_2, dry, ppm	291 ± 4	300	260	260

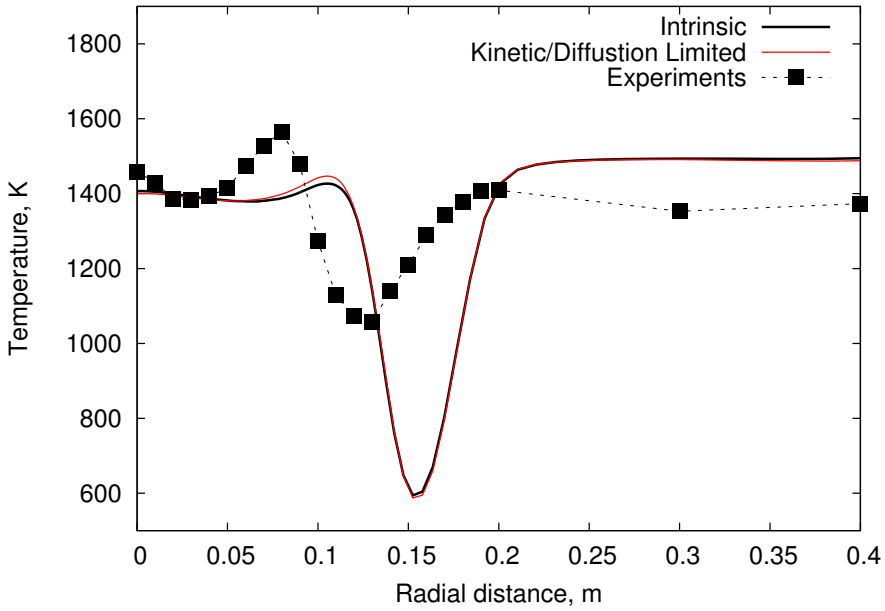

Figure 5.16: Comparison of the results obtained when employing the Intrinsic and the Kinetics/Diffusion-Limited Rate char combustion models with the experimantal data - the flame profiling at the distance of z = 0.075 m away from the burner (air non-preheated case).

SO_2 concentrations are in good agreements with the mass balance calculations. However, the predicted O_2 concentration in the flue gas overpredicts the experimental measurements and mass balance, in a similar manner to the numerical predictions presented in the previous sections. Also the temperature of the flue gases is also overpredicted when compared with the experimental data.

It has been observed that in the non-preheated case the char combustion sub-models do not significantly influence the CFD predictions. However, according to the previous study [43], the Intrinsic Model has been found to be more accurate for the coal combustion simulations and therefore this model has been chosen for use in further studies.

5.3.4 Sub-models applied to the numerical simulations

The numerical set-up and choice of models was validated in Sections 5.3.3.1 - 5.3.3.4 for the air non-preheated case by comparing sensitivity studies of the two-step reaction mechanism, turbulence models, devolatilization and char combustion sub-models. This investigation was required so that the most appropriate sub-models may be applied in the further studies in Chapter 6.

The final choice of the sub-models and numerical solution methods, based on the investigations and literature review, are listed in Table 5.9. The CFD simulations for the air non-preheated case were performed in ANSYS Fluent on a 3D axisymmetric mesh consisting of 1 million cells. The 2nd order upwind scheme has been used for the spatial discretization and for the pressure formulation the PRESTO model has been employed. Thermal conductivity has been used in order to take into account the thermal boundary conditions of the combustion test facility. For the gas phase combustion, the two-step Eddy-Dissipation model has been chosen with the empirical values of mixing rates based on Visser [131]. The devolatilisation was modelled using the Single Kinetic Rate model and char combustion using the Intrinsic model. Radiation was solved using the Discrete Ordinates models with gas radiative properties modelled by the WSGG model.

5.4 Conclusions

In this chapter, the mass and energy balances and the CFD simulations of the pulverised coal combustion have been validated against the experimental data in the air non-preheated case. Moreover, the mass and energy balances for the air preheated and oxy-coal cases have been compared with the experimental data. The furnace and burner geometry

Table 5.9: The proposed final model formulation for pulverised coal combustion.

	Sub-model
Mesh	1M cells, 3D axi symmetric
Spatial discretization	2^{nd} order upwind
Pressure formulation	PRESTO
Thermal wall boundary condition	Thermal conductivity
Devolatilization	The Single Kinetic Rate Model
Gas-phase combustion model	2-step Eddy-Dissipation
Char combustion	The Intrinsic Model
Turbulence	Standard k-ε
Radiation	Discrete Ordinates
Gas radiative properties	WSGG model

were simplified for the CFD simulations and a detailed investigation into the different turbulence models and approaches to modelling volatiles and char combustion were performed. Further, the results obtained from the numerical calculations were compared against the experimental data and theoretical calculations.

The main findings of this investigation are outlined as follows:

- For the prediction of the reaction rates during the combustion modelling of the pulverized coal, which are being controlled by the turbulent mixing and calculated by employing the Eddy-Dissipation model, the empirical constants based on Visser [131] were found to be in better agreement with the experimental data than those proposed by Magnussen [155]. Therefore, the empirical constants for the turbulent chemistry interaction model based on Visser [131] are recommended for pulverised coal combustion CFD modelling.

- The sensitivity of the different turbulence models within the RANS

approach, namely, the Standard k-ε, the Realizable k-ε and the Reynolds Stress model have an insignificant influence on the numerical results. Therefore, in order to reduce the computational cost then the Standard k-ε model has been used. However, in the future more advanced turbulence models are recommended when sufficient computational resources are available, especially for an accurate prediction in the near burner region.

- The devolatilization of the pulverised coal combustion when modelled by the Single-Kinetic Rate and the Constant Rate model give similar results. The different char combustion sub-models, namely the Intrinsic and the Kinetic/Diffusion Limited model, that are employed in the combustion CFD modelling do not have a substantial effect on the CFD results.

- The WSGG approach to modelling the gaseous radiative properties achieved accurate predictions of the radiative properties of the combustion gases during the coal combustion in an air atmosphere against the experimental data obtained for the non-preheated air-coal case. These findings are in good agreement with previous studies [43]. However, the SIR results from the numerical calculations employing the WSGG model for the radiative properties of the gases during combustion of pulverised coal overpredict the experimental data by about 25%. Therefore, emphasising the need for further investigations on the radiative properties.

Overall, the CFD predictions were successfully validated against the experimental data for the non-preheated combustion of pulverised coal. However, the combination of the advanced turbulence models, radiative properties and gasification reactions could provide further improvements and should be investigated in the future.

5.5 Summary

In this Chapter a validation study of the UKCCSRC PACT 250 kW Combustion Rig facility has been presented. The experimental measurements collected during the experimental campaign, presented in Chapter 4, were compared with the numerical and theoretical calculations of the mass and energy balances. Also a sensitivity study on the different CFD sub-models for the two-step reaction mechanism, turbulence, devolatilization and char combustion has been investigated.

It is found that the theoretical calculations, both the stoichiometry of the combustion and the energy balance match well with the CFD results. The sensitivity study and the application of different sub-models for the turbulence modelling, devolatilization and char combustion have assisted in the development of a reliable CFD model for pulverised coal combustion, which is able to accurately reproduce the experimental data and therefore can be used with confidence in further studies and industrial applications.

Chapter 6

Coal and biomass combustion in a 15 kW jet flame

This chapter presents the numerical predictions of coal and biomass combustion in a 15 kW jet flame. The CFD results are compared against experimental data. The settings for the coal and biomass combustion simulations are based on the study from Chapter 4 for coal combustion. A literature review of the state-of-art for biomass combustion was presented in Chapters 2 and 3. This comparison assists in identifying the difficulties with the numerical modelling of biomass and the limitations in the sub-models currently used for pulverised biomass fuel combustion.

Further, a theoretical estimations of pollutant emissions from biomass combustion have been performed with proposed emission reduction techniques.

6.1 Experimental measurements

The experimental data and design of the experimental rig used for validation of this work were published by Weber [174]. Since detailed information about the process for the evaluation of the experimental measurements can be found in this publication, then only a brief description of

the facility is presented here. The experimental rig is a second-generation of the facility used previously for the co-firing combustion studies [192] and refuse-derived-fuels combustion study [193].

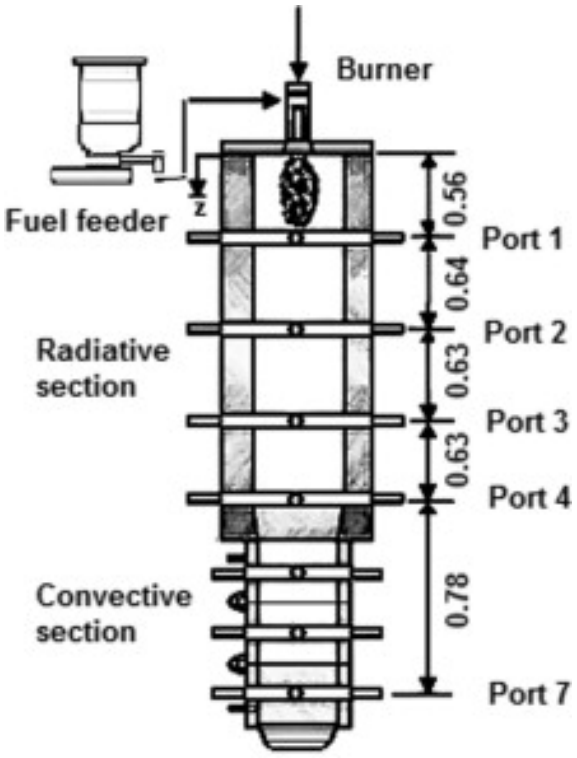

Figure 6.1: Schematic of the experimental 15 kW jet flame rig [174].

6.1.1 Furnace

The experimental facility, shown in Figure 6.1 consists of a down-fired jet flame combustion chamber. This rig is capable of burning pulverised solid fuel, namely coal and biomass.

The furnace is approximately 3 m long and has a cylindrical shape with an inner diameter of 0.3 m. The experimental rig is divided into two sections: the radiative and convective sections. The higher temperature - radiation section is followed by the lower temperature - convective section. The former is equipped with heating elements which keep the walls of the combustion chamber at a constant temperature, 1373 K.

In this study, only a 2.5 m long radiative section of the furnace is taken into consideration. This is mainly because of the availability of the experimental measurements for this section and the set temperature on the furnace walls. The first section of the furnace, where the radiation heat transfer plays a significant role in the heat transfer analysis, has four viewing ports that allow measurements to be taken.

6.1.2 Burner

The experimental facility is equipped with the scale-down version of the IFRF burner, which has two possible configurations, depending on the fuel type used, namely for coal and different types of biomass. A schematic of the no-swirl burner with dimensions of the fuel and combustion air inlets are depicted in Figure 6.2. On the left-hand side, a schematic of the biomass burner geometry has been presented, whereas, on the right-hand side the dimensions of the coal burner geometry can be found.

For the biomass mode, the fuel is supplied to the combustion chamber through the central fuel injection which has a diameter of 8 mm, whereas for the coal combustion mode, the fuel is provided through the inner annulus inlet with the inner and outer diameter of 12 mm and 16 mm, respectively. Both the coal and biomass are supplied to the combustion chamber with the carrier air. The combustion air enters the furnace through the outer annulus inlet with the inner and outer diameters of 20 mm and 36 mm, respectively.

The burner quarl shape, for both the biomass and coal combustion modes, fits the equation $r(x) = 18 + 0.0416664 \cdot x^2 - 0.0007716 \cdot x^3$, where r and x are given in millimetres, and r and x are the radial and axial distances, respectively. The quarl outlet is twice the size of the inlet and has a diameter of 72 mm.

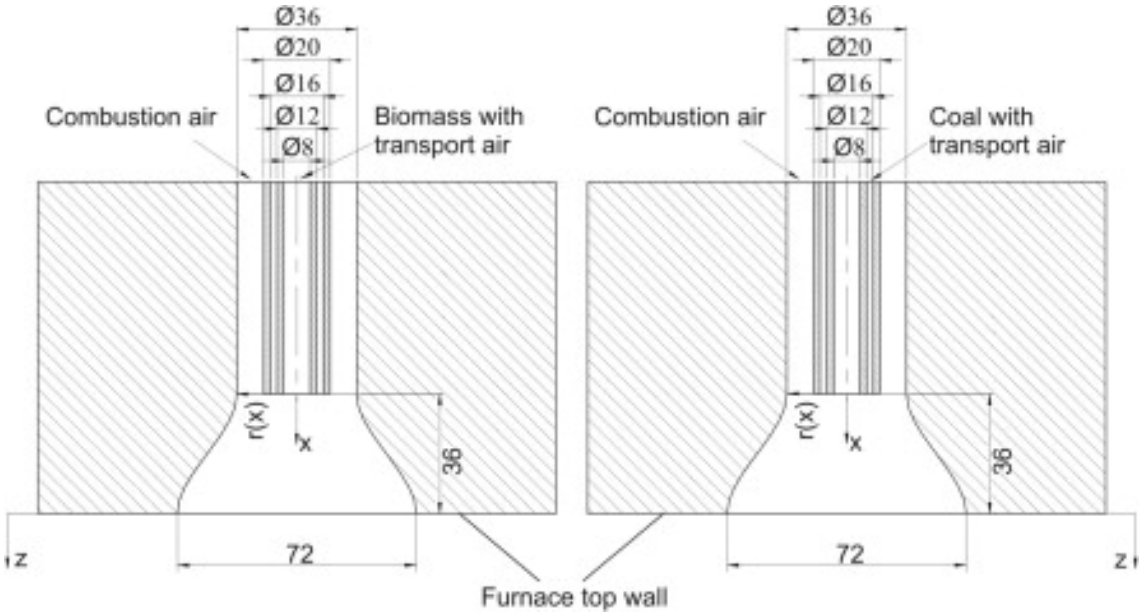

Figure 6.2: Schematics of the IFRF coal and biomass burners [174].

6.1.3 Fuel

The experimental rig was supplied with the South African Middelburg coal for the coal combustion experiments and with different types of biomass, namely mixed wood, sawdust, grain residue and fermentation residue, for the biomass combustion cases. However, due to the focus on woody biomass and coal, in the CFD study only three types of fuel are considered, namely coal, mixed wood and sawdust.

The particle size distribution obtained from the sieve analysis for Middelburg coal, mixed wood and sawdust is shown in Figure 6.3. It can be observed that the difference between the coal and biomass particle size distribution is significant. In the coal sample there are 80% of the particles having a diameter below 100 µm, whereas, in the biomass sample there are 20% of the particles having a diameter below 100 µm. The particle size distribution obtained from the sieve analysis for two types of biomass, mixed wood and sawdust, have a similar profile.

Table 6.1: Proximate and ultimate analyses of coal, mixed wood, sawdust, fermentation and grain residue [174].

	Middelburg coal	Mixed wood	Sawdust	Fermentation residue	Grain residue
Proximate analysis, wt.% (as fired)					
Moisture	6.1	6.6	6.7	14.7	12.1
Ash	10.0	1.7	0.5	7.3	6.2
Volatiles	30.4	75.5	78.4	60.4	66.2
Fixed carbon	53.5	16.2	14.4	17.6	15.5
Ultimate analysis, wt.% (as fired)					
C	66.2	46.5	47.5	40.0	40.3
H	4.0	5.6	5.9	4.8	5.4
S	0.87	0.03	0.06	0.24	0.18
N	1.75	0.26	0.09	1.54	2.14
Cl	< 0.05	0.02	0	0.33	0.15
O	11.0	39.3	39.2	31.1	33.5
Calorific values, MJ/kg (as fired)					
GCV	26.4	18.3	18.8	15.6	16.3
LCV	25.3	17.0	17.3	14.2	14.8

The proximate and ultimate analysis, and calorific value of the Middelburg coal, mixed wood, sawdust, fermentation residue and grain residue are compared and summarized in Table 6.1. The significant difference in the fuel composition and calorific value of coal and biomass are as follows:

- It is observed that the moisture content for coal, sawdust and mixed wood are similar, being about 6 wt.% ÷ 7 wt.%, whereas for the fermentation and grain residue this value is doubled.
- The ash content in the woody biomass samples is much lower than in coal, whereas fermentation residue and grain residue have the ash content at similar level to coal.
- The volatile matter content of the biomass is significantly higher than in coal.
- The carbon content is higher in coal, whereas the content of the hydrogen is higher in biomass.
- There is less sulphur and less nitrogen in the woody biomass in comparison to coal. The fermentation residue has similar nitrogen content to coal and grain residue fuel nitrogen is the highest among analysed types of biomass and is higher than coal fuel nitrogen.
- Woody biomass fuel has about 39% of oxygen and there is about 32% of oxygen in the fermentation and grain residue , whereas the oxygen content in coal is about 11%, which indicates that biomass fuel may need less oxidizer for complete combustion.
- Biomass fuel is characterized by a lower heating value in comparison to coal fuel, and thus more biomass fuel has to be supplied to the combustion chamber to achieve any given thermal input when compared with the coal fuel.

The differences between coal and biomass fuel may have a significant impact on the combustion performance and on the numerical predictions of

biomass combustion; therefore using models developed for the coal combustion in numerical predictions of the biomass combustion may not be accurate and this is investigated in this chapter.

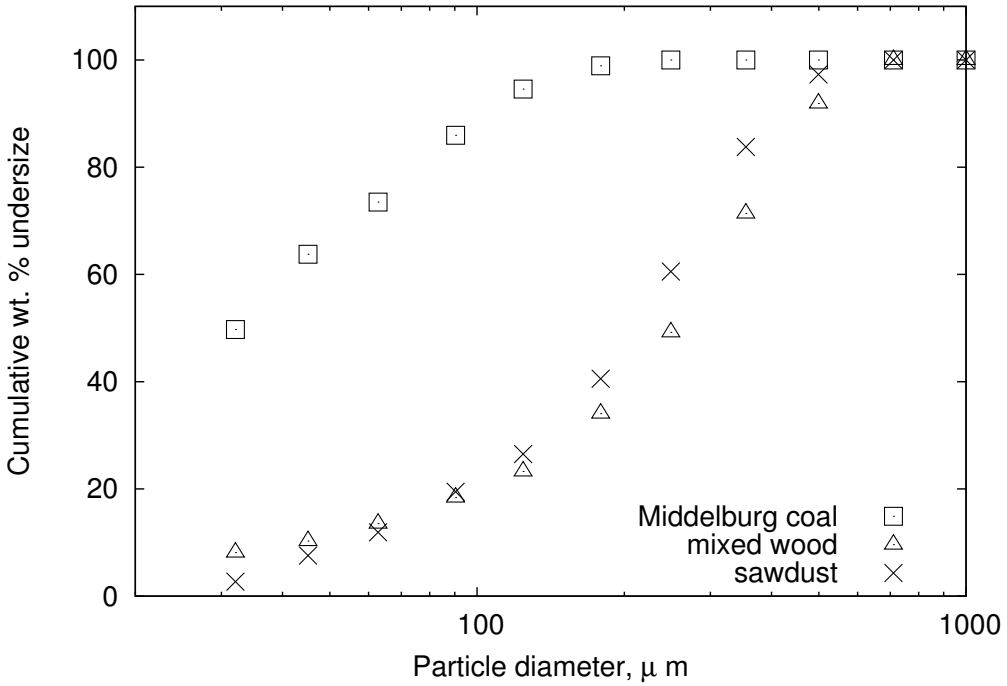

Figure 6.3: Particle size distribution of Middelburg coal, mixed wood and sawdust [174].

6.1.4 Particle Size Distribution

To account for the different sizes of the particles within the fuel sample, the Rosin-Rammler distribution function is used, as introduced in Section 4.4.2.2. The Rosin-Rammler distribution function is based on the assumption that there is an exponential relationship between the particle diameter d and the mass fraction of the pulverised fuel particle diameter greater than d, named Y_d:

$$Y_d = exp\left[-\left(\frac{d}{\bar{d}}\right)^n\right] \tag{6.1}$$

where:

d – particle diameter, m,

$\bar{d}$ – mean particle diameter, m,

Y_d – mass fraction of particles with a diameter greater than d,

n_s – spread parameter.

The particle diameter size distribution function that describes the Middelburg coal particle size distribution is depicted in Figure 6.4(a). It can be noticed that the Rosin-Rammler particle size distribution fits the sieve data for the Middelburg coal. The biomass Rosin-Rammler particle size distribution is presented in Figures 6.4(b) and 6.4(c) for mixed wood and sawdust, respectively. The Rosin-Rammler particle size distribution has been found to slightly overpredict the particle size for the particles with small diameter, which means that in the CFD calculations the number of the smallest particles will be overpredicted. However, for the large particles, the Rosin-Rammler curve fits well with the sieve analysis, which gives a good indication of the particle size for the CFD analysis. The minimum, maximum and mean diameters and the spread parameter used for the Rosin-Rammler particle size distribution for Middelburg coal, mixed wood and sawdust have been listed in Table 6.2. The mean diameter for coal fuel is 45.9 µm, 305.3 µm for mixed wood and 256.2 µm for sawdust. Further, in comparison to coal fuel, the biomass particles have larger diameter by about 6 times, which can significantly influence the combustion performance.

6.1.5 Operating conditions

Among the experimental cases presented in [174], four cases have been investigated in the numerical simulation analysis, namely the coal non-preheated and preheated, non-preheated sawdust and non-preheated

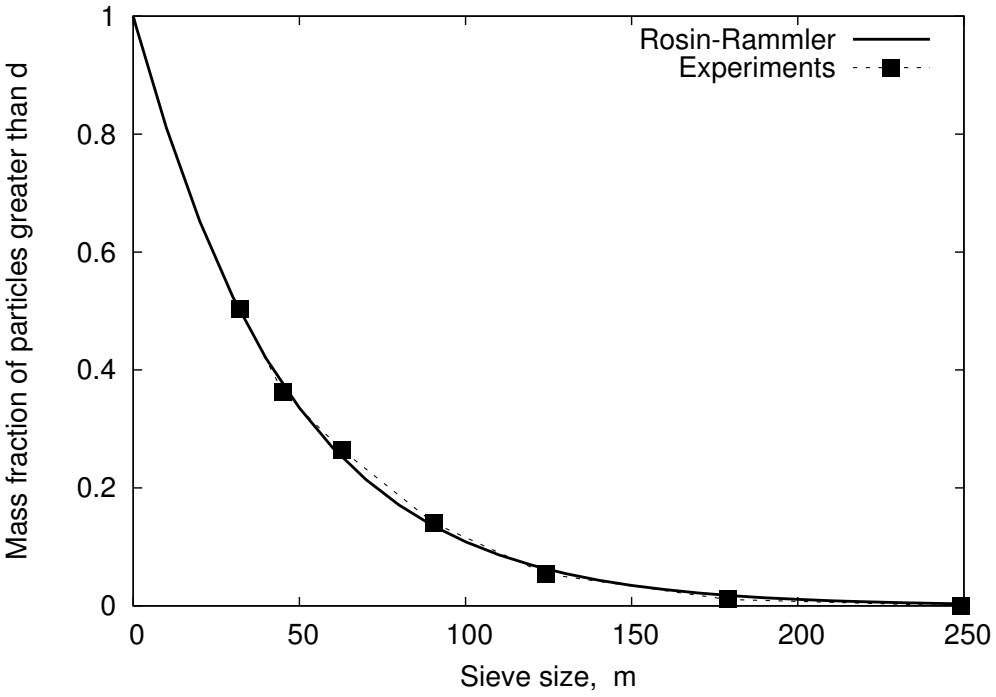
Rosin-Rammler
Experiments
Mass fraction of particles greater than d
Sieve size, m
0
0.2
0.4
0.6
0.8
1
0
50
100
150
200
250

(a)

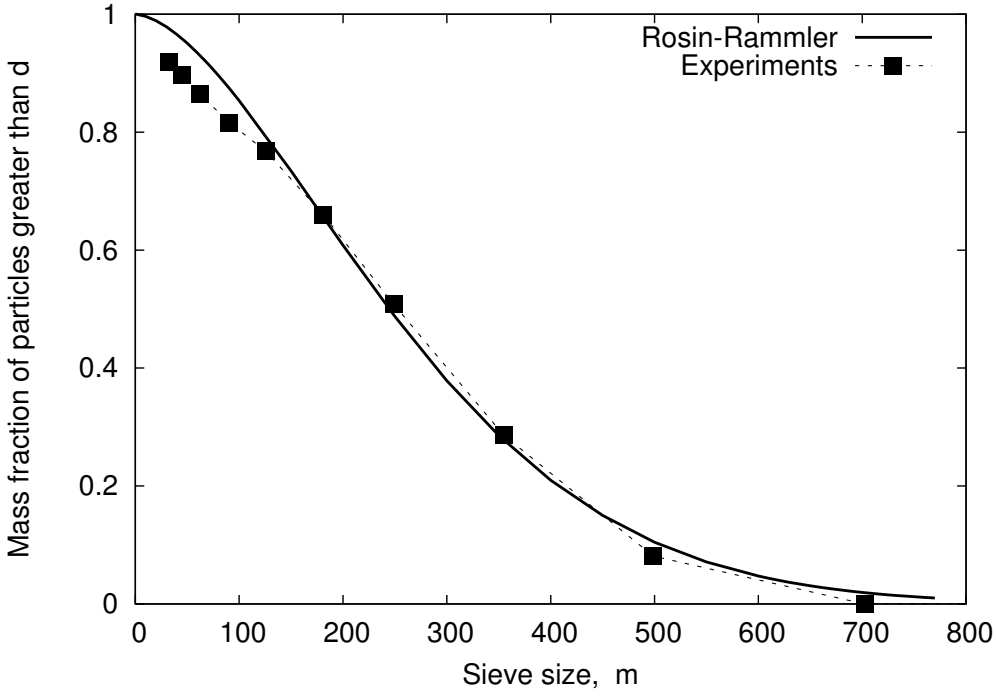
Rosin-Rammler
Experiments
Mass fraction of particles greater than d
Sieve size, m
0
0.2
0.4
0.6
0.8
1
0
100
200
300
400
500
600
700
800

(b)

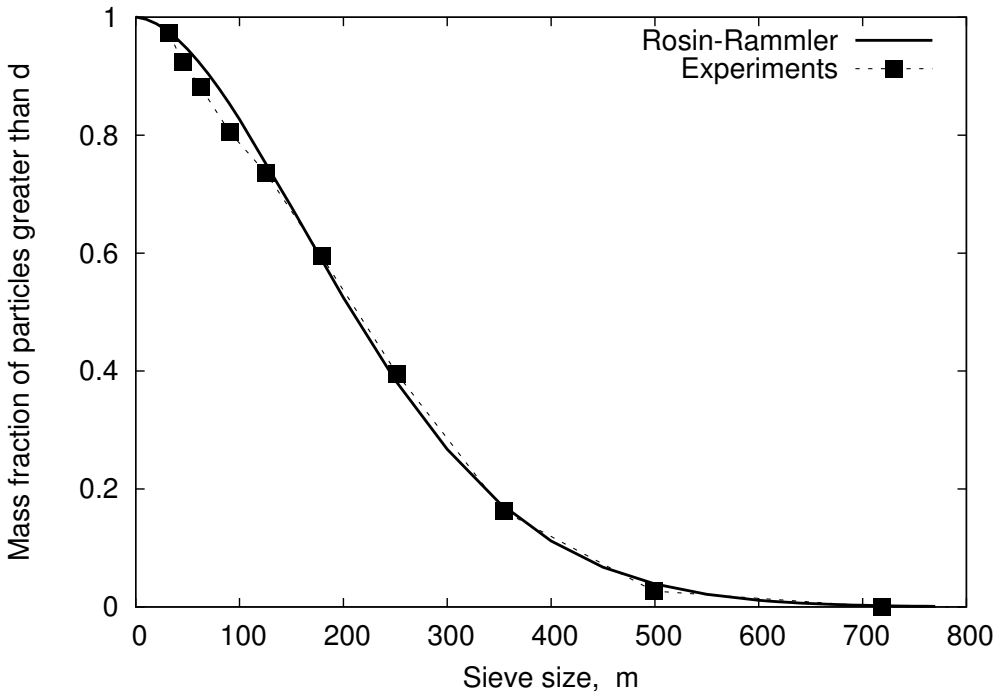

(c)

Figure 6.4: Rosin-Rammler particle size distribution fit for (a) Middelburg coal, (b) mixed wood and (c) sawdust.

Table 6.2: The Rosin-Rammler parameters.

	Middelburg coal	Mixed wood	Sawdust
Min. diameter, m	$1.00 \cdot 10^{-6}$	$1.00 \cdot 10^{-6}$	$1.00 \cdot 10^{-6}$
Max. diameter, m	$2.49 \cdot 10^{-4}$	$7.11 \cdot 10^{-4}$	$7.11 \cdot 10^{-4}$
Mean diameter, μm	45.9	305.3	256.0
Spread parameter	1.025	1.650	1.764

mixed wood cases. The thermal input for each analysed case is approximately 15 kW, and the excess air ratio in each case has been kept within the range λ = 1.2 – 1.3 in order to provide conditions for the complete combustion process.

The difference between the coal non-preheated and preheated case is the temperature of the combustion air, which is 298 K and 523 K for the

non-preheated and preheated cases, respectively. The other parameters for both cases were kept constant.

Both the carrier and combustion air were kept at the same value at the ambient temperature of 298 K for the sawdust and mixed wood combustion.

The experimental operating conditions for each type of fuel are listed in Table 6.3. The Middelburg coal, mixed wood and sawdust have been supplied to the furnace at different feed rates to keep the same thermal input to the combustion chamber. As the coal has the highest calorific value among the analysed fuels, its mass flow rate is the lowest when compared with biomass fuels. The calorific value of the mixed wood and sawdust is similar, therefore the feed rate is increased by 50% for both types of biomass when comparing with the coal mass flow rate supplying the jet flame combustion rig.

6.1.6 Measurements taken on a 15 kW jet flame

Several measurements have been taken and presented in the previous sections on the jet flame combustion rig and these are described in detail in [174]. Among other experimental data, the measurements of the temperature and the oxygen concentration at the centreline of the rig, the oxygen concentration, temperature and CO concentration measured at Port 3 are used for the CFD model validation and are therefore now presented.

The in-flame temperatures have been measured with a suction pyrometer in the range 1173 – 1573 K with an accuracy of $\pm$ 25 K. The in-flame gas composition was measured using a gas sampling probe and a set of analysers. The measurements of the axial temperature and oxygen concentration are presented in Figures 6.5 and 6.6, respectively. The measurements presented in these figures are for the coal non-preheated

Table 6.3: Experimental operating conditions for the 15 kW jet flame combustion of the Middelburg coal - non-preheated and preheated cases, mixed wood and sawdust cases [174].

	Middelburg coal	Mixed wood	Sawdust
Mass flow rate, kg/h	2.1	3.2	3.1
Excess air ratio λ	1.21	1.30	1.21
Wall temp, K	1373	1373	1373
Transport air			
Temperature, K	298	298	298
Mass flow rate, kg/h	12.1	10.0	8.0
Velocity, m/s	32.7	47.3	37.8
Combustion air			
Temperature, K	298/523	298	298
Mass flow rate, kg/h	10.1	13.4	13.9
Velocity, m/s	3.4/6.0	4.5	4.7
Thermal input			
Fuel/preheat, kW	14.8/none(0.1)	15.0/none	14.9/none

and preheated cases, and mixed wood and biomass cases. The difference between the coal non-preheated and preheated cases is visible in the temperature profiles along the furnace axis (Figure 6.5): the case with preheat has a higher axial temperature of combustion gases by about 20 K when compared with the coal case without preheat. The biomass cases, namely the mixed wood and sawdust, do not reach temperatures that are present during coal firing. The temperature at the distance of 0.5 m from the furnace top is lower by about 150 K and 200 K for mixed wood and sawdust, respectively, when compared with the coal combustion cases. The mixed wood combustion results in higher axial temperature in the combustion gases than sawdust with peak temperatures at a distance of 1 m from the furnace top wall. The peak temperature of the combustion gases when firing with biomass is moved further down the combustion chamber, away from the burner end, while for the coal-fired cases the peak temperature is closer to the burner end and reaches a peak value 0.5 m away from the furnace top.

Table 6.4: Measurement data at Port 3 [174].

	Middelburg coal		Mixed wood	Sawdust
	non-preheated	preheated		
Temperature, K	1369	1398	1440	1412
CO, ppm	40	71	3	16
O_2, %	3.8	3.7	5.7	4.3

The measurements of the oxygen concentration at the axis of the combustion rig, presented in Figure 6.6, indicate how fast is the oxidation process of the coal, mixed wood and sawdust. It is observed that the oxygen is

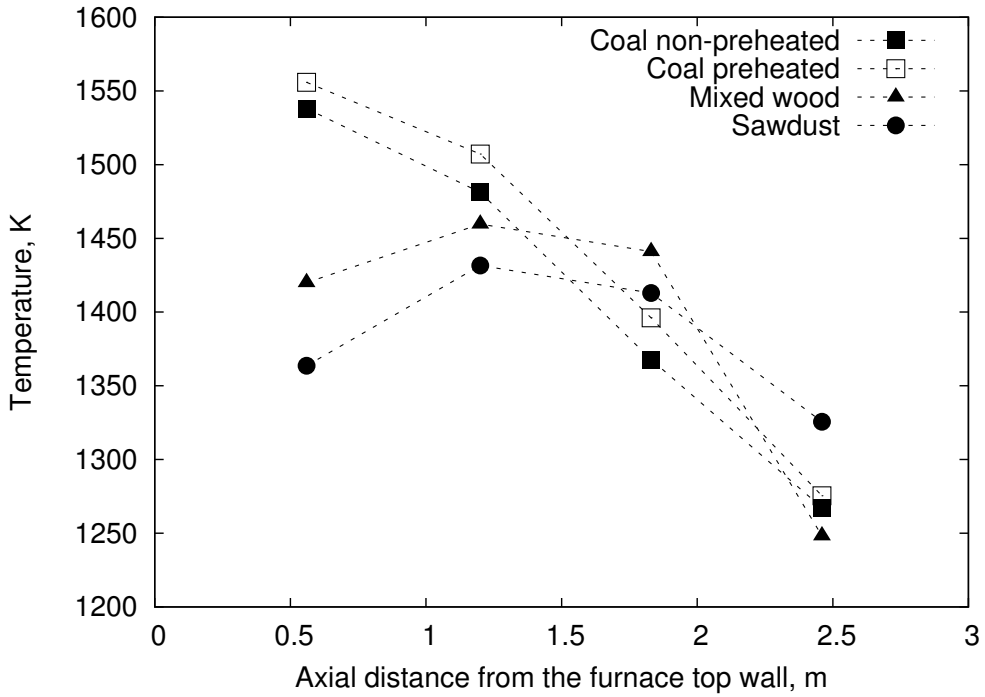

Figure 6.5: Temperature measurements taken along the furnace axis for the coal preheated and non-preheated cases and mixed wood and sawdust cases [174].

consumed the fastest in the coal preheated case. The highest oxygen concentration and therefore the slowest oxidation process has been found in the case of mixed wood combustion. Neither the mixed wood nor sawdust cases reaches complete combustion when leaving the radiation section, as the oxygen concentration at the Port 3 is 5.7% and 4.3% for mixed wood and sawdust, respectively. The measurements of the temperature and CO concentration are listed in Table 6.4.

6.2 Study on biomass emissions

In this section a theoretical study to asses the potential levels of emission from biomass combustion has been undertaken. The type of biomass has significant impact on the emissions level that are produced during its combustion. While there is the positive effect of biomass combustion in

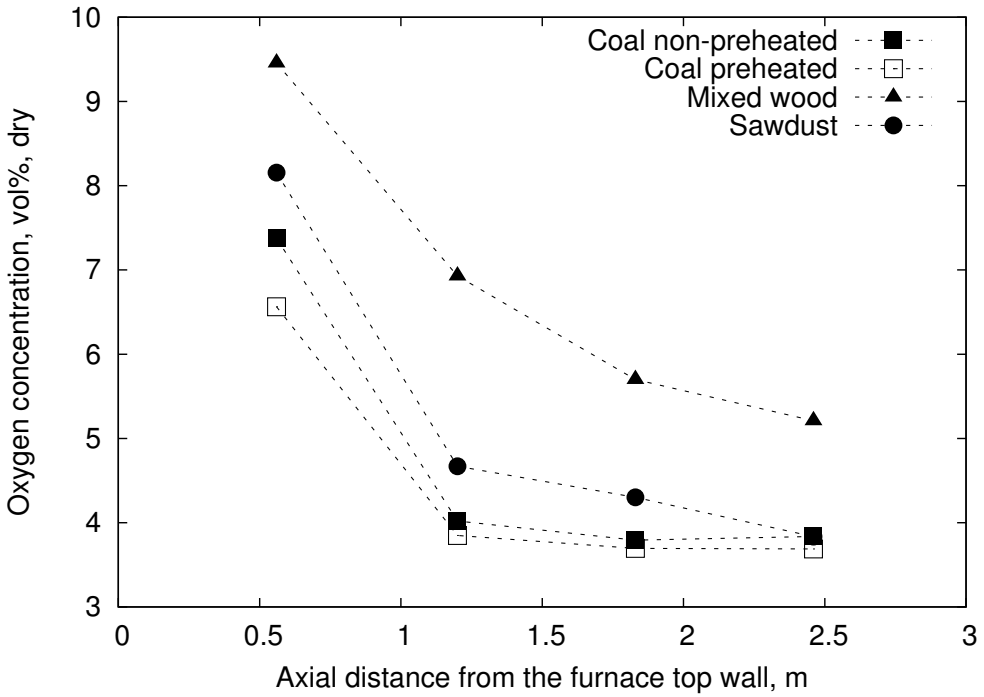

Figure 6.6: Oxygen concentration measurements taken along the furnace axis for the coal preheated and non-preheated cases and mixed wood and sawdust cases [174].

terms of CO_2 emissions, which was explained in Section 2.3.1, biomass combustion releases other pollutants, such as SO_x and NO_x. The concentrations of these pollutants is strictly regulated, therefore, it is important to control their emissions either by combustion control techniques or post-combustion technologies. To identify the emissions level of SO_x and NO_x for the biomass fuel, namely mixed wood, sawdust, fermentation residue and grain residue, the mass and energy balances for each fuel have been performed. Also, the biomass fuel has been compared with Middelburg coal and this is summarised in Table 6.6; the SO_x and NO_x values are given in ppm corrected to 6% exit O_2. The stoichiometry of combustion has been calculated for similar combustion conditions, namely the heat input at 15 kW and the excess air at 15% has been kept constant for each case. The composition of the compared fuels is listed in Table 6.1.

Table 6.5: Mass and energy balance of the 15 kW jet flame fired with coal, mixed wood, sawdust, fermentation and grain residue at λ = 1.15 with combustion air at temperature of 25°C.

	Middelburg coal	Mixed wood	Sawdust	Fermentation residue	Grain residue
Fuel mass flow rate, kg/h	2.13	3.18	3.12	3.80	3.65
Air mass flow rate, kg/h	20.92	20.31	20.78	21.50	21.17
Products of combustion, kg/h	22.84	23.43	23.89	25.03	24.59
Exit temperature, °C	1096	1167	1140	1115	1118
Adiabatic flame temperature, °C	2041	2004	1969	1861	1897
Exit O_2,wt.%	2.8	2.6	2.6	2.6	2.6
Exit N_2,wt.%	70.4	66.5	66.7	66.1	66.3
Exit CO_2,wt.%	22.7	23.1	22.8	22.4	22.0
Exit H_2O,wt.%	3.9	7.7	7.8	8.8	9.0
Exit SO_x, ppm	671	35	68	318	233
Exit NO_x, ppm	620	491	147	712	960

6.2.1 SO_x emissions

For the calculations of the SO_x emissions is has been assumed that all the all sulphur in the fuel is converted to SO_x. The comparison of SO_x emission levels for coal and different types of biomass fuel is depicted in Figure 6.7. The highest value of SO_x emissions come from coal combustion and this is due to highest coal sulphur content among other fuels. The biomass combustion reduces SO_x emissions, however, the level of reduction strongly depends on the type of biomass. The mixed wood and sawdust have the lowest fuel sulphur and in consequence the lowest predicted SO_x emissions among other fuels.

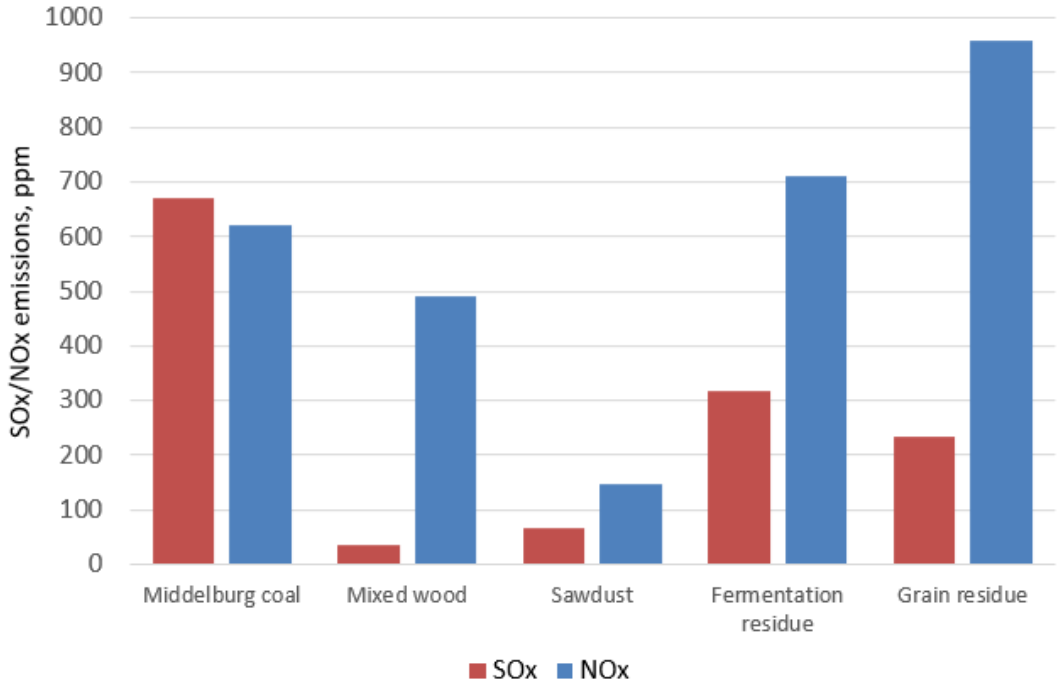

Figure 6.7: The SO_x and NO_x emissions comparison for Middelburg coal and biomass fuels: mixed wood, sawdust, fermentation and grain residue (at λ = 1.15, given on dry volumetric basis corrected to 6% exit O_2).

6.2.2 NO_x emissions

During the combustion process there are three different mechanisms for the formation of NO_x, namely thermal NO_x, fuel NO_x and prompt NO_x as introduced in Section 2.3.4. The fuel and thermal NO_x emissions calculations are described in next sections. For the purposes of this analysis it is assumed that in this situation the contribution from prompt NO_x is minimal and can be neglected. All the values are given on dry volumetric basis corrected to 6% exit O_2.

6.2.2.1 Fuel NO_x

If all fuel nitrogen is converted to NO_x then the NO_x emission is calculated to be 2366 ppm, 532 ppm, 18 ppm, 3681 ppm and 4857 ppm for coal, mixed wood, sawdust, fermentation residue and grain residue, respectively. However, only 17% of the fuel nitrogen of coal [174] was found to be converted to NO_x and it is predicted to be 402 ppm. About 60% of fuel nitrogen from the mixed wood and sawdust [174] is converted to NO_x, which gives 388 ppm and 11 ppm NO_x, respectively. About 18% of the fermentation residue and grain residue [174] fuel nitrogen is converted to NO_x, which contributes to 645 ppm and 874 ppm of NO_x, respectively. Similar to SO_x emissions, the fuel NO_x depends on the fraction of nitrogen in the fuel. Thus, depending of type of biomass, the fuel NO_x can either increase or decrease NO_x emissions in comparison to emissions that originate from coal combustion.

6.2.2.2 Thermal NO_x

Thermal NO_x is a function of the adiabatic flame temperature and excess air. For the air combustion of coal and biomass fuels at 15% excess air, the adiabatic flame temperature calculated based on the energy balance is 2041°C, 2004°C, 1969°C, 1861°C and 1897°C for coal, mixed wood, sawdust, fermentation residue and grain residue, respect-

ively. Based on these temperatures, the thermal NO_x was calculated [194] and prediction are listed in Table 6.6. It has to be outlined that the adiabatic flame temperature used for calculation of thermal NO_x is much higher than the average temperature in the combustion chamber. Therefore, the predicted thermal NO_x emissions are considered as the worst-case scenario.

6.2.2.3 Total NO_x

Adding the thermal and fuel NO_x emissions gives a total value of 620 ppm, 491 ppm, 147 ppm, 712 ppm and 960 ppm for coal, mixed wood, sawdust, fermentation residue and grain residue, respectively. The comparison of NO_x emission for coal and different types of biomass fuel is depicted in Figure 6.7. It can be concluded that sawdust has the lowest predictions of NO_x emissions, whereas the fermentation and grain residues have the highest values, mainly because of the contribution of fuel NO_x for these types of biomass fuel. Therefore, there is a potential of NO_x emissions reduction while displacing coal with biomass. However, this depends on the type of biomass being used. The woody biomass has the benefit of lowering the NO_x emissions among other biomass fuels compared in this study.

Theoretical values of NO_x emissions compared with the experimental data are overpredicted by about 25%, however are in line with all of the considered fuels. This is because the measured values of NO_x are already reduced by air-staging, which is not included in baseline theoretical calculations, which give the value of the highest possible NO_x emissions.

Table 6.6: NO_x emissions originated from coal, mixed wood, sawdust, fermentation residue and grain residue combustion (at λ = 1.15, given on dry volumetric basis corrected to 6% exit O_2).

	Middelburg coal	Mixed wood	Sawdust	Fermentation residue	Grain residue
Measured NO_x	603	454	130	593	1024
Fuel-N conversion to NO_x, %	17	60	60	18	18
Fuel NO_x	580	461	130	812	1098
Thermal NO_x	173	136	109	54	68
Total NO_x	753	597	179	866	1166

6.2.3 Emissions reduction

Wet or dry scrubbers are capable of removing up to 95% [195, 196] of SO_x, resulting in an emissions level of 34 ppm, 2 ppm, 3 ppm, 16 ppm and 12 ppm for coal, mixed wood, sawdust, fermentation residue and grain residue, respectively.

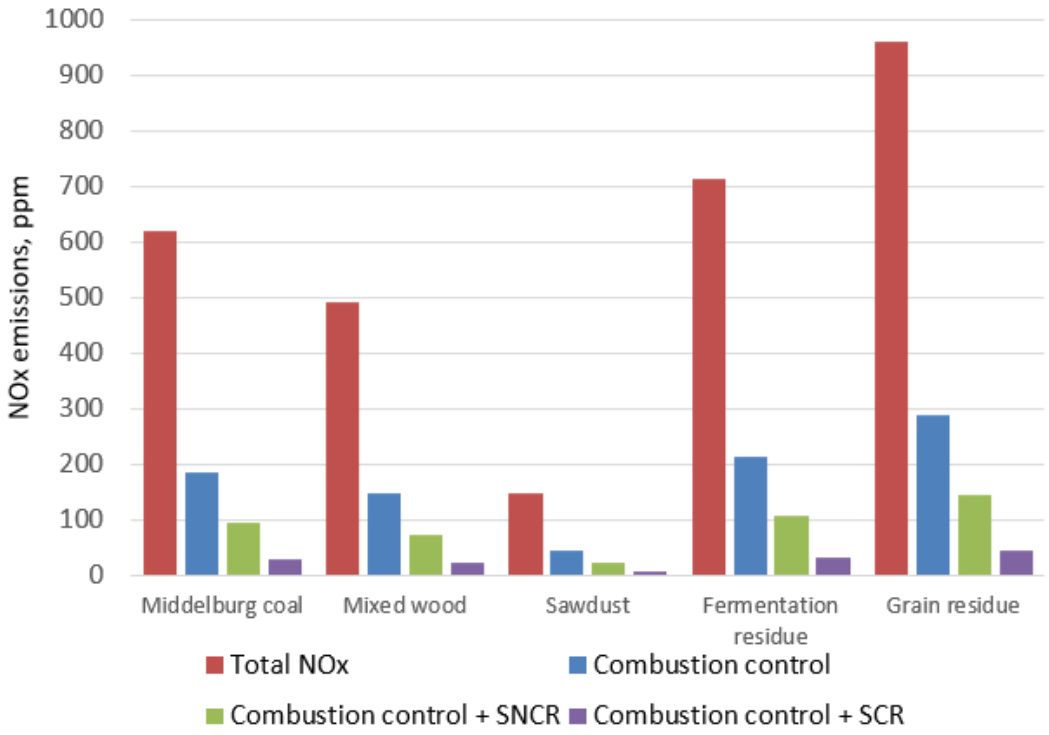

Figure 6.8: The impact of the NO_x combustion control reduction techniques and SNCR/SCR technologies on the NO_x emissions for coal and biomass fuels (at λ = 1.15, given on dry volumetric basis corrected to 6% exit O_2).

Application of the combustion control techniques for NO_x emissions reduction, namely air staging, fuel staging, recycling of the flue gas, and water injection, described in Section 2.3.4, can reduce the NO_x emissions by up to 70% [197], resulting in the estimated value of 186 ppm, 147 ppm, 44 ppm, 214 ppm and 288 ppm of total NO_x emissions for coal, mixed wood, sawdust, fermentation residue and grain residue, re-

spectively. There are two possible post-combustion technologies that can be applied for further removal of NO_x from the flue gases, namely SNCR and SCR with efficiency of about 50% and 85% [198], respectively. The technology that is currently being used in industry is SNCR due to its lower cost [199]. The impact of the NO_x combustion control reduction techniques and SNCR/SCR technologies on the NO_x emissions for coal and different types of biomass fuel is presented in Figure 6.8. The SCNR technology can reduce the NO_x emissions for coal, mixed wood, sawdust, fermentation residue and grain residue to 93 ppm, 74 ppm, 22 ppm, 107 ppm and 144 ppm, respectively. Whereas, implementation of the SCR technology can result in emissions of NO_x at level of 28 ppm, 22 ppm, 7 ppm, 32 ppm and 43 ppm for coal, mixed wood, sawdust, fermentation residue and grain residue, respectively.

6.3 Numerical approach

Both the geometry and the computational grid of the 15 kW furnace are generated using the ANSYS ICEM CFD version 15.0. The mesh has been implemented in the commercial CFD software ANSYS Fluent version 15.0, where the numerical calculations were performed.

6.3.1 Computational grid

The computational mesh includes the burner and a 2.5 m long radiative section of the furnace. Taking the advantage of the geometrical symmetry of the burner and the furnace, only one quarter of the geometry is modelled and periodic symmetry is assumed on the furnace axis boundary. The symmetry of the burner, its simple design and no-swirl flame allowed for the construction of a two-dimensional axisymmetric model of the rig in order to reduce the computational cost.

The mesh resolution is increased in the burner, near-burner region and

in the region where the combustion process takes place, which is between Port 2 and Port 3 in the radiative section of the furnace, and gradually increases in size away from the flame, which is visible in Figure 6.9. The computational grid uses a fully structured hexahedral meshing scheme.

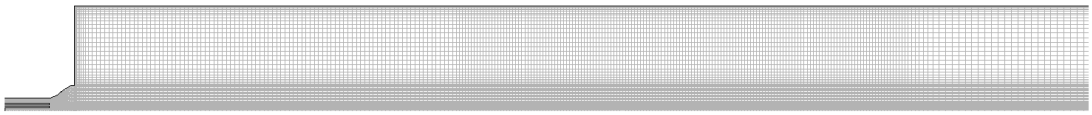

Figure 6.9: Computational mesh of the furnace with the increased number of elements in the near-burner region and combustion zone.

6.3.2 Grid independence study

A grid independence study has been performed for three alternative meshes, consisting of: 9,000 cells (coarse), 36,000 cells (medium) and 250,000 cells (fine). Predictions of the axial temperature and the dry oxygen concentration of the combustion gas were used as an assessment criteria. Further, the temperature profiles, dry oxygen concentration and axial component of the velocity were compared along the four traverses are depicted in Figure 6.10.

In Figures 6.11(a) and 6.11(b) a comparison of the prediction of the axial temperature and the dry oxygen concentration along the furnace axis for the meshes taken into consideration during the grid independence study is presented, respectively. A comparison of the axial velocity, the dry oxygen concentration and the temperature profiles along the four traverses is depicted in Figures 6.12, 6.13 and 6.14, respectively.

It can be observed that the coarse, medium and fine mesh produce similar results on the axis of the furnace, as the prediction of the temperature profiles and the dry oxygen concentration along the furnace axis are overlapped for the 9,000, 36,000 and 250,000 cells mesh. However, dif-

Figure 6.10: Schematic of the location of the four traverses taken for comparison of the profiles of temperature, oxygen concentration and axial component of the velocity at the distance of 0.1, 0.2, 0.35 and 0.6 m away from the furnace top wall.

ferences can be observed on the traverses, especially those further away from the burner. The temperature profile along the traverse 3, near the axis of the furnace (Figure 6.12(c)), and the traverse 4, near the wall of the furnace (Figure 6.12(d)) have slightly different profiles between the coarse mesh and the medium mesh. However, on further refinement of the mesh the predicted profile is similar to that for the medium mesh. Similar situations can be observed in the dry oxygen concentration profiles along the traverse 3 in Figure 6.13(c)), where the medium mesh and the fine mesh profiles overlap. Table 6.7 shows the numerical predictions compared with the experimental measurements at Port 3 for the coarse, medium and fine meshes. It can be observed that there is an imperceptible difference between those results for the three meshes. The numerical predictions of gas temperatures and oxygen concentrations at the Port 3 for each mesh match well the experimental data. Further, the CFD predictions of CO are best predicted by the fine mesh. Therefore, since the medium and the fine mesh produce very similar results, the medium mesh with 36,000 elements has been chosen for further studies in order to reduce the computational time and cost. The minimum grid length of this mesh is 0.6 mm in the near-burner and flame region, and up to 40.4 mm in the far field. The maximum aspect ratio is 43.3 and minimum orthogonality is 0.8.

6.3.3 Numerical set-up of the combustion process

The CFD model is formulated using an Eulerian-Lagrange frame of reference. The continuous gas phase combustion was modelled with the Eulerian frame of reference, whereas the fuel particles motion and combustion of the solid fuel particles were tracked in a Lagrangian frame of reference. The constant exchange of momentum, heat and mass transfer between the phases were accounted for by using source/sink terms in the

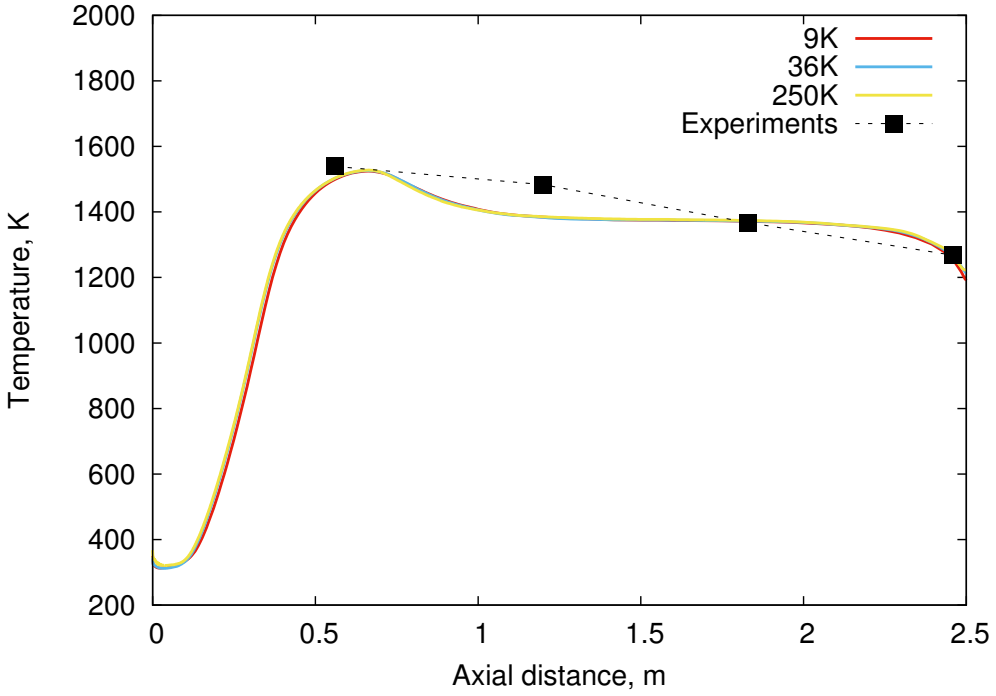

(a)

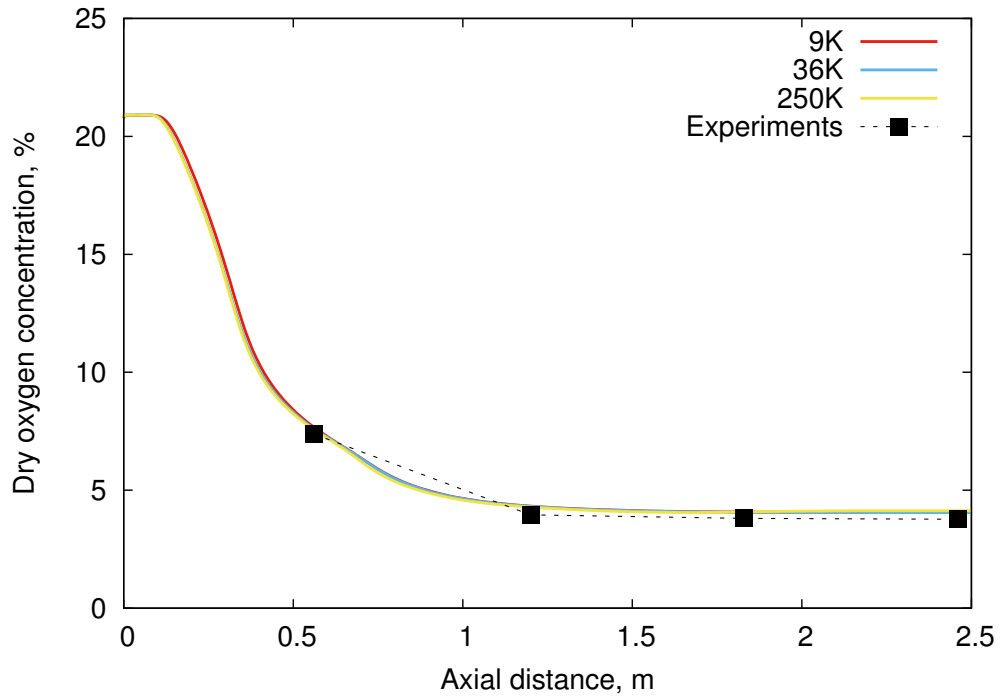

(b)

Figure 6.11: (a) The axial temperature profile and (b) the axial dry oxygen concentration of the combustion gas for 9,000, 36,000 and 250,000 elements mesh.

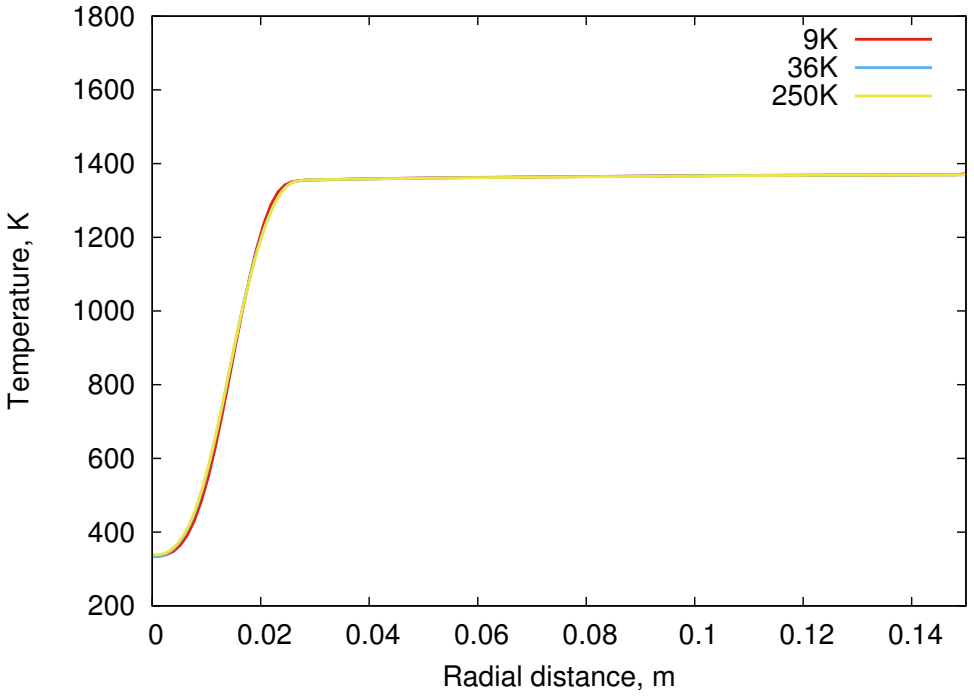
9K
36K
250K
Temperature, K
Radial distance, m
1800
1600
1400
1200
1000
800
600
400
200
0
0.02
0.04
0.06
0.08
0.1
0.12
0.14

(a)

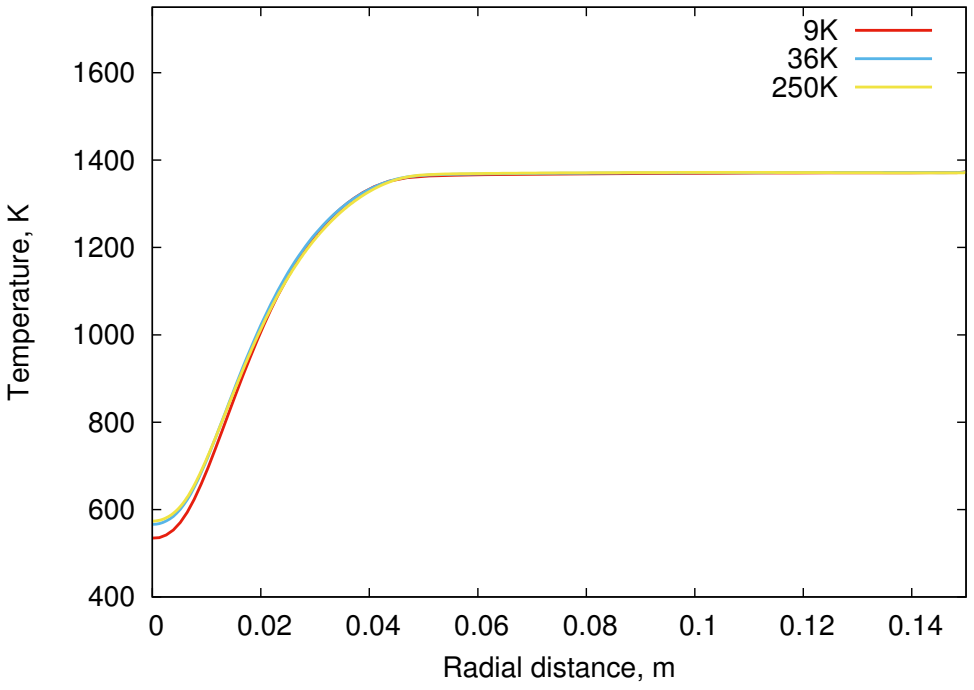
9K
36K
250K
Temperature, K
Radial distance, m
1600
1400
1200
1000
800
600
400
0
0.02
0.04
0.06
0.08
0.1
0.12
0.14

(b)

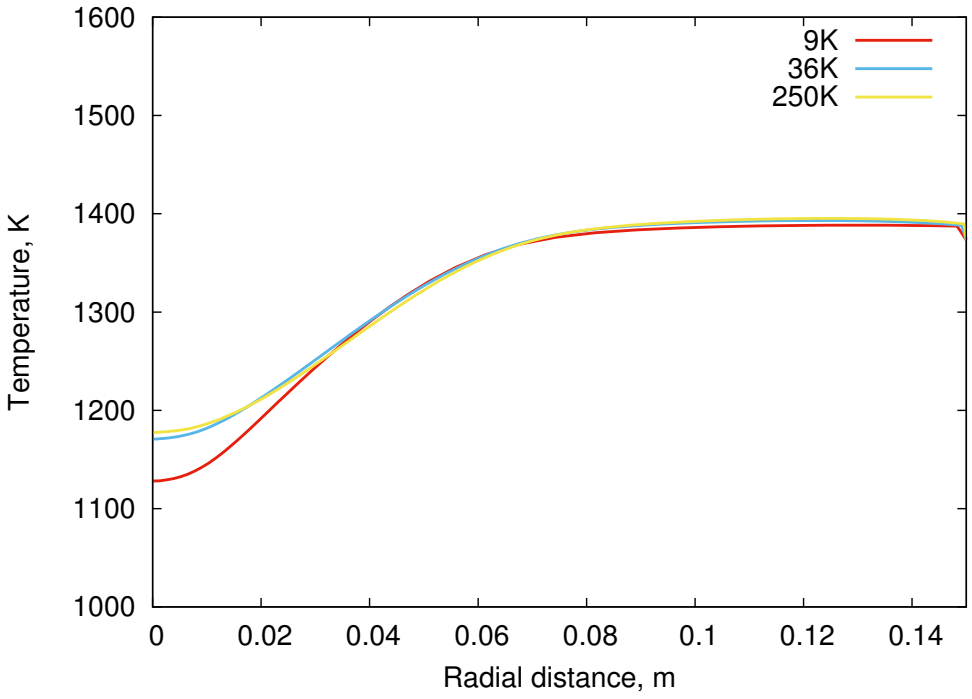

(c)

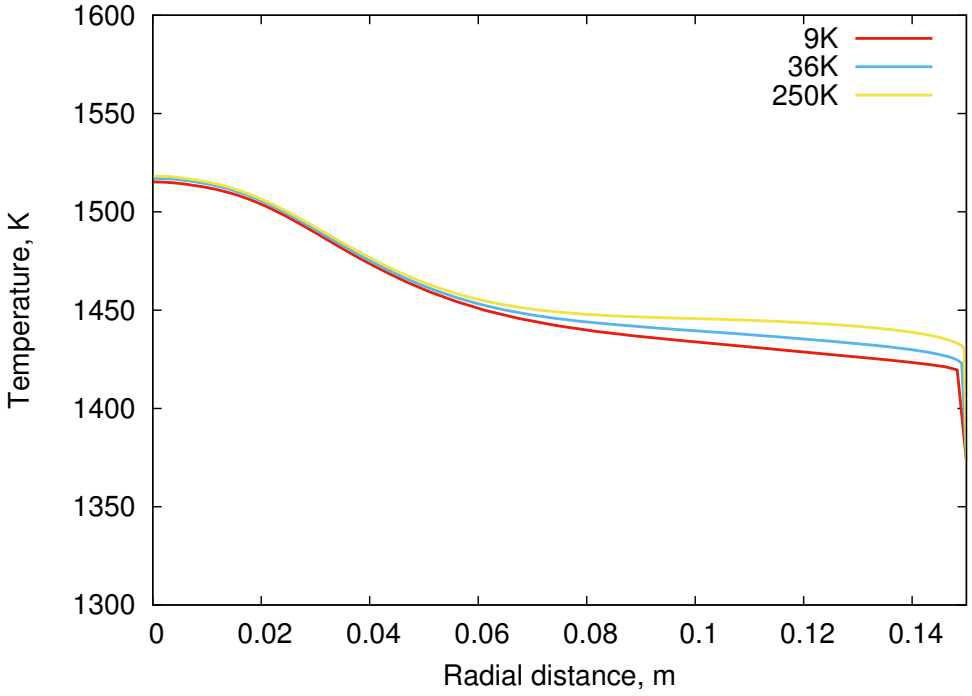

(d)

Figure 6.12: Temperature profiles along (a) traverse 1, (b) traverse 2, (c) traverse 3 and (d) traverse 4 for the three meshes.

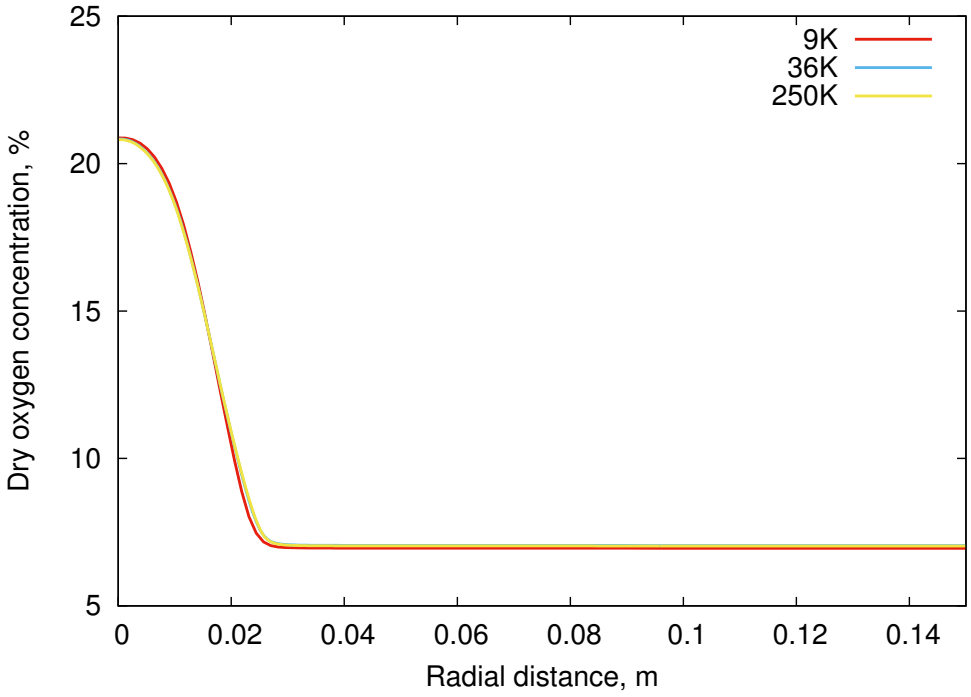
Dry oxygen concentration, %
Radial distance, m
9K
36K
250K
25
20
15
10
5
0
0.02
0.04
0.06
0.08
0.1
0.12
0.14

(a)

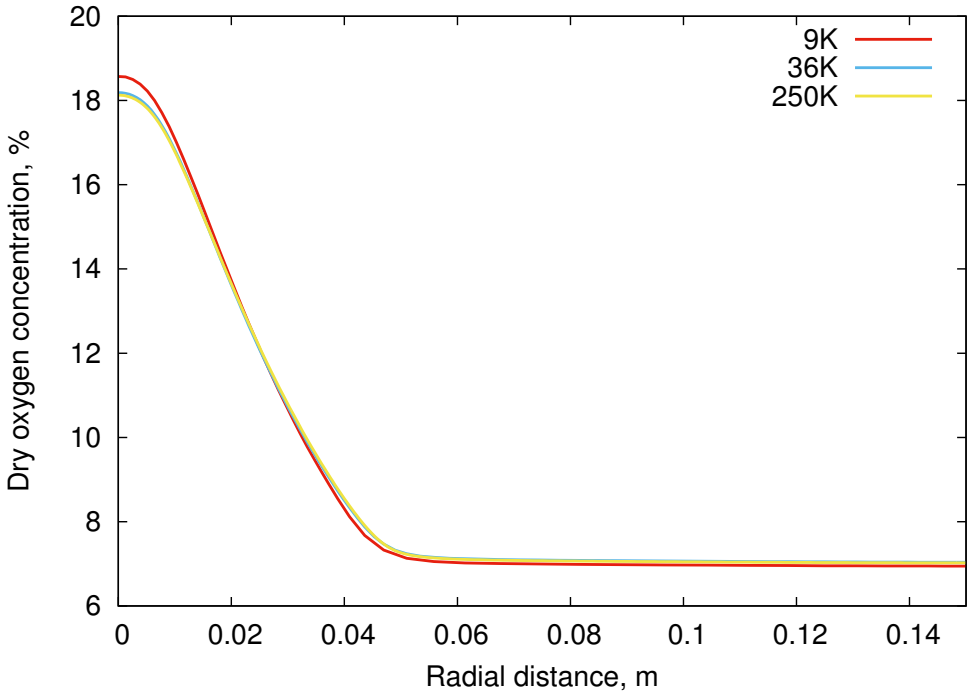
Dry oxygen concentration, %
Radial distance, m
9K
36K
250K
20
18
16
14
12
10
8
6
0
0.02
0.04
0.06
0.08
0.1
0.12
0.14

(b)

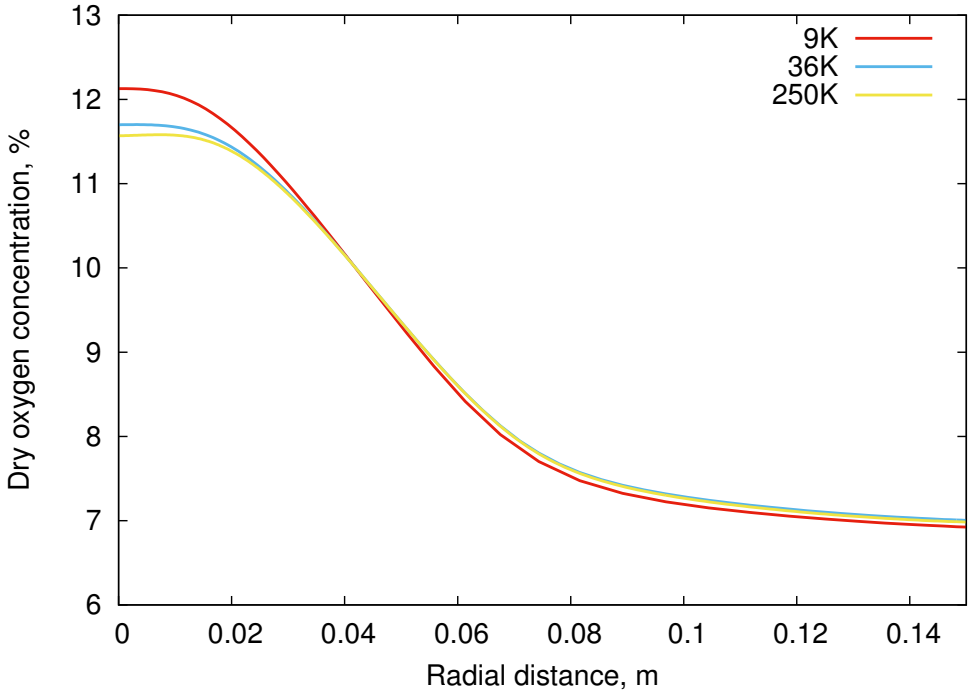

(c)

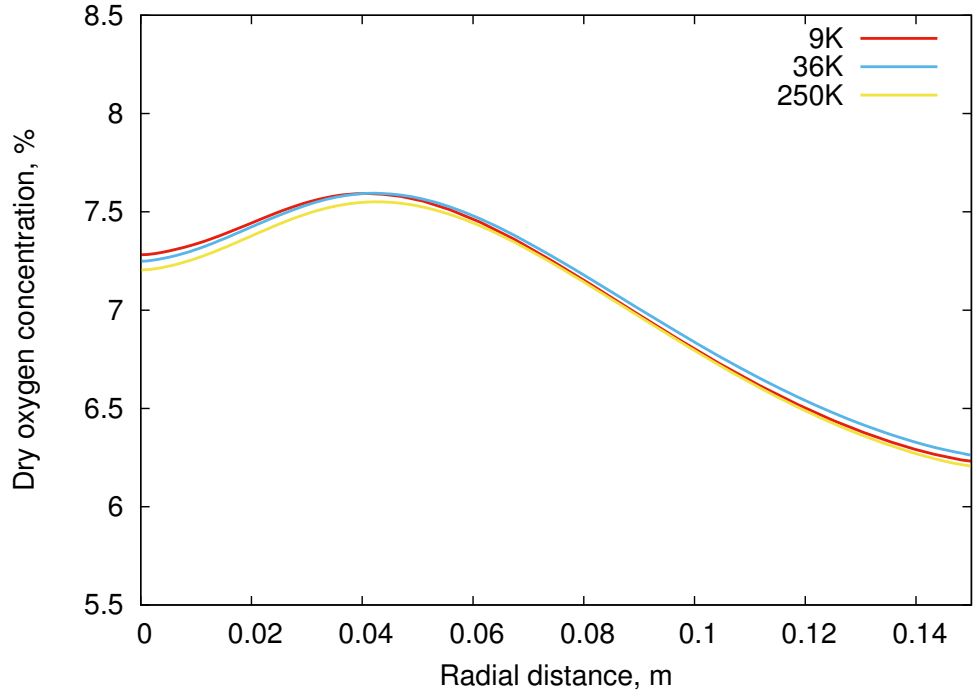

(d)

Figure 6.13: Dry oxygen concentration along (a) traverse 1, (b) traverse 2, (c) traverse 3 and (d) traverse 4 for the three meshes.

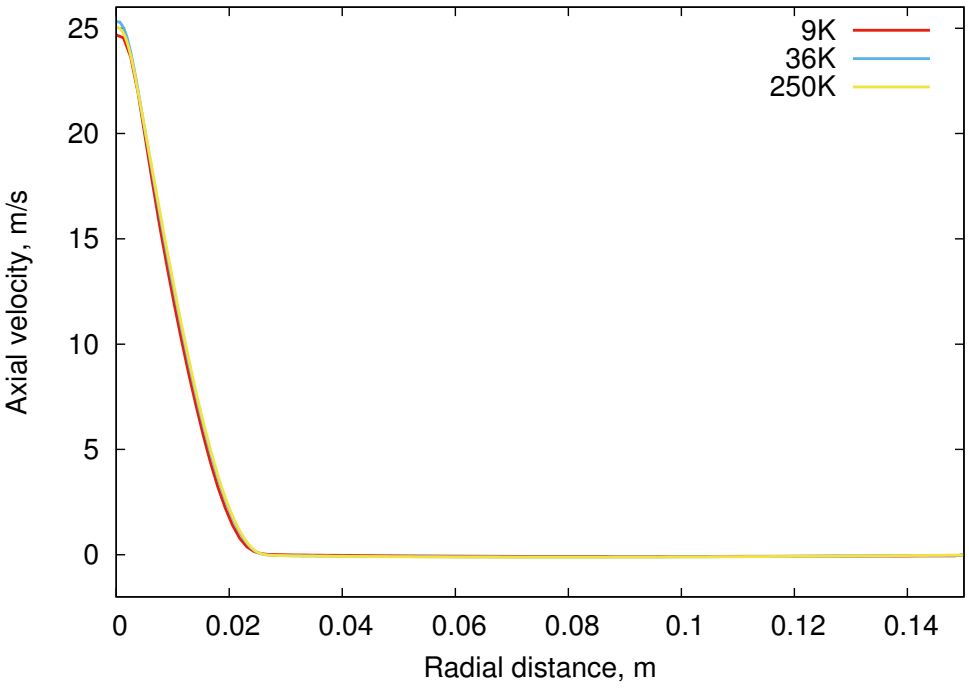
9K
36K
250K
Axial velocity, m/s
Radial distance, m
25
20
15
10
5
0
0
0.02
0.04
0.06
0.08
0.1
0.12
0.14

(a)

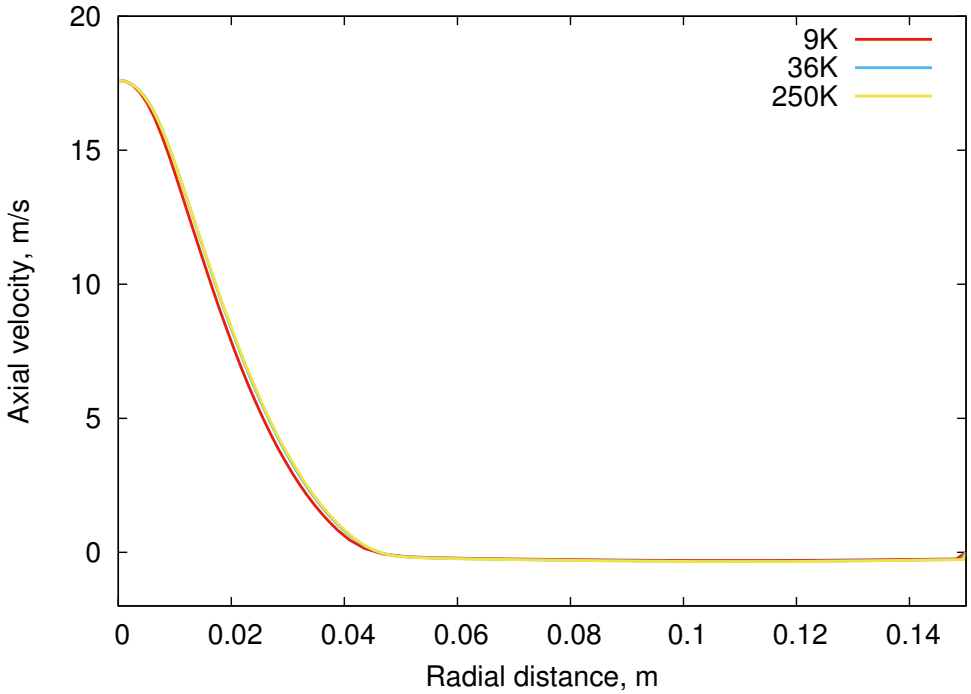
9K
36K
250K
Axial velocity, m/s
Radial distance, m
20
15
10
5
0
0
0.02
0.04
0.06
0.08
0.1
0.12
0.14

(b)

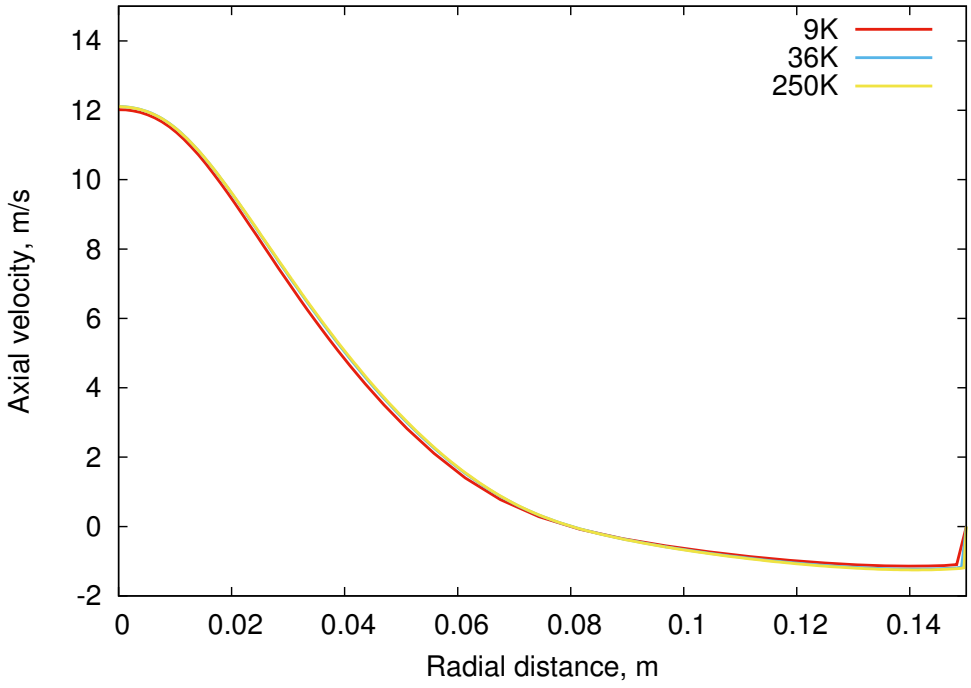

(c)

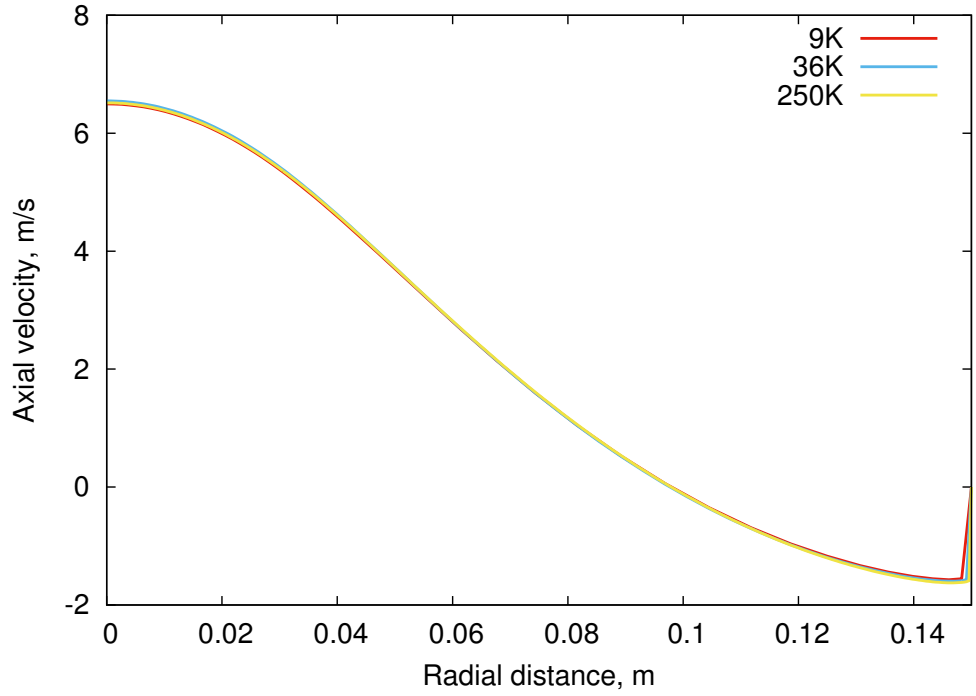

(d)

Figure 6.14: Axial velocity along (a) traverse 1, (b) traverse 2, (c) traverse 3 and (d) traverse 4 for the three meshes.

Table 6.7: Comparison of experimental data and CFD predictions for different computational grids, namely 9,000, 36,000 and 250,000 elements mesh - temperature, CO and dry oxygen concentration at the Port 3.

	Experimental data	CFD		
		9K	36K	250K
Temperature, K	1369	1371	1372	1374
CO, ppm	40	64	65	43
O_2, %	3.8	4.1	4.1	4.1

governing equations for the gas phase and the solid particles. Stochastic particle tracking was carried out by the discrete random walk model, and the particles of pulverised solid fuel were assumed to be spherical in shape.

The steady-state Reynolds-averaged Navier-Stokes (RANS) approach was applied. Because of the jet no-swirl flame, the Realizable k-ε model has been used for turbulence closure, since this turbulence model is considered to provide a good numerical prediction without excessive computational cost. The influence of the walls was simulated with a scalable wall function in order to further relax the cell count requirements.

Since only the radiation section of the furnace is modelled, the dominant form of heat transfer in this part of the combustion chamber is radiation and it was modelled using the Discrete Ordinates (DO) model with the three directions (3 x 3) to discretize each octant of the angular space. The gas radiative properties of the combustion gases were calculated using the Weighed Sum of Gray Gas (WSGG) Model, which was found to successfully predict the coal air combustion cases [43].

The particle temperature is evaluated using the heat balance equation [147]:

$$m_p c_p \frac{dT_p}{dt} = hA_p \left(T_\infty - T_p\right) + \varepsilon_p A_p \sigma \left({\theta_R}^4 - {T_p}^4\right) - f\frac{dm_p}{dt} H_r \qquad (6.2)$$

where:

m_p – mass of the particle,

c_p – specific heat of the particle,

T_p – temperature of the particle,

ε_p – emissivity of the particle,

T_∞ – gas temperature,

θ_R – radiation temperature,

H_r – the heat of reaction released by the surface reaction,

f – the fraction of heat absorbed by the particle,

h – the heat transfer coefficient based on a spherical shaped particle.

A two-step reaction mechanism was used for the volumetric reactions of the devolatilization process and the Eddy-Dissipation model was used to account for the turbulence-chemistry interaction. The homogeneous reactions of the volatile matter are followed by the heterogeneous char combustion reactions [182]:

$$\text{Volatiles} + \text{O}_2 = \text{CO} + \text{H}_2\text{O} \tag{6.3}$$

$$\text{CO} + 0.5\text{O}_2 = \text{CO}_2 \tag{6.4}$$

$$\text{C(char)} + 0.5\text{O}_2 = \text{CO} \tag{6.5}$$

$$\text{CO} + 0.5\text{O}_2 = \text{CO}_2 \tag{6.6}$$

The methodology used to describe the combustion of coal and biomass particles has been presented [43] (coal) and in [98, 99, 105] (biomass).

6.3.3.1 Boundary conditions

As a boundary condition, the temperature of the wall of the radiation section has been used and has been kept at the constant value of 1373 K. The wall emissivity was assumed to be 0.8 based on a previous study [43]. Further, the burner walls, quarl and top wall of the furnace were set to be

adiabatic following the assumption of negligible impact of the heat transfer within the burner on the combustion process. The mass flow inlets were used for the fuel and air flows entering the combustion chamber. The flue gas leaving the furnaces was set using the pressure outlet boundary conditions.

6.3.4 Coal combustion

The coal volatile matter combustion was modelled with a two-step reaction mechanism. The Single-Rate Model [153] was used for the devolatilization of the coal particle, where the volatile release depends on the history of the particle temperature. For the char combustion process, the Intrinsic Model developed by Smith [107] was used based on the sensitivity study in Chapter 5. The choice of the sub-models used for the coal combustion simulation has been investigated in the previous chapter. The parameters employed for the devolatilization and char combustion for Middelburg coal are listed in Table 6.8.

6.3.5 Biomass combustion

As mentioned in the previous section, two types of biomass are analysed in this chapter, namely mixed wood and sawdust. Since the biomass combustion models are not fully developed in commercial CFD codes, the evaluation of the models used for the coal simulations were used for the biomass numerical predictions. The models for coal combustion were validated with the experimental measurements in the previous chapter. For the modelling of the biomass combustion, many sub-models and parameters were kept in line with the coal combustion cases with known properties characteristic of the analysed biomasses, such as density, devolatilization rates and specific heat.

The devolatilization of the biomass fuel is modelled with a single-rate model [153], where the kinetic values for the Arrhenius equation, namely

the pre-exponential factor (A), and activation energy (E) for wood and sawdust were based on the literature [82, 99] and $A = 6.0 \cdot 10^{13}$ 1/s and $E = 2.5 \cdot 10^{8}$ J/kmol, respectively.

Biomass char combustion was modelled in a similar way to that of coal combustion using the Intrinsic model [107]. However, to account for the higher reactivity rates of the biomass char compared to coal char, the reaction rate was increased by a factor of 4 based on the literature [99].

The list of chemical and thermophysical properties employed in the CFD model for the biomass, namely mixed wood and sawdust is summarized in Table 6.8.

6.4 Results

6.4.1 Coal combustion

It was found that the CFD predictions for the coal combustion have a good agreement with the experimental data, as presented in Figure 6.15 for the coal non-preheated case and in Figure 6.16 for the coal preheated case. The CFD predictions of the axial temperature profile of the combustion gases and comparison against the experimental data for the coal non-preheated case and the coal preheated case can be found in Figures 6.15 and 6.16, respectively.

The coal non-preheated and preheated cases and their numerical results fit well with the experimental data, hence it can be assumed that the models describing coal combustion are accurate and predict the coal combustion process well. The axial temperature at the Port 2, at the distance of 1.2 m away from the burner, is slightly underpredicted. However, it should to be taken into account that the suction pyrometry method used in the coal and biomass experiments in these investigations measures the

Table 6.8: Chemical and thermophysical properties of Middelburg coal, mixed wood and sawdust.

	Middelburg coal	Mixed wood	Sawdust
Devolatilization - single-rate model			
Pre-exponential factor A, 1/s	$3.8 \cdot 10^{14}$	$6.0 \cdot 10^{13}$	$6.0 \cdot 10^{13}$
Activation energy E, J/kmol	$2.3 \cdot 10^{8}$	$2.5 \cdot 10^{8}$	$2.5 \cdot 10^{8}$
Char burnout - intrinsic model			
Pre-exponential factor A, 1/s	0.030198	0.120792	0.120792
Thermophysical properties			
Char yield predicted	40.80	9.26	9.26
Volatiles predicted	48.6	88.9	88.9
Thermal conductivity, W/mK	0.0454	0.1200	0.1200
Density, kg/m^3	1400	500	500
Specific heat, J/kgK	1680	1670	1670
Emissivity	0.9	0.9	0.9
Porosity	0.5	0.5	0.5
Ignition temperature, K	700	500	500

average temperature for the volume of the fluid and the experimental data have ± 25 K accuracy, whereas the ANSYS Fluent result gives a value at a specific point of the domain.

The comparison of the experimental data and numerical predictions for the coal non-preheated and preheated case at Port 3 is listed in Tables 6.9 and 6.10, respectively. Numerical predictions of the gas temperature at Port 3 matches well with the experimental measurements for both coal cases with and without preheat. The dry oxygen concentration at Port 3 in both coal cases is overpredicted by 10%, which indicated that the oxidation consumption is slightly underestimated in the CFD model. Further, the CO concentration in the gas at Port 3 is overpredicted for the coal preheated and non-preheated cases, which is a result of incomplete combustion due to the slow oxidation rates. However, there is a slight discrepancy between the numerical predictions and experimental data, although the predicted values are within the experimental measurements accuracy.

Table 6.9: Comparison of the numerical predictions with the experimental data for the Port 3 for the coal non-preheated case.

	Experimental data	CFD
Temperature, K	1369	1371
CO, ppm	40	179
O_2, %	3.8	4.2

Both the temperature profile along the axis and the oxygen composition along the furnace axis fits within the measurement data, which illustrates that the sub-models used for the CFD modelling have been used

Table 6.10: Comparison of the numerical predictions with the experimental data for the Port 3 for coal preheated case.

	Experimental data	CFD
Temperature, K	1398	1371
CO, ppm	71	180
O_2, %	3.7	4.2

correctly and accurately describe the coal combustion process for the analysed combustion chamber.

In Figures 6.17(a) and 6.17(b), the temperature contours of the combustion gas are depicted for the coal non-preheated and preheated cases, respectively. The dry oxygen concentration contours for the coal non-preheated are presented in Figure 6.18(a) and for the coal preheated case in Figure 6.18(b). The contours of the temperature and dry oxygen concentration of the combustion gas in the furnace for the coal non-preheated case and coal preheated case are similar to the difference in the preheated case. The secondary oxidizer is preheated and this introduces a higher temperature in the combustion chamber which enhances the combustion process. Therefore, the high temperature region is closer to the burner in the case of the preheated secondary oxidizer and thus a slightly faster oxygen consumption can be noticed in the near-burner region for the coal preheated case.

6.4.1.1 Effect of the radiation - WSGG and FSCK models

This sensitivity study investigates the radiation behaviours when employing refined radiative property models, using the full-spectrum correlated FSCK model compared with the conventional use of the weighted sum of grey gases (WSGG) model and the constant values of the particle radiation properties. The impact of using the non-grey radiation model of gases through the FSCK on coal combustion cases has been investigated

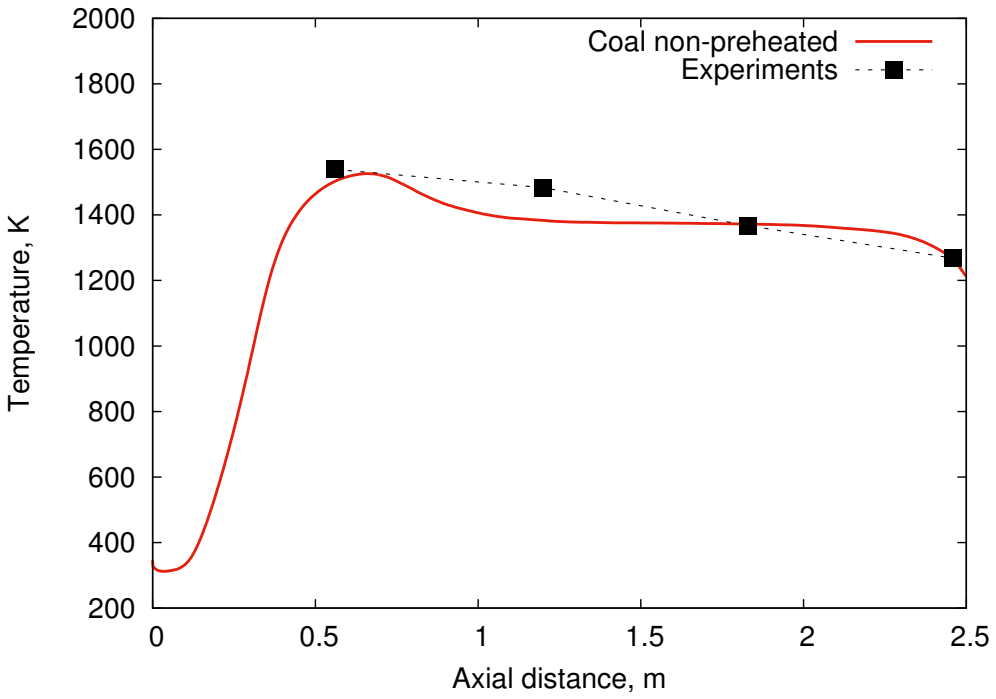

(a)

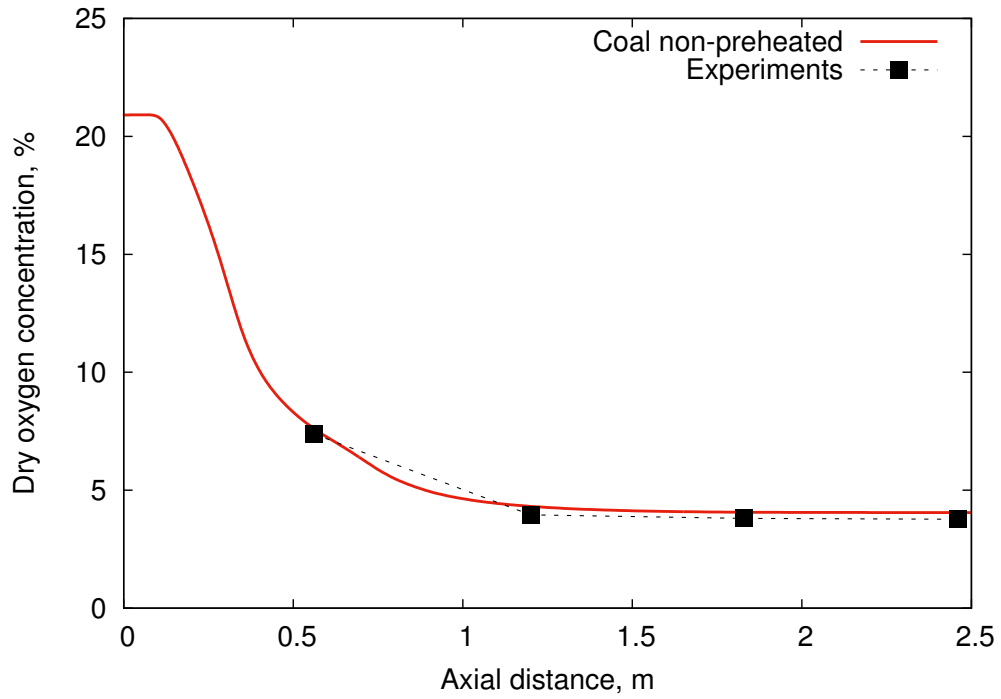

(b)

Figure 6.15: (a) Temperature profile and (b) dry oxygen concentration of the combustion gas along the furnace axis compared against experimental data for the Middelburg coal non-preheated case.

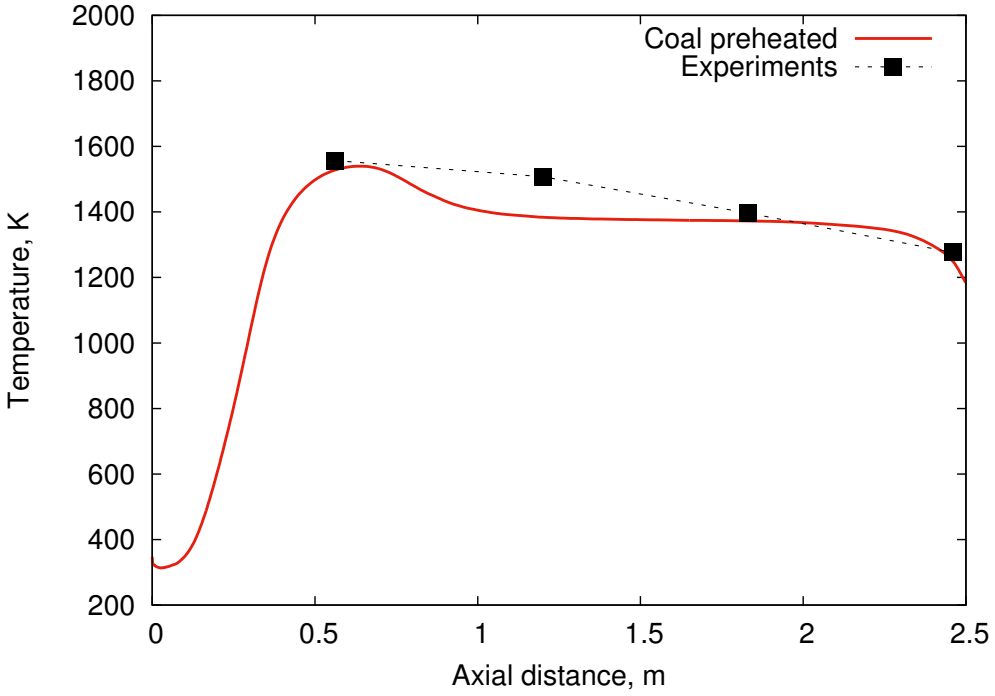

(a)

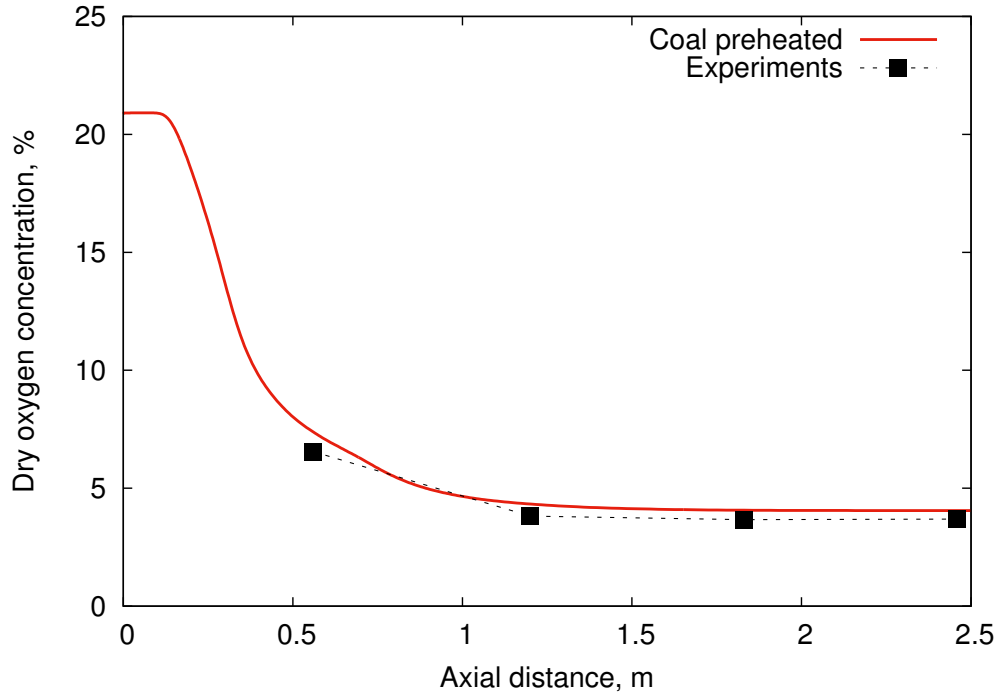

(b)

Figure 6.16: (a) Temperature profile and (b) dry oxygen concentration of the combustion gas along the furnace axis compared agaist experimental data for the Middelburg coal preheated case.

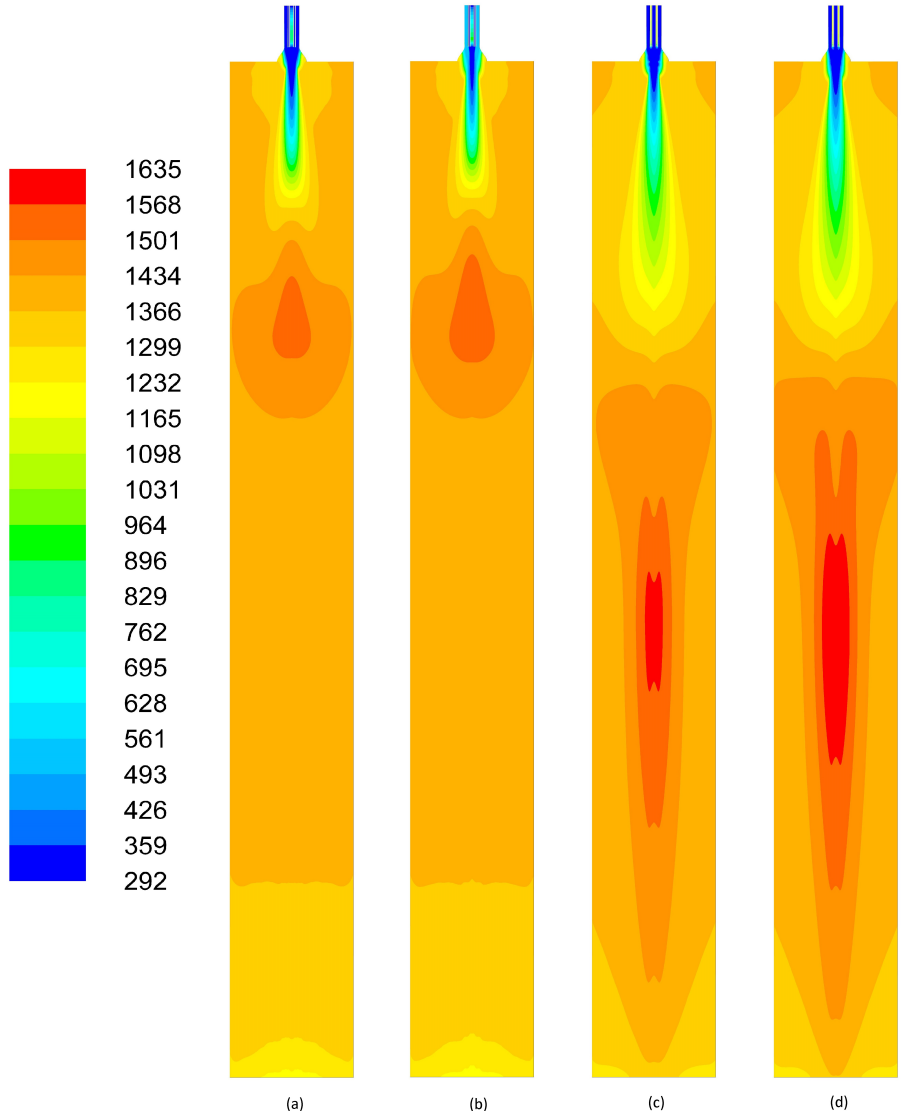

Figure 6.17: (a) Temperature contours of the combustion gas for the coal non-preheated case, (b) coal preheated case , (c) mixed wood and (d) sawdust.

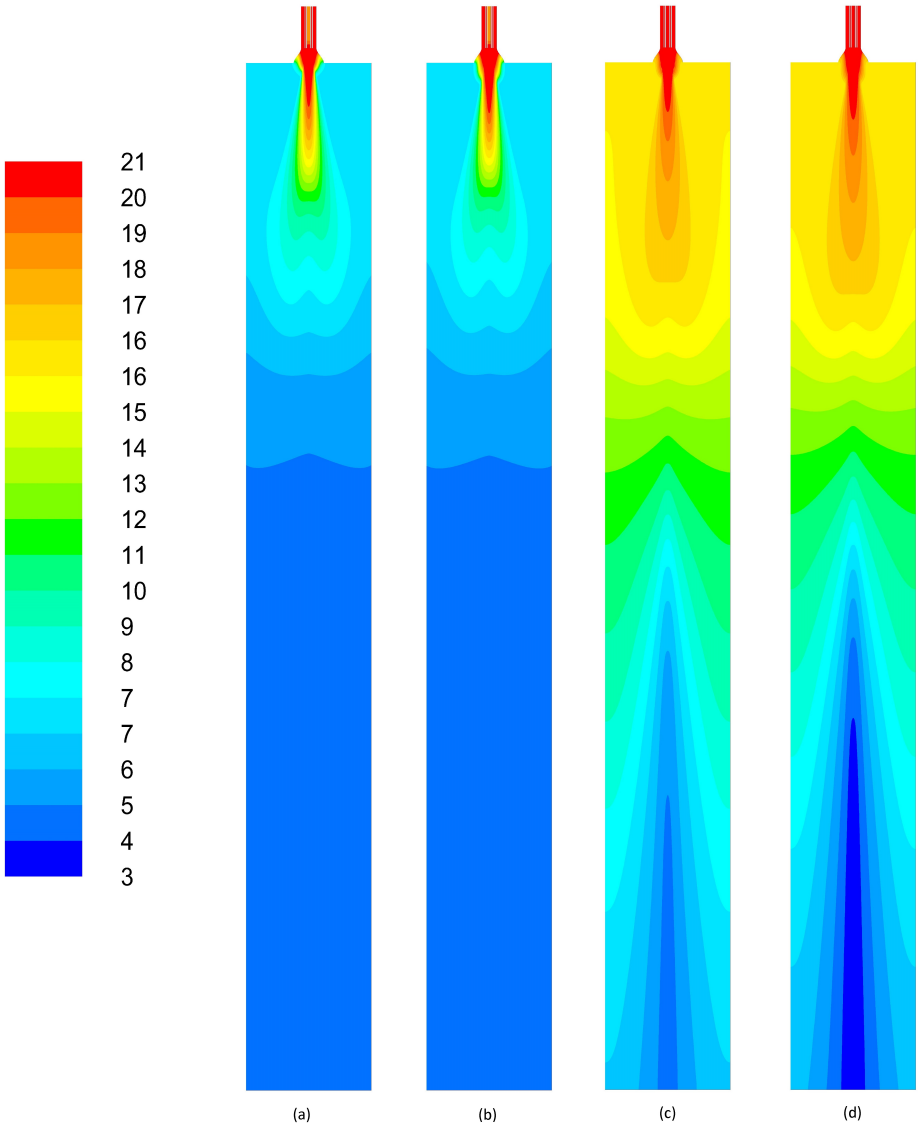

Figure 6.18: (a) Dry oxygen concentration contours of the combustion gas for the coal non-preheated case, (b) coal preheated case, (c) mixed wood and (d) sawdust.

in this section.

Figure 6.19 shows the temperature of the combustion gases on the furnace axis and oxygen concentration along the burner axis and these results have been compared for two radiation properties models, namely the WSGG and FSCK models for coal non-preheated gas. Similar comparisons for the coal preheated case can be found in Figure 6.20. In both cases the numerical results for the WSSG and FSCK models are predicting well the experimental data. Moreover, significant difference between models used for predictions have not been noticed.

The comparison of the CFD results when using the WSGG and FSCK models and experimental data at Port 3 for the coal non-preheated case and coal preheated case can be found in Table 6.11 and in Table 6.12, respectively. In general the results match well with the experimental data and there are no significant differences in the results when using the WSGG and FSCK models. The significant difference between the WSGG and FSCK models is expected in oxy-fuel combustion cases, since the combustion gas composition is different than during the air combustion.

Table 6.11: Comparison of the numerical predictions when using the the WSSG and FSCK models with the experimental data at the Port 3 for the coal non-preheated case.

	Experimental data	CFD	
		WSGG	FSCK
Temperature, K	1369	1371	1372
CO, ppm	40	179	178
O_2, %	3.8	4.2	4.2

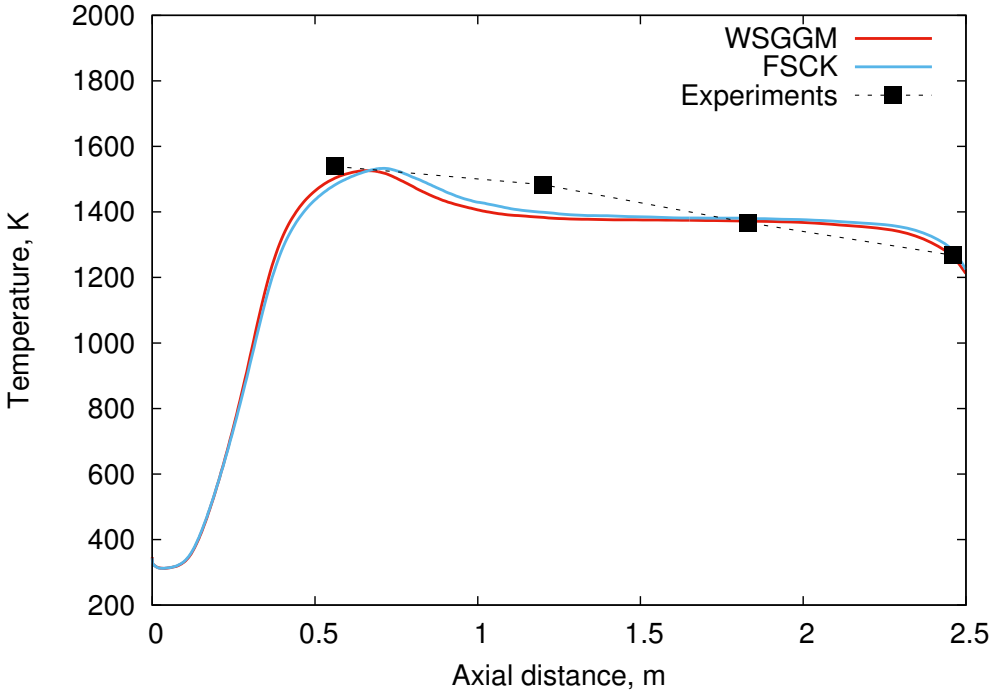

(a)

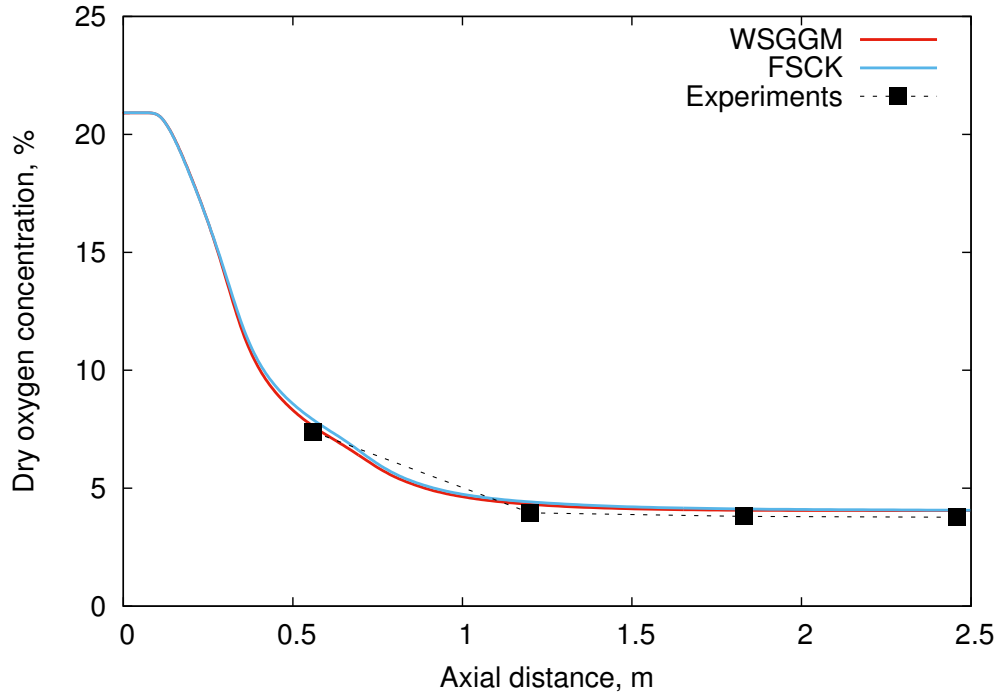

(b)

Figure 6.19: Comparison of the CFD results obtained when using the WSGG and FSCK models for the radiation properties of the combustion gases for the coal non-preheated case.

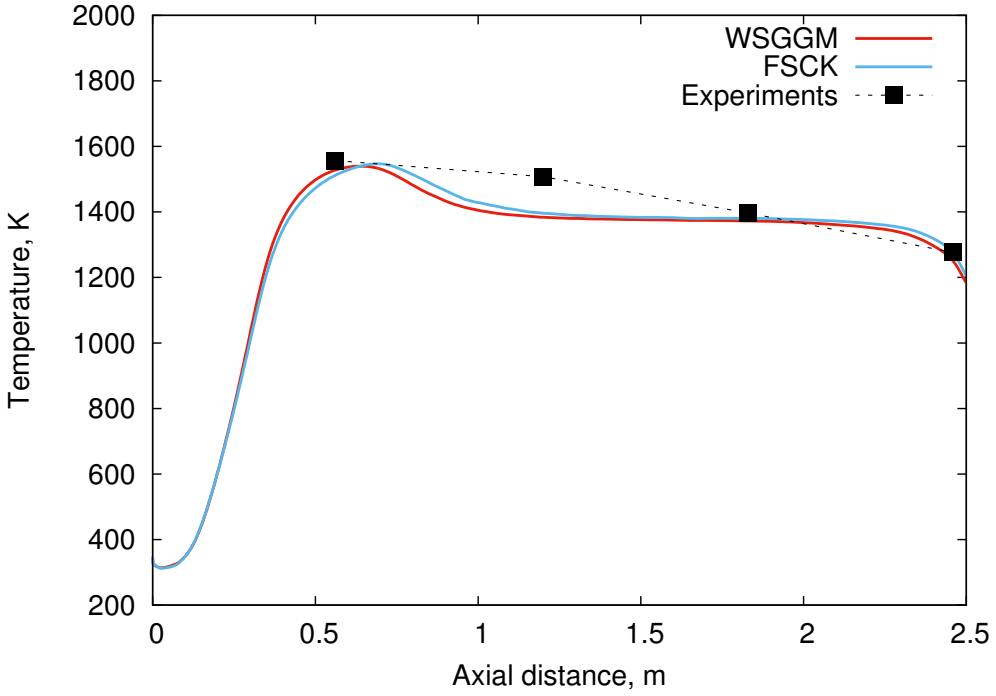

(a)

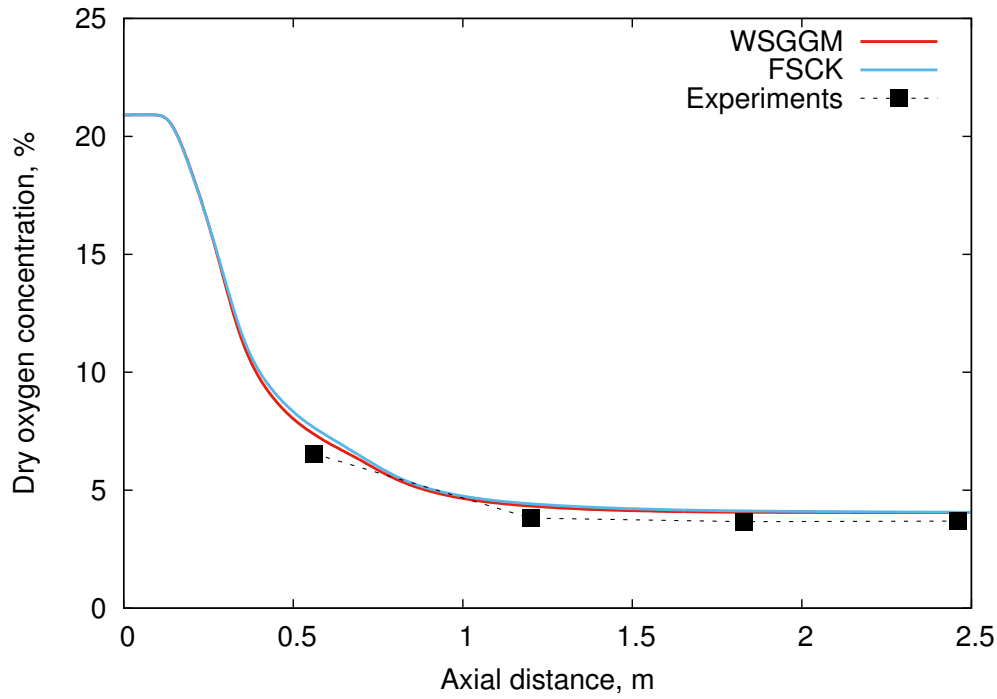

(b)

Figure 6.20: Comparison of the CFD results obtained when using the WSGG and FSCK models for radiation properties of the combustion gases for the coal preheated case.

Table 6.12: Comparison of the numerical predictions for WSSG and FSCK model with experimental data for the Port 3 for coal preheated case.

	Experimental data	CFD	
		WSGG	FSCK
Temperature, K	1398	1371	1372
CO, ppm	71	180	179
O_2, %	3.7	4.2	4.1

6.4.2 Biomass combustion

Numerical predictions for biomass combustion have been compared with the experimental data and are depicted in Figures 6.21 and 6.22 for the mixed wood and sawdust investigations, respectively. The CFD predictions of the axial temperature profile of the combustion gases and comparison against the experimental data for mixed wood and sawdust can be found in Figures 6.21(a) and 6.22(a), respectively. Further, the comparison of the dry oxygen concentration of the combustion gas and the experimental data along the furnace axis are depicted in Figures 6.21(b) and 6.22(b) for mixed wood and sawdust, respectively. The trend in the axial temperature profile and oxygen concentration is well predicted. However, the CFD predictions do not fit the experimental data as good as that of coal. These discrepancies can be seen in Figures 6.21(b) and 6.22(b), where the oxygen concentration of the combustion gas on the axis of the furnace is overpredicted in the near-burner region for both the mixed wood and sawdust. Moreover, this delay can be seen in the Figures 6.21(a) and 6.22(a), where the temperature profiles of the combustion gas along the axis of the furnace are depicted. Further, it is observed that the peak temperature in the flame is moved further downstream.

The delay in the CFD predictions needs to be addressed and it is possibly due to the not accurate surface area to volume ratio of the biomass

particles in the CFD model. This ratio may be to small, therefore there is a slower heat transfer and combustion. Further, there is not enough consumption of the oxygen in the CFD calculations, which means that the combustion process is slowed down.

Also, this discrepancy between the experimental data and the numerical predictions can be explained after analysis of the particle size distribution of the biomass particles presented in Figure 6.3. The biomass pulverised particles, both mixed wood and sawdust, are large in comparison to the coal particles. Therefore, the larger is the particle then the heat exchange process takes longer, and thus it takes longer to reach any given temperature.

The comparison of the experimental data and numerical predictions for mixed wood and sawdust at Port 3 is listed in Table 6.13 and in Table 6.14, respectively. It is observed that the numerical predictions at Port 3 are slightly different than those obtained from the experimental measurements. The temperature for both the mixed wood and sawdust is overpredicted, the dry oxygen concentration is slightly underpredicted for the biomass and the dry CO concentration in the gas is overpredicted. This discrepancy between the numerical predictions and the experimental data shows the prediction limitations in the models developed for coal when used for modelling the biomass combustion.

In Figures 6.17(c) and 6.17(d), the temperature contours of the combustion gas are depicted for the mixed wood and sawdust case, respectively, and compared with the coal preheated and non-preheated predictions of the temperature distribution within the furnace.

The dry oxygen concentration contours for the mixed wood are presented in Figure 6.18(c) and for the sawdust case in Figure 6.18(d). The oxygen fraction in the combustion gas illustrates the oxidation rates of the fuel and this assists in the understanding of the mechanism of the oxygen consumption and distribution inside the jet flame combustion rig.

The contours of the temperature and dry oxygen concentration of the combustion gas in the furnace for the mixed wood case and sawdust case are similar. Significant differences can be observed with the gas temperature distribution and the oxygen concentration within the combustion chamber between the coal and the biomass cases. In the coal cases, the high temperature region, and therefore the flame is located close to the burner end, whereas for the biomass cases the high temperature region and therefore the flame is moved further down the combustion rig. In consequence the combustion is slowed down and the oxygen consumption is delayed in the biomass cases when compared with the coal-fired cases.

The high temperature region is longer in the sawdust case than in the mixed wood case. Further, the combustion process is more rapid in the sawdust case than in the mixed wood case. This can be explained by the sawdust particles being smaller than the particles in the mixed wood, and this allows the sawdust to enhance the combustion process. In both the mixed wood and the sawdust cases, the temperature and dry oxygen concentration have different contours from that in the coal cases, and this shows the difference between these two types of fuels and their impact on the performance of the combustion process.

Table 6.13: Comparison of the numerical predictions with the experimental data at the Port 3 for the mixed wood case.

	Experimental data	CFD
Temperature, K	1440	1417
CO, ppm	3	134
O_2, %	5.7	7.3

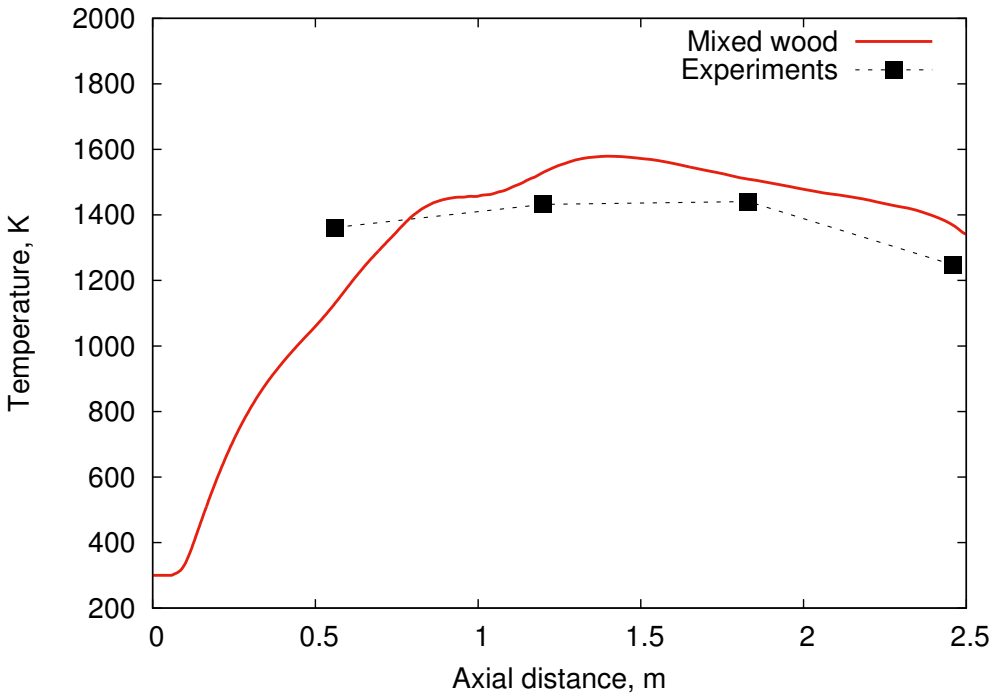

(a)

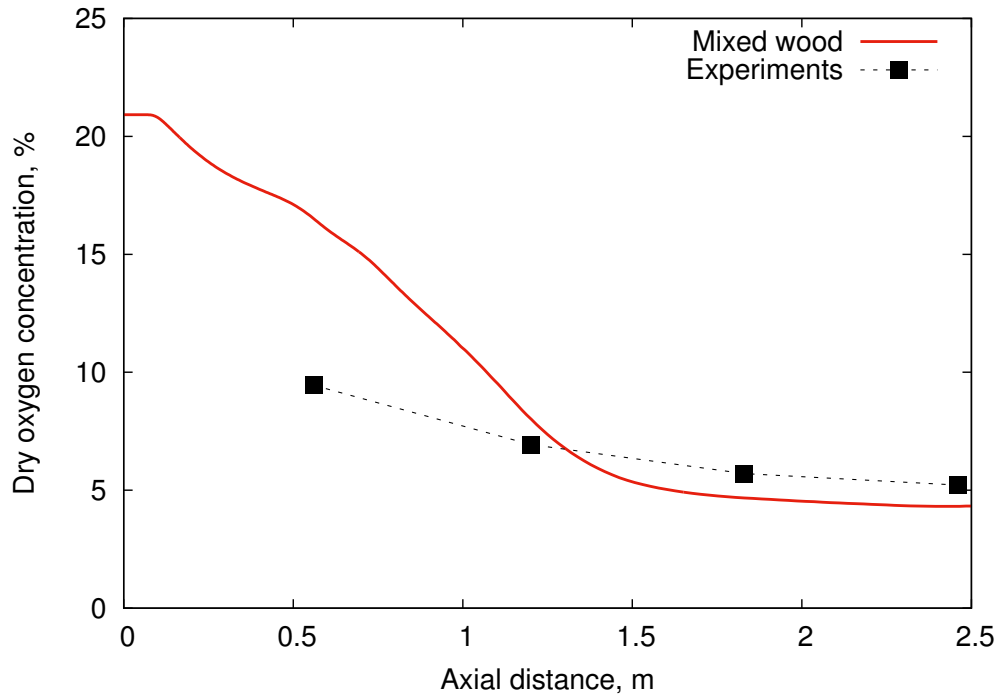

(b)

Figure 6.21: (a) Temperature profile and (b) dry oxygen concentration of the combustion gas along the furnace axis. The CFD predictions compared against the experimental data for the mixed wood case

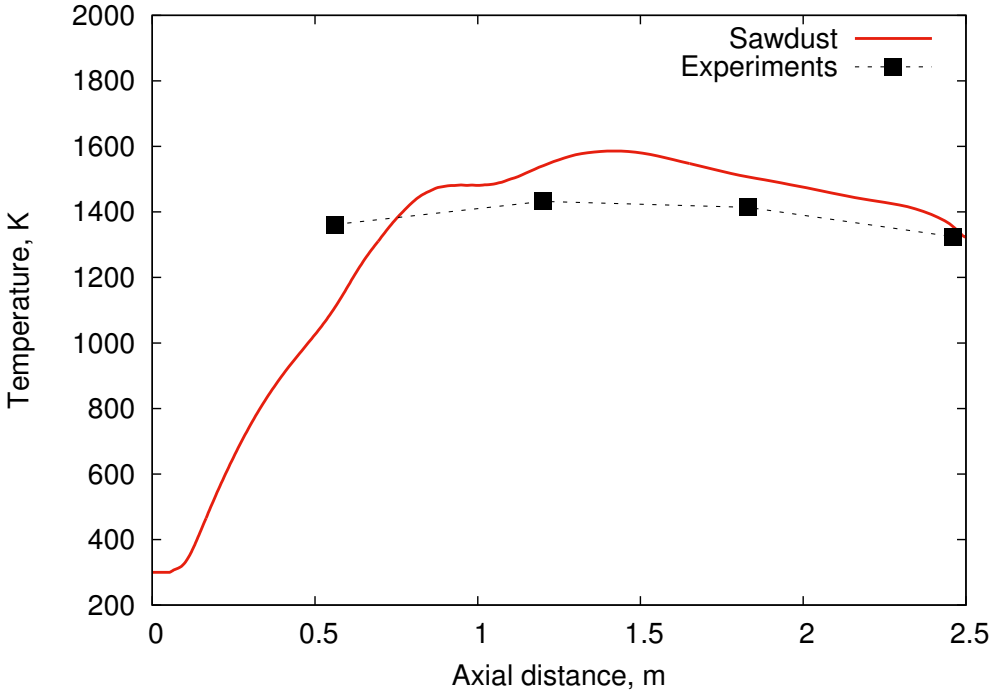

(a)

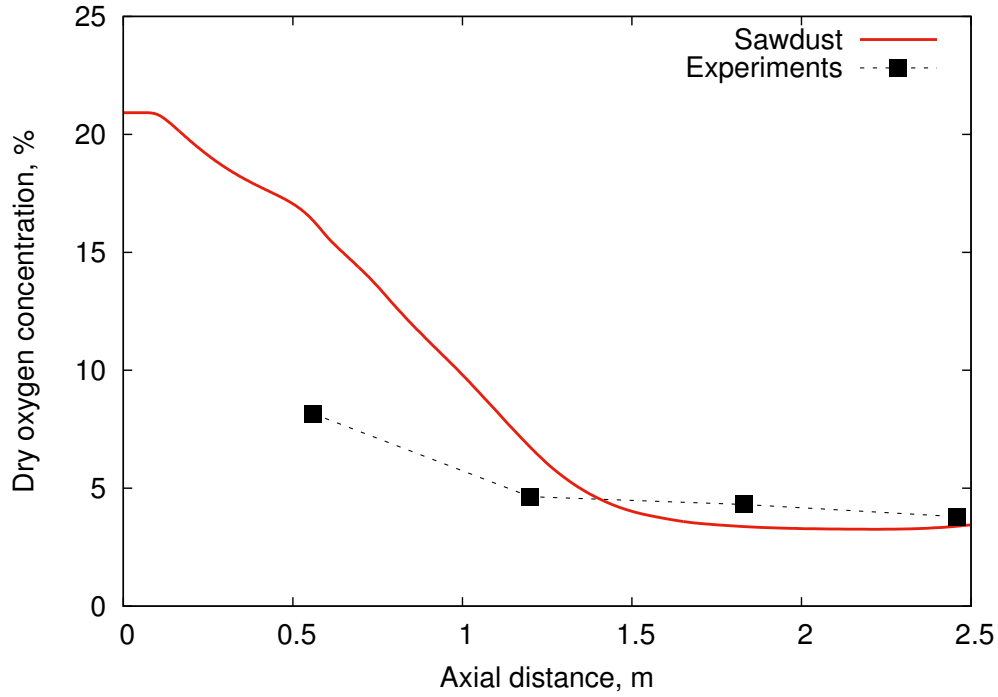

(b)

Figure 6.22: (a) Temperature profile and (b) dry oxygen concentration of the combustion gas along the furnace axis. The CFD predictions compared against the experimental data for the sawdust case.

Table 6.14: Comparison of the numerical predictions with the experimental data at the Port 3 for the sawdust case.

	Experimental data	CFD
Temperature, K	1412	1424
CO, ppm	16	104
O_2, %	4.3	6.7

6.4.2.1 Effect of the radiation - WSGG and FSCK models

Following the sensitivity study for the coal combustion when using non-grey radiation behaviours of the gases, the same comparison has been investigated for biomass combustion. As in the coal cases, the two models that describe the radiation properties for the combustion gases, namely the WSGG and FSCK models have been investigated and compared.

The results of this comparison is presented in Figure 6.23 for the mixed wood combustion, in Figure 6.24 for the sawdust combustion. Figures 6.23(a) and 6.24(a) show the results of the gas temperature profile along the combustion chamber axis obtained using the WSGG and FSCK models compared with the experimental data for mixed wood and sawdust, respectively. The numerical predictions of the oxygen concentration of the combustion gas within the combustion rig compared against the experimental data for mixed wood and sawdust can be found in Figures 6.23(b) and 6.24(b), respectively.

In both cases, for mixed wood and sawdust combustion the numerical simulations overpredict the experimental data. However, the results obtained using the WSGG model is found to be in better agreement with the CFD predictions than those obtained using the FSCK model. The temperature for the biomass cases is underpredicted in the near-burner region, and overpredicted further down the combustion chamber. Accordingly,

the concentration of the oxygen is overpredictied in the first section of the combustion chamber and underpredicted after the location of Port 2.

As it can be observed in Figures 6.19 and 6.20, the WSGG and FSCK models predict the coal combustion within the experimental accuracy and this gives similar numerical predictions. However, for biomass combustion numerical predictions when using the WSGG model has been found to give better results. Therefore, the WSGG model will be used in all the further studies in this thesis. In addition, the FSCK model is more computationally expensive in comparison to the WSGG model.

Table 6.15: Comparison of the numerical predictions when using the WSSG and FSCK models with the experimental data for at Port 3 the for the mixed wood case.

	Experimental data	CFD	
		WSGG	FSCK
Temperature, K	1440	1419	1595
CO, ppm	3	134	129
O_2, %	5.7	7.3	7.0

Table 6.16: Comparison of the numerical predictions when using the WSSG and FSCK models with the experimental data for at Port 3 the for the sawdust case.

	Experimental data	CFD	
		WSGG	FSCK
Temperature, K	1412	1424	1589
CO, ppm	16	130	121
O_2, %	4.3	6.7	6.6

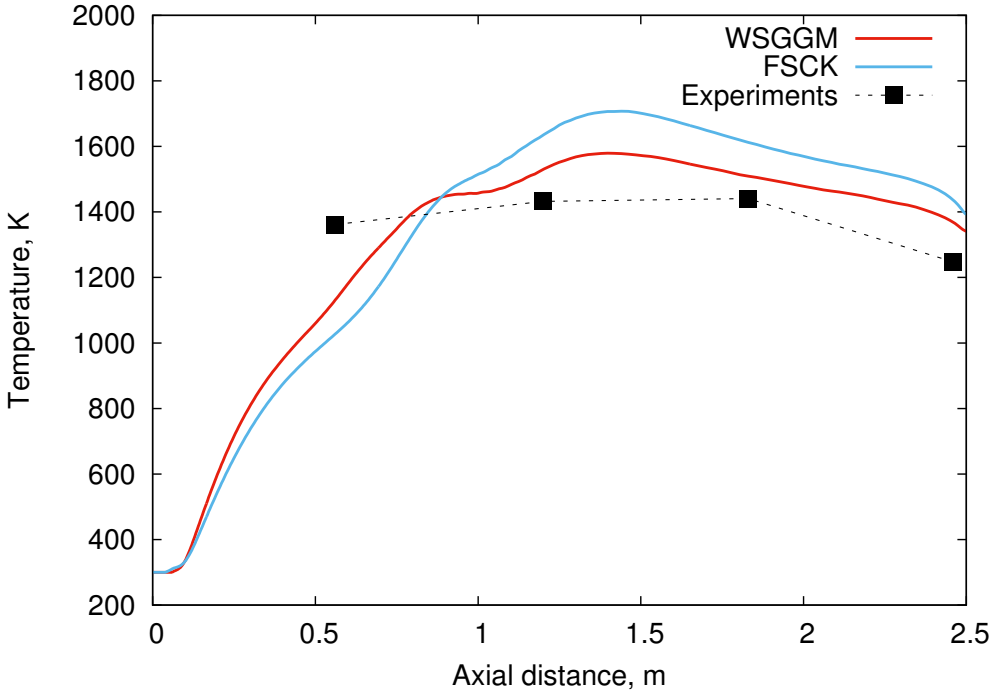

(a)

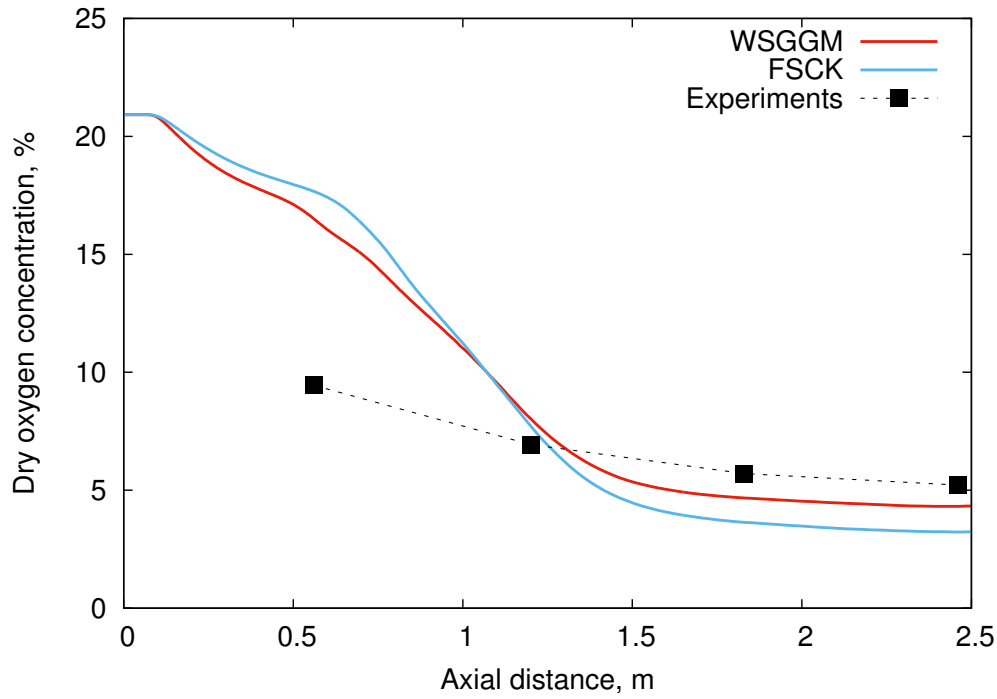

(b)

Figure 6.23: Comparison of the resuts obtained when using the WSGG and FSCK models for the radiation properties of the combustion gases for the mixed wood case.

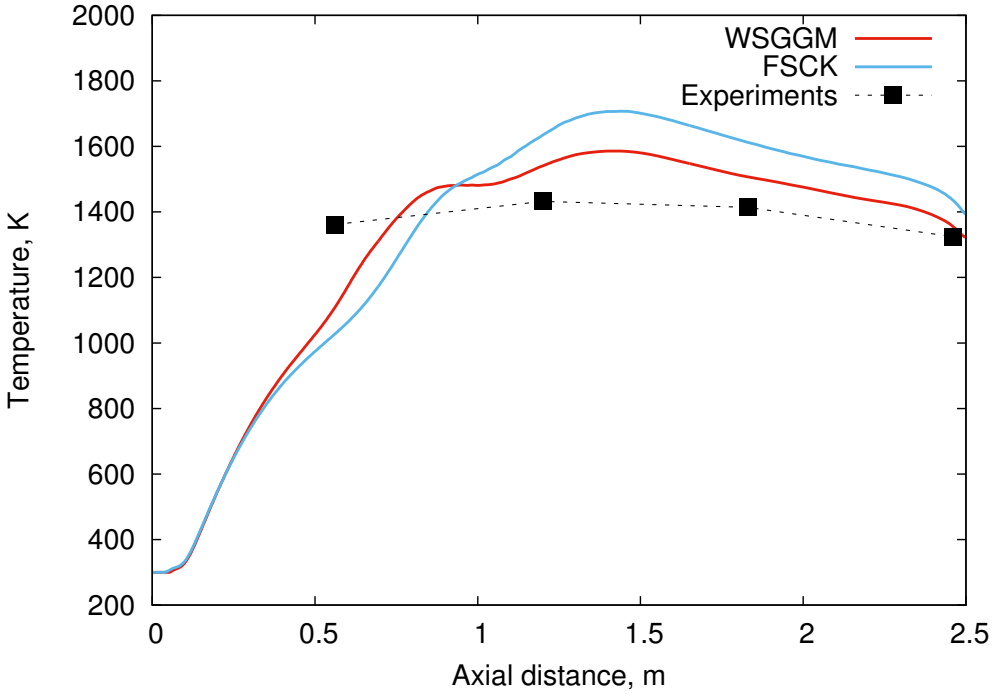

(a)

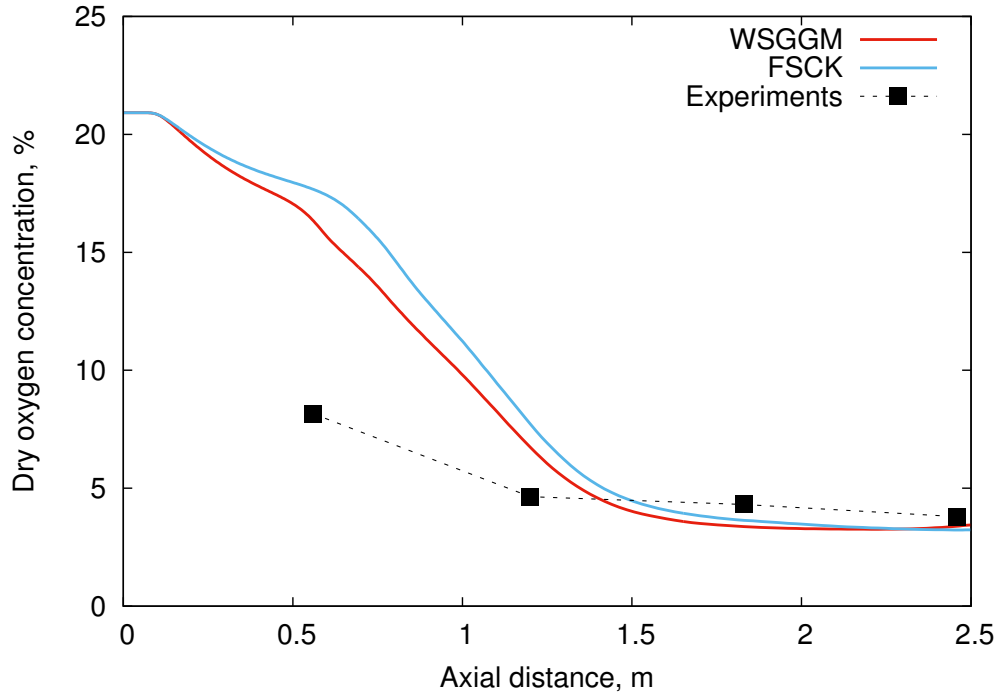

(b)

Figure 6.24: Comparison of the resuts obtained when using the WSGG and FSCK models for the radiation properties of the combustion gases for the sawdust case.

6.5 Conclusions

In this chapter, the theoretical calculation of emissions released during coal and biomass combustion have been compared with the experimental data. It can be concluded that emissions from biomass combustion significantly depend on the biomass fuel composition. In general, woody biomass combustion reduces the SO_x and NO_x emissions.

The coal and two biomass combustion in 15 kW jet flame furnace have been modelled and the results obtained compared with experimental data. The CFD settings and models used for the coal combustion have been adapted from the previous chapter where different models for the coal combustion have been investigated. The combustion of Middelburg high volatile coal and biomass fuel, namely mixed wood and sawdust have been fired in 15 kW thermal input. The coal has been replaced with biomass with a change in the burner design. Both types of fuel has been combusted under similar conditions. Firing different fuels in the same furnace, at the same heat input and excess air, gives an indication of the differences in the combustion performance between the different fuels.

From the CFD point of view, the replacement of the fuel used for the simulations gives the opportunity to validate the predictions of the numerical models used in the simulations.

It is found that the coal combustion has been predicted well and within the experimental accuracy. The FSCK model for the radiative properties of the combustion gases has been compared with the previously used WSGG model and both the WSGG and FSCK models have been found to predict the combustion performance well.

It is found that the in-flame temperatures of the coal flame has been higher by about 100^{o}C for the coal combustion than biomass and ignition is faster in the coal cases during the experimental programme [174]. The CFD predictions of the temperature profiles along the axis for both the mixed wood and sawdust presented in this chapter are in good agree-

ment with the experimental data. However, the axial temperature profile is underpredicted in the near-burner region and overpredicted further downstream. Further, the oxygen concentration along the combustion chamber axis is overpredicted in the near-burner region and slightly underpredicted in the region further away from the burner. Both the temperature profile and oxygen concentration discrepancies along the furnace axis in the near-burner region are the consequence of delay of the combustion reactions predicted by CFD. The introduction of the FSCK model does not improve the results as obtained in the WSGG model in the biomass cases, and this is similar to coal combustion. The delay in the combustion prediction for biomass cases may be explained by the large and irregular in shape biomass particles. The assumption of the spherical shape of the particle can cause the delays in the combustion of biomass fuel and therefore lower than the experimental data temperatures and the higher oxygen concentration in the near-burner region.

Coal has been replaced with two biomass fuels, namely mixed wood and sawdust. Because the commercially available CFD models, including ANSYS Fluent, are not fully developed for the biomass combustion, the coal combustion models have been used to predict the biomass combustion. However, the properties of the biomass fuel has been taken into account.

6.6 Summary

This study presented an analysis of pulverised coal and biomass combustion and showed how well the biomass combustion can be predicted using models validated for coal combustion.

In the CFD model it is assumed that biomass combustion is modelled as a coal fuel, including the steps in the solid fuel combustion, namely heating-up, evaporation of moisture, release of volatiles and surface com-

bustion. Further, similar sub-models were used to simulate the biomass and coal by simply taking into account the different properties of these two fuels. Also, similar to the coal particles, the biomass particles were assumed to be spherical in shape.

However, the pulverised biomass has irregular shape particles due to the fibrous nature of the biomass. The non-spherical particles of the biomass can influence the particle heat exchange with the combustion gases and then impact on the combustion performance and temperature distribution within the combustion chamber. Further, the irregular shape of the biomass particles may have an impact on the particle aerodynamic behaviour, and thus the particle trajectory inside the furnace, its motion and residence time. However, this is out of the scope of this thesis and have not been investigated.

The non-spherical shape of the biomass, among others, has been found to have a possible influence on the CFD predictions. Therefore, an investigation of the biomass shape is presented in the next chapter.

Chapter 7

Theoretical study of the biomass particle size and shape

7.1 Introduction

In Chapter 6, the limitations of the coal models applied to biomass combustion have been outlined. In this chapter, the main focus is given to the pulverised biomass particle shape and size and to the application of these parameters into the CFD modelling.

As mentioned in Chapters 2 and 3, milling of the fibrous biomass results in its irregular shape and large size [79]. The irregular shape of the biomass particles may affect the heat and mass transfer to and from the particle. Moreover, large particles may introduce the potential of thermal conductivity inside the particle [79]. These two aspects have been investigated and validated against the available experimental data [174].

7.2 Particle shape

The shape of the biomass particle is extremely irregular in comparison to coal particles and this is a consequence of the high content of cellulose, hemicellulose and lignin [200]. Therefore, for the CFD model-

ling the influence of biomass particle shape cannot be ignored, as various particle shapes result in different surface area, which are essential to the processes of heat and mass transfer [79].

For simplicity, the commercial CFD software makes the assumption of spherical particle shape. This is because the sphere, among other shapes, is defined by only one parameter, namely the radius. The spherical shape of a particle introduced into the mass and heat transfer calculations simplifies and economises the computational cost, as a point on the surface of the particle has the same distance (radius) in any direction from its centre point.

Even the recent, expensive online sensing techniques, such as electrostatic [201, 202] and digital imaging [203], have many difficulties in obtaining the exact information on the fuel particle size and shape. Hence, simplifications to the particle shapes and sizes are a necessity in numerical studies in order to minimise the uncertainties and reduce the computational expense [160]. Thus two dimensionless parameters are introduced, namely the shape factor and aspect ratio.

7.2.1 Shape Factor (Sphericity)

The shape factor (SF) is a dimensionless quantity that numerically describes the sphericity of the particle. The definition of the shape factor is introduced to account for the deviation in the particle shape [204]. This term is a compactness measure of how close is the actual particle shape to its spherical shape.

SF of the particle is described as the ratio of the surface area of the sphere which has the same volume as the given particle and the surface area of the actual particle [205]:

$$SF = \frac{\pi^{\frac{1}{3}}(6V_p)^{\frac{2}{3}}}{A_p} \tag{7.1}$$

where:

V_p – the volume of the particle,

A_p – the surface area of the particle.

In the case of a cylindrical particle, the SF is the ratio of the surface area of a sphere of volume equivalent to the actual particle and the actual surface area of the cylindrical particle and it is given as follows:

$$SF = \frac{4 \cdot \pi r_{sph}^2}{2 \cdot \pi r_{cyl}^2 + 2 \cdot \pi r_{cyl} \cdot l_{cyl}} \tag{7.2}$$

where:

r_{sph} – the radius of the sphere that has the same volume of the cylindrical particle,

r_{cyl} – the radius of the cylindrical particle,

l_{cyl} – the length of the cylindrical particle.

The shape factor value is less than or equal to one. A shape factor equal to one represents the 'ideal' case - spherical particle. The lower is the shape factor, the higher is the degree of deviation from the spherical shape.

7.2.2 Aspect Ratio

Another dimensionless quantity that describes the particle shape is the aspect ratio (AR) and this numerically describes the shape of the particle, independent of its size. The dimensions of the particles are usually measured from two-dimensional cross-sections or projections. Thus the aspect ratio does not represent the actual width and height of the particle but, rather, the proportion of the particle between the largest diameter and the smallest diameter of the particle. The aspect ratio gives a description of

the elongation of the particle as follows:

$$A_R = \frac{d_{\max}}{d_{\min}} \tag{7.3}$$

where:

$d_{\min}$ – the smallest particle diameter,

$d_{\max}$ – the largest particle diameter.

For a cylindrical particle, the aspect ratio is obtained as follows:

$$AR = \frac{l_{cyl}}{r_{cyl}} \tag{7.4}$$

where:

l_{cyl} – the length of the cylindrical particle,

r_{cyl} – the radius of the cylindrical particle.

The aspect ratio value, as for the shape factor, equal to one represents the ideal case, and it is when the particle maximum and minimum diameters (lengths) are the same. The higher is the aspect ratio, the higher is the degree of deviation from the ideal case.

7.2.3 Comparison of different particle shapes

To evaluate the best way to describe the irregular particle shapes, a number of shapes, namely the sphere, cylinder, cuboid, ellipsoid, pentagonal prism and cone have been compared in the theoretical analysis of the heat exchange between the particle and the combustion gases, and these are depicted in the Figure 7.1.

Assuming that every shape has a similar volume (volume of a sphere with a diameter of d = 0.005 m) and the aspect ratio in the range 1.5 – 10, the shape factor has been compared and a summary is listed in Table 7.1. The aspect ratios have been assumed based on the electron microscopy

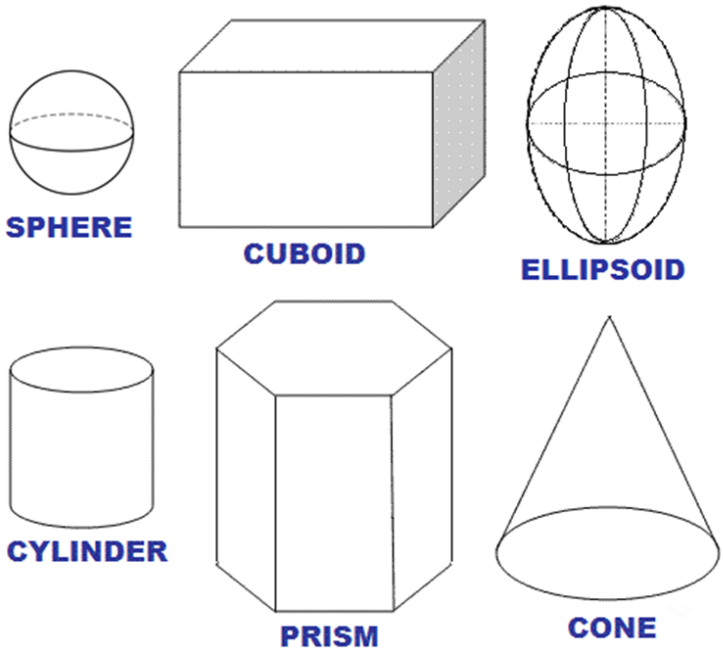

Figure 7.1: Shapes considered for the heat exchange analysis of the irregular particle shape.

images [160]. It can be observed in Table 7.1 that the more the shape of the particle deviates from the sphere and consequently having higher value of AR, the more does the SF decrease.

Table 7.1: Influence of the aspect ratio on the particle shape factor compared with equivalent sphere with diameter of d = 0.005 m.

	Aspect Ratio (AR)				
	1.5	2.5	5	7.5	10
sphere	1	1	1	1	1
ellipsoid	0.97	0.89	0.73	0.65	0.59
cylinder	0.86	0.80	0.70	0.63	0.58
cone	0.79	0.76	0.67	0.60	0.56
pentagonal prism	0.82	0.77	0.66	0.60	0.55
cuboid	0.79	0.74	0.64	0.58	0.53

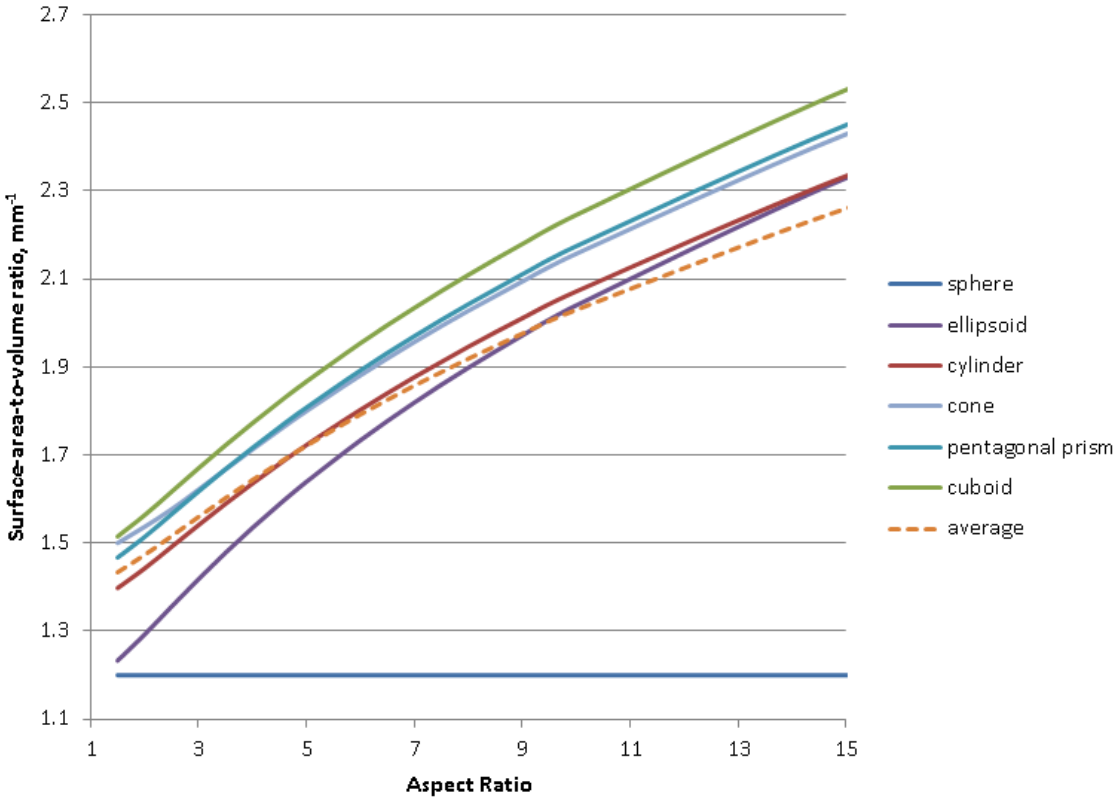

Figure 7.2: The surface-area-to-volume ratio dependence on the aspect ratio of the sphere, cylinder, cuboid, ellipsoid, pentagonal prism and cone compared with the equivalent sphere with diameter of d = 0.005 m.

Table 7.2: Influence of the aspect ratio of the particle surface area extension compared with the equivalent sphere.

	Aspect Ratio (AR)				
	1.5	2.5	5	7.5	10
ellipsoid	3%	13%	37%	55%	70%
cylinder	16%	24%	44%	59%	73%
cone	26%	31%	50%	66%	88%
pentagonal prism	22%	30%	51%	67%	81%
cuboid	26%	35%	56%	73%	87%
average	19%	27%	47%	64%	78%

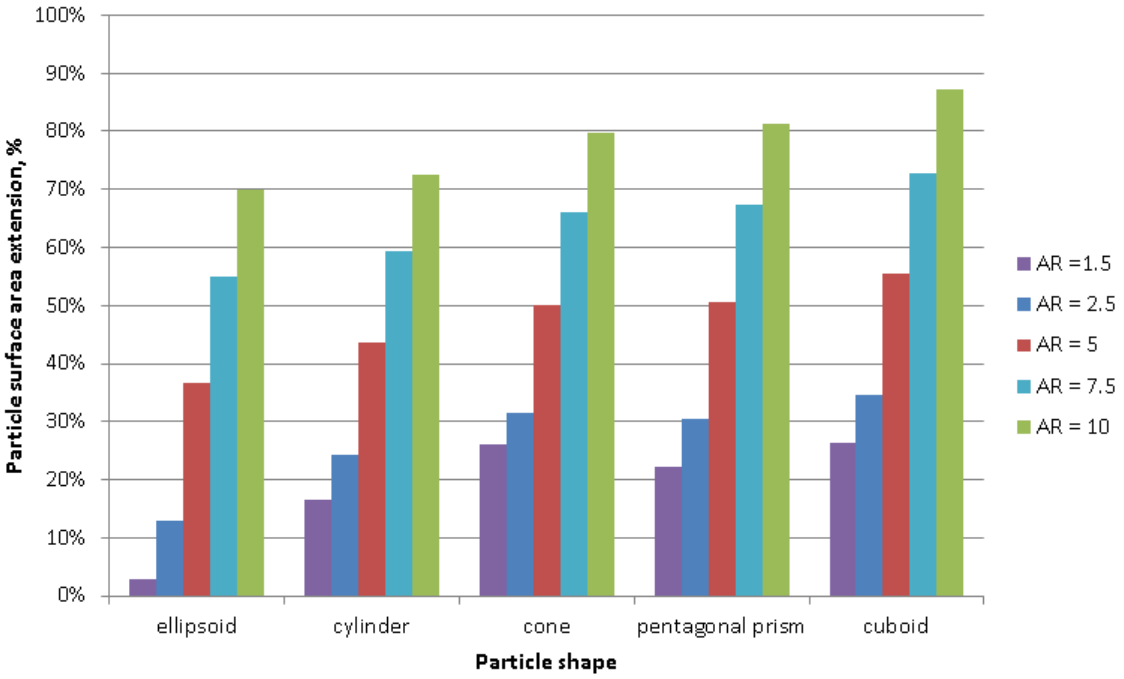

Figure 7.3: The surface area extension of the sphere, cylinder, cuboid, ellipsoid, pentagonal prism and cone compared with the equivalent sphere.

Further, the surface-area-to-volume (SA/V) ratio of each of the particle shapes have been calculated, which is the amount of surface area per unit

volume of the particle. This ratio, when compared against the spherical particle of the same volume gives a representation of the extension of the surface area of the non-spherical particles. The AR dependence on the SA/V ratio of the sphere, cylinder, cuboid, ellipsoid, pentagonal prism and cone is presented in Figure 7.2. The surface area of the irregular in shape particles with different AR, namely 1.5, 2.5, 5, 7.5 and 10 have been compared with the surface are of the equivalent sphere of the same volume, and the percentage of the surface area extension is depicted in Figure 7.3 and listed in Table 7.2. It can be noticed that the SA/V ratio significantly increases with increasing AR, and this, in consequence, extends the surface area of the particles. The cuboid has been found to have the largest SA/V ratio despite the AR, whereas the smallest value of the SA/V ratio has been assigned to ellipsoids and cylinders. The surface area extension depends on the AR value and shows a linear behaviour. The non-spherical particles extend the surface area by about 19% with AR = 1.5, 27% with AR = 2.5, 47% with AR = 5, 64% with AR = 7.5 and 78% with AR = 10 in average for the compared particle shapes.

7.3 Heat transfer

Heat transfer has a direction as well as a magnitude. Further, the rate of heat conduction in a specified direction is proportional to the temperature gradient, which is the change in the temperature per unit length in that direction [147]. In general, heat conduction in a medium is three-dimensional. However, heat conduction in a medium is said to be one-dimensional when conduction is significant in one dimension only [147]. In this section, the assumption of one-dimensional heat transfer has been applied, as the sphere is defined by only one parameter.

7.3.1 Thermally thin particles

The non-spherical particles introduced in previous section and their impact on the heat-up curve has been investigated in this section. The particles, namely the sphere, cylinder, cuboid, ellipsoid, pentagonal prism and cone with similar volume and the same aspect ratio have been introduced into the environment at a constant temperature and their heating values have been compared.

The initial temperature of the particles has been assumed to be ambient (298 K). Further, the temperature of the combustion gases has been assumed to be 1200 K, as the average temperature in the combustion chamber. All of the particles are considered to be thermally thin, therefore, there is no thermal conduction within the particle and the temperature remains uniform at all times during the heat transfer process.

The temperature of the particles has been calculated using the energy balance of the particle [147]:

$$hA_p \left(T_\infty - T\right) dt = m_p C_p dT \tag{7.5}$$

where:

h – the heat transfer coefficient,

A_p – the particle surface area,

T_∞ – the temperature of the environment,

m_p – the mass of the particle,

C_p – the specific heat of the particle.

Figure 7.4 shows the influence of different particle shapes on their temperature as a function of time. It can be noticed that particles with smaller SF reach the temperature of the environment faster and this is a consequence of SA/V ratio. The ideal sphere heats up the slowest when compared with all the other particle shapes. The next particle shapes which heat up in the slowest way in comparison to the other shapes is the

ellipsoid. This can be explained by the shape factor of this shape, which is very close to the sphere, namely SF = 0.88. There is no significant difference in the heating up curve if the particle has the shape of a cone, cylinder, cuboid or pentagonal prism. Also, the higher the AR, the less significant is the impact of the particle shape. This comparison gives an indication that the surface area of the particle plays a more significant role in its heat-up than its actual shape.

As the surface area has been found to be the key component in the interaction between the solid particle and the gas phase in the heat exchange process then the shape of the particle can be neglected, as long as the effective surface area is included in the calculations of the heat transfer. Due to the outcome of this analysis, for the further research presented in this thesis, the assumption of an extended surface area based on a cylinder is taken into consideration.

Figure 7.5 shows the temperature of the cylindrical particles with different aspect ratios as a function of time, highlighting the influence of the elongation of the cylindrical particle on its heat up curve. It is assumed that the cylindrical particles, despite the different AR, have similar volume as the sphere with the diameter is d = 0.005 m. Further, their dimensions and surface area change and thus their respective shape factors change. As the biomass aspect ratio, according to the literature, is usually in the range 2 – 15 [79], this range of aspect ratios has been depicted. It can be noticed that the higher is the aspect ratio of the cylindrical particle, then the quicker the particle heats up. For comparison, the spherical particle after 10 s of residence time reaches the temperature of about 750 K, whereas the cylindrical particle with AR = 4 reaches the temperature of 800 K, at the same time a cylindrical particle with AR = 15 reaches the temperature of about 1000 K.

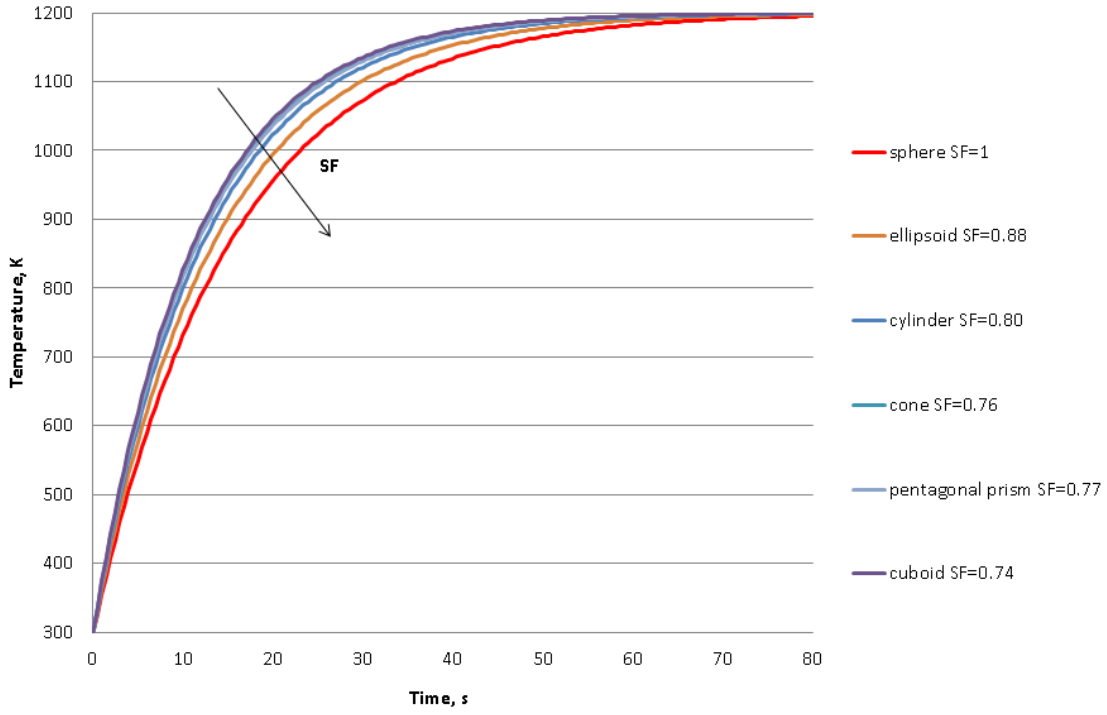
Temperature, K
Time, s
SF
sphere SF=1
ellipsoid SF=0.88
cylinder SF=0.80
cone SF=0.76
pentagonal prism SF=0.77
cuboid SF=0.74

(a)

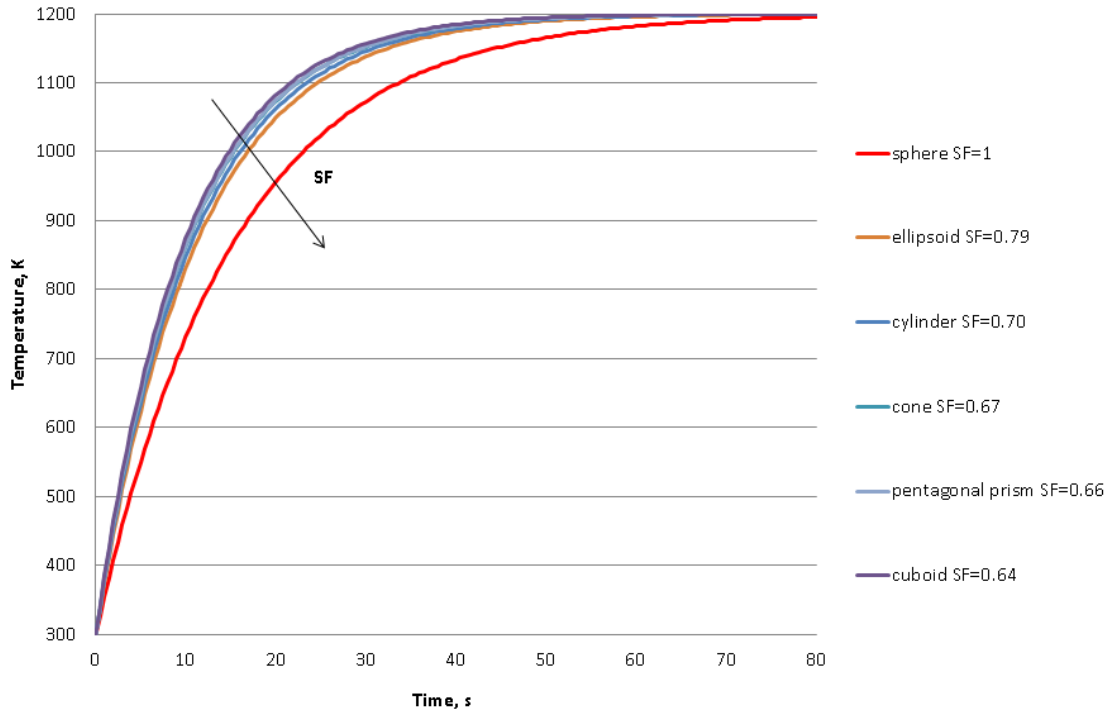
Temperature, K
Time, s
SF
sphere SF=1
ellipsoid SF=0.79
cylinder SF=0.70
cone SF=0.67
pentagonal prism SF=0.66
cuboid SF=0.64

(b)

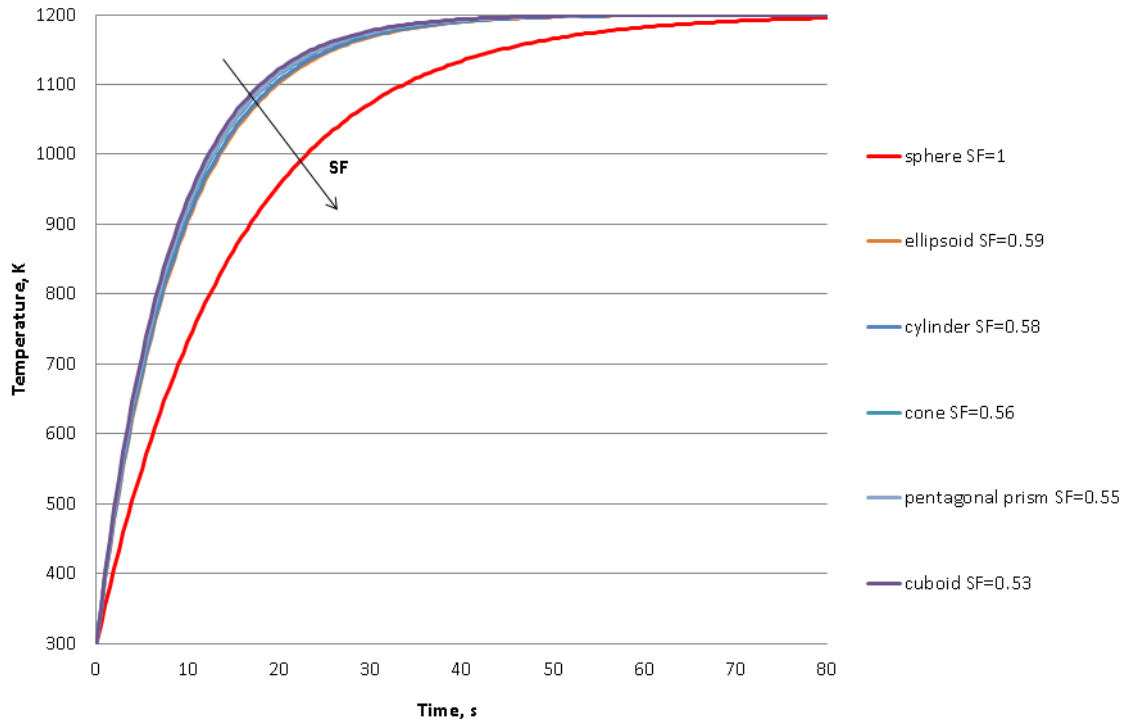

(c)

Figure 7.4: Influence of the particle shape on its temperature as a function of time (for the equivalent sphere with a diameter of d = 0.005 m) (a) AR = 2.5, (b) AR = 5 and (c) AR = 10.

7.3.2 Thermally thick particles

The assumption of uniform temperature across the particle body is applicable when the Biot number is $Bi \leq 0.1$ [147]. The Biot number can be defined as the ratio of the convection at the surface of the body and the conduction within the body:

$$Bi = \frac{h}{k/L_c} = \frac{hL_c}{k} \tag{7.6}$$

where:

L_c – a characteristic length of the particle, defined as the ratio of the particle volume to its surface area, as follows

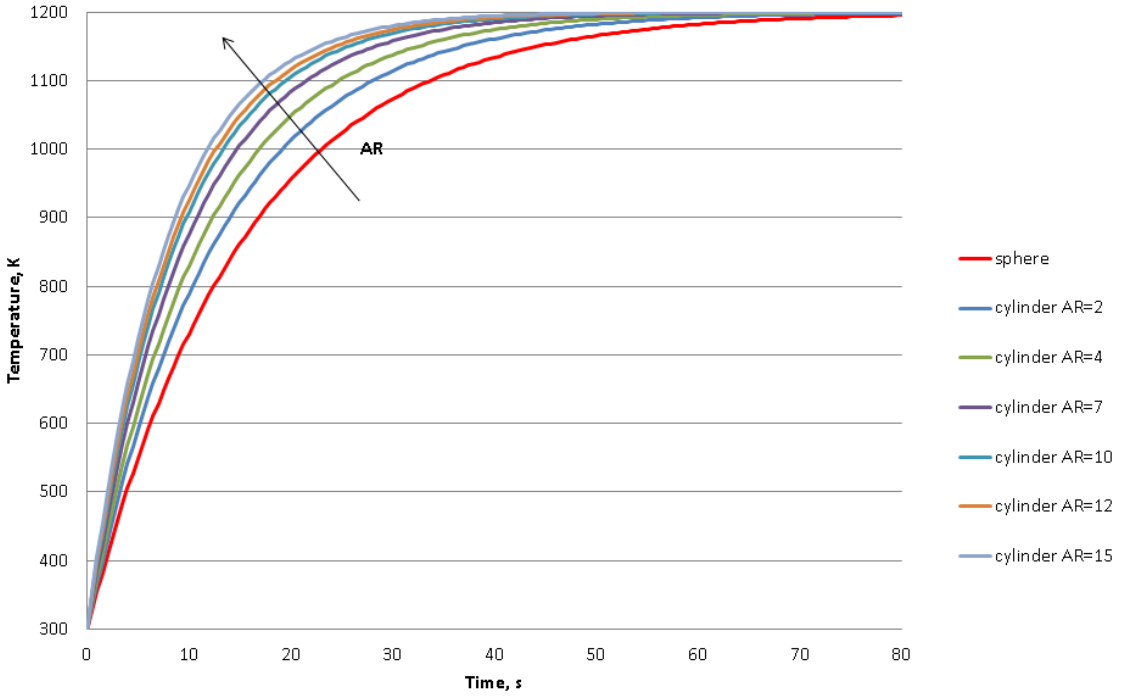

Figure 7.5: The temperature of the cylindrical particles as a function of time at various AR compared against the equivalent sphere with a diameter of d = 0.005 m.

$$L_c = \frac{V_p}{A_p} \tag{7.7}$$

In the CFD codes the particles are assumed to be thermally thin, which means that the temperature throughout the particle is constant and therefore there is no thermal conduction within the particle. The criterion of uniform temperature distribution throughout the body is exact when the thermal resistance of the particle body to the heat conduction within the body is zero, i.e. the Biot number is zero. This approach in describing the heat transfer is applicable for small particles with high thermal conductivity. However, in the case of larger particles with lower thermal conductivity then this assumption is not applicable.

When a large particle is introduced into a hot surroundings then heat is first convected to the body and subsequently conducted within the body [147]. Consequently, when the Biot number is greater than about 0.1 then

the particle should be considered to be thermally thick.

The general form of the heat conduction is expressed in the differential form by Fourier's law for one-dimensional heat conduction as follows:

$$\dot{Q}_{cond} = -kA_p \frac{dT}{dx} \tag{7.8}$$

where:

k – the thermal conductivity of the material,

$\frac{dT}{dx}$ – the temperature gradient.

The one-dimensional transient heat conduction equation for a spherical particle is given by

$$\frac{k}{r^2}\frac{\partial}{\partial r}\left(r^2 \frac{\partial T}{\partial r}\right) + \dot{g} = \rho C_p \frac{\partial T}{\partial t} \tag{7.9}$$

where:

r – the sphere radius,

ρ – the constant density,

C_p – constant specific heat.

To reduce the number of parameters, the dimensionless temperature $\theta(x,t)$, dimensionless heat transfer coefficient (Biot number) Bi, dimensionless distance from the centre X and the dimensionless time (Fourier number) τ have been introduced. The one-dimensional transient heat transfer for a spherical particle is given by [147]:

$$\theta(r,t) = \frac{T(r,t) - T_\infty}{T_i - T_\infty} = A_1 e^{-{\lambda_1}^2 \tau} \frac{sin(\lambda_1 r/r_0)}{\lambda_1 r/r_0} \tag{7.10}$$

where A_1 and λ_1 are functions of only the Biot number and τ > 0.2.

The particle is initially at a uniform temperature T_i = 298 K. At time t = 0, the particle is placed in a medium at a constant temperature T_∞. The particles with the same diameter (d = 0.01 m) and the same physical

properties (ρ = 550 kg/m^3, C_p = 1500 J/kgK) and environmental conditions (h = 50 W/m^{2}K, T_∞ = 1200 K) have been investigated and compared here.

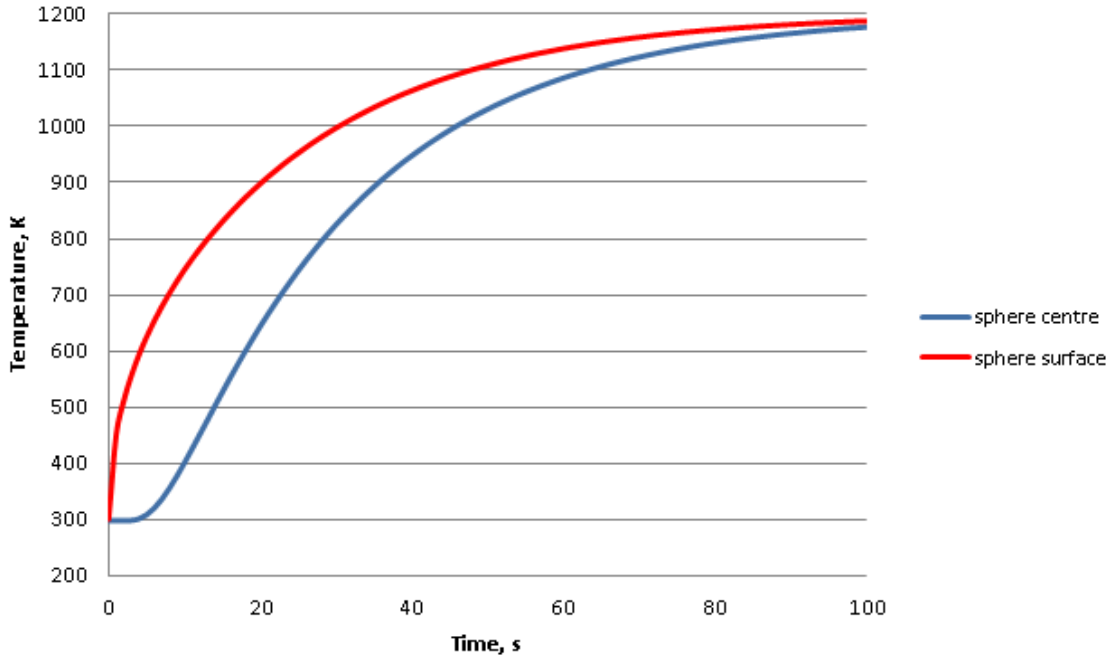

Figure 7.6: Transient temperature profile as a function of time for a sphere with diameter of d = 0.005 m at the centre and at the surface of the particle.

The temperature profile of the spherical particle during the heating up process increases rapidly and eventually becomes uniform when it reaches the temperature of the environment, i.e. when the particle reaches the thermal equilibrium with its surroundings. Figure 7.6 shows the temperature profile of the spherical particle as a function of time at the centre of the particle and at its surface. The thermal conductivity has been assumed to be k = 0.11 W/mK based on [48, 206]. It is observed that the surface of the particle heats up faster than the inner parts of the particle and the interior part of the particle reaches the temperature of the environment slower than the particle outer surface and this is

due to the heat conduction within the particle. It is observed that there is a visible difference between the temperature profile at the centre of the particle and its surface. The sphere centre maintains the initial temperature when introduced into the high temperature medium but, in contrast to the surface of the particle, immediately starts to increase its temperature. The surface of the particle heats up much more rapidly in comparison to the particle centre, which creates a thermal gradient within the particle, which is significant for the first 30 s of the particle (with diameter d = 0.01 m) heat-up.

To investigate the temperature profile on the surface of the spherical particle, two different assumptions have been compared, namely the particle is isothermal during the heating up process and when the thermal conduction within the particle is included (thermally thick particle).

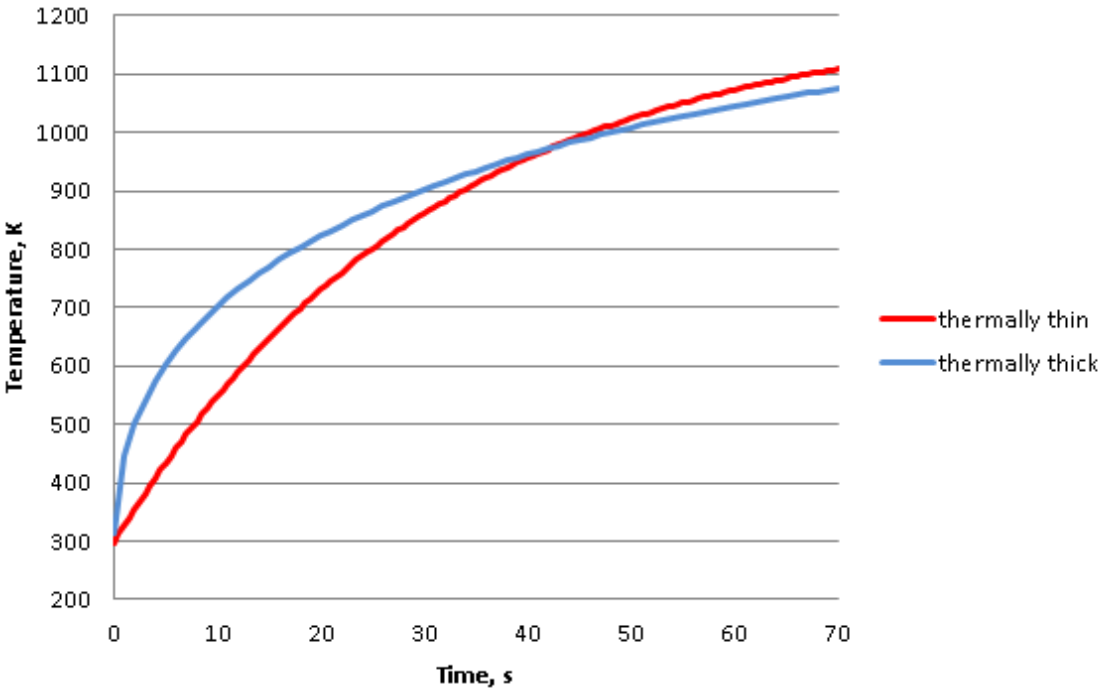

Figure 7.7: Transient surface temperature for thermally thin and thermally thick spherical particles with a diameter of d = 0.01 m.

Figure 7.7 shows a comparison of the temperature on the surface of

the spherical particles for the thermally thin and thermally thick spherical particles. For thermally thick particles, the external surface heats up quicker than for the thermally thin particle surfaces when the particles are introduced into a high temperature medium. However, the surface of the thermally thin particles reach the external environment temperature faster than the thermally thick particles. After 10 s of residence time, the thermally thin particle reaches a temperature of 550 K, while the thermally thick particle reaches a temperature of 700 K. This indicates that the thermally thick approach may have a significant influence on the heat exchange between the large biomass particles and the surrounding combustion gases in the combustion chambers and therefore influence the biomass combustion performance.

Figure 7.8 shows the impact of the biomass thermal conductivity on the thermally thick particles heat-up curve. The temperature on the surface and at the centre of the particle with a diameter of d = 0.01 m have been compared for the $\pm$ 20% change in the baseline thermal conductivity value k = 0.11 W/mK. It can be observed that the main difference is at the particle centre heat-up curve, which indicates that with decreasing value of thermal conductivity the thermal gradient within the particle increases. Also, with the decreasing thermal conductivity the particle surface heats up slightly faster.

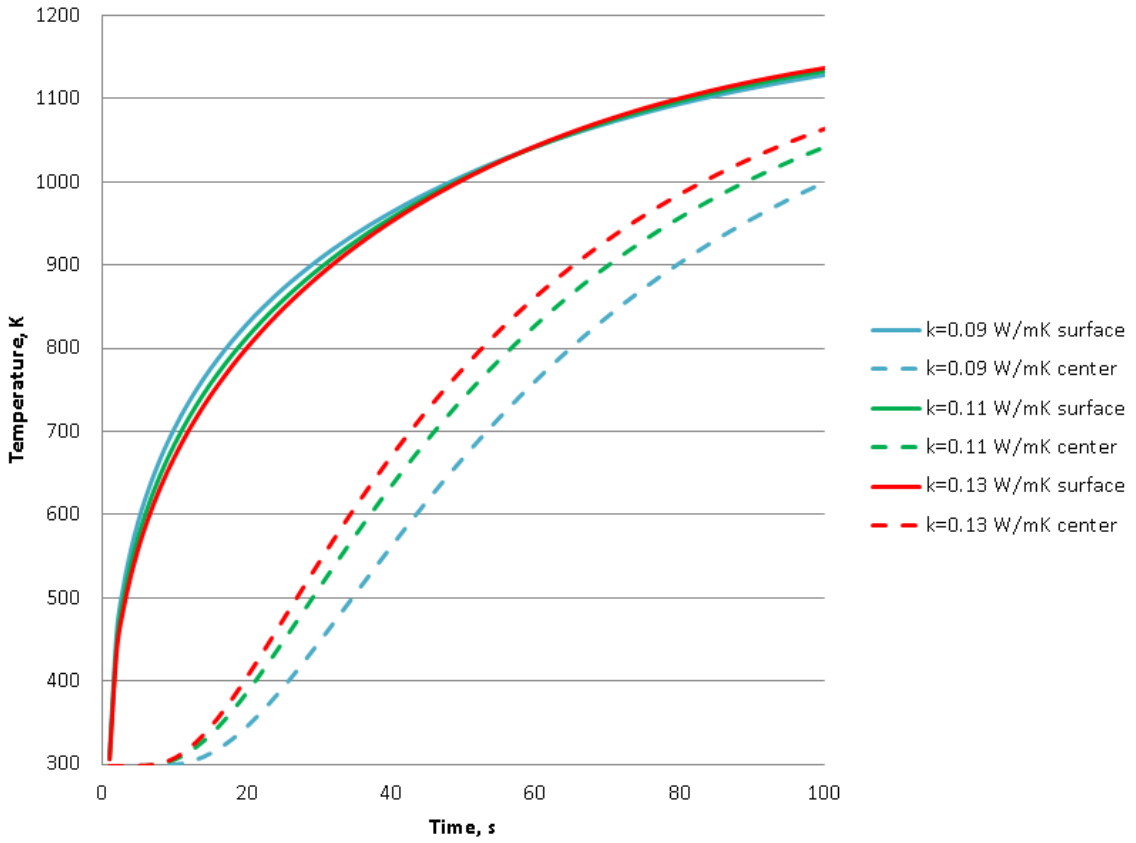

Figure 7.8: Influence of the thermal conductivity on the transient surface and centre temperature for thermally thick particles with a diameter of d = 0.01 m.

7.4 Application of irregular biomass particle shapes into a 15 kW jet flame

7.4.1 Influence of the particles AR and SF on the particle temperature

The influence of the particle shape and size on the heat transfer has been implemented in the CFD code by means of user defined functions. Firstly, the code for the particle heating, vaporization of water, boiling of water, devolatilization and char combustion has been written for spherical particles and the results obtained are compared with the standard ANSYS Fluent predictions (with the assumption of a spherical particle

shape) of the particle temperature. The spherical particle with SF = 1 and cylindrical particles with different SF, namely with SF of 0.58, 0.87, 0.8 and 0.7 and corresponding AR of 1, 2.5, 5 and 10, respectively, have been compared. The spherical and cylindrical particles have the same volume, but the cylindrical particles, due to the increasing aspect ratio and elongation of the particle, have a lower shape factor.

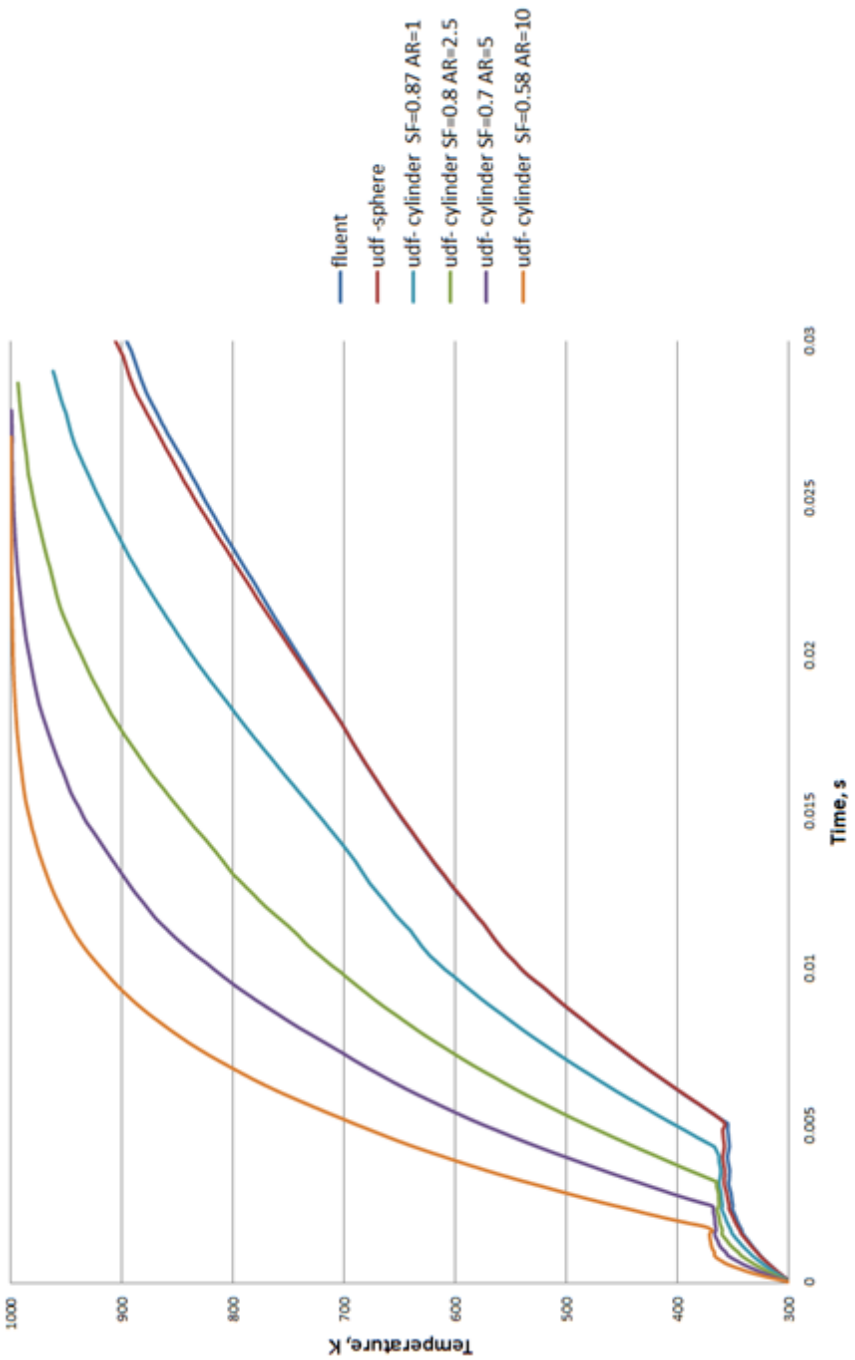

Figure 7.9: Influence of the particle shape - comparison with Fluent predictions.

The particle shape factor and the aspect ratio have been incorporated into the user defined function in order to include the irregular shape, and consequently, extended external surface area, of the biomass in the CFD model. Figure 7.9 shows the particle temperature predictions for spherical and cylindrical particles as a function of time. Firstly, the in-house code has been compared with ANSYS Fluent predictions to investigate the accuracy of the developed UDF. It is found that the values predicted by the UDF for a spherical particle overlaps the Fluent predictions for the particles temperature, thus illustrating the validity of the code. Further, the in-house code has been modified and the particles surface area has been extended when the particle SF and AR have been introduced. It can be observed that as the aspect ratio increases, and consequently the shape factor of the cylindrical particle decreases, the particle undertakes the stages of combustion quicker.

The UDFs have been incorporated in the biomass combustion cases introduced in Chapter 6. Figures 7.10 and 7.11 show the temperature contours and oxygen concentration contours comparison for biomass combustion with different shape factors, respectively. The spherical shape particles have been compared with cylindrical particles with a SF of 0.87, 0.8 and 0.7 and AR 1, 2.5 and 5, respectively. It can be observed in Figure 7.10 that the temperature contours differ between the cases. The spherical particles have the longest high temperature region, which indicates that the flame is the longest in that case. In the cases with the cylindrical particles assumption, the high temperature region is shorter and more concentrated. Further, in Figure 7.11 it can be observed that the oxygen consumption is more intense for cylindrical particles when comparing with the spherical biomass particles.

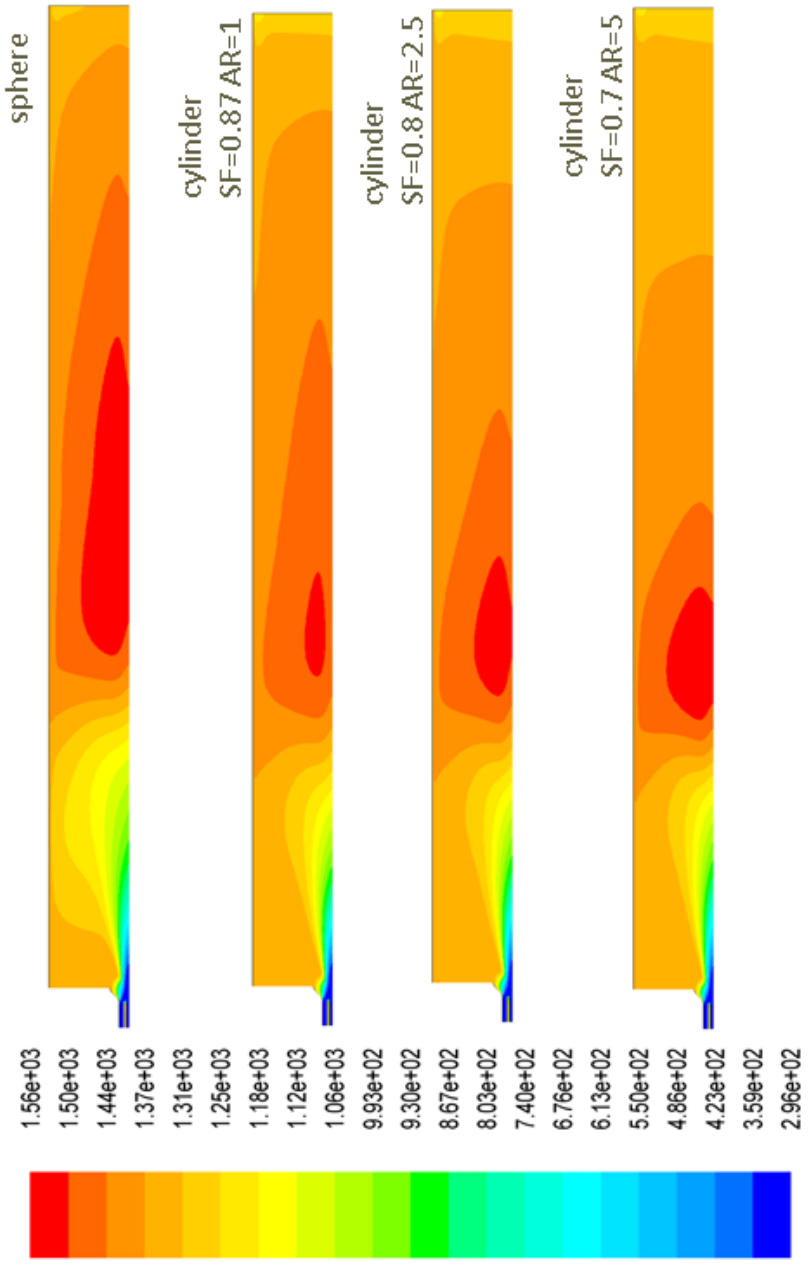

Figure 7.10: Temperature contours for the mixed wood combustion - influence of particle shapes.

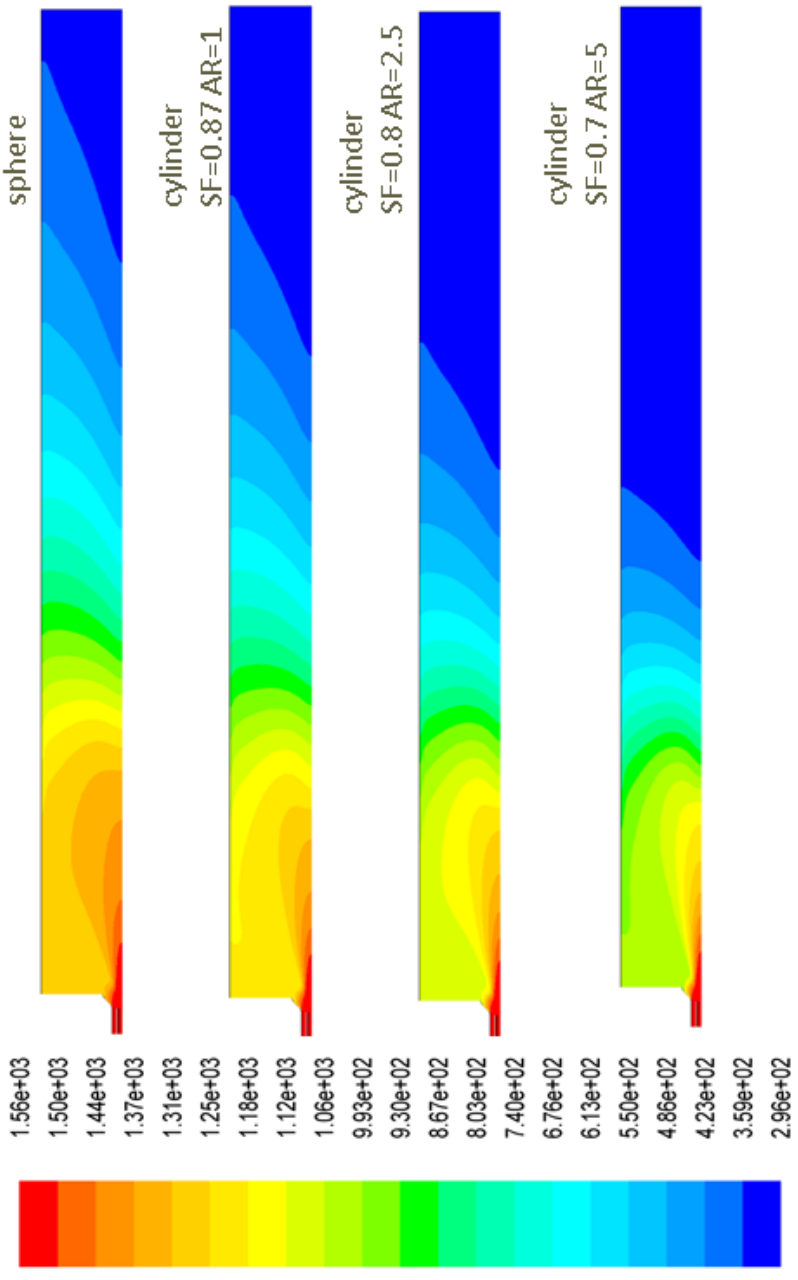

Figure 7.11: Oxygen concentration contours for the mixed wood combustion - influence of particle shapes.

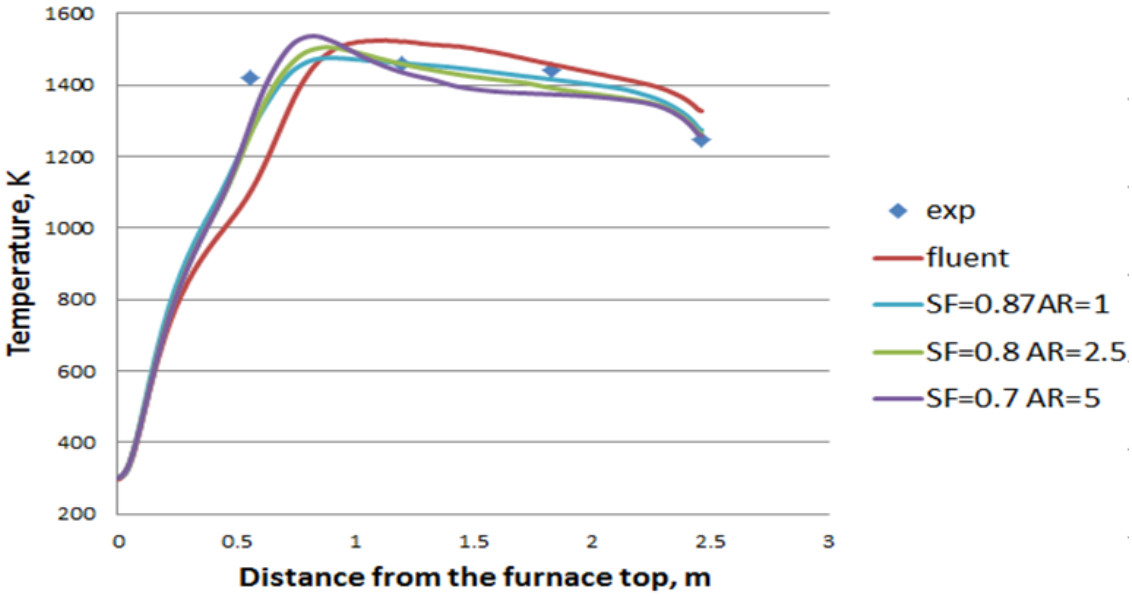

Figure 7.12: Effect of particle shape of mixed wood, namely a SF of 1, 0.87 and 0.8, on the temperature predictions compared with the experimental data.

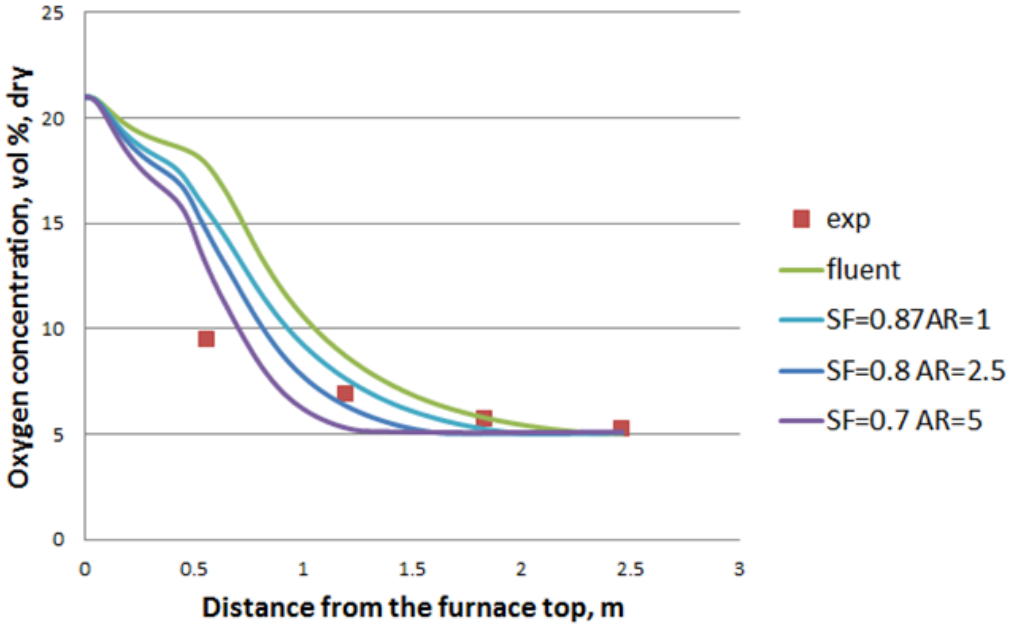

Figure 7.13: Effect of the particle shape of mixed wood, namely a SF of 1, 0.87 and 0.8, on the oxygen level predictions compared with the experimental data.

Figure 7.12 shows the temperature profile for a spherical particle as predicted by ANSYS Fluent (called 'fluent' on the figure) compared with the user defined function for particles with a different shape factor and aspect ratio and the experimental data for the 15 kW jet flame combustion chamber. The assumption of a spherical particle significantly delays the combustion gases to reach the experimental measurements of the temperature profile along the axis of the furnace. Particles with lower shape factors, namely with SF of 0.87, 0.8 and 0.7 and AR 1, 2.5 and 5, respectively, are in better agreement with the experimental data, which can be explained by the enhanced heat exchange process through the extended surface area of the particles.

The oxygen consumption is higher in the near burner region for particles with high AR and low SF, because the combustion is more rapid in this region for particles with an extended surface area. Figure 7.13 shows the profile of the oxygen concentration within the combustion gases across the furnace axis. It is observed that the particles with lower shape factor oxidize faster and consume the available oxygen in the combustion gases.

For both cases, the best agreement with the experimental data have particles with an aspect ratio 2.5 and shape factor 0.8, which is the literature value for the average aspect ratio of the biomass particles.

7.4.2 Influence of the thermal gradient in large biomass particles

The user defined function for particle heating, vaporization, boiling, devolatilization and char combustion has been extended to transient heat conduction within the biomass particles. Figures 7.14 and 7.15 show the effect of the thermally thick and thermally thin particles on the temperature and oxygen concentration along the furnace axis, respectively. It is observed that there is no significant influence of the thermal gradient on

the particle temperature profile and the oxygen level in the combustion gases in comparison to the thermally thin particles, which neglects the thermal conductivity within the particles. This can be explained by the fact that the residence time of the analysed particles is very short and this is because it is a jet flame combustion. Particles have almost straight line trajectories and there is no recirculation zone within the combustion chamber, and this is because it is a jet flame combustion. Therefore, this case does not show significant importance of the thermal gradient within biomass particles. However, this study does give a good indication that the code developed is producing good and reliable insight into how the extended surface area of the irregular biomass particles influence the combustion performance.

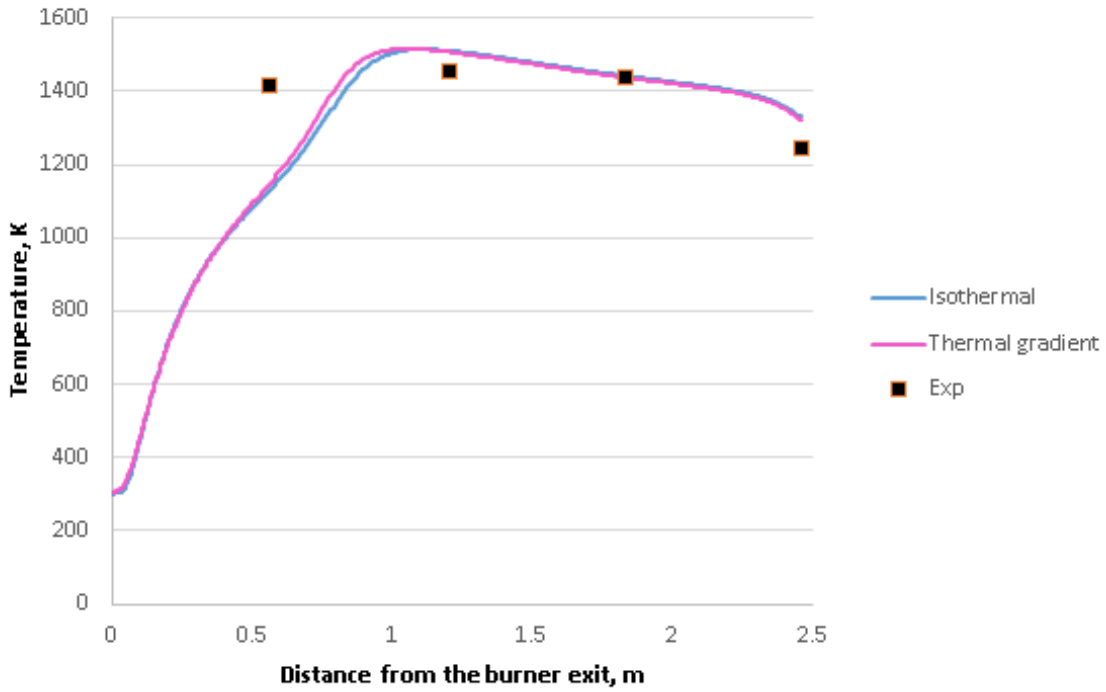

Figure 7.14: Effect of the thermal gradient in the particles of mixed wood compared with isothermal particles and the experimental data on the temperature predictions along the furnace axis (SF = 0.8 and AR = 2.5).

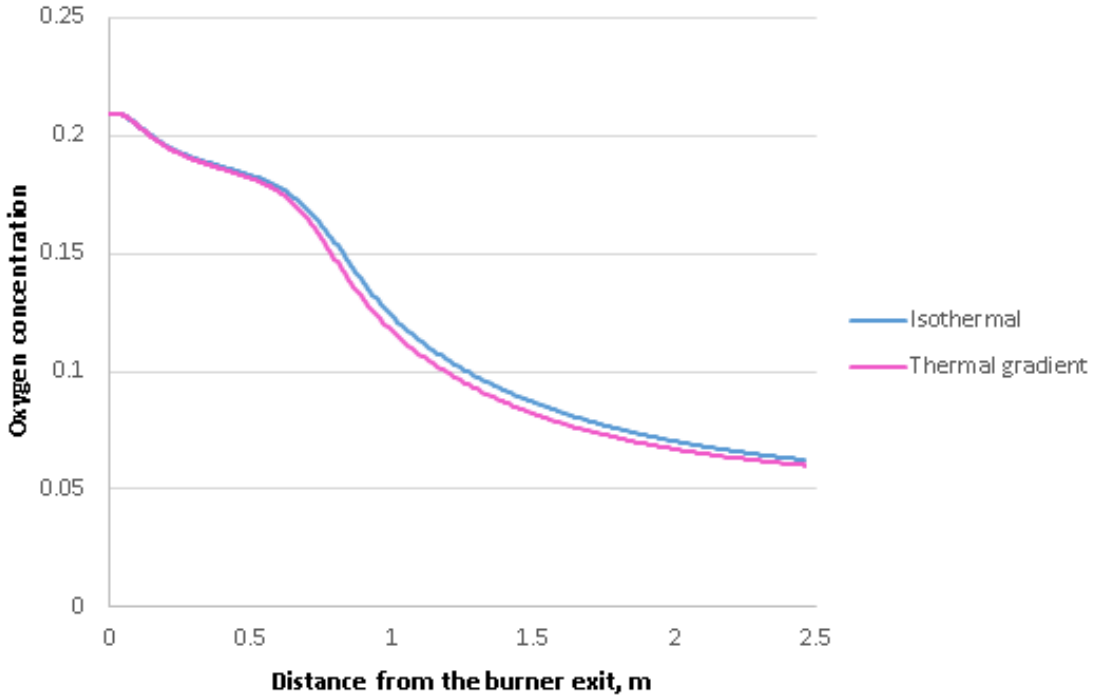

Figure 7.15: Effect of the thermal gradient in the particles of mixed wood compared with isothermal particles on the oxygen level predictions (SF = 0.8 and AR = 2.5).

7.5 Conclusions

In this chapter different particle shapes and their influence on the heat-up curve and combustion performance have been analysed and compared. It has been found that the particle shape has a significant influence on the particle temperature and its heating up, as the irregular shape of the biomass particles extends the contact surface area of the particle with the combustion gases. The higher is the deviation from the ideal shape of the particle - sphere, then the particle surface area increases, the aspect ratio increases, the shape factor decreases and the particle heats up faster than the sphere. Among the different proposed shapes, the cylindrical particle has been found to be a good approximation of the biomass

particle shape in terms of the assumption of the external surface area of the irregular in shape biomass particles. The theoretical calculations for thermally thin particles and analytical calculations for particles with included thermal conductivity within the particles have been performed. It has been found that the incorporation of the thermal gradient in the heat transfer analysis does not significantly influence the numerical predictions of the jet flame combustion. However, it may have a significant impact for large in size biomass particles in the industrial boilers with recirculation zones. Therefore, it is recommended to include the thermal gradient within the particles in the CFD predictions of the combustion of large in size biomass particles.

7.6 Summary

Particle shape plays a significant role in the accurate prediction of the biomass heat exchange between the particle and surrounding combustion gases present in the combustion chamber and therefore the combustion performance. The thermal gradient may be important for large size biomass particles in the CFD predictions of the industrial boilers with extended residence time via recirculation zones. The in-house UDF, including the irregular biomass particle shape and large size of the particles, has been successfully developed and validated with the experimental data.

Chapter 8

Conclusions and future work

8.1 Conclusions

The main question addressed in this thesis are as follows: Is it possible to predict biomass combustion using models which were developed for coal combustion? If not, what are the limitations of using coal combustion models for biomass combustion and how should the model be developed to give accurate predictions of the biomass combustion. In order to answer this question, a number of novel and original developments have been investigated and the results presented and critically analysed.

Experiments on the 250 kW UKCCSRC PACT Combustion Test Facility have been performed in order to investigate the influence of the non-preheated and preheated air on the coal combustion performance and NO_x emissions. The preheat of the combustion air has been found to increase the NO_x emissions. Also, the coal has been replaced with biomass fuel and the main issues related with biomass combustion has been identified, such as high moisture content and large size of the particles which create many challenges while firing this type of fuel.

Further, numerous more experimental measurements were undertaken during the campaign for the validation of the CFD model of coal combustion, such as temperature measurements, flue gas composition

and SIR on the furnace walls. A comprehensive sensitivity analysis of the CFD sub-models for air coal combustion was completed on a 250 kW PACT facility and validated with experimental data. From this analysis, a recommendation for utility boiler modelling, which requires a compromise between accuracy and computational requirement, has been proposed. Further, the CFD model for the PACT facility boiler was employed for the air firing case and validated against the measured data collected during the experimental programme. Also, the CFD modelling predictions and the experimental measurements have been compared with a calculated mass and energy balance for this facility.

The sub-models used for the 250 kW PACT combustion test facility CFD simulations and validated with measurement data, were implemented for the prediction of the 15 kW jet flame combustion. The CFD predictions were compared with the experimental data and it was found that there was good agreement. The models that were identified to give good predictions for both the 250 kW combustion test facility and the 15 kW jet flame combustion chamber were used for biomass combustion. A wide range of properties were used in the CFD modelling and the limitation of the CFD modelling of biomass combustion has been thoroughly investigated, analysed and summarized.

The biomass shape and size have been identified to have a significant influence on the CFD predictions of the biomass combustion performance. Therefore a detailed investigation of the particle shape and size has been performed and a code for the biomass particle combustion has been developed to include the irregular biomass particle shape and the large size of the particles through the inclusion of the thermal conductivity within the large in size biomass particles. The developed code has been implemented in the CFD modelling and the results validated against the experimental data for the 15 kW biomass jet combustion. It was found that the CFD predictions indicate a better agreement with the experimental data

when the irregular shape and large size particles have been included in the simulations.

Solid biomass has an important role as a fuel that can replace coal in large scale power generation. The retrofitting of coal fired boilers to biomass combustion and the development of boilers designed to fire biomass fuel is already being employed. On a domestic scale, in the UK between 2012 and 2019, the Drax power station has demonstrated that the biomass combustion technology is practical and commercially viable [48]. Further, in 2016, the Lynemouth coal-fired plant was converted into a biomass-fuelled power plant [49].

Biomass fuel combustion for a large scale plant operation benefits in the reduction of NO_x, SO_2, dust and CO_2 emissions, and thus it supports the climate change targets. The emissions from the coal and biomass combustion have been compared. It has been found that biomass combustion gives a potential for the reduction in the CO_2, NO_x and SO_x emissions, however, this depends on the biomass fuel composition. Nevertheless, biomass combustion needs more investigation and development in order to reduce the potential operational problems and increases the efficiency of the biomass combustion. Several of these issues have been specifically addressed in this thesis and contribute towards the following:

- Obtaining a better understanding of the biomass combustion process;
- Illustrating the limitations in the commercially used sub-models employed in the CFD code, which give accurate predictions for coal combustion, but this needs development for biomass combustion predictions;
- Identifying of the pollutant emissions from the biomass fuel and ways to tackle them;
- Developing sub-models for biomass combustion that incorporate the

irregular shape and size of the biomass particles;

- Obtaining a better understanding of the non-spherical shape of the particles and its influence on the heat transfer and therefore combustion performance;
- Obtaining a better understanding of the thermal conductivity within the particle for large in size particles of biomass fuel;
- Validating the coal combustion CFD models and biomass CFD predictions with experimental data;
- Investigating areas for further development for accurate biomass CFD modelling.

8.2 Topics for further research

A good topic of possible future research would be the simulation of the biomass combustion for a large scale boiler with the implementation of the developed code for irregular shape biomass particles and the employment of the thermal gradients within the biomass particles.

Another topic of possible further research would be the simulation of biomass combustion under air and oxy-fuel conditions using both the RANS and LES approaches, together with irregular biomass particle shape and thermal gradient model. Further, the LES approach may produce better insight into the turbulence and mixing of the combustion gases and this may give better numerical predictions of the turbulent mixing in the near-burner region.

Further work is required in the development of a predictive chemical kinetic model of biomass devolatilization. Further, it would be beneficial to include the division of the biomass particles into three components: cellulose, hemicellulose and lignin and the implementation of separate devolatilization parameters for these components. This may give more

accurate predictions of the devolatilization of biomass, rather than the usage of a single devolatilization parameter.

Further laboratory scale experiments to establish the accurate kinetics of the biomass combustion and properties is required. Suggested future experiments are to predict accurate devolatilization rates and char combustion rates, as well as the structural composition of biomass - cellulose, hemicellulose and lignin.

The single biomass combustion experimental investigation of the biomass combustion stages, swelling, thermal gradient, thermal conductivity, solid particle density, devolatilization rates, high temperature volatile yields would be beneficial for a better understanding of the biomass combustion process and a more accurate CFD modelling.

Experiments on particle shape would also be beneficial in order to predict the particle size distribution based on the particle shape. The particle size distribution should be measured in 3D based on the volume rather than the particle size diameter. The Rosin-Rammler particle distribution predicts well the coal particle size distribution, however, for biomass fuel it needs further development in order to describe the accurate particle size distribution.

Implementation of the potassium released from the biomass fuel would be also beneficial. Therefore, experimental investigations on potassium release during the thermal conversion of the biomass fuel is needed. This topic of further research is connected to the understanding of the interaction between the potassium in the biomass fuel and the other accompanying inorganic content that is present in the biomass fuel. This is of importance since it can then lead to the development of the ash behaviour control, which will help to control the ash fouling and slagging in pulverised fuel boilers.

In conclusion, biomass combustion offers a great opportunity to reduce the CO_2 emissions. Therefore, a key focus is on the CFD modelling

of biomass combustion. When the biomass combustion is predicted accurately using CFD modelling, the development and optimisation of the burners and boilers can take place and the implementation of this technology. Also, when air biomass combustion is predicted accurately, the development of oxy biomass combustion can take place and the retrofitting of the biomass boiler into oxy-fuel use ready for commercialisation. Oxy biomass combustion offers negative carbon dioxide emissions and this will ultimately increase the lifespan of the limited fossil fuels that remain in the world. Further development of biomass combustion and oxy-biomass combustion will be crucial in the large-scale deployment of BECCS.

Bibliography

[1] International Energy Agency, "World Energy Outlook 2019." https://doi.org/10.1787/caf32f3b-en.

[2] British Petroleum, "BP Energy Outlook 2016." https://www.bp.com/content/dam/bp/business-sites/en/global/corporate/pdfs/energy-economics/energy-outlook/bp-energy-outlook-2016.pdf.

[3] International Energy Agency, "World Energy Outlook - Executive Summary." https://webstore.iea.org/world-energy-outlook-2013, 2013.

[4] World Energy Council, "World Energy Resources: 2013 Survey." https://www.worldenergy.org/publications/entry/world-energy-resources-2013-survey.

[5] British Petroleum, "BP Statistical Review of World Energy 2018." https://www.bp.com/content/dam/bp/business-sites/en/global/corporate/pdfs/energy-economics/statistical-review/bp-stats-review-2018-full-report.pdf.

[6] British Petroleum, "BP Energy Outlook 2018." https://www.bp.com/content/dam/bp/business-sites/en/global/corporate/pdfs/energy-economics/energy-outlook/bp-energy-outlook-2018.pdf.

[7] International Energy Agency, "Technology Roadmap - Carbon Capture and Storage." https://webstore.iea.org/technology-roadmap-carbon-capture-and-storage-2013, 2013.

[8] GeoHive, "The World's Population." http://www.geohive.com/earth/his{_}history3.aspx. Accessed: 2016-06-20.

[9] International Energy Agency, "World Energy Outlook 2017." https://www.iea.org/reports/world-energy-outlook-2017.

[10] ExxonMobil, "2018 Outlook for Energy: A View to 2040." https://www.aop.es/wp-content/uploads/2019/05/2018-Outlook-for-Energy-Exxon.pdf.

[11] British Petroleum, "BP Statistical Review of World Energy 2019." https://www.bp.com/content/dam/bp/business-sites/en/global/corporate/pdfs/energy-economics/statistical-review/bp-stats-review-2019-full-report.pdf.

[12] International Energy Agency, "World Energy Outlook 2018." https://www.iea.org/reports/world-energy-outlook-2018.

[13] United States Energy Information Administration, "International Energy Outlook 2016." https://www.eia.gov/outlooks/ieo/pdf/0484(2016).pdf.

[14] World Resources Institute, "CCS Guidelines: Guidelines for Carbon Dioxide Capture, Transport, and Storage." http://pdf.wri.org/ccs_guidelines.pdf, 2011.

[15] Carbon Dioxide Information Analysis Center (CDIAC), "Annual CO_2 emissions." http://cdiac.ornl.gov/CO2_Emission/. Accessed: 2018-12-20.

[16] Ritchie, Hannah and Roser, Max, "CO_2 and other Greenhouse Gas Emissions." https://ourworldindata.org/co2-and-other-greenhouse-gas-emissions. Accessed: 2018-12-20.

[17] International Energy Agency, "Global Energy & CO_2 Status Report 2018." https://webstore.iea.org/global-energy-co2-status-report-2018.

[18] F. Chambers and M. Ogle, eds., *Climate Change: Critical Concepts in the Environment, Volume 1*. Taylor & Francis, 2002.

[19] A. F. Ghoniem, "Needs, resources and climate change: Clean and efficient conversion technologies," *Progress in Energy and Combustion Science*, vol. 37(1), pp. 15–51, 2011.

[20] International Energy Agency, "Energy and Climate Change - World Energy Outlook Special Report." https://webstore.iea.org/weo-2015-special-report-energy-and-climate-change, 2015.

[21] Intergovernmental Panel on Climate Change, "Climate Change 2007: Synthesis Report." https://www.ipcc.ch/report/ar4/syr/.

[22] Intergovernmental Panel on Climate Change, "Climate Change 2014 Synthesis Report Summary Chapter for Policymakers." https://www.ipcc.ch/site/assets/uploads/2018/02/AR5_SYR_FINAL_SPM.pdf.

[23] Department Of Energy and Climate Change, "Climate Change Act 2008." http://www.legislation.gov.uk/ukpga/2008/27/pdfs/ukpga_20080027_en.pdf.

[24] Committee on Climate Change, "Global Action on Climate Change." https://www.theccc.org.uk/tackling-climate-change/the-legal-landscape/global-action-on-climate-change/, 2008.

[25] United Kingdom Advanced Power Generation Technology Forum, "Cleaner Fossil Power Generation in the 21st Century - Moving Forward." https://www.apgtf-uk.com/index.php/publications/publications-2014/doc_download/15-cleaner-fossil-power-generation-in-the-21st-century/-moving-forward-2014, 2014.

[26] A. Adamantiades and I. Kessides, "Nuclear power for sustainable development: Current status and future prospects," *Energy Policy*, vol. 37(12), pp. 5149–5166, 2009.

[27] B. J. P. Buhre, L. K. Elliott, C. D. Sheng, R. P. Gupta, and T. F. Wall, "Oxy-fuel combustion technology for coal-fired power generation," *Progress in Energy and Combustion Science*, vol. 31(4), pp. 283–307, 2005.

[28] S. Van Loo and J. Koppeja, eds., *The Handbook of Biomass Combustion and Co-firing*. Earthscan, 2008.

[29] United States Department of Energy - National Energy Technology Laboratory, "Report of the Interagency Task Force on Carbon Capture and Storage," 2010.

[30] T. F. Wall, "Combustion processes for carbon capture," *Proceedings of the Combustion Institute*, vol. 31(1), pp. 31–47, 2007.

[31] C. Fu and T. Gundersen, "Techno-economic analysis of CO_2 conditioning processes in a coal based oxy-combustion power plant," *International Journal of Greenhouse Gas Control*, vol. 9, pp. 419–427, 2012.

[32] Y. Tan, W. Nookuea, H. Li, E. Thorin, and J. Yan, "Property impacts on Carbon Capture and Storage (CCS) processes: A review," *Energy Conversion and Management*, vol. 118, pp. 204–222, 2016.

[33] J. Gibbins and H. Chalmers, "Carbon capture and storage," *Energy Policy*, vol. 36(12), pp. 4317–4322, 2008.

[34] D. Y. Leung, G. Caramanna, and M. M. Maroto-Valer, "An overview of current status of carbon dioxide capture and storage technologies," *Renewable and Sustainable Energy Reviews*, vol. 39, pp. 426–443, 2014.

[35] Scottish Carbon Capture and Storage (SCCS), "www.sccs.org.uk." http://www.sccs.org.uk. Accessed: 2016-06-16.

[36] L. Chen, S. Z. Yong, and A. F. Ghoniem, "Oxy-fuel combustion of pulverized coal: Characterization, fundamentals, stabilization and CFD modeling," *Progress in Energy and Combustion Science*, vol. 38(2), pp. 156–214, 2012.

[37] M. B. Toftegaard, J. Brix, P. a. Jensen, P. Glarborg, and A. D. Jensen, "Oxy-fuel combustion of solid fuels," *Progress in Energy and Combustion Science*, vol. 36(5), pp. 581–625, 2010.

[38] S. P. Deolalkar and S. P. Deolalkar, "Chapter 1 - Carbon Capture and Storage (CCS)," in *Designing Green Cement Plants*, pp. 49–58, Butterworth-Heinemann, 2016.

[39] T. Wall, Y. Liu, C. Spero, L. Elliott, S. Khare, R. Rathnam, F. Zeenathal, B. Moghtaderi, B. Buhre, C. Sheng, R. Gupta, T. Yamada, K. Makino, and J. Yu, "An overview on oxyfuel coal combustion - State of the art research and technology development," *Chemical Engineering Research and Design*, vol. 87(8), pp. 1003–1016, 2009.

[40] L. Elwell and W. Grant, "Technology options for capturing CO_2," *Power*, vol. 150(8), pp. 60–65, 2006.

[41] M. Kanniche, R. Gros-Bonnivard, P. Jaud, J. Valle-Marcos, J.-M. Amann, and C. Bouallou, "Pre-combustion, post-combustion and oxy-combustion in thermal power plant for CO_2 capture," *Applied Thermal Engineering*, vol. 30(1), pp. 53–62, 2010.

[42] J. Smart, P. O'Nions, and G. Riley, "Radiation and convective heat transfer, and burnout in oxy-coal combustion," *Fuel*, vol. 89(9), pp. 2468–2476, 2010.

[43] K. Stechly, G. Wecel, and D. B. Ingham, "CFD modelling of air and oxy-coal combustion," *International Journal of Numerical Methods for Heat & Fluid Flow*, vol. 24(4), pp. 825 – 844, 2014.

[44] J. Smart, G. Lu, Y. Yan, and G. Riley, "Characterisation of an oxy-coal flame through digital imaging," *Combustion and Flame*, vol. 157(6), pp. 1132–1139, 2010.

[45] R. Doctor and A. Palmer, "Transport of CO_2," in *IPCC Special Report on Carbon Dioxide Capture and Storage* (B. Metz, O. Davidson, H. C. de Coninck, M. Loos, and L. A. Meyer, eds.), pp. 179–194, Cambridge University Press, 2005.

[46] J. Wolf and Dong, *Biomass Combustion Science, Technology and Engineering*. Elsevier, 2013.

[47] J. M. Jones, A. R. Lea-Langton, L. Ma, M. Pourkashanian, and A. Williams, *Pollutants Generated by the Combustion of Solid Biomass Fuels*. SpringerBriefs in Applied Sciences and Technology, London: Springer London, 2014.

[48] P. Mason, L. Darvell, J. Jones, M. Pourkashanian, and A. Williams, "Single particle flame-combustion studies on solid biomass fuels," *Fuel*, vol. 151, pp. 21–30, 2015.

[49] Power Technology, "Lynemouth Biomass Power Station, Northumberland." `https://www.power-technology.com/projects/lynemouth-biomass-power-station-northumberland/`. Accessed: 2018-10-01.

[50] European Technology Platform for Zero Emission Fossil Fuels Power Plants (ZEP Platform) and Steering Committee of the European Biofuels Technology Platform (EBTP), "Biomass with CO_2 Capture and Storage (Bio-CCS)," 2012.

[51] D. P. Plant, "Carbon dioxide now being captured in first of its kind BECCS pilot." https://www.drax.com/press_release/world-first-co2-beccs-ccus/. Accessed: 2019-06-24.

[52] H. K. Versteeg and W. Malalaskekera, *An Introduction to Computational Fluid Dynamics*. Harlow: Pearson Prentice Hall, 2007.

[53] A. Pawar, "Computational Fluid Dynamics: An Emerging Field in Engineering," *Journal of Engineering Research and Studies*, vol. 3(1), pp. 96–100, 2012.

[54] T. Dixon, A. Mann, F. Plaza, and W. Gilfillan, "Development of advanced technology for biomass combustion - CFD as an essential tool," *Fuel*, vol. 84(10), pp. 1303–1311, 2005.

[55] A. Williams, M. Pourkashanian, and J. Jones, "Combustion of pulverised coal and biomass," *Progress in Energy and Combustion Science*, vol. 27(6), pp. 587–610, 2001.

[56] World Energy Council, "World Energy Resources Bioenergy 2016." https://www.worldenergy.org/assets/images/imported/2016/10/World-Energy-Resources-Full-report-2016.10.03.pdf.

[57] World Bioenergy Association, "WBA Global Bioenergy Statistics 2016." https://worldbioenergy.org/uploads/WBA%20Global%20Bioenergy%20Statistics%202016.pdf.

[58] A. Demirbas, "Combustion characteristics of different biomass fuels," *Progress in Energy and Combustion Science*, vol. 30(2), pp. 219–230, 2004.

[59] D. J. Bushnell, C. Haluzok, and A. Dadkhah-Nikoo, "Biomass Fuel Characterizatio : Testing and Evaluating the Combustion Characteristics of Selected Biomass Fuels: Final Report," 1990.

[60] P. McKendry, "Energy production from biomass (part 1): overview of biomass," *Bioresource Technology*, vol. 83, no. 1, pp. 37 – 46, 2002.

[61] DEFRA, "UK Biomass Strategy." http://www.globalbioenergy.org/uploads/media/0705_Defra_-_UK_Biomass_Strategy_01.pdf, 2007.

[62] Thounrtcnhillstar, "Types of agriculture waste." http://thounrtcnhillstar.typepad.com/. Accessed: 2016-07-19.

[63] Air Quality Expert Group , "The Potential Air Quality Impacts from Biomass Combustion." https://uk-air.defra.gov.uk/assets/documents/reports/cat11/1708081027_170807_AQEG_Biomass_report.pdf.

[64] T. Nussbaumer, "Combustion and Co-combustion of Biomass: Fundamentals, Technologies, and Primary Measures for Emission Reduction," *Energy and Fuels*, vol. 17(6), pp. 1510–1521, 2003.

[65] The American Forest & Paper Association, "Forest Biomass Residuals Worthy of Carbon Neutral Recognition." https://afandpa.org/docs/default-source/1pgrs/2019-fall-update/carbon-neutral-recognition-august-2019.pdf, 2019.

[66] Demirbas, Ayhan, "Biomass resource facilities and biomass conversion processing for fuels and chemicals," *Energy Conversion and Management*, vol. 42(11), pp. 1357–1378, 2001.

[67] BrightMags, "Biomass carbon neutrality.." http://brightmags.com/how-does-biomass-work/. Accessed: 2016-07-19.

[68] Mladenovic, Milica and Paprika, Milijana and Marinkovic, Ana, "Denitrification techniques for biomass combustion," *Renewable and Sustainable Energy Reviews*, vol. 82, pp. 3350 – 3364, 2018.

[69] J. Zink and H. Goodnight, "Low NO_x burner." http://www.google.com/patents/US4004875, 1977. Accessed: 2016-07-19.

[70] G. Wielgosinski, P. Lechtanska, and O. Namiecinska, "Emission of some pollutants from biomass combustion in comparison to hard coal combustion," *Journal of the Energy Institute*, vol. 90, no. 5, pp. 787 – 796, 2017.

[71] J. D. McDonald, E. M. F. Barbara Zielinska, J. C. Sagebiel, J. C. Chow, and J. G. Watson, "Fine Particle and Gaseous Emission Rates from Residential Wood Combustion," *Environmental Science and Technology*, vol. 34, no. 11, pp. 2080 – 2091, 2000.

[72] D. S. Clery, P. E. Mason, C. M. Rayner, and J. M. Jones, "The effects of an additive on the release of potassium in biomass combustion," *Fuel*, vol. 214, pp. 647 – 655, 2018.

[73] J. E. Houck and J. Crouch, "Updated Emissions Data for Revision of AP-42 Section 1.9, Residential Fireplaces," *U.S. Environmental Protection Agency*, 2002.

[74] P. E. Mason, J. M. Jones, L. I. Darvell, and A. Williams, "Gas phase potassium release from a single particle of biomass during high temperature combustion," *Proceedings of the Combustion Institute*, vol. 36, no. 2, pp. 2207 – 2215, 2017.

[75] A. Demirbas, "Estimating of Structural Composition of Wood and Non-Wood Biomass Samples," *Energy Sources*, vol. 27(8), pp. 761–767, 2005.

[76] H. Lu, *Experimental and modelling investigation of biomass particle combustion*. PhD thesis, Brigham Young University, 2006.

[77] A. J. Baker, "Wood Fuel Properties and Fuel Products from Woods," in *Fuelwood Management and Utilization Seminar*, (Michigan State Univc., East Lansing, MI), pp. 14–25, 1982.

[78] H. Yang, R. Yan, H. Chen, D. H. Lee, and C. Zheng, "Characteristics of hemicellulose, cellulose and lignin pyrolysis," *Fuel*, vol. 86(12-13), pp. 1781–1788, 2007.

[79] H. Lu, E. Ip, J. Scott, P. Foster, M. Vickers, and L. L. Baxter, "Effects of particle shape and size on devolatilization of biomass particle," *Fuel*, vol. 89(5), pp. 1156–1168, 2010.

[80] A. Williams, R. Backreedy, R. Habib, J. Jones, and M. Pourkashanian, "Modelling coal combustion: the current position," *Fuel*, vol. 81(5), pp. 605–618, 2002.

[81] T. Abbas, P. G. Costen, and F. C. Lockwood, "Solid fuel utilization: From coal to biomass," *Symposium (International) on Combustion*, vol. 26(2), pp. 3041–3058, 1996.

[82] R. Backreedy, L. Fletcher, J. Jones, L. Ma, M. Pourkashanian, and A. Williams, "Co-firing pulverised coal and biomass: a modeling approach," *Proceedings of the Combustion Institute*, vol. 30(2), pp. 2955–2964, 2005.

[83] A. Williams, J. Jones, and M. Pourkashanian, "Co-firing coal/biomass and the estimation of burnout and NO_x formation." `http://www.coalresearchforum.org/20080604_b79_williams.pdf`, 2008. Accessed: 2016-07-19.

[84] J. M. Jones, M. Pourkashanian, A. Williams, and D. Hainsworth, "A comprehensive biomass combustion model," *Renewable Energy*, vol. 19(1-2), pp. 229–234, 2000.

[85] C. V. da Silva, M. L. S. Indrusiak, and A. B. Beskow, "CFD Analysis of the Pulverized Coal Combustion Processes in a 160 MWe Tangentially-Fired-Boiler of a Thermal Power Plant," *Journal of the Brazilian Society of Mechanical Sciences and Engineering*, vol. 32(4), pp. 427–436, 2010.

[86] I. Constenla, J. L. Ferrín, and L. Saavedra, "Numerical study of a 350 MWe tangentially fired pulverized coal furnace of the As Pontes Power Plant," *Fuel Processing Technology*, vol. 116, pp. 189–200, 2013.

[87] P. Edge, S. R. Gubba, L. Ma, R. Porter, M. Pourkashanian, and A. Williams, "LES modelling of air and oxy-fuel pulverised coal combustion - Impact on flame properties," *Proceedings of the Combustion Institute*, vol. 33(2), pp. 2709–2716, 2011.

[88] J. Fan, L. Qian, Y. Ma, P. Sun, and K. Cen, "Computational modeling of pulverized coal combustion processes in tangentially fired furnaces," *Chemical Engineering Journal*, vol. 81(1-3), pp. 261–269, 2001.

[89] A. G. Clements, S. Black, J. Szuhánszki, K. Stechly, A. Pranzitelli, W. Nimmo, and M. Pourkashanian, "LES and RANS of air and oxy-coal combustion in a pilot-scale facility: Predictions of radiative heat transfer," *Fuel*, vol. 151, pp. 146–155, 2015.

[90] A. A. Bhuiyan and J. Naser, "Computational modelling of co-firing of biomass with coal under oxy-fuel condition in a small scale furnace," *Fuel*, vol. 143, pp. 455–466, 2015.

[91] D. Gera, M. Mathur, M. Freeman, and W. O'Dowd, "Moisture and char reactivity modeling in pulverized coal combustors," *Combustion Science and Technology*, vol. 172(1), pp. 35–69, 2001.

[92] S. Rehfeldt, C. Kuhr, M. Ehmann, C. Bergins, G. Scheffknecht, and J. Maier, "Basic experiments and CFD calculations of air and oxyfuel firing of lignite and bituminous coals in 0.5 and 1 MW scale combustion test facilities," *The 34th international technical conference on clean coal and fuel systems*, 2009.

[93] C. R. Shaddix and A. Molina, "Particle imaging of ignition and devolatilization of pulverized coal during oxy-fuel combustion," *Proceedings of the Combustion Institute*, vol. 32(2), pp. 2091–2098, 2009.

[94] J. Brix, P. A. Jensen, and A. D. Jensen, "Coal devolatilization and char conversion under suspension fired conditions in O_2/N_2 and O_2/CO_2 atmospheres," *Fuel*, vol. 89(11), pp. 3373–3380, 2010.

[95] R. Khatami, C. Stivers, and Y. A. Levendis, "Ignition characteristics of single coal particles from three different ranks in O_2/N_2 and O_2/CO_2 atmospheres," *Combustion and Flame*, vol. 159(12), pp. 3554–3568, 2012.

[96] A. Molina and C. R. Shaddix, "Ignition and devolatilization of pulverized bituminous coal particles during oxygen/carbon dioxide coal combustion," *Proceedings of the Combustion Institute*, vol. 31(2), pp. 1905–1912, 2007.

[97] S. Pickard, S. Daood, M. Pourkashanian, and W. Nimmo, "Co-firing coal with biomass in oxygen- and carbon dioxide-enriched atmospheres for CCS applications," *Fuel*, vol. 137, pp. 185–192, 2014.

[98] S. Black, J. Szuhánszki, A. Pranzitelli, L. Ma, P. Stanger, D. Ingham, and M. Pourkashanian, "Effects of firing coal and biomass under oxy-fuel conditions in a power plant boiler using CFD modelling," *Fuel*, vol. 113, pp. 780–786, 2013.

[99] L. Ma, J. Jones, M. Pourkashanian, and A. Williams, "Modelling the combustion of pulverized biomass in an industrial combustion test furnace," *Fuel*, vol. 86(12-13), no. 12-13, pp. 1959–1965, 2007.

[100] L. Ma, M. Gharebaghi, R. Porter, M. Pourkashanian, J. Jones, and A. Williams, "Modelling methods for co-fired pulverised fuel furnaces," *Fuel*, vol. 88(12), pp. 2448–2454, 2009.

[101] N. Nikolopoulos, M. Agraniotis, I. Violidakis, E. Karampinis, A. Nikolopoulos, P. Grammelis, C. Papapavlou, S. Tzivenis, and E. Kakaras, "Parametric investigation of a renewable alternative for utilities adopting the co-firing lignite/biomass concept," *Fuel*, vol. 113, pp. 873–897, 2013.

[102] A. A. Bhuiyan and J. Naser, "Numerical Modeling of Biomass Co-combustion with Pulverized coal in a Small Scale Furnace," *Procedia Engineering*, vol. 105, pp. 504–511, 2015.

[103] A. A. Bhuiyan and J. Naser, "CFD modelling of co-firing of biomass with coal under oxy-fuel combustion in a large scale power plant," *Fuel*, vol. 159, pp. 150–168, 2015.

[104] A. A. Bhuiyan and J. Naser, "Thermal characterization of coal/straw combustion under air/oxy-fuel conditions in a swirl-stabilized furnace: A CFD modelling," *Applied Thermal Engineering*, vol. 93, pp. 639–651, 2016.

[105] J. Szuhánszki, S. Black, A. Pranzitelli, L. Ma, P. Stanger, D. Ingham, and M. Pourkashanian, "Evaluation of the Performance of a Power Plant Boiler Firing Coal, Biomass and a Blend Under Oxy-fuel Conditions as a CO_2 Capture Technique," *Energy Procedia*, vol. 37, pp. 1413–1422, 2013.

[106] Y. Chen, S. Charpenay, A. Jensen, M. A. Wójtowicz, and M. A. Serio, "Modeling of biomass pyrolysis kinetics," *Symposium (International) on Combustion*, vol. 27(1), pp. 1327–1334, 1998.

[107] I. Smith, "The combustion rates of coal chars: A review," *Symposium (International) on Combustion*, vol. 19(1), pp. 1045–1065, 1982.

[108] A. Haider and O. Levenspiel, "Drag coefficient and terminal velocity of spherical and nonspherical particles," *Powder Technology*, vol. 58(1), pp. 63–70, 1989.

[109] J. F. Wendt, *Computational Fluid Dynamics - An Introduction*, vol. 44. Berlin: Springer, third ed., 2009.

[110] R. Viskanta and M. Mengüç, "Radiation heat transfer in combustion systems," *Progress in Energy and Combustion Science*, pp. 97–160, 1987.

[111] G. Yeoh and K. Yuen, *Computational Fluid Dynamics in Fire Engineering*. Amsterdam, Boston: Elsevier/Academic Press, 2009.

[112] I. Glassman and R. A. Yetter, *Combustion*. London: Academic Press, 2008.

[113] T. Poinsot and D. Veynante, "Theoretical and Numerical Combustion," *Combustion and Flame*, vol. 32, p. 534, 2005.

[114] ANSYS Fluent, "ANSYS Fluent 12.0 User's Guide," *Ansys Inc*, pp. 1–2498, 2009.

[115] B. Launder and D. Spalding, "The numerical computation of turbulent flows," *Computer Methods in Applied Mechanics and Engineering*, vol. 3(2), pp. 269–289, 1974.

[116] T.-H. Shih, W. W. Liou, A. Shabbir, Z. Yang, and J. Zhu, "A new k-ϵ eddy viscosity model for high reynolds number turbulent flows," *Computers & Fluids*, vol. 24(3), pp. 227–238, 1995.

[117] M. M. Gibson and B. E. Launder, "Ground effects on pressure fluctuations in the atmospheric boundary layer," *Journal of Fluid Mechanics*, vol. 86(3), p. 491, 2006.

[118] B. E. Launder, "Second-moment closure: present... and future?," *International Journal of Heat and Fluid Flow*, vol. 10(4), pp. 282–300, 1989.

[119] B. E. Launder, G. J. Reece, and W. Rodi, "Progress in the development of a Reynolds-stress turbulence closure," *Journal of Fluid Mechanics*, vol. 68(3), pp. 537–566, 1975.

[120] R. Porter, F. Liu, M. Pourkashanian, A. Williams, and D. Smith, "Evaluation of solution methods for radiative heat transfer in gaseous oxy-fuel combustion environments," *Journal of Quantitative Spectroscopy and Radiative Transfer*, vol. 111(14), pp. 2084–2094, 2010.

[121] R. A. Bialecki, *Solving heat radiation problems using the boundary element method*. Southampton, Boston: Computational Mechanics, 1993.

[122] M. F. Modest, *Radiative Heat Transfer*, vol. 18. Amsterdam, Boston: Academic Press, second ed., 2003.

[123] C. E. Baukal, *Oxygen-enhanced combustion*. Boca Raton: CRC Press, second ed., 2013.

[124] J. Y. Murthy and S. R. Mathur, "Finite Volume Method for Radiative Heat Transfer Using Unstructured Meshes," *Journal of Thermophysics and Heat Transfer*, vol. 12(3), pp. 313–321, 1998.

[125] H. Hottel and A. F. Sarofim, *Radiative transfer*, vol. 15(5). New York: McGraw-Hill, 1967.

[126] T. F. Smith, Z. F. Shen, and J. N. Friedman, "Evaluation of Coefficients for the Weighted Sum of Gray Gases Model," *Journal of Heat Transfer*, vol. 104(4), p. 602, 1982.

[127] R. Jovanovic, B. Rasuo, P. Stefanovic, D. Cvetinovic, and B. Swiatkowski, "Numerical investigation of pulverized coal jet flame characteristics under different oxy-fuel conditions," *International Journal of Heat and Mass Transfert*, vol. 58(1), pp. 467–494, 1999.

[128] B. Franchetti, F. C. Marincola, S. Navarro-Martinez, and A. Kempf, "Large Eddy Simulation of a pulverised coal jet flame," *Proceedings of the Combustion Institute*, vol. 34, no. 2, pp. 2419 – 2426, 2013.

[129] J. Cai, M. Handa, and M. F. Modest, "Eulerian - Eulerian multi-fluid methods for pulverized coal flames with nongray radiation," *Combustion and Flame*, vol. 162, no. 4, pp. 1550 – 1565, 2015.

[130] F. Lockwood and A. Salooja, "The prediction of some pulverized bituminous coal flames in a furnace," *Combustion and Flame*, vol. 54, no. 1, pp. 23 – 32, 1983.

[131] B. Visser, J. Smart, W. V. D. Kamp, and R. Weber, "Measurements and predictions of quarl zone properties of swirling pulverised coal flames," *Symposium (International) on Combustion*, vol. 23, no. 1, pp. 949 – 955, 1991. Twenty-Third Symposium (International) on Combustion.

[132] M. Y. Chernetskiy, V. A. Kuznetsov, A. A. Dekterev, N. A. Abaimov, and A. F. Ryzhkov, "Comparative analysis of turbulence model effect on description of the processes of pulverized coal combustion at flow swirl," *Thermophysics and Aeromechanics*, vol. 23, no. 4, pp. 591–602, 2016.

[133] R. Backreedy, L. Fletcher, L. Ma, M. Pourkashanian, and A. Williams, "Modelling pulverised coal combustion using a detailed coal combustion model," *Combustion Science and Technology*, vol. 178, no. 4, pp. 763–787, 2006.

[134] M. Gharebaghi, R. Irons, L. Ma, M. Pourkashanian, and A. Pranzitelli, "Large Eddy Simulation of oxy-coal combustion in an industrial combustion test facility," *International Journal of Greenhouse Gas Control*, vol. 5, pp. S100 – S110, 2011.

[135] M. Muller, U. Schnell, S. Grathwohl, JorgMaier, and G. Scheffknecht, "Evaluation of Oxy-coal Combustion Modelling at Semi-industrial Scale," *Energy Procedia*, vol. 23, pp. 197 – 206, 2012. The 6th Trondheim Conference on CO_2 Capture, Transport and Storage.

[136] M. Stollinger, B. Naud, D. Roekaerts, N. Beishuizen, and S. Heinz, "PDF modeling and simulations of pulverized coal combustion - Part 2: Application," *Combustion and Flame*, vol. 160, no. 2, pp. 396 – 410, 2013.

[137] G. Olenik, O. Stein, and A. Kronenburg, "LES of swirl-stabilised pulverised coal combustion in IFRF furnace No. 1," *Proceedings of the Combustion Institute*, vol. 35, no. 3, pp. 2819 – 2828, 2015.

[138] M. Rabacal, B. Franchetti, F. C. Marincola, F. Proch, M. Costa, C. Hasse, and A. Kempf, "Large Eddy Simulation of coal combustion in a large-scale laboratory furnace," *Proceedings of the Combustion Institute*, vol. 35, no. 3, pp. 3609 – 3617, 2015.

[139] C. Galletti, G. Coraggio, and L. Tognotti, "Modelling oxy-coal flames in a semiindustrial furnace," *Journal of the International Flame Research Foundation*, 2014.

[140] A. J. Black, *Oxy-fuel combustion for carbon capture using computational fluid dynamics*. PhD thesis, Energy Technology and Innovation Innitiative, University of Leeds, 2014.

[141] P. Edge, P. Heggs, M. Pourkashanian, and P. Stephenson, "Integrated fluid dynamics-process modelling of a coal-fired power plant with carbon capture," *Applied Thermal Engineering*, vol. 60, no. 1, pp. 456 – 464, 2013.

[142] J.-E. A. Kim, C. Ryu, W. Yang, Y. J. Kim, H.-Y. Park, and H.-P. Kim, "Assessment of combustion and heat transfer in Youngdong

100 MWe retrofit boiler for demonstration of oxy-coal combustion," *International Journal of Greenhouse Gas Control*, vol. 17, pp. 250 – 258, 2013.

[143] W. Kordylewski, *Spalanie i paliwa*. Wroclaw: Oficyna Wydawnicza Politechniki Wroclawskiej, 2008.

[144] R. Kurose, H. Watanabe, and H. Makino, "Numerical Simulations of Pulverized Coal Combustion," *KONA Powder and Particle Journal*, vol. 27, pp. 144–156, 2009.

[145] D. Gera, M. P. Mathur, M. C. Freeman, and A. Robinson, "Effect of Large Aspect Ratio of Biomass Particles on Carbon Burnout in a Utility Boiler," *Energy & Fuels*, vol. 16(6), pp. 1523–1532, 2002.

[146] A. Williams, M. Pourkashanian, and J. Jones, "The combustion of coal and some other solid fuels," *Proceedings of the Combustion Institute*, vol. 28(2), pp. 2141–2162, 2000.

[147] Y. Çengel, *Heat and mass transfer: a practical approach*. McGraw-Hill, 2007.

[148] H. Kobayashi, J. B. Howard, and A. F. Sarofim, "Coal devolatilization at high temperatures," *Symposium (International) on Combustion*, vol. 16, pp. 411–425, 1977.

[149] D. Anthony, J. Howard, H. Hottel, and H. Meissner, "Rapid devolatilization of pulverized coal," *Symposium (International) on Combustion*, vol. 15(1), pp. 1303–1317, 1975.

[150] L. L. Baxter and A. L. Robinson, "Engineering Models of Biomass Combustion Processes. Biomass for Energy and Industry," 2000.

[151] J. Riaza, J. Gibbins, and H. Chalmers, "Ignition and combustion of single particles of coal and biomass," *Fuel*, vol. 202, pp. 650 – 655, 2018.

[152] M. M. Baum and P. J. Street, "Predicting the Combustion Behaviour of Coal Particles," *Combustion Science and Technology*, vol. 3(5), pp. 231–243, 1971.

[153] S. Badzioch and P. G. Hawksley, "Kinetics of thermal decomposition of pulverized coal particles," *Industrial & Engineering Chemistry Process Design and Development*, vol. 9(4), pp. 521–530, 1970.

[154] M. J. Wornat, R. H. Hurt, K. A. Davis, and N. Y. C. Yang, "Single-particle combustion of two biomass chars," *Symposium (International) on Combustion*, vol. 26, pp. 3075–3083, 1996.

[155] B. Magnussen and B. Hjertager, "On mathematical modeling of turbulent combustion with special emphasis on soot formation and combustion," *Symposium (International) on Combustion*, vol. 16(1), pp. 719–729, 1977.

[156] D. Fletcher, B. Haynes, F. Christo, and S. Joseph, "A CFD based combustion model of an entrained flow biomass gasifier," *Applied Mathematical Modelling*, vol. 24(3), pp. 165–182, 2000.

[157] J. Porteiro, J. Míguez, E. Granada, and J. Moran, "Mathematical modelling of the combustion of a single wood particle," *Fuel Processing Technology*, vol. 87(2), pp. 169–175, 2006.

[158] J. Larfeldt, "Modelling and measurements of the pyrolysis of large wood particles," *Fuel*, vol. 79(13), pp. 1637–1643, 2000.

[159] A. Saddawi, J. M. Jones, A. Williams, and M. A. Wójtowicz, "Kinetics of the thermal decomposition of biomass," *Energy & Fuels*, vol. 24(2), pp. 1274–1282, 2010.

[160] S. Gubba, L. Ma, M. Pourkashanian, and A. Williams, "Influence of particle shape and internal thermal gradients of biomass particles on pulverised coal/biomass co-fired flames," *Fuel Processing Technology*, vol. 92(11), pp. 2185–2195, 2011.

[161] M. Momeni, C. Yin, S. Knudsen Kær, and S. L. Hvid, "Comprehensive Study of Ignition and Combustion of Single Wooden Particles," *Energy & Fuels*, vol. 27(2), pp. 1061–1072, 2013.

[162] M. Momeni, C. Yin, S. K. Kær, T. B. Hansen, P. A. Jensen, and P. Glarborg, "Experimental Study on Effects of Particle Shape and Operating Conditions on Combustion Characteristics of Single Biomass Particles," *Energy & Fuels*, vol. 27(1), pp. 507–514, 2013.

[163] R. S. Miller and J. Bellan, "Analysis of Reaction Products and Conversion Time in the Pyrolysis of Cellulose and Wood Particles," 1996.

[164] C. Di Blasi, "Kinetic and Heat Transfer Control in the Slow and Flash Pyrolysis of Solids," *Industrial & Engineering Chemistry Research*, vol. 35(1), pp. 37–46, 1996.

[165] A. Bharadwaj, L. L. Baxter, and A. L. Robinson, "Effects of Intraparticle Heat and Mass Transfer on Biomass Devolatilization: Experimental Results and Model Predictions," *Energy & Fuels*, vol. 18(4), pp. 1021–1031, 2004.

[166] C. Di Blasi, "Influences of physical properties on biomass devolatilization characteristics," *Fuel*, vol. 76(10), pp. 957–964, 1997.

[167] R. Jalan and V. Srivastava, "Studies on pyrolysis of a single biomass cylindrical pellet - kinetic and heat transfer effects," *Energy Conversion and Management*, vol. 40(5), pp. 467–494, 1999.

[168] P. Horbaj, "Model of the Kinetics of Biomass Pyrolysis," *Drevársky Výskum*, vol. 42(4), pp. 15–23, 1997.

[169] T. Liliedahl and K. Sjöström, "Heat transfer controlled pyrolysis kinetics of a biomass slab, rod or sphere," *Biomass and Bioenergy*, vol. 15(6), pp. 503–509, 1998.

[170] A. Janse, R. Westerhout, and W. Prins, "Modelling of flash pyrolysis of a single wood particle," *Chemical Engineering and Processing: Process Intensification*, vol. 39(3), pp. 239–252, 2000.

[171] V. Benedetti, F. Patuzzi, and M. Baratieri, "Characterization of char from biomass gasification and its similarities with activated carbon in adsorption applications," *Applied Energy*, vol. 227, pp. 92 – 99, 2018.

[172] Y. B. Yang, V. N. Sharifi, J. Swithenbank, L. Ma, L. I. Darvell, J. M. Jones, M. Pourkashanian, and A. Williams, "Combustion of a Single Particle of Biomass," *Energy & Fuels*, vol. 22(1), pp. 306–316, 2008.

[173] H. Lu, W. Robert, G. Peirce, B. Ripa, and L. L. Baxter, "Comprehensive Study of Biomass Particle Combustion," *Energy & Fuels*, vol. 22(4), pp. 2826–2839, 2008.

[174] R. Weber, Y. Poyraz, A. M. Beckmann, and S. Brinker, "Combustion of biomass in jet flames," *Proceedings of the Combustion Institute*, vol. 35(3), pp. 2749–2758, 2015.

[175] R. Mehrabian, S. Zahirovic, R. Scharler, I. Obernberger, S. Kleditzsch, S. Wirtz, V. Scherer, H. Lu, and L. L. Baxter, "A CFD model for thermal conversion of thermally thick biomass particles," *Fuel Processing Technology*, vol. 95, pp. 96–108, 2012.

[176] J. Szuhanszki, *Advanced Oxy-fuel Combustion for Carbon Capture and Sequestration*. PhD thesis, Energy Technology and Innovation Innitiative, University of Leeds, 2014.

[177] T. Rooijmans, "Suction pyrometer user manual," 2012.

[178] MEDTHERM-Corporation, "Operating Instructions and Calibration Records. GTW-50-24-21584 Combination Furnace Heat Flux Probe," 2012.

[179] J. H. Harker and J. R. Backhurst, *Fuel and Energy*. London; New York: Academic Press, 1981.

[180] M. A. Field, D. W. Gill, B. B. Morgan, and P. G. W. Hawksley, *Combustion of pulverised coal*. The British Coal Utilisation Research Association, 1967.

[181] M. A. Boles and Y. A. Cengel, *Thermodynamics: An Engineering Approach*. Tata McGraw Hill, 2011.

[182] J. Szargut, *Termodynamika techniczna*. Gliwice: Wydawnictwo Politechniki Śląskiej, 2013.

[183] Y. A. Cengel and M. A. Boles, *Thermodynamics: An Engineering Approach*. Boston, London: McGraw-Hill, 2002.

[184] K. J. Wark and D. E. Richards, *Thermodynamics 6th edition*. Boston, London: WCB/McGraw-Hill, 1999.

[185] M. W. Chase, J. L. Curnutt, J. R. Downey, R. A. McDonald, A. N. Syverud, and E. A. Valenzuela, "JANAF Thermochemical Tables, 1982 Supplement," *Journal of Physical and Chemical Reference Data*, vol. 11, no. 3, p. 695, 1982.

[186] O. T. Stein, G. Olenik, A. Kronenburg, F. Cavallo Marincola, B. M. Franchetti, A. M. Kempf, M. Ghiani, M. Vascellari, and C. Hasse, "Towards comprehensive coal combustion modelling for LES," in *Flow, Turbulence and Combustion*, 2013.

[187] X. Wen, H. Jin, O. T. Stein, J. Fan, and K. Luo, "Large Eddy Simulation of piloted pulverized coal combustion using the velocity-scalar joint filtered density function model," *Fuel*, 2015.

[188] X. Wen, K. Luo, H. Jin, and J. Fan, "Large Eddy Simulation of piloted pulverised coal combustion using extended flamelet/progress

variable model," *Combustion Theory and Modelling*, vol. 21, no. 5, pp. 925–953, 2017.

[189] D. B. Spalding, "Mixing and chemical reaction in steady confined turbulent flames," *Symposium (International) on Combustion*, 1971.

[190] P. J. Edge, P. J. Heggs, M. Pourkashanian, P. L. Stephenson, and A. Williams, "A reduced order full plant model for oxyfuel combustion," *Fuel*, 2012.

[191] K. K. Pillai, "The Influence of Coal Type on Devolatilization and Combustion in Fluidized Beds," *Journal of the Energy Institute*, vol. 54, pp. 142–150, 1981.

[192] T. Kupka, K. Zając, and R. Weber, "Effect of Fuel Type and Deposition Surface Temperature on the Growth and Structure of an Ash Deposit Collected during Co-firing of Coal with Sewage Sludge and Sawdust," *Energy & Fuels*, vol. 23, pp. 3429–3436, 2009.

[193] R. Weber, T. Kupka, and K. Zając, "Jet flames of a refuse derived fuel," *Combustion and Flame*, vol. 156, no. 4, pp. 922–927, 2009.

[194] D. Pershing and J. Wendt, "Pulverized coal combustion: The influence of flame temperature and coal composition on thermal and fuel NO_x," *Symposium (International) on Combustion*, vol. 16, no. 1, pp. 389 – 399, 1977.

[195] G. Cao and R. Orrù, *Current Environmental Issues and Challenges*. SpringerLink : Bücher, Springer Netherlands, 2014.

[196] A. Ritchie, E. de Jonge, C. Hugi, and D. Cooper, "Service Contract on Ship Emissions: Assignment, Abatement and Market-based Instruments, Task 2c - SO_2 Abatement. Final Report." `https://ec.europa.eu/environment/air/pdf/task2_so2.pdf`, 2005.

[197] H. Teng and T.-S. Huang, "Control of NO_x emissions through combustion modifications for reheating furnaces in steel plants," *Fuel*, vol. 75, no. 2, pp. 149 – 156, 1996.

[198] S. Mahmoudi, J. Baeyens, and J. P. Seville, "NO_x formation and selective non-catalytic reduction (SNCR) in a fluidized bed combustor of biomass," *Biomass and Bioenergy*, vol. 34, no. 9, pp. 1393 – 1409, 2010.

[199] J. L. Sorrels, D. D. Randall, C. R. Fry, and K. S. Schaffner, "Selective Noncatalytic Reduction," *US Environmental Protection Agency: Washington, DC, USA*, 2015.

[200] Q. Guo, X. Chen, and H. Liu, "Experimental research on shape and size distribution of biomass particle," *Fuel*, vol. 94, pp. 551 – 555, 2012.

[201] J. Shao, K. Jan, and Y. Yan, "Comparative study of electrostatic sensors with circular and probe electrodes for velocity measurement of pulverised coal," *Yi Qi Yi Biao Xue Bao/Chinese Journal of Scientific Instrument*, 2007.

[202] J. Shao, J. Krabicka, and Y. Yan, "Velocity measurement of pneumatically conveyed particles using intrusive electrostatic sensors," in *IEEE Transactions on Instrumentation and Measurement*, 2010.

[203] R. M. Carter, Y. Yan, and S. D. Cameron, "On-line measurement of particle size distribution and mass flow rate of particles in a pneumatic suspension using combined imaging and electrostatic sensors," *Flow Measurement and Instrumentation*, 2005.

[204] H. Wadell, "The coefficient of resistance as a function of Reynolds number for solids of various shapes," *Journal of the Franklin Institute*, vol. 217(4), pp. 459–490, 1934.

[205] H. Wadell, "Volume, Shape, and Roundness of Quartz Particles," *The Journal of Geology*, vol. 43, no. 3, pp. 250–280, 1935.

[206] P. Mason, L. Darvell, J. Jones, and A. Williams, "Comparative Study of the Thermal Conductivity of Solid Biomass Fuels," *Energy Fuels*, vol. 30(3), pp. 2158–2163, 2016.